

TRANSPORT AND MAGNETIC PROPERTIES OF CORRELATED ELECTRON SYSTEMS

BY WENHU XU

A dissertation submitted to the
Graduate School—New Brunswick
Rutgers, The State University of New Jersey
in partial fulfillment of the requirements
for the degree of
Doctor of Philosophy
Graduate Program in Physics and Astronomy

Written under the direction of
Gabriel Kotliar
and approved by

New Brunswick, New Jersey

October, 2014

© 2014

Wenhu Xu

ALL RIGHTS RESERVED

ABSTRACT OF THE DISSERTATION

Transport and Magnetic Properties of Correlated Electron Systems

by Wenhui Xu

Dissertation Director: Gabriel Kotliar

This thesis investigates the transport and magnetic properties of correlated electron systems in the framework of dynamical mean field theory.

In Chapter 2, the bad metallic transport in a doped Mott insulator is described by the Boltzmann theory of a hidden Fermi liquid, in which the quasiparticle scattering rate follows quadratic temperature and energy dependence far beyond the canonical Fermi liquid scale T_{FL} . The quasiparticle renormalization is strongly dependent on temperature and energy, giving rise to the non-Fermi liquid transport, such as linear-in- T resistivity.

Chapter 3 focuses on the thermoelectric power of correlated metals. The thermoelectric power in the high-frequency limit S^* and in the Kelvin formula S_K are compared with the transport limit S_0 . S^* and S_K can be computed with much less effort than S_0 . S_K captures the contribution from renormalized density of states and is a better approximation of S_0 for a strongly correlated metal, while for a weakly correlated metal, when S_0 is dominated by the band velocity contribution, S^* is a better indicator of S_0 .

In Chapter 4, the phase diagram of a periodic Anderson model with the hybridization strength V as the tuning parameter is studied. The vanishing of the heavy Fermi liquid phase, characterized by a diminishing Fermi liquid scale T_{FL} , is accompanied by

the emergence of antiferromagnetic ordering. The dynamic spin susceptibility in the vicinity of magnetic instability indicates a momentum-independent, or localized picture of critical spin fluctuations.

Chapter 5 discusses the the colossal Nernst effect and anomalies of the magnetoresistance in correlated semiconductor FeSb_2 . A phenomenological analysis based on Boltzmann theory suggests that a highly dispersive quasiparticle relaxation time is the key to understand the anomalous transport in FeSb_2 .

Preface

Majority of the work in Chapter 2 is published in “**Hidden Fermi Liquid, Scattering Rate Saturation, and Nernst Effect: A Dynamical Mean-Field Theory Perspective**”, Wenhu Xu, Kristjan Haule, and Gabriel Kotliar, *Phys. Rev. Lett.* 111, 036401 (2013).

Part of the work in Chapter 3 is published in “**High-frequency thermoelectric response in correlated electronic systems**”, Wenhu Xu, Cédric Weber, and Gabriel Kotliar, *Phys. Rev. B* 84, 035114 (2012).

The work in Chapter 4 is original and in preparation for publication.

Part of the work in Chapter 5 is published in “**Highly dispersive electron relaxation and colossal thermoelectricity in the correlated semiconductor FeSb₂**”, Peijin Sun, Wenhu Xu, Jan M. Tomczak, Gabriel Kotliar, Martin Sørdergraad, Bo B. Iversen, and Frank Steglich, *Phys. Rev. B* 88, 245203 (2014).

Acknowledgements

First of all, I would like to thank my advisor, Gabriel Kotliar for his direction and encouragement throughout this thesis work. Working with Gabi has been a challenging and exciting experience. I also appreciate him for the financial support during the last few years.

I am very grateful to Kristjan Haule for his willingness to share his wisdom and knowledge in condensed matter physics and scientific computing.

I would like to thank Cédric Weber for his guidance and help in the early stage of my candidacy years. Also many thanks go to former and current members in the group, Adriano, Jan, Hyowon, Nicola, Xiaoyu, and Hongbin, for many interesting and fruitful discussions.

Special thanks to my friends, Xueyun, Bin, Yuanjun, Wenshuo, Wei, Can, Yanan and Qibin, for the jokes, news, random or deep thoughts shared at lunch time and in the office.

I would like to thank Weida Wu, Greg Moore, and Camille Aron for participating in my thesis committee.

Last but not least, this thesis is dedicated to my parents, for their love and patience.

Table of Contents

Abstract	ii
Preface	iv
Acknowledgements	v
List of Figures	ix
1. Introduction	1
1.1. Landau's Fermi Liquid	1
1.2. Anomalous Transport and Magnetic Properties in Correlated Electron Materials	3
1.3. The Linear Response Theory	7
1.4. Dynamical Mean Field Theory	13
1.4.1. Two-particle Correlation Functions in DMFT	14
1.4.2. Impurity Solvers	15
1.5. Outline	17
2. Hidden Fermi Liquid	19
2.1. Quasiparticles in a Doped Mott Insulator	20
2.2. Transport in Hidden Fermi Liquid	23
2.2.1. Boltzmann Theory of Quasiparticle Transport	23
2.2.2. Scattering Rate Saturation	24
2.2.3. Non-Fermi liquid Transport	27
2.3. Spectral Properties of Hidden Fermi Liquid	30
2.3.1. The Fermi Energy of Hidden Quasiparticles	30
2.4. Spin Fluctuations	33

2.4.1.	Local Spin Fluctuations	33
2.4.2.	The Lattice Spin Susceptibility	38
2.5.	Conclusion	44
3.	Thermoelectric Power in Correlated Metal	46
3.1.	Thermoelectric power at finite frequency	48
3.1.1.	General formalism	48
3.1.2.	The high-frequency limit L_{ij}^*	50
3.2.	Kelvin formula	54
3.3.	Analytic and Numerical Results in a One-band Hubbard Model	54
3.3.1.	Low temperature limit.	58
3.3.2.	High temperature limit.	63
3.3.3.	Numerical results	65
3.4.	Conclusion	69
4.	Local Magnetism in Periodic Anderson Model	70
4.1.	Phase diagram	72
4.2.	The heavy Fermi liquid	72
4.3.	Lattice susceptibility and antiferromagnetic ordering	75
4.3.1.	Static susceptibility	75
4.3.2.	Dynamic susceptibility	79
4.3.3.	The Fermi surface	82
4.4.	Conclusion	89
5.	Thermoelectricity in FeSb₂	90
5.1.	Linear Response Theory in a Weak Magnetic Field	91
5.2.	Experimental Facts on FeSb ₂	93
5.3.	The Boltzmann Transport Theory	95
5.4.	Conclusion	102

Appendix A. Retarded two-particle correlation function in the Keldysh formalism	103
Appendix B. Analytical Continuation	111
B.1. Padé Approximant	111
B.2. Maximum Entropy Method	112
B.3. Dynamic Local Spin Susceptibility	113
Appendix C. General Sommerfeld Expansion	116
Appendix D. Linear Response Theory of Thermo- and Magneto-electric Transport	120
D.1. Thermal Transport	120
D.2. Hall Conductivity in a Weak Magnetic Field	123
References	132

List of Figures

1.1.	Quasiparticle scattering near the Fermi surface.	2
1.2.	Resistivity of copper-oxide high-temperature superconductors (left) and ruthenates (right). Reprinted from Ref. [1]. Copyright (2003) by the American Physical Society.	4
1.3.	Thermopower of $\text{La}_{1-x}\text{Sr}_x\text{VO}_3$. The compound is insulating for $x =$ 0.00 and $x = 0.10$ and metallic for other doping levels. Reprinted from Ref. [2]. Copyright (2011) by the American Physical Society.	5
1.4.	(a): Doping-driven phase diagram of $\text{CeCu}_{6-x}\text{Au}_x$. (b) and (c): \mathbf{Q} -dependence of the dynamical magnetic susceptibility, $\Im\chi(\mathbf{Q}, E)$ for $\text{CeCu}_{5.9}\text{Au}_{0.1}$ along the middle and lower trajectory in the inset of (a) at fixed $E = 0.035\text{meV}$ and at selected temperatures. Reprinted by permission from Macmillan Publishers Ltd: Nature ([3]), copyright (2000).	7
1.5.	Diagrammatic representation of the ladder expansion of the two-particle correlation function $\Pi(i\omega_n, i\omega_{n'}; i\Omega_m \mathbf{k}, \mathbf{k}'; \mathbf{q})$. See Eq. 1.24.	12
1.6.	Diagrammatic representation of Bethe-Salpeter of vertex function $\Gamma(i\omega_n, i\omega_{n'}; i\Omega_m \mathbf{k}, \mathbf{k}'; \mathbf{q})$. See Eq. 1.25.	12
1.7.	DMFT self-consistent loop.	14
2.1.	Spectral function $A_{\mathbf{k}}(\omega)$ along $\Gamma - X - M - \Gamma$ in Brillouin zone at (a) $T = 0.0075$, (b) $T = 0.025$, (c) $T = 0.1$, and (d) $T = 0.125$. (e) Local density of states. (f) Roots of Eq. 2.3 at different temperatures.	21

2.2.	Transport properties. (a) Resistivity. (b) Hall angle. (c) Seebeck coefficient. (d) Nernst coefficient. Points labeled “exact exp.” are obtained using Eqs. 2.6. Points labeled “QP approx.” are obtained using Eqs. 2.8. Points labeled “expansion” are obtained using the general Sommerfeld expansion detailed in App. C. The units are expressed in terms of universal constants, \hbar , k_B , e , in-plane lattice constant a , and out-of-plane lattice constant c	25
2.3.	(a) Quasiparticle scattering rate $\Gamma_{\mathbf{k}_F}^*$. The inset shows the estimation of $(k_F l^*)^{-1}$. (b) $\Gamma_{\mathbf{k}_F}^*$ as a function of T^2 for $T \lesssim T_{sat}/2$. (c) Quasiparticle renormalization factor $Z_{\mathbf{k}_F}$ for $T \lesssim T_{sat}/2$	26
2.4.	Bulk spin susceptibility χ_{bulk} (a) and charge susceptibility $dn/d\mu$ (b). The inset of (a) shows $1/\chi_{bulk}$	28
2.5.	Spectral function $A_{\mathbf{k}}(\omega)$ (red solid line) for (a) $\mathbf{k} = (0.38\pi, 0.38\pi)$ and (b) $\mathbf{k} = (0.54\pi, 0.54\pi)$. $T = 0.015$. The black dashed line is the Lorentzian function whose parameters are determined by the poles of Green’s function $G_{\mathbf{k}}(\omega)$	31
2.6.	(a): QP scattering rate as a function of QP energy. The dashed lines are quadratic functions which fit the low energy part of the scattering rate. (b): QP renormalization. The upper horizontal line marks $Z_{Hub} = 1 - n/2 = 0.575$, which is the renormalization factor of the lower Hubbard band given by Hubbard I approximation. The lower horizontal line marks $Z_G = \delta = 0.15$, which is the renormalization factor at $T = 0$ given by the Gutzwiller approximation.	32
2.7.	(a): QP scattering rate and the imaginary part of self energy. $T = 0.005$. (b): Emergence of Fermi liquid scaling of self energy.	32
2.8.	$\chi_S(\omega)$ in the local moment regime. Imaginary part (left) and real part (right).	34
2.9.	$\chi_S(\omega)$ in the hidden Fermi liquid regime. Imaginary part (left) and real part (right).	35

2.10. $\chi_S(\omega)$ in the Fermi liquid regime. Imaginary part (left) and real part (right).	35
2.11. Cumulative spectral weight of local dynamic spin susceptibility.	36
2.12. (a): Static local susceptibility χ_S^0 . (b): Local spin fluctuation energy scale Γ . Red crosses are found by locating the maximum of $\Im\chi_S(\omega)$. Black dots are obtained by fitting the low energy slope of $\Im\chi_S(\omega)$	38
2.13. (a): Spin-lattice relaxation time. (b) The deviation from Korringa-Shiba relation.	39
2.14. Upper: \mathbf{Q} -dependent static magnetic susceptibility for $Q = (0, 0)$ (black), $(\pi/2, \pi/2)$ (red), $(3\pi/4, 3\pi/4)$ (blue), $Q_m \simeq (0.88\pi, 0.88\pi)$ (green) and (π, π) (yellow). Lower: Fermi Surface at $T = 0.0025$. The black arrow indicates the nesting vector, which is $Q_N \simeq (0.95\pi, 0.95\pi)$	42
2.15. \mathbf{Q} -dependent dynamic susceptibility $\chi''(\mathbf{Q}, \omega)$ along the contour $(0, 0) - (\pi, \pi) - (\pi, 0) - (0, 0)$ for various temperatures.	43
3.1. $U = 1.75D$ and $n = 0.85$. (a): S_0 , S_K , S^* and S^{**} as function of temperature. The dashed lines represents the high temperature limit S_{MH} using Mott-Heikes formula. (b): Chemical potential μ . Red dots are from DMFT simulation with n fixed to 0.85. Black line is interpolation to the red dots. Blue line is computed from atomic limit.	67
3.2. $U = 0.75D$ and $n = 0.8$. S_0 , S_K , S^* and S^{**} as function of temperature. The dashed lines represents the high temperature limit S_{MH} using Mott-Heikes formula.	68

4.1.	V - T phase diagram of periodic Anderson model. (a) “Small Fermi surface” denotes the phase with decoupled conduction electrons and local moments. “Large Fermi surface” denotes the phase of heavy Fermi liquid, where the composite quasiparticles have a large Fermi surface. They are separated for small V by a line of orbital selective Mott transition (T_{MI}), which extends to a crossover for larger values of V , as indicated by blue dashed lines. See Sec. 4.3.3. (b) The red dashed line marks the trend of T_{FL} extracted from T^2 behavior of resistivity (See Sec. 4.2). The black dashed line marks the antiferromagnetic ordering temperature (See. 4.3.1).	73
4.2.	Resistivity ρ as a function of T^2 for $V = 3.0, 2.5, 2.25, 2.0$. The dashed line is obtained by fitting a few points at lowest temperatures along with the origin ($T^2 = 0, \rho = 0$) to a linear function.	74
4.3.	The quasiparticle scattering rate and quasiparticle weight of c -electrons, for $V = 3.0$ ((a) and (c)) and $V = 2.25$ ((b) and (d)). The scattering rate is dependent on T^2 to emphasize its similar behavior to resistivity.	75
4.4.	Bulk susceptibility of a heavy Fermi liquid system.	76
4.5.	Static magnetic susceptibility $\chi(\mathbf{Q})$ for (from above to below) $V = 2.5$ and $V = 2.0$. On the left side is $\chi(\mathbf{Q})$ as a function of \mathbf{Q} along $(0, 0, 0)$ to (π, π, π) for different temperatures. On the right hand side is $\chi(\mathbf{Q}, T)$ as a function of temperature T for $\mathbf{Q} = 0$ (bulk susceptibility), $\mathbf{Q} = \mathbf{Q}_N = (0.72\pi, 0.72\pi, 0.72\pi)$ and also local susceptibility χ_{loc} , on logarithmic scales.	76
4.6.	Static magnetic susceptibility $\chi(\mathbf{Q})$ for (from above to below) $V = 1.75$ and $V = 1.5$. On the left side is $\chi(\mathbf{Q})$ as a function of \mathbf{Q} along $(0, 0, 0)$ to (π, π, π) for different temperatures. On the right hand side is $\chi(\mathbf{Q}, T)$ as a function of temperature T for $\mathbf{Q} = 0$ (bulk susceptibility), $\mathbf{Q} = \mathbf{Q}_N = (0.72\pi, 0.72\pi, 0.72\pi)$ and also local susceptibility χ_{loc} , on logarithmic scales.	77
4.7.	The Kondo temperature T_K as a function of hybridization.	78
4.8.	$1/\chi(\mathbf{Q})$ for $V = 1.5$, $V = 1.4$ and $V = 1.3$ at low temperatures.	80

4.9. Imaginary part of dynamic magnetic susceptibility $\Im\chi(\mathbf{Q}, E)$ with $\mathbf{Q} = \mathbf{Q}_N = (0.72\pi, 0.72\pi, 0.72\pi)$ at selected temperatures. $V = 2.0$ leads to a paramagnetic Fermi liquid ground state, while $V = 1.5$ is in the close vicinity of antiferromagnetic instability at $T_N \simeq 0$	81
4.10. Imaginary part of dynamic susceptibility along the selected contour in Brillouin zone $((0, 0, 0) - (\pi, \pi, \pi) - (\pi, 0, 0) - (0, 0, 0))$ for $V = 2.0$ (left) and $V = 1.5$ (right) at selected temperatures.	83
4.11. Energy cut of dynamic magnetic susceptibility. Figure in the above shows the energy cut at $E = 0.001$ of $\Im\chi(\mathbf{Q}, E)$ of periodic Anderson lattice with $V = 1.5$, for selected temperatures. \mathbf{Q} along the diagonal direction from $(0, 0, 0)$ to (π, π, π) . Figure in the below shows experimental data from inelastic neutron scattering on $\text{CeCu}_{5.9}\text{Au}_{0.1}$. Reprinted by permission from Macmillan Publishers Ltd: Nature ([3]), copyright (2000). . .	84
4.12. Cut of Fermi surface at $k_z = 0$ for $V = 2.0$ (above), $V = 1.5$ (middle) and $V = 1.3$ (below). On the left is the Fermi surface cut of c -electrons. On the right is the Fermi surface cut of f -electrons. $T = 0.01$	86
4.13. Cut of Fermi surface at $k_z = 0$ for $V = 2.0$ for $T = 1.0$. On the left is the Fermi surface cut of c -electrons. On the right is the Fermi surface cut of f -electrons.	87
4.14. Effective hybridization, defined as $-\sum_k G_{cf}(k, i\omega = \pi T)$, as a function of V at $T = 0.02$, $T = 0.005$ and $T = 0.0025$. Points of $T = 0.02$ are obtained by CTQMC, and points at $T = 0.005$ and $T = 0.0025$ are obtained using ED impurity solver.	87
4.15. $\Im\Sigma_f(i\omega)$ for $V = 0.5$	88
5.1. Resistivity $\rho(T)$ (main panel) and Hall coefficient $R_H(T)$ measured at $B = 1T$ [inset (a)] for FeSb_2 and FeAs_2 . Inset (b): isothermal Hall resistivity $\rho_H(B)$ for FeSb_2 . Reprinted from Ref. [4]. Copyright (2013) by the American Physical Society.	94

5.2.	(a) Thermopower $S(T)$ and (b) Nernst coefficient $\nu(T)$ for FeSb ₂ and FeAs ₂ . The inset of (a) shows the thermal conductivity. The inset of (b) shows $\nu(T)$ in a double-log scale. Notice that the magnitude of $\nu(T)$ of FeSb ₂ is larger than that of FeAs ₂ by two orders. Reprinted from Ref. [4]. Copyright (2013) by the American Physical Society.	96
5.3.	Electrical and thermal Hall mobility, μ_H and μ_t , of FeSb ₂ and FeAs ₂ . The inset shows the dimensionless ratio $(\nu/\mu_H)/(k_B/e)$ for the two systems. Reprinted from Ref. [4]. Copyright (2013) by the American Physical Society.	97
5.4.	The magnetoresistance $MR(T)$ for FeSb ₂ (main panel) and FeAs ₂ (inset) at selected magnetic fields. Re-scaled squared Hall mobility, $\mu_H^2(T)$ is shown by the green dashed lines. For FeAs ₂ , the similar temperature dependence of $MR(T)$ and $\mu_H^2(T)$ is evident over a broad range of temperature ($10K < T < 100K$), while for FeSb ₂ , $MR(T)$ and $\mu_H^2(T)$ show very different temperature dependence. Reprinted from Ref. [4]. Copyright (2013) by the American Physical Society.	98
B.1.	Dynamic local susceptibility at $T \simeq 0.00156$. Left: $\chi_S(i\Omega)$ on imaginary axis. Right: $\Im\chi_S(\omega)$ on real axis, obtained by Padé approximants using values of $\chi_S(i\Omega)$ of different number on Matsubara frequencies, and obtained by the MaxEnt method (red cross).	114
B.2.	Dynamic local susceptibility at $T = 0.0075$. Left: $\chi_S(i\Omega)$ on imaginary axis. Right: $\Im\chi_S(\omega)$ on real axis, obtained by Padé approximants and the MaxEnt method.	115
B.3.	Dynamic susceptibility at $T = 0.02$. Left: $\Im\chi_S(\omega)$. Right: $\Re\chi_S(\omega)$ and $\chi_S(i\Omega)$	115
C.1.	Conductivities computed using Eq. C.1 (“QP approx.”) and using the general Sommerfeld expansion of Eq. C.9 — C.12 (“expansion”).	119

Chapter 1

Introduction

1.1 Landau's Fermi Liquid

The band theory of electronic structure [5] is the standard theory of solids. It has achieved extraordinary success in describing structural, magnetic, transport, and spectroscopic properties of simple metals, semiconductors, and insulators. The band theory treats weakly interacting electrons moving in a periodic potential of nuclei. The Coulomb interactions between electrons are treated by perturbation theory and, in the density functional theory, by the local density approximation, general gradient approximation, or the GW method, for realistic electronic structure calculations [6, 7, 8, 9, 10].

The “ansatz” of the nearly free electrons in solids is not trivial. Its validity roots in the Fermi liquid theory, which was proposed by L. Landau [11], and later developed [12] by means of diagrammatic techniques and renormalization group. In the renormalization group formulation [13], the Coulomb interaction flows to zero as the energy cutoff approaches to the Fermi surface. Hence the low-energy excitations of interacting electrons can be understood as non-interacting fermions with renormalized parameters, e.g., the effective mass. These low-energy excitations are also termed as “quasiparticles”. In solids, the width of the electron bands (the Fermi energy) near the Fermi surface is a few eV s. Therefore the picture of quasiparticles is justified for temperature of $\leq 10^3 K$, relevant to most condensed matter experiments and applications.

Quasiparticles are charge carriers. At low temperature, the resistivity of a Fermi liquid follows a quadratic temperature dependence, $\rho \simeq \rho_0 + aT^2$. The residue resistivity ρ_0 is usually small and attributed to elastic scattering of non-magnetic impurities. The

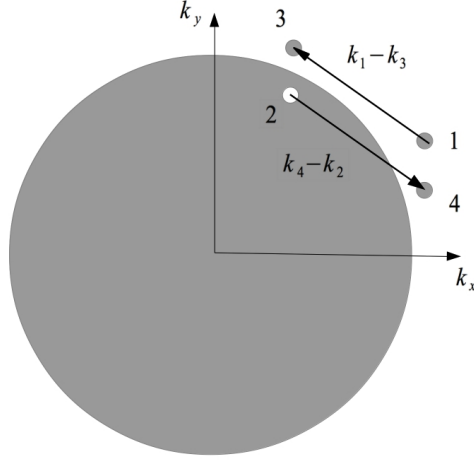


Figure 1.1: Quasiparticle scattering near the Fermi surface.

T^2 term comes from the residue Coulomb interaction between quasiparticles. This can be understood based on Pauli exclusion principle and the conservation of energy [14].

Consider a quasiparticle with momentum \mathbf{k}_1 above the Fermi surface interacts with another one with \mathbf{k}_2 below the Fermi surface, as illustrated in Fig. 1.1. As a result, two quasiparticles with \mathbf{k}_3 and \mathbf{k}_4 emerge above the Fermi surface. By the Fermi's golden rule, the scattering rate is

$$\frac{1}{\tau} \propto \int \delta(\epsilon_1 + \epsilon_2 - \epsilon_3 - \epsilon_4) d^3 p_2 d^3 p_3, \quad (1.1)$$

where $\epsilon_i = \hbar^2 k_i^2 / (2m) - E_F$ is the quasiparticle excitation energy. \mathbf{k}_2 and \mathbf{k}_3 are confined within a narrow shell of width $\sim \epsilon_1$. Thus the scattering rate is proportional to $(\epsilon_1 / E_F)^2$. At low temperature, only quasiparticles with $\epsilon_1 \sim k_B T$ can be excited and participate in the transport, thus $\rho \propto 1/\tau \propto T^2$.

Another consequence of the Pauli principle is that the heat capacity and thermopower of a Fermi liquid is small. At low temperature, the total energy of excited quasiparticles near the Fermi surface is $\delta E \simeq \frac{1}{2} (k_B T)^2 \rho_F$, where ρ_F is the density of states at the Fermi surface. Therefore the heat capacity is linear in temperature

$c_V = \partial E / \partial T \propto k_B (k_B T) / E_F$. This also leads to small thermopower, or Seebeck coefficient. The thermopower S measures the entropy s carried by each charge carrier [15]. Since $c_V = T(\partial s / \partial T)$, S is also linear in temperature and $S \sim (k_B / e)(k_B T / E_F)$ at low temperature.

It is very helpful to estimate the magnitude of resistivity and thermopower of a Fermi liquid. The vanishing scattering rate $1/\tau \propto T^2$ indicates the mean free path of quasiparticles is much larger than the lattice spacing, $l \gg a \sim 1/k_F$ and a Fermi liquid is a good metal. The Drude formula applies

$$\rho \simeq \frac{\hbar}{e^2} \frac{3\pi^2}{k_F^3 l} \sim \frac{\hbar a}{e^2} \frac{1}{k_F a} \ll \frac{\hbar a}{e^2} \sim 1 m\Omega \cdot cm. \quad (1.2)$$

Remind that $E_F \sim 1eV$ in solids, the thermopower is approximately

$$S \sim \frac{k_B}{e} \frac{k_B T}{E_F} \simeq 86 \mu V / K \times \frac{k_B T}{E_F} \ll 86 \mu V / K. \quad (1.3)$$

A simple metal conforms to these estimations. For example, the resistivity of copper at room temperature is $1.68 \times 10^{-3} m\Omega \cdot cm$, and the thermopower of copper at room temperature is $1.84 \mu V / K$.

1.2 Anomalous Transport and Magnetic Properties in Correlated Electron Materials

During last decades, the advancements in experimental techniques have helped discover more and more complex compounds that fall outside the scope of Landau's Fermi liquid theory. These compounds include, to name a few, transition metal oxides, organic superconductors, and heavy fermion systems. They are characterized by the strong Coulomb interaction between electrons on the localized orbitals such as d - and f -shells and are categorized as **correlated electron materials**. Fig. 1.2 and Fig. 1.3 show the resistivity and thermopower in some transition metal oxides to illustrate key aspects of the anomalous behaviors of correlated electron materials.

Fig. 1.2 compiles the resistivity of copper-oxide high temperature superconductors (left) and ruthenates (right). The positive $d\rho/dT$ slope extends to as much as one thousand Kelvin, while the magnitude of resistivity extends to a few $m\Omega \cdot cm$. The

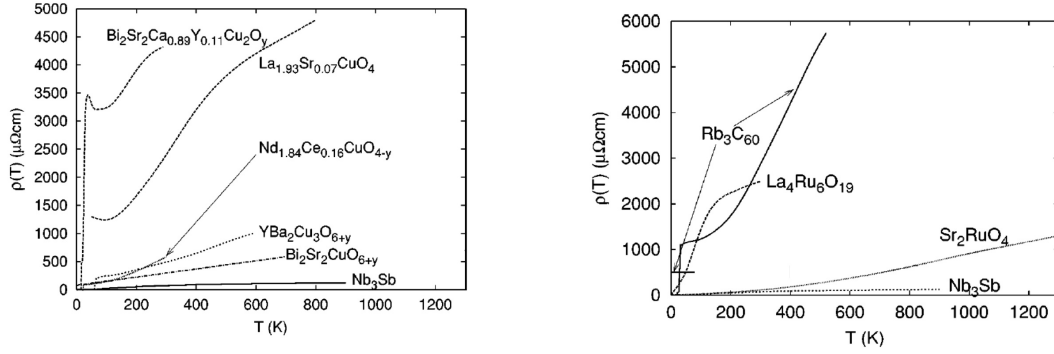


Figure 1.2: Resistivity of copper-oxide high-temperature superconductors (left) and ruthenates (right). Reprinted from Ref. [1]. Copyright (2003) by the American Physical Society.

Drude formula (Eq. 1.2) would lead to a short mean free path of a few Ås, which is comparable to the lattice constant. This means the quasiparticles undergo scattering events so frequently that it may not sustain its individuality for more than a few unit cells. The validity of quasiparticles as well-defined excitations carrying charge and energy is thus under question. Materials with a positive $d\rho/dT$ and resistivity of $m\Omega\cdot\text{cm}$ are also called “**bad metals**”.

The Drude formula is only a crude approximation based on a semi-classical picture of electrons, thus it is not yet undoubtful that resistivity of $m\Omega\cdot\text{cm}$ should indicate a short mean free path and breakdown of quasiparticles. But Emery and Kivelson [16] made a step forward. They argued that as the temperature was lowered, no crossover occurred in the temperature dependence of resistivity, hence the breakdown of quasiparticles at high temperature should persist at low temperature, indicating a **non-Fermi liquid** ground state.

Let us turn to the thermopower. Fig. 1.3 shows the thermopower of $\text{La}_{1-x}\text{Sr}_x\text{VO}_3$ for various doping levels. At $x = 0.00$ and $x = 0.10$, the compound is a Mott-insulator. The Coulomb interaction on d -orbitals dominates and localizes the electrons. As more holes are doped, the carriers acquire kinetic energy and the compound undergoes an insulator-to-metal transition. The thermopower of the metallic states increases rapidly with temperature and reaches to more than $\sim 20\mu\text{V}/\text{K}$ at 300K for doping from $x = 0.12$ to 0.18 .

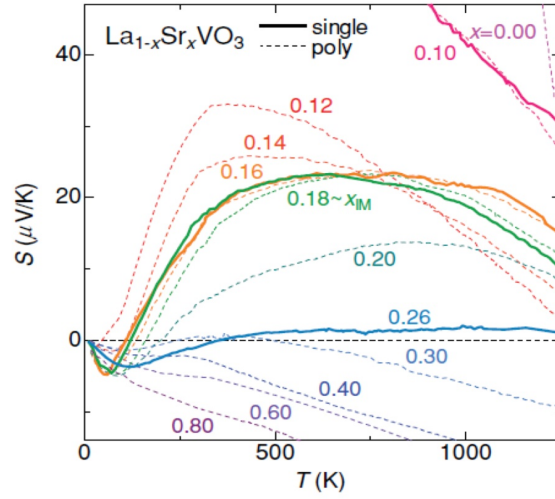


Figure 1.3: Thermopower of $\text{La}_{1-x}\text{Sr}_x\text{VO}_3$. The compound is insulating for $x = 0.00$ and $x = 0.10$ and metallic for other doping levels. Reprinted from Ref. [2]. Copyright (2011) by the American Physical Society.

Besides, the thermopower exhibits a non-monotonic dependence on temperature. The large thermopower at 300K would indicate a large portion of electrons, comparable to the total volume of the Fermi sphere, are excited and their entropy is transported with charge current. This suggests the Fermi energy is $E_F \sim 10^3\text{K} \sim 0.1\text{eV}$, much smaller than the width of d -bands from LDA calculations.

Another class of correlated electron materials is the heavy fermion systems. Unlike the transition metal oxides where the d -orbitals play the dual role of localized and itinerant degrees of freedom, in its simplest picture (the periodic Anderson model), a heavy fermion system is composed of local degrees of freedom (f -orbitals in most cases) and the bath of itinerant (conducting) electrons. Examples of heavy fermion systems include $\text{CeCu}_{6-x}\text{Au}_x$, $\text{Ce}_{1-x}\text{La}_x\text{Ru}_2\text{Si}_x$, CeCu_2Si_2 , CeCoIn_2 and so on [17]. At high temperature, the local moments are effectively independent of the conduction bath. The temperature dependence of magnetic susceptibility follows a Curie's law, $\chi(T) \propto 1/T$ and the conduction bath can be considered as a band of weakly interacting electrons. As temperature is lowered, the screening of the local moments (the Kondo effect) takes place due to the hybridization between the local and itinerant degrees of

freedom. At low temperature, a Fermi liquid ground state emerges, as manifested by a T^2 -dependence in resistivity below a scale T_{FL} of usually a few Kelvins. Surprisingly, specific heat measurement indicates the effective mass of quasiparticles in the Fermi liquid can be as large as hundreds of that of weakly interacting electrons, giving the name “**heavy fermion**”.

The Fermi liquid scale T_{FL} can be controlled by external parameters, such as pressure, doping, and magnetic field. A class of fascinating phenomena is that when T_{FL} is tuned to zero, ordering electronic state, such as superconductivity or magnetism could emerge. Fig. 1.4 shows the phase diagram of $\text{CeCu}_{6-x}\text{Au}_x$ with the doping as a tuning parameter. The dashed line in Fig. 1.4 (a) sketches T_{FL} as the doping approaches to $x \simeq 0.1$, while the red line indicates antiferromagnetic transition temperature T_N when $x \geq 0.1$. The vanishing of T_{FL} suggests the Kondo screening becomes barely effective and the local moments should behave like free spins in the paramagnetic regions above T_{FL} . To understand how the antiferromagnetic ordering could emerge from the nearly-free spins, the nature of spin fluctuations in the vicinity of $T_{FL} \simeq 0$ and $T_N \simeq 0$, which can be measured by the dynamic spin susceptibility in neutron scattering experiments, is of central interest.

Summarily, the transport and magnetic properties of correlated electron materials exhibits unconventional behaviors that fall outside the scope of standard band theory and Landau’s Fermi liquid theory. Simple estimation based on the Drude formula (Eq. 1.2 and Eq. 1.3) leads to consequences that can possibly disintegrate the quasiparticle picture. In the heavy fermion systems, the Fermi liquid ground state is sensitive to external parameters (pressure, doping, magnetic field) and magnetic and/or superconducting order emerges in the vicinity of the vanishing Fermi liquid. The interplay between the itinerant and localized character of electrons is the source of these exotic phenomena and also poses unprecedented challenges and opportunities to condensed matter theorists.

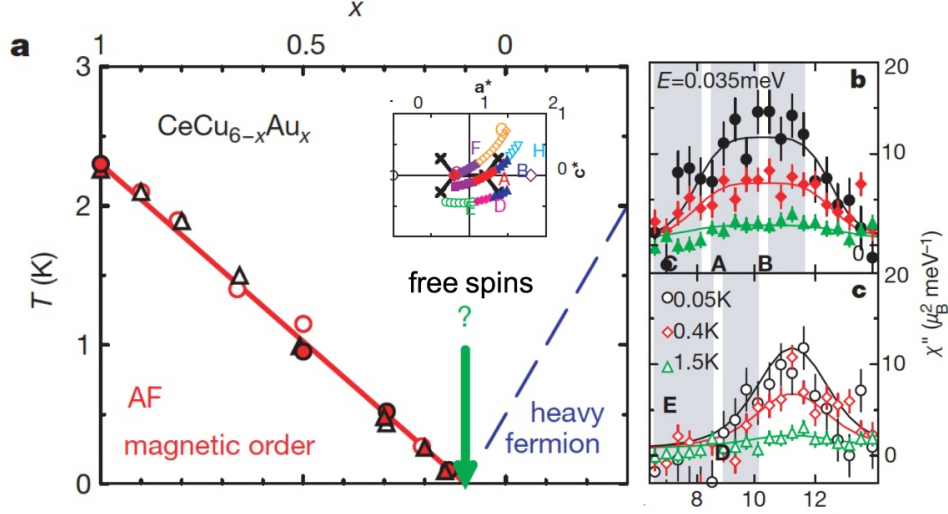


Figure 1.4: (a): Doping-driven phase diagram of $\text{CeCu}_{6-x}\text{Au}_x$. (b) and (c): \mathbf{Q} -dependence of the dynamical magnetic susceptibility, $\Im\chi(\mathbf{Q}, E)$ for $\text{CeCu}_{5.9}\text{Au}_{0.1}$ along the middle and lower trajectory in the inset of (a) at fixed $E = 0.035\text{meV}$ and at selected temperatures. Reprinted by permission from Macmillan Publishers Ltd: Nature ([3]), copyright (2000).

1.3 The Linear Response Theory

The theoretical efforts to understand the correlated electron systems in this thesis are mainly based on analytic and numerical calculation of transport properties (resistivity, thermopower, Hall mobility, Nernst coefficient) and magnetic susceptibilities of model Hamiltonian of correlated electrons. Transport and magnetic response functions in a solid are formulated in the framework of Kubo's linear response theory [18].

For completeness and without losing generality, I derive the electrical conductivity at finite temperature as an illustrating example, which follows the presentation in standard textbook [19].

Assume a system is described initially by an unperturbed Hamiltonian operator H . The density matrix at initial time is the time-independent density matrix at equilibrium state, $\rho_0 = \exp(-\beta(H - \mu N))/Z$. A time-dependent perturbation H' is adiabatically switched on. $H' = 0$ at the initial time at $t = -\infty$. I save the explicit argument of time $H'(t)$ for the Heisenberg picture of H' , $H'(t) = \exp(iHt)H'\exp(-iHt)$. The time-dependent density matrix $\rho(t)$ for the system with H' satisfies the equation of

motion

$$\frac{d\rho(t)}{dt} = -i[H + H', \rho(t)]. \quad (1.4)$$

The expectation value of the electric current driven by $H'(t)$ is

$$J_\alpha^e = Tr[\hat{j}_\alpha^e \rho(t)]. \quad (1.5)$$

\hat{j}_α^e is the α -component of the **charge** current operator.

It is convenient to separate the time-dependence due to H' in $\rho(t)$, by writing $\rho(t) = \rho_0 + f(t)$. Thus $f(-\infty) = 0$ and the leading order in $f(t)$ is proportional to H' . Substituting $\rho(t)$ into Eq. 1.4, the equation for $f(t)$ is

$$i \frac{df(t)}{dt} = [H, f(t)] + [H', \rho_0] + [H', f]. \quad (1.6)$$

I have used the fact $[H, \rho_0] = 0$. The last term on the right hand side of Eq. 1.6 is of $O(H')^2$, and we are left with

$$i \frac{df(t)}{dt} - [H, f] = [H', \rho_0]. \quad (1.7)$$

It is straightforward to show that

$$f(t) = (-i) \exp(-iHt) \left\{ \int_{-\infty}^0 dt' [H'(t'), \rho_0] \right\} \exp(iHt). \quad (1.8)$$

The electric current is then

$$J_\alpha^e(\mathbf{r}, t) = Tr \left[\hat{j}_\alpha^e(\vec{r}) f(t) \right]. \quad (1.9)$$

I have assumed there is no net current without the perturbation.

Using the cyclic property of the trace, we have

$$\begin{aligned} J_\alpha^e(\mathbf{r}, t) &= (-i) Tr \left\{ \int_{-\infty}^0 dt' [H'(t'), \rho_0] \hat{j}_\alpha^e(\vec{r}, t) \right\} \\ &= (-i) \int_{-\infty}^0 dt' Tr \left\{ \rho_0 \left[\hat{j}_\alpha^e(\vec{r}, t), H'(t') \right] \right\} \\ &= (-i) \int_{-\infty}^0 \langle [\hat{j}_\alpha^e(\vec{r}, t), H'(t')] \rangle, \end{aligned} \quad (1.10)$$

where $\hat{j}_\alpha^e(\vec{r}, t) = \exp(iHt) \hat{j}_\alpha^e(\vec{r}) \exp(-iHt)$ is the current operator in the Heisenberg picture and $\langle \dots \rangle$ is the average value in the equilibrium state.

The perturbation due to an electric field is

$$\begin{aligned} H' &= - \sum_{\alpha} \int d^3r \hat{j}_{\alpha}^e(\mathbf{r}) A_{\alpha}(\mathbf{r}, t) \\ &= \frac{i}{\omega} \hat{j}_{\alpha}^e(\mathbf{q}) E_{\alpha} \exp(-i\omega t). \end{aligned} \quad (1.11)$$

\mathbf{q} and ω are the wavevector and frequency of the electric field. The Coulomb gauge, $\nabla \cdot \mathbf{A} = 0$, is adopted. The current in Eq. 1.10 becomes

$$\begin{aligned} J_{\alpha}^e(\mathbf{r}, t) &= \frac{1}{\omega} \sum_{\beta} E_{\beta}(\mathbf{r}, t) \exp(-i\mathbf{q} \cdot \mathbf{r}) \int_{-\infty}^t dt' \exp[i\omega(t - t')] \langle [\hat{j}_{\alpha}^e(\mathbf{r}, t), \hat{j}_{\beta}(\mathbf{q}, t')] \rangle \\ &= \sum_{\beta} \sigma_{\alpha\beta}(\mathbf{q}, \omega) E_{\beta}(\mathbf{r}, t), \end{aligned} \quad (1.12)$$

which is the **linear response** equation for the charge current induced by a weak electric field. The electric conductivity measures the proportionality between the current and driving field.

The electrical conductivity $\sigma_{\alpha\beta}(\mathbf{q}, \omega)$ is thus

$$\sigma_{\alpha\beta}(\mathbf{q}, \omega) = \frac{1}{\omega} \exp(-i\mathbf{q} \cdot \mathbf{r}) \int_{-\infty}^t dt' \exp[i\omega(t - t')] \langle [\hat{j}_{\alpha}^e(\mathbf{r}, t), \hat{j}_{\beta}(\mathbf{q}, t')] \rangle. \quad (1.13)$$

Averaging over all the volume V leads to

$$\sigma_{\alpha\beta}(\mathbf{q}, \omega) = \frac{1}{\omega V} \int_{-\infty}^{\infty} dt \exp(i\omega t) \Theta(t) \langle [\hat{j}_{\alpha}^{\dagger}(\mathbf{q}, t), \hat{j}_{\beta}(\mathbf{q}, 0)] \rangle. \quad (1.14)$$

A straightforward way to proceed the calculation of Eq. 1.14 is to adopt the Matsubara formalism in the imaginary time. This is also introduced in most many-body textbook [19, 20, 21] as the standard technique for correlation functions at finite temperature. First we define retarded correlation function in real time t ,

$$\Pi_{AB}^R(t) = -i\Theta(t) \langle [A(t), B(0)] \rangle \quad (1.15)$$

and the imaginary-time (τ) correlation function,

$$\Pi_{AB}(\tau) = -\langle T_{\tau} A(\tau) B(0) \rangle, \quad (1.16)$$

where T_{τ} is the time-ordering on the imaginary axis. The correlation function in real axis and imaginary frequencies are defined by Fourier transformation,

$$\Pi_{AB}^R(\omega) = \int_{-\infty}^{\infty} dt e^{i\omega t} \Pi_{AB}^R(t), \quad (1.17)$$

$$\Pi_{AB}(i\omega_n) = \int_0^{\beta} d\tau e^{i\omega_n \tau} \Pi_{AB}(\tau). \quad (1.18)$$

The Lehmann representation of $\Pi_{AB}^R(\omega)$ and $\Pi_{AB}(i\omega_n)$ leads to

$$\Pi_{AB}^R(\omega) = \frac{1}{Z} \sum_{n,m} \frac{\langle n|A|m\rangle\langle m|B|n\rangle}{\omega + i0^+ + E_n - E_m} [\exp(-\beta E_n) - \zeta \exp(-\beta E_m)], \quad (1.19)$$

and,

$$\Pi_{AB}(\omega_n) = \frac{1}{Z} \sum_{n,m} \frac{\langle n|A|m\rangle\langle m|B|n\rangle}{i\omega_n + E_n - E_m} [\exp(-\beta E_n) - \zeta \exp(-\beta E_m)], \quad (1.20)$$

where 0^+ is the positive infinitesimal. $\zeta = 1$ if A and B are bosonic operators and $\zeta = -1$ if A and B are fermionic operators. $|n\rangle$ and $|m\rangle$ are eigenstates of the full many-body Hamiltonian H . Z is the partition function. In the expression for conductivity, Eq. 1.14, A and B are current operators, which are quadratic combination of fermionic operators and $\zeta = 1$.

In principle, we can approach either in the real-time or the imaginary-time domain. It turns out the formalism in the imaginary axis is less complicated than that in the real axis. Thus it is more convenient to carry out the finite-temperature calculation of correlation functions in the imaginary axis. Besides, numerical methods of high precision, such as quantum Monte Carlo method, are available for the imaginary-time formalism. Therefore in many cases, correlation functions are first computed for selected Matsubara frequencies $\{i\omega_n\}$, and numerical methods of analytic continuation, such as Padé approximant [22] or maximum entropy method [23], are implemented to obtain the physical information on the real axis.

The current-current correlation function for electrical conductivity is

$$\Pi_{\alpha\beta}(\mathbf{q}, i\Omega_m) = \int_0^\beta d\tau \exp(i\Omega_m \tau) \langle T_\tau \hat{j}_\alpha^e(\mathbf{q}, \tau) \hat{j}_\beta(\mathbf{q}, 0) \rangle \quad (1.21)$$

in Matsubara frequency. The current operator, in terms of fermionic operators, is written as

$$\hat{j}_\alpha^e(\mathbf{q}) = e \sum_{\mathbf{k}} v_\alpha(\mathbf{k}) c_{\mathbf{k}+\mathbf{q}/2}^\dagger c_{\mathbf{k}-\mathbf{q}/2}. \quad (1.22)$$

e is the elementary charge. Hence $\Pi_{\alpha\beta}(\mathbf{q}, i\Omega_m)$ can be written as a two-particle correlation function $\Pi(i\omega_n, i\omega_{n'}; i\Omega_m | \mathbf{k}, \mathbf{k}'; \mathbf{q})$ dressed by the band velocity $v_\alpha(\mathbf{q})$,

$$\Pi_{\alpha\beta}(\mathbf{q}, i\Omega_m) = T^2 \sum_{n, n'} \sum_{\mathbf{k}, \mathbf{k}'} ev_\alpha(\mathbf{k} + \mathbf{q}/2) \Pi(i\omega_n, i\omega_{n'}; i\Omega_m | \mathbf{k}, \mathbf{k}'; \mathbf{q}) ev_\beta(\mathbf{k}' - \mathbf{q}/2). \quad (1.23)$$

$\Pi(i\omega_n, i\omega_{n'}; i\Omega_m | \mathbf{k}, \mathbf{k}'; \mathbf{q})$ has the ladder expansion in terms of single particle Green's function and particle-hole **irreducible** vertex,

$$\begin{aligned} \Pi(i\omega_n, i\omega_{n'}; i\Omega_m | \mathbf{k}, \mathbf{k}'; \mathbf{q}) &= -\frac{1}{T} G(\mathbf{k} + \mathbf{q}, i\omega_n + i\Omega_m) G(\mathbf{k}, i\omega_n - i\Omega_m) \delta_{\mathbf{k}\mathbf{k}'} \delta_{nn'} \\ &\quad + G(\mathbf{k} + \mathbf{q}, i\omega_n + i\Omega_m) G(\mathbf{k}, i\omega_n - i\Omega_m) \\ &\quad \times \Gamma^i(i\omega_n, i\omega_{n'}; i\Omega_m | \mathbf{k}, \mathbf{k}'; \mathbf{q}) \\ &\quad \times G(\mathbf{k}' + \mathbf{q}, i\omega_{n'} + i\Omega_m) G(\mathbf{k}', i\omega_{n'} - i\Omega_m) \\ &\quad + \dots \\ &= G(\mathbf{k} + \mathbf{q}, i\omega_n + i\Omega_m) G(\mathbf{k}, i\omega_n - i\Omega_m) \\ &\quad + G(\mathbf{k} + \mathbf{q}, i\omega_n + i\Omega_m) G(\mathbf{k}, i\omega_n - i\Omega_m) \\ &\quad \times \Gamma^f(i\omega_n, i\omega_{n'}; i\Omega_m | \mathbf{k}, \mathbf{k}'; \mathbf{q}) \\ &\quad \times G(\mathbf{k}' + \mathbf{q}, i\omega_{n'} + i\Omega_m) G(\mathbf{k}', i\omega_{n'} - i\Omega_m) \end{aligned} \quad (1.24)$$

$G(\mathbf{k}, i\omega_n)$ is the single-particle Green's function. $\Gamma^i(i\omega_n, i\omega_{n'}; i\Omega_m | \mathbf{k}, \mathbf{k}'; \mathbf{q})$ is the **irreducible vertex**. $\Gamma^f(i\omega_n, i\omega_{n'}; i\Omega_m | \mathbf{k}, \mathbf{k}'; \mathbf{q})$ is the **full vertex**. Eq. 1.24 is represented schematically in Fig. 1.5, with the shaded boxes representing the irreducible vertex and the black boxes representing the full vertex.

The full vertex condenses all the **ladder** summation of irreducible vertex and can

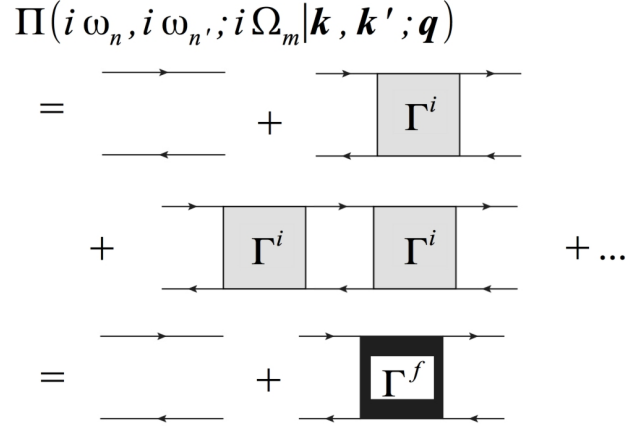


Figure 1.5: Diagrammatic representation of the ladder expansion of the two-particle correlation function $\Pi(i\omega_n, i\omega_{n'}; i\Omega_m | \mathbf{k}, \mathbf{k}'; \mathbf{q})$. See Eq. 1.24.

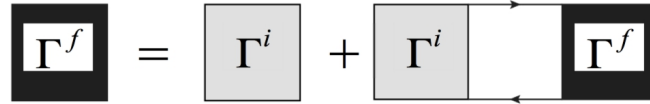


Figure 1.6: Diagrammatic representation of Bethe-Salpeter of vertex function $\Gamma(i\omega_n, i\omega_{n'}; i\Omega_m | \mathbf{k}, \mathbf{k}'; \mathbf{q})$. See Eq. 1.25.

be written in a form of iterative equation, also known as Bethe-Salpeter equation,

$$\begin{aligned}
 \Gamma^f(i\omega_n, i\omega_{n'}; i\Omega_m | \mathbf{k}, \mathbf{k}'; \mathbf{q}) &= \Gamma^i(i\omega_n, i\omega_{n'}; i\Omega_m | \mathbf{k}, \mathbf{k}'; \mathbf{q}) \\
 &+ T^2 \sum_{i\nu} \sum_{\mathbf{p}} \Gamma^i(i\omega_n, i\nu; i\Omega_m | \mathbf{k}, \mathbf{p}; \mathbf{q}) \\
 &\quad \times G(\mathbf{p} + \mathbf{q}, i\nu + i\Omega_m) G(\mathbf{p}, i\nu) \\
 &\quad \times \Gamma^f(i\nu, i\omega_{n'}; i\Omega_m | \mathbf{p}, \mathbf{k}'; \mathbf{q}),
 \end{aligned} \tag{1.25}$$

as shown in Fig. 1.6.

It is also possible to formulate the retarded two-particle correlation function in real-time from the beginning, which will employ the Keldysh formalism for closed-contour ordered Green's function. The resulting perturbative expansion of retarded correlation function also has the ladder structure and the vertex functions satisfy the Bethe-Salpeter equation. The details for the real-time formalism are left in App. A.

The ladder expansion in Eq. 1.24 and the Bethe-Salpeter equation are general results for two-particle retarded correlation functions and can be simply extended to many physical quantities of interest. For example, by dressing the correlation functions with band velocities (Eq. 1.23), we can compute the current-current correlation functions, while dressing with the Pauli matrices leads to the spin-spin correlation functions, or the spin susceptibility.

1.4 Dynamical Mean Field Theory

The linear response theory expresses the measurable quantities of interest in terms of correlation functions, yet computing correlation functions of a many-particle system is still a non-trivial task. Except for a few cases, such as one-dimensional models, exact analytic solutions are not available. Approximate methods are needed.

Dynamical mean field theory (DMFT) extends the Weiss mean field theory of spin models to quantum model of interacting fermions [24, 25, 26, 27]. Given a lattice model of solids, for example the Hubbard model, DMFT first focuses on a single lattice site. The **local** degrees of freedom (many-body configurations) on the selected site are fully preserved, and the rest of the lattice is described by a bath of free fermions which hybridize with the local single site. This non-interacting medium corresponds to the Weiss field in the mean field theory of spin models. Formally, the DMFT equations can be derived using the cavity method, in which all the degrees of freedom of the lattice other than the selected site are integrated out. The cavity method results in an effective action for the local degrees of freedom which, in the limit of infinite spatial dimensions ($d \rightarrow \infty$), is equivalent to an impurity with interacting electrons hybridized with a non-interacting bath. This reduction from lattice model to an Anderson impurity model is also called “**truncation**”.

The physical quantities of the lattice model are constructed from the local irreducible quantities of the effective impurity model. This is a consequence of the limit of infinite dimensions. When $d \rightarrow \infty$, the irreducible quantities (self energy and interacting vertex) of the lattice model become momentum-independent and are the same as those

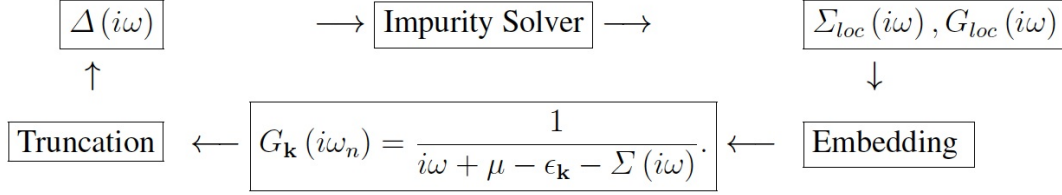


Figure 1.7: DMFT self-consistent loop.

of the effective impurity model [24]. The single-particle Green's function is thus

$$G(\mathbf{k}, i\omega) = \frac{1}{i\omega + \mu - \epsilon_{\mathbf{k}} - \Sigma_{loc}(i\omega)}, \quad (1.26)$$

where μ is the chemical potential and $\epsilon_{\mathbf{k}}$ is the bare energy dispersion of the lattice model. Similarly, the two-particle correlation functions for transport and magnetic properties as described in Sec. 1.3 can be calculated with $G(\mathbf{k}, i\omega)$ and the irreducible vertex functions of the impurity model. This step is also called “**embedding**”.

In the spin models, the Weiss field on the selected spin is determined by the averaged moment of the surrounding spins which, in a translational invariant lattice, is equivalent to the local moment of the selected spin in the Weiss field. This closes the self-consistent loop. The same prescription applies to DMFT. The hybridization function $\Delta(i\omega)$ encapsulates the hybridization between the impurity and all the bath degrees of freedom and plays the role of Weiss field. $\Delta(i\omega)$ is determined by the local quantities, such as $\Sigma_{loc}(i\omega)$ and $G_{loc}(i\omega)$ via the Dyson's equation for impurity model,

$$G_{loc}(i\omega) = \frac{1}{i\omega - \Delta(i\omega) - \Sigma_{loc}(i\omega)}. \quad (1.27)$$

$G_{loc}(i\omega)$ is the local Green's function and determined by

$$G_{loc}(i\omega) = \sum_{\mathbf{k}} G(\mathbf{k}, i\omega) = \sum_{\mathbf{k}} \frac{1}{i\omega + \mu - \epsilon_{\mathbf{k}} - \Sigma_{loc}(i\omega)}. \quad (1.28)$$

Eq. 1.27 and Eq. 1.28 constitutes the self-consistent loop of DMFT. Fig. 1.7 sketches the self-consistent loop of DMFT.

1.4.1 Two-particle Correlation Functions in DMFT

The ideas of truncation and embedding also apply to the calculation of two-particle correlation functions. In the limit of infinite dimension, the two-particle irreducible

vertex functions are dependent on only frequencies [28]. Analogous to the procedure for single-particle Green's functions, the impurity solver first computes the local two-particle correlation function Π_{loc} and full vertex function Γ_{loc}^f . The local irreducible vertex function Γ_{loc}^i is solved from the Bethe-Salpeter equation for the impurity model, that is, all single- and two-particle quantities in Eq. 1.24 and Eq. 1.25 are local quantities and have no momentum dependence. Then the momentum-dependent correlation functions are calculated by same set of equations, but with the momentum-dependence recovered only for the single-particle lines.

The calculation of current-current correlation function in Eq. 1.23, can be further simplified for the case of $\mathbf{q} = 0$, which is relevant for optical conductivity and transport properties such as resistivity, thermopower, and Hall effect. The observation is that since the irreducible vertex function is momentum-independent, and the band velocity $v_\alpha(\mathbf{k})$ is an odd function of \mathbf{k} , thus after the summation over \mathbf{k} , the vertex terms in the ladder expansion (Eq. 1.24) all vanish and only the first term of two single-particle lines (the bubble diagram) is left.

1.4.2 Impurity Solvers

In practice, the DMFT loop is initialized by a reasonable guess of the $\Delta(i\omega)$. The impurity solver takes $\Delta(i\omega)$ and computes $\Sigma(i\omega)$. Following Eq. 1.27 and 1.28, $\Sigma(i\omega)$ is used to update $\Delta(i\omega)$ for the next iteration. Therefore the impurity solver is at the heart of a DMFT calculation. Impurity solvers based on two numerical methods are adopted in this thesis, exact diagonalization (ED) and continuous time quantum Monte Carlo (CTQMC).

The exact diagonalization solver [27] replaces the continuum of the bath by finite number of discrete bath sites. The hybridization function is parametrized by

$$\Delta_{ED}(i\omega) = \sum_a \frac{|V_a|^2}{i\omega - E_a}, \quad (1.29)$$

where E_i is energy levels of the bath sites and V_i is the hybridization amplitude between bath site i and the impurity. The impurity model is then diagonalized by numerical method, for example the Lanczos algorithm. With the knowledge of eigenstates of the

impurity model, the local correlation functions are computed using the Lehmann representation (Eq. 1.19 and Eq. 1.20). Thus the ED solver works equally on real and imaginary axis. Without diagonalizing the full Hamiltonian, the Lanczos algorithm calculates the lowest eigenvalues and eigenvectors. The shortcoming of the ED solver is the limited size of the bath, because the dimension of the Hilbert space increases exponentially with the number of bath sites, which is a universal barrier for exact diagonalization methods. At most $N_{bath} = 15$ bath sites is achievable. DMFT calculations based on the ED solver is preferred when investigating the ground state properties of correlated systems, such as spectral weight transfer in single-particle spectral function, optical conductivity near a Mott-transition [29]. Semiquantitatively, the ED solver is also used to compute finite temperature properties, such as the trend of temperature dependence and the magnitude of transport quantities such as resistivity and thermopower (see Ch. 3).

The CTQMC algorithm is a Monte Carlo method that samples a Markov chain in the space of all Feynman diagrams of perturbative expansion of correlation functions [30, 31, 32]. Unlike the Hirsch-Fye Monte Carlo [33], it does **not** introduce discretization of the imaginary time, giving the name “continuous time”. The input file of CTQMC solver is list of values of $\Delta(i\omega_n)$ at all Matsubara frequencies up to a high energy cutoff, thus no parametrization as in the ED solver is used and the full bath degrees of freedom are included. Nevertheless, since CTQMC works on the imaginary axis, analytic continuation is needed. to extract physical information on real-axis from the imaginary-time data.

Two methods of analytic continuation are widely used, the maximum entropy (ME) method and the Padé approximant. Given the correlation function on imaginary axis, $G(\tau)$, from the Monte Carlo sampling, along with the knowledge of sampling errors, the ME method attempts to find the most probable solution of the spectral function $A(\omega) = -\frac{1}{\pi}\Im G^R(\omega)$ satisfying [23]

$$G(\tau) = -\frac{1}{\pi} \int_{-\infty}^{\infty} d\omega \frac{\Im G^R(\omega) \exp(-\tau\omega)}{1 \pm \exp(-\beta\omega)}. \quad (1.30)$$

$\Im G^R(\omega)$ is the imaginary part of the retarded correlation function $G^R(\omega)$ in real frequency. The real part of $G^R(\omega)$ can be computed from the Kramers-Kronig relation.

The Padé approximant method [22] finds a continued fraction representation of correlation function $G(i\omega_n)$ in the complex plane given the values at selected Matsubara frequencies $i\omega_i$,

$$R_N(z) = \frac{a_1}{1 + \frac{a_2(z-i\omega_1)}{1 + \frac{a_3(z-i\omega_2)}{1 + \dots \frac{a_N(z-i\omega_{N-1})}{1}}}}. \quad (1.31)$$

The coefficients a_k are determined by

$$R_N(i\omega_k) = G(i\omega_k), \quad \text{for } i = 1, \dots, N. \quad (1.32)$$

More details of analytic continuation are given in the App. B.

1.5 Outline

The following chapters are organized as follows.

In Ch. 2, the transport properties of a doped Mott insulator in one-band Hubbard model are studied. The main features of the bad metallic transport in correlated materials are recognized. A Boltzmann theory is formulated in terms of hidden quasiparticles. The transport properties are reproduced by the Boltzmann theory over a wide temperature range. The temperature and energy dependence of the hidden quasiparticles's scattering rate and renormalization are studied in detail. Results of local and lattice spin susceptibilities are also discussed.

In Ch. 3, from the linear response theory of thermal transport, a set of expressions for computing the high-frequency limit S^* of thermopower are derived. These expressions can be evaluated with ease in particular within the DMFT framework. A detailed comparison of S^* , S_K (thermopower estimated by the Kelvin formula), and S_0 (the transport thermopower) are presented. Analytic results in the low and high temperature limit, as well as numerical results at intermediate temperatures for weakly and strongly correlated metals are discussed, to elucidate the predicting power of S^* and S_K .

In Ch. 4, resistivity and magnetic susceptibility are studied with the hybridization

amplitude V as a tuning parameter of the periodic Anderson model. The Fermi liquid scale T_{FL} is extracted from the T^2 behavior of resistivity and the crossover from a Curie's to Pauli's paramagnetism. Upon the vanishing of T_{FL} , antiferromagnetic ordering temperature T_N and vector \mathbf{Q}_N are identified from the divergence of susceptibility $\chi(\mathbf{Q})$. A V - T phase diagram is presented. The dynamical lattice susceptibility is also computed to understand the nature of spin fluctuations in the paramagnetic region of the phase diagram.

In Ch. 5, the effect of a weak magnetic field to the linear response theory for electrical and thermal transport is explained. Then the anomalous transport, in particular the Nernst coefficient and magnetoresistance, in the correlated semiconductor FeSb_2 , is briefly described. A phenomenological analysis based on Boltzmann theory is presented. Both pros and cons of the theory in understanding the anomalous transport are discussed.

Chapter 2

Hidden Fermi Liquid

Fermi liquids [11] are good conductors. Quasiparticles (QPs) with a mean free path much longer than their wavelength are responsible for the electric transport, and the resistivity vanishes quadratically at low temperatures. The Landau theory is very robust and when reformulated in terms of a transport kinetic equation, it can be used to describe situations where Landau QPs are strictly speaking not well defined, namely when the QP scattering rate is comparable to their energy, such as the electron-phonon coupled system above the Debye temperature [34].

The metallic state of many strongly correlated materials is not described by the Landau theory in a wide range of temperatures. Quadratic temperature dependence of the resistivity occurs in a very narrow or vanishing range of temperatures. The interpretation of the resistivity in terms of the standard model of transport which is based on QPs is problematic since it leads to mean free paths shorter than the (QP) de Broglie wavelength as stressed by Emery and Kivelson [16]. The transport properties of these “bad metals” thus require a novel framework for their theoretical interpretation.

Dynamical mean-field theory (DMFT) [27], provides a nonperturbative framework for the description of strongly correlated materials. It links observable quantities to a simpler, but still interacting, reference system (a quantum impurity in a self-consistent medium) rather than to a free electron system; hence, it gives access to physical regimes outside the scope of Landau theory.

In a broad temperature range, the single-site DMFT description of the one-band Hubbard model at large U and finite doping results in transport and optical properties with anomalous temperature dependence [35, 36, 37, 38, 39, 40, 41, 42], reminiscent of those observed in bad metals. Corresponding studies of half filled metallic systems [43,

44, 45, 46] also reveal bad metallic behavior in a narrower temperature region since at high temperatures the resistivity is insulatinglike.

Landau QPs only emerge below an extremely low temperature, T_{FL} , which is much lower than the renormalized kinetic energy or Brinkman-Rice scale $T_{BR} \sim \delta W$ with δ the doping level and W the bare bandwidth. T_{BR} is the natural scale for the variation of physical quantities with doping at zero temperature [47, 37]. A recent comprehensive DMFT study of the Hubbard model with a semicircular bare density of states found that the transport properties above T_{FL} are described in terms of resilient QPs with a strong particle-hole asymmetry [41]. This asymmetry arises from the asymmetric pole structure in the self-energy characterizing the proximity to the Mott insulator [48].

In this chapter we investigate the problem of bad metal transport. By expressing the DMFT transport coefficients in terms of QP quantities we find several surprising results: a) the QP scattering rate has a quadratic behavior for temperatures much larger than T_{FL} and crosses over to a saturated behavior around T_{sat} . b) The temperature dependence of the transport coefficients is anomalous (in the sense that it does not reflect the T dependence of the QP scattering rate) and arises from the temperature dependent changes of the QP dispersion near the Fermi level. c) The temperature dependence of the QP dispersion affects differently the diagonal and off-diagonal charge and thermal transport coefficients but the Mott relation [49, 50] is valid when $T_{FL} < T < T_{sat}/2$.

2.1 Quasiparticles in a Doped Mott Insulator

We study the one-band Hubbard Hamiltonian on the two-dimensional square lattice with nearest neighbor hopping

$$H = -t \sum_{\langle ij \rangle, \sigma} c_{i\sigma}^\dagger c_{j\sigma} + U \sum_i c_{i\uparrow}^\dagger c_{i\uparrow} c_{i\downarrow}^\dagger c_{i\downarrow}. \quad (2.1)$$

We set the full bare bandwidth $W = 8t$ to $W = 1$ as the unit of energy and temperature, and present results for $U/W = 1.75$, for which the system is a Mott insulator at half filling. The doping level of the metallic state is fixed at $\delta = 15\%$ ($n = 0.85$). We use the continuous time quantum Monte Carlo (CTQMC) method [30] and the implementation

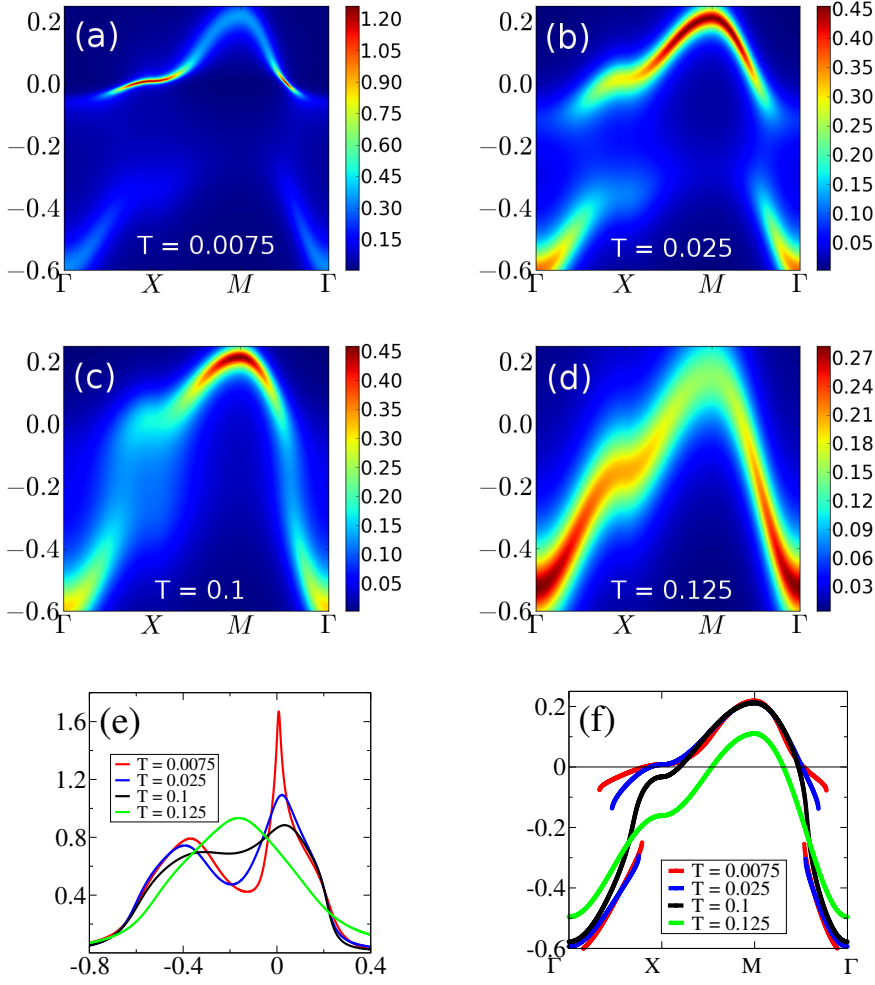


Figure 2.1: Spectral function $A_{\mathbf{k}}(\omega)$ along $\Gamma - X - M - \Gamma$ in Brillouin zone at (a) $T = 0.0075$, (b) $T = 0.025$, (c) $T = 0.1$, and (d) $T = 0.125$. (e) Local density of states. (f) Roots of Eq. 2.3 at different temperatures.

of Ref. [32] to solve the auxiliary impurity problem. We use Padé approximants to analytically continue the self-energy.

The one-electron spectral function is defined as

$$A_{\mathbf{k}}(\omega) = -\frac{1}{\pi} \frac{\Im \Sigma(\omega)}{(\omega + \mu - \epsilon_{\mathbf{k}} - \Re \Sigma(\omega))^2 + \Im \Sigma(\omega)^2}, \quad (2.2)$$

in terms of the bare band dispersion $\epsilon_{\mathbf{k}} = -(1/4)(\cos(k_x) + \cos(k_y))$ and the self-energy $\Sigma(\omega)$. $A_{\mathbf{k}}(\omega)$ at different temperatures are plotted in Fig. 2.1 1(a)-1(d).

Several characteristics of the evolution of $A_{\mathbf{k}}(\omega)$ with temperature are important.

The solutions of the following equation

$$\omega + \mu(T) - \epsilon_{\mathbf{k}} - \Re \Sigma(\omega, T) = 0, \quad (2.3)$$

faithfully reproduce the location of the peaks in $A_{\mathbf{k}}(\omega)$ and how they evolve with temperature (Fig. 2.1(f)). We do not describe in the following the upper Hubbard band at positive energies of order U .

There are two distinct temperature regimes separated by a crossover scale $T_{sat} \simeq 2T_{BR}/3 = 0.1$, which also sets the saturation scale of QP scattering rate as will be explained later. Above T_{sat} , say at $T = 0.125$, $A_{\mathbf{k}}(\omega)$ has one peak, i.e., Eq. 2.3 has only one root for each \mathbf{k} and displays a continuous dispersion over the whole Brillouin zone. Below T_{sat} , Eq. 2.3 can have multiple roots. The high temperature band breaks into two parts, which together with the upper Hubbard band form the characteristic DMFT three-peak structure of the local density of states (LDOS, Fig. 2.1(e)). The breakup of these bands also leads to the separation of the optical spectrum into a Drude peak and a midinfrared feature, characteristic of many correlated systems, which provided the earliest experimental tests of the DMFT picture of correlated materials [35, 36, 43, 44].

There is always a dispersive QP feature in an $\sim k_B T$ energy window at the Fermi energy. $\omega_{\mathbf{k}}^*$ denotes the root of Eq. 2.3 closest to the Fermi level for a given \mathbf{k} . It evolves *continuously* with temperature from zero up to very high temperatures where there is no sharp peak in the LDOS (Fig. 2.1(e)). The dispersive excitations evolve continuously from strongly renormalized QPs located near the Luttinger Fermi surface with Fermi crossings around the X point and on the $\Gamma-M$ line for $T \ll T_{sat}$ (Fig. 2.1(a-b)), to holes in the lower Hubbard band (located near the M point) (Fig. 2.1(d)) for $T \gg T_{sat}$, as the spin degrees of freedom gradually unbind from the charge, with increasing temperature. The QP velocity is nearly temperature independent only below T_{FL} and above T_{sat} . The mass enhancement ($1/Z$), decreases with increasing temperature, from a large value ~ 5 below T_{FL} (Fig. 2.1(a)) to a value $\sim 1.5 \simeq (1 - n/2)^{-1}$ at high temperatures (Fig. 2.1(d)).

2.2 Transport in Hidden Fermi Liquid

2.2.1 Boltzmann Theory of Quasiparticle Transport

We now turn to the transport properties and focus on the electric current induced by electric fields and thermal gradients

$$\mathbf{J}_e = \bar{\sigma}^0 \cdot \mathbf{E} - \bar{\sigma}^1 \cdot \nabla T. \quad (2.4)$$

$\bar{\sigma}^0$ is charge conductivity matrix, and $\bar{\sigma}^1$ is the thermal conductivity. Several quantities of interest are resistivity(ρ), Hall angle(θ_H), Seebeck coefficient(S), and Nernst coefficient(ν) [50]. They are representative measures of magneto- and thermoelectric transport properties and can be expressed in terms of elements of conductivity matrices,

$$\begin{aligned} \rho &= \frac{1}{\sigma_{xx}^0}, & \tan \theta_H &= -\frac{\sigma_{yx}^0}{\sigma_{xx}^0}, \\ S &= -\frac{\sigma_{xx}^1}{\sigma_{xx}^0}, & \nu &= -\frac{1}{B} \left(\frac{\sigma_{yx}^1}{\sigma_{xx}^0} - \frac{\sigma_{xx}^1 \sigma_{yx}^0}{(\sigma_{xx}^0)^2} \right). \end{aligned} \quad (2.5)$$

Within the DMFT treatment of the one-band Hubbard model, current vertex corrections vanish and the transport properties can be interpreted directly in terms of one-electron spectral function [35, 38, 39]

$$\begin{aligned} \sigma_{xx}^\alpha &= 2\pi \sum_{\mathbf{k}} \Phi_{\mathbf{k}}^{xx} \int d\omega \left(-\frac{\partial f(\omega)}{\partial \omega} \right) \left(\frac{\omega}{T} \right)^\alpha A_{\mathbf{k}}^2(\omega), \\ \frac{\sigma_{yx}^\alpha}{B} &= \frac{4\pi^2}{3} \sum_{\mathbf{k}} \Phi_{\mathbf{k}}^{yx} \int d\omega \left(-\frac{\partial f(\omega)}{\partial \omega} \right) \left(\frac{\omega}{T} \right)^\alpha A_{\mathbf{k}}^3(\omega), \end{aligned} \quad (2.6)$$

with $\alpha = 0$ or 1 for charge or thermal conductivity. We consider the limit of a weak magnetic field, hence the off-diagonal conductivities are proportional to B . $\Phi_{\mathbf{k}}^{xx} = \epsilon_{\mathbf{k}}^{x2}$ and $\Phi_{\mathbf{k}}^{yx} = (\epsilon_{\mathbf{k}}^y)^2 \epsilon_{\mathbf{k}}^{xx} - \epsilon_{\mathbf{k}}^y \epsilon_{\mathbf{k}}^x \epsilon_{\mathbf{k}}^{yx}$ are transport functions in terms of the bare band dispersion $\epsilon_{\mathbf{k}}$ and its derivatives. The derivatives are denoted by the corresponding superscripts, $\epsilon_{\mathbf{k}}^\alpha = \partial \epsilon_{\mathbf{k}} / \partial k_\alpha$.

To recast Eqs. 2.6 in terms of QPs, we linearize Eq. 2.3 at $\omega = \omega_{\mathbf{k}}^*$ and define $Z_{\mathbf{k}} = (1 - \frac{\partial \Re \Sigma(\omega)}{\partial \omega})^{-1}|_{\omega=\omega_{\mathbf{k}}^*}$. Then the low energy part of the one-electron Green's function can be approximated as

$$G_{\mathbf{k}}(\omega) \simeq \frac{Z_{\mathbf{k}}}{(\omega - \omega_{\mathbf{k}}^*) + i\Gamma_{\mathbf{k}}^*}. \quad (2.7)$$

Thus $Z_{\mathbf{k}}$ is the QP renormalization factor (or QP weight) and $\Gamma_{\mathbf{k}}^* = -Z_{\mathbf{k}}\Im\Sigma(\omega_{\mathbf{k}}^*)$ is the QP scattering rate.

Then the integrals in Eqs. 2.6 can be performed analytically and lead to

$$\begin{aligned}\sigma_{xx}^{\alpha} &\simeq \sum_{\mathbf{k}} \left(-\frac{\partial f(\omega)}{\partial \omega} \right)_{\omega_{\mathbf{k}}^*} \Phi_{\mathbf{k}}^{*xx} \left(\frac{\omega_{\mathbf{k}}^*}{T} \right)^{\alpha} \tau_{\mathbf{k}}^*, \\ \frac{\sigma_{yx}^{\alpha}}{B} &\simeq \frac{1}{2} \sum_{\mathbf{k}} \left(-\frac{\partial f(\omega)}{\partial \omega} \right)_{\omega_{\mathbf{k}}^*} \Phi_{\mathbf{k}}^{*yx} \left(\frac{\omega_{\mathbf{k}}^*}{T} \right)^{\alpha} (\tau_{\mathbf{k}}^*)^2.\end{aligned}\quad (2.8)$$

$\tau_{\mathbf{k}}^* = (\Gamma_{\mathbf{k}}^*)^{-1}$ is the QP lifetime. The transport functions are renormalized by $Z_{\mathbf{k}}$. $\Phi_{\mathbf{k}}^{*xx} = (\epsilon_{\mathbf{k}}^{*x})^2$ and $\Phi_{\mathbf{k}}^{*yx} = (\epsilon_{\mathbf{k}}^{*y})^2 \epsilon_{\mathbf{k}}^{*xx} - \epsilon_{\mathbf{k}}^{*y} \epsilon_{\mathbf{k}}^{*x} \epsilon_{\mathbf{k}}^{*yx}$, with $\epsilon_{\mathbf{k}}^{*\alpha(\beta)} = Z_{\mathbf{k}} \epsilon_{\mathbf{k}}^{\alpha(\beta)} (\alpha, \beta = x, y)$.

This reformulation leads to a transparent interpretation in terms of QPs with temperature dependent dispersion $\omega_{\mathbf{k}}^*$. Eqs. 2.8 have a form similar to the solution of the kinetic equations from Boltzmann theory [5]. The essential difference from the Prange-Kadanoff treatment of the electron-phonon problem [34] is the strong temperature dependence of the QP dispersion brought in by $Z_{\mathbf{k}}$.

First we validate the simplified description of transport, Eqs. 2.8 (“QP approx.”), by benchmarking it against the results of the exact DMFT expressions, Eqs. 2.6 (“exact exp.”), for the resistivity, Hall angle, Seebeck coefficient, and Nernst coefficient. The quantitative agreement between Eqs. 2.8 and Eqs. 2.6 is evident, as shown in Fig. 2.2(a-d). The QP approximation faithfully reproduces the results of all transport quantities over the whole temperature range, extending to temperatures well above T_{sat} .

2.2.2 Scattering Rate Saturation

Fig. 2.3(a) shows the QP scattering rate on Fermi surface, i.e., $\Gamma_{\mathbf{k}_F}^*$ with $\omega_{\mathbf{k}_F}^* = 0$ (for later use we also write $\tau_{\mathbf{k}_F}^* = (\Gamma_{\mathbf{k}_F}^*)^{-1}$ as the QP lifetime and $Z_{\mathbf{k}_F}$ as the renormalization factor at Fermi surface). T_{sat} demarcates the nonmonotonic temperature dependence of $\Gamma_{\mathbf{k}_F}^*$. Below T_{sat} , $\Gamma_{\mathbf{k}_F}^*$ increases and reaches a maximum at T_{sat} . Above T_{sat} , $\Gamma_{\mathbf{k}_F}^*$ decreases very slowly and eventually approaches to a value moderately smaller than the maximum. This confirms that T_{sat} characterizes the crossover between two distinct scattering behaviors. The inset of Fig. 2.3(a) shows estimated values of $(k_F l^*)^{-1}$ with k_F an estimation of the average Fermi momentum by assuming a circular Fermi surface

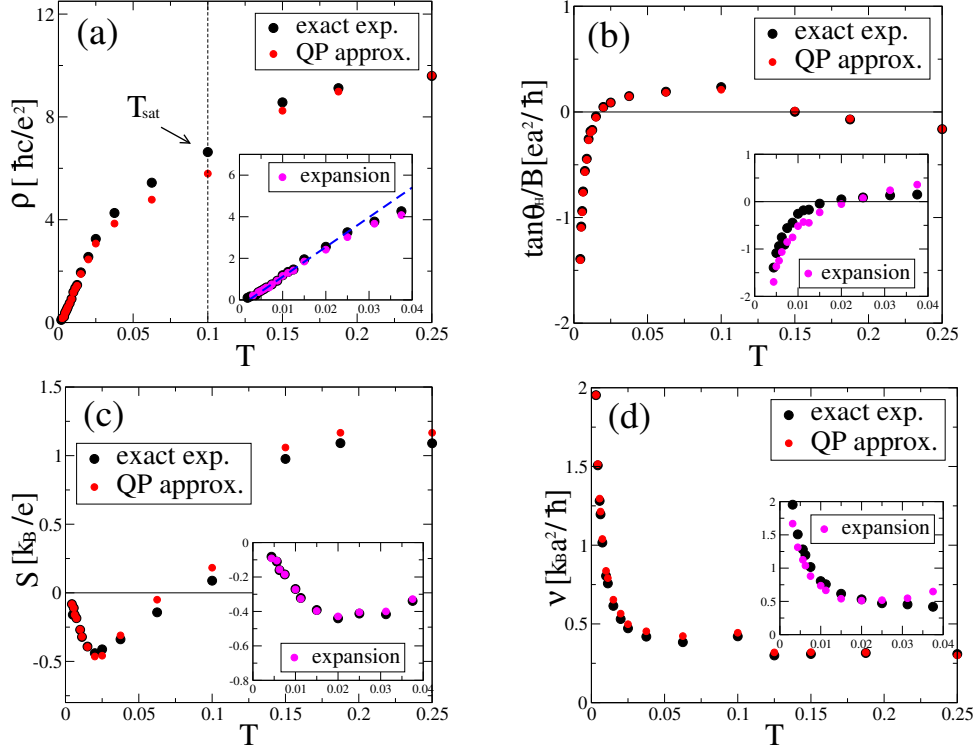


Figure 2.2: Transport properties. (a) Resistivity. (b) Hall angle. (c) Seebeck coefficient. (d) Nernst coefficient. Points labeled “exact exp.” are obtained using Eqs. 2.6. Points labeled “QP approx.” are obtained using Eqs. 2.8. Points labeled “expansion” are obtained using the general Sommerfeld expansion detailed in App. C. The units are expressed in terms of universal constants, \hbar , k_B , e , in-plane lattice constant a , and out-of-plane lattice constant c .

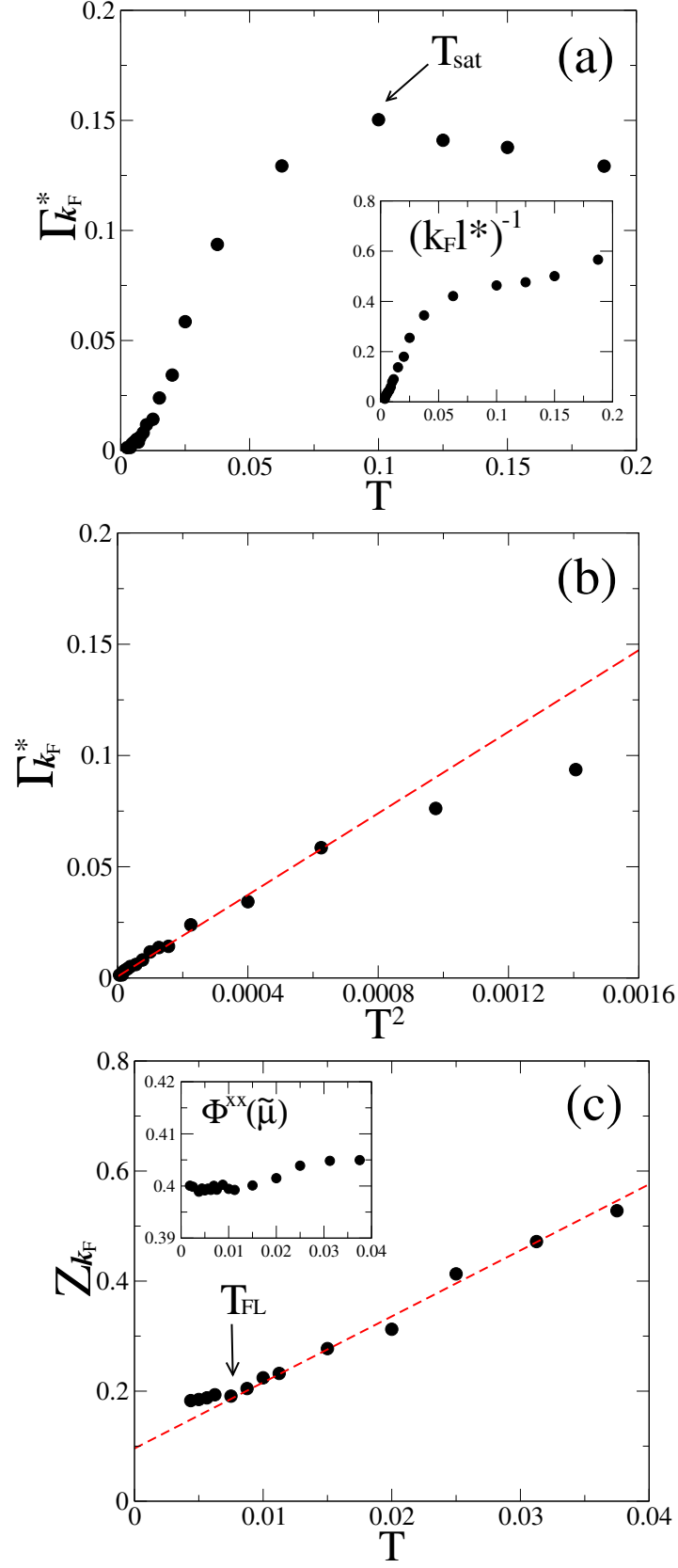


Figure 2.3: (a) Quasiparticle scattering rate $\Gamma_{\mathbf{k}_F}^*$. The inset shows the estimation of $(k_F l^*)^{-1}$. (b) $\Gamma_{\mathbf{k}_F}^*$ as a function of T^2 for $T \lesssim T_{\text{sat}}/2$. (c) Quasiparticle renormalization factor $Z_{\mathbf{k}_F}$ for $T \lesssim T_{\text{sat}}/2$.

containing $(1 - \delta)/2$ electrons per spin and with $l^* = v_{\mathbf{k}_F}^* \times \tau_{\mathbf{k}_F}^*$ the QP mean free path, where $v_{\mathbf{k}_F}^* = \sqrt{\langle v_{\mathbf{k}}^{*2} \rangle}$ with $\langle \dots \rangle$ averaging over the Fermi level. At low temperatures, $(k_F l^*)^{-1}$ increases with temperature, as expected in a good metal, and crosses over to a much slower increase, or saturated behavior, around $T_{sat}/2$. Above $T_{sat}/2$, $(k_F l^*)^{-1} \simeq 0.5$, and does not exceed the Mott-Ioffe-Regel bound, which states that $(k_F l^*)^{-1} < 1$ in a metal. The QPs behave as expected in Boltzmann transport theory in the full temperature range, reaching the nondegenerate limit at $T \gg T_{sat}$. Notice that above T_{FL} , $\Im \Sigma(0)$ is not quadratic in temperature; only $\Gamma_{\mathbf{k}_F}^* = -Z_{\mathbf{k}_F} \Im \Sigma(0)$ is quadratic.

Fig. 2.4 shows the bulk spin susceptibility χ_{bulk} and charge susceptibility $dn/d\mu$. The spin susceptibility can be well fit by $\chi_{bulk}(T) \propto \frac{1}{T - T_0}$, where $T_0 \simeq 0.04$, as indicated in the inset of Fig. 2.4. The charge susceptibility behaves differently. Above $T = 0.025$, albeit the (bad) metallic resistivity, $dn/d\mu$ exhibits an insulating behavior, that is, increases with lowered temperature. Below $T = 0.025$, $dn/d\mu$ shows a metallic behavior.

2.2.3 Non-Fermi liquid Transport

The anomalies in the transport properties are the result of the strong temperature dependence of the renormalized dispersion. This is best understood by means of a general Sommerfeld expansion of Eqs. 2.8, which is explained in App. C and works well below $T_{sat}/2$. For this purpose we define $\Phi^{*xx/yy}(\epsilon) = \sum_{\mathbf{k}} \Phi_{\mathbf{k}}^{*xx/yy} \delta(\epsilon - \omega_{\mathbf{k}}^*)$ and the energy dependent QP lifetime $\tau^*(\epsilon) = \tau_{\mathbf{k}}^*$ when $\epsilon = \omega_{\mathbf{k}}^*$, with scattering rate $\Gamma^*(\epsilon) = (\tau^*(\epsilon))^{-1}$. For $|\epsilon| \lesssim T$, $\Phi^{*xx/yy}(\epsilon)$ is expanded to linear order in ϵ . To keep the asymmetry in $\Gamma^*(\epsilon)$, which is important for the thermoelectric transport, we expand $\Gamma^*(\epsilon)$ to cubic order in ϵ , and treat the linear and cubic order as corrections to the zeroth and quadratic terms, which are dominant in the Fermi liquid regime at low temperatures. The insets in Fig. 2.2 compare the estimation using this expansion (purple dots) and the results of the full expressions (black dots). The agreement is evident and the expansion quantitatively captures the variation below $T_{sat}/2$.

The inset of Fig. 2.2(a) shows the linearity of resistivity, a typical non-Fermi-liquid behavior [51], up to $T_{sat}/4 \simeq 0.025$, as indicated by the linear fitting (blue dashed line). Surprisingly the QP scattering rate $\Gamma_{\mathbf{k}_F}^*$ has a quadratic temperature dependence also

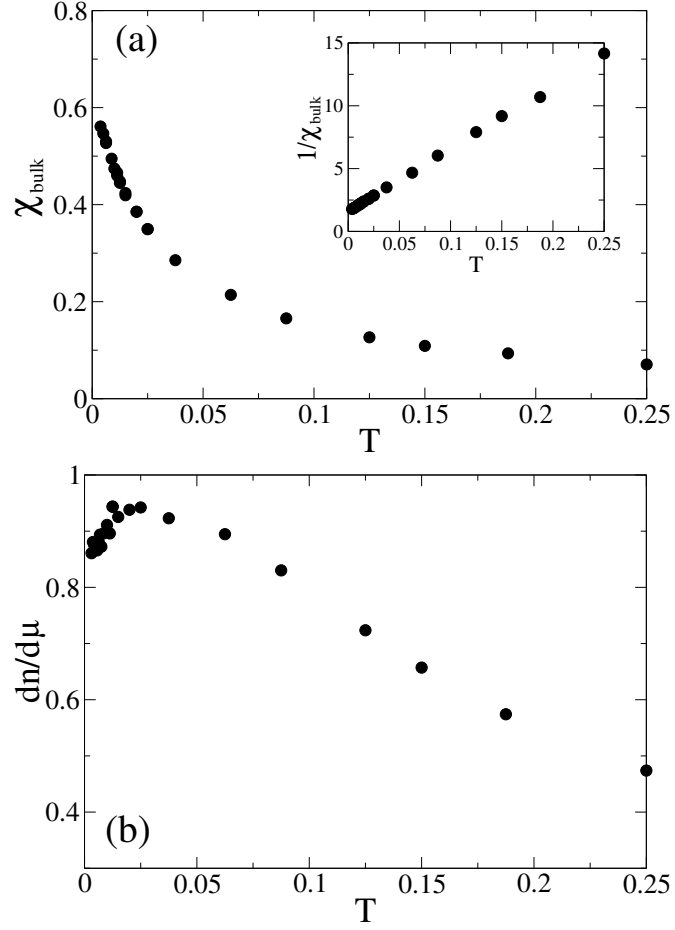


Figure 2.4: Bulk spin susceptibility χ_{bulk} (a) and charge susceptibility $dn/d\mu$ (b). The inset of (a) shows $1/\chi_{\text{bulk}}$

up to $T_{sat}/4$ (Fig. 2.3(b)). This is due to the strong temperature dependence of $Z_{\mathbf{k}_F}$ (Fig. 2.3(c)). In fact, the leading order in the general Sommerfeld expansion gives

$$\rho \simeq (Z_{\mathbf{k}_F} \Phi^{xx}(\tilde{\mu}) \tau_{\mathbf{k}_F}^*)^{-1}, \quad (2.9)$$

where $\Phi^{xx}(\tilde{\mu}) = \sum_{\mathbf{k}} \Phi_{\mathbf{k}}^{xx} \delta(\tilde{\mu} - \epsilon_{\mathbf{k}})$ with $\tilde{\mu} = \mu - \Re \Sigma(0)$ and we have used $\Phi^{*xx}(0) = Z_{\mathbf{k}_F} \Phi^{xx}(\tilde{\mu})$. $Z_{\mathbf{k}_F} \simeq 0.1 + 12T$ for $T_{FL} < T < T_{sat}/4$, leads to the quasilinear resistivity and also affects all other transport coefficients in Eqs. 2.8. The temperature dependence of $Z_{\mathbf{k}_F}$ becomes negligible only below the Fermi liquid temperature $T_{FL} \simeq T_{sat}/15$. $\Phi^{xx}(\tilde{\mu})$ is very weakly temperature dependent as shown in the inset of Fig. 2.3(c). Above T_{sat} , the resistivity is quasilinear in temperature with a slope smaller than that below $T_{sat}/4$, while the QP scattering rate is saturated. The general Sommerfeld expansion cannot be used at high temperatures, but the discrepancy between the scattering rate and resistivity can be traced to the variation of $\tilde{\mu}$ with temperature, leading to the shift of QP band relative to the Fermi window $-\partial f(\omega)/\partial \omega$.

Similarly, the leading order in the Hall angle (Fig. 2.2(b)) is given by $\tan \theta_H/B \simeq Z_{\mathbf{k}_F} \Phi^{yx}(\tilde{\mu}) \tau_{\mathbf{k}_F}^*/2\Phi^{xx}(\tilde{\mu})$ and indicates the sign change at $T \simeq T_{sat}/4$ is due to the sign change in $\Phi^{yx}(\tilde{\mu})$, a consequence of the evolution of Fermi surface from a holelike one to an electronlike one. For the Seebeck coefficient (Fig. 2.2(c)), the expansion leads to

$$S \simeq \left(-\frac{\pi^2}{3}T\right) \left(\frac{d \ln \Phi^{*xx}(0)}{d\epsilon} + \frac{d \ln \tau^*(0)}{d\epsilon}\right). \quad (2.10)$$

The asymmetry in scattering rate competes with the asymmetry in the QP band structure; hence, instead of sign change, S shows a nonmonotonic temperature dependence below $T_{sat}/2$.

The Nernst coefficient ν (Fig. 2.2(d)) rises steeply below $T_{sat}/4$, and provides a good probe of the temperature dependence of $\tau_{\mathbf{k}_F}^*$. The leading orders in the expansion give

$$\nu \simeq \left(-\frac{\pi^2}{3}T\right) \left[\tau_{\mathbf{k}_F}^* \frac{d}{d\epsilon} \left(\frac{\Phi^{*yx}(0)}{\Phi^{*xx}(0)}\right) + \frac{\Phi^{*yx}(0)}{\Phi^{*xx}(0)} \frac{d\tau^*(0)}{d\epsilon}\right]. \quad (2.11)$$

In the square lattice near half filling, the asymmetry in the band structure dominates and leads to $\nu \propto \tau_{\mathbf{k}_F}^* T \propto 1/T$. This rise is seen in many materials [50] before ν drops linearly in T at very low temperature ¹.

¹Disorder in real materials cuts off the divergence of $\tau_{\mathbf{k}_F}^*$ and ν is thus linear in T at very low

2.3 Spectral Properties of Hidden Fermi Liquid

The spectral function of a doped Mott insulator has been shown in Fig. 2.1, which exhibits the emergence of the coherent hidden QPs from the weakly renormalized Hubbard bands as temperature drops to below the Brinkman-Rice scale. Besides, the temperature dependence of the QP renormalization gives rise to the non-Fermi liquid transport at low temperature, such as the linear temperature dependence of resistivity. This section will presents a more detailed discussion of the QP characteristics of the hidden Fermi liquid. The doping dependence of the effective Fermi energy will also be discussed.

2.3.1 The Fermi Energy of Hidden Quasiparticles

In deriving the transport equation of QPs, we determine the QP excitation energy $\omega_{\mathbf{k}}^*$ by the poles of one-particle Green's function $G_{\mathbf{k}}(\omega)$, that is, they are solutions of Eq. 2.3,

$$\omega_{\mathbf{k}}^* + \mu - \epsilon_{\mathbf{k}} - \Re\Sigma(\omega_{\mathbf{k}}^*) = 0. \quad (2.12)$$

Hence $G_{\mathbf{k}}(\omega)$ has the following approximate form, Eq. 2.7

$$G_{\mathbf{k}}(\omega) \simeq \frac{Z_{\mathbf{k}}}{(\omega - \omega_{\mathbf{k}}^*) + i\Gamma_{\mathbf{k}}^*}, \quad (2.13)$$

with $Z_{\mathbf{k}} = \frac{1}{1 - \frac{\partial \Re\Sigma(\omega_{\mathbf{k}}^*)}{\partial \omega}}$ and $\Gamma_{\mathbf{k}}^* = Z_{\mathbf{k}} \Im\Sigma(\omega_{\mathbf{k}}^*)$. The approximate QP spectral function thus has a Lorentzian form,

$$A_{\mathbf{k}}^{QP}(\omega) = \frac{Z_{\mathbf{k}}}{\pi} \frac{\Gamma_{\mathbf{k}}^*}{(\omega - \omega_{\mathbf{k}}^*)^2 + (\Gamma_{\mathbf{k}}^*)^2}. \quad (2.14)$$

Fig. 2.5 compares the exact spectral function $A_{\mathbf{k}}(\omega)$ (red solid line) and $A_{\mathbf{k}}^{QP}(\omega)$ (black dashed line) at two lattice momentum, $\mathbf{k}_a = (0.38\pi, 0.38\pi)$ is below the Fermi surface and $\mathbf{k}_b = (0.54\pi, 0.54\pi)$ is above the Fermi surface. The temperature is $T = 0.015$, which is above the Fermi liquid temperature $T_{FL} \simeq 0.075$. It is obvious that the peak of $A_{\mathbf{k}}(\omega)$ is faithfully represented by the Lorentzian function. The QP excitation energy determines the position of the Lorentzian peak. In Fig. 2.5, the excitations

temperatures. This linearity is sometimes taken as a signature of Fermi-liquid behavior.

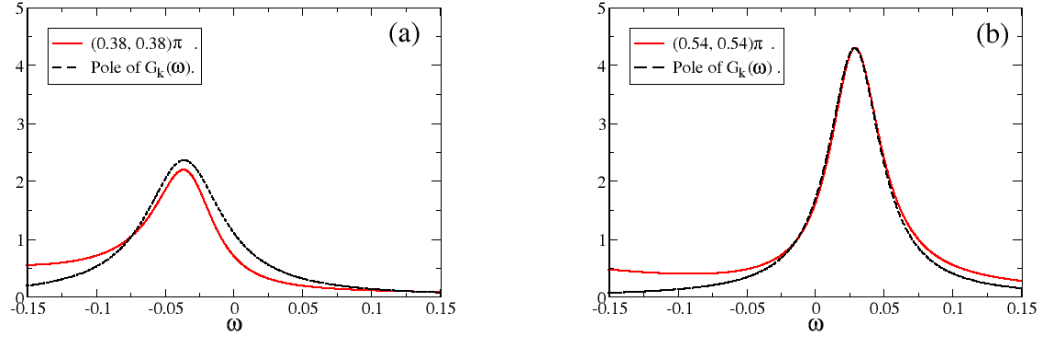


Figure 2.5: Spectral function $A_{\mathbf{k}}(\omega)$ (red solid line) for (a) $\mathbf{k} = (0.38\pi, 0.38\pi)$ and (b) $\mathbf{k} = (0.54\pi, 0.54\pi)$. $T = 0.015$. The black dashed line is the Lorentzian function whose parameters are determined by the poles of Green's function $G_{\mathbf{k}}(\omega)$.

energies are $\omega_{\mathbf{k}_a} \simeq -0.04$ and $\omega_{\mathbf{k}_b} \simeq 0.03$, both of which are much larger than the Fermi liquid scale T_{FL} .

Fig. 2.6 shows variation of the QP scattering rate (a) and renormalization factor (a) with respect to QP energy for $T = 0.005$ and $T = 0.015$. The two vertical dashed lines in Fig. 2.6(a) marked the low energy window within which the low energy part of the scattering rate can be fit by quadratic functions, as indicated by the dashed curves. Apparently, the QP scattering rate is quadratic in QP energy for $|\omega_{\mathbf{k}}^*| < 0.05$. If we take the width of this window as the **effective Fermi energy** of QPs, E_F^{eff} , then $E_F^{eff} \simeq 0.1 \sim T_{BR}$, which is much larger than the T_F from transport measurement. Notice that at $T = 0.015 > T_F$, the quadratic scattering rate still holds within the same energy window, only with the curvature becomes smaller and the minimum rises.

At this point, it is helpful to compare the scattering rate with the imaginary part of self energy. These two quantities are usually taken as synonyms for Landau's Fermi liquid since the QP renormalization is a temperature independent constant there. Fig. 2.7 (a) shows the imaginary part exhibits strong particle-hole asymmetry while the QP scattering rate is symmetric for particle and hole excitations within the window of effective QP Fermi energy. In fact, the particle-hole symmetry for a Landau's Fermi liquid, only emerges at very low temperature and very close to the Fermi surface. This can be

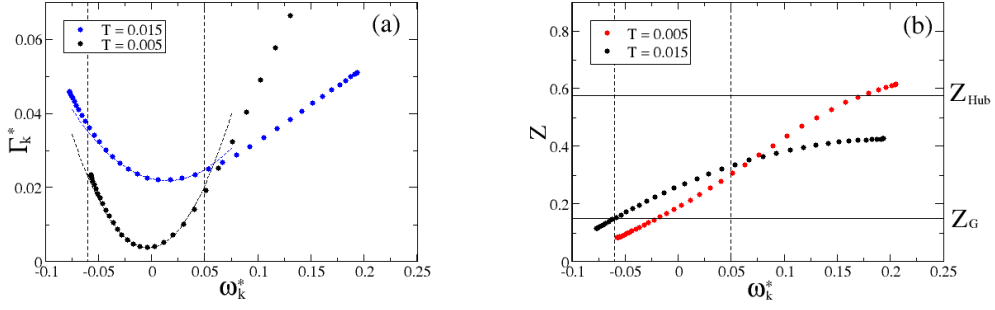


Figure 2.6: (a): QP scattering rate as a function of QP energy. The dashed lines are quadratic functions which fit the low energy part of the scattering rate. (b): QP renormalization. The upper horizontal line marks $Z_{Hub} = 1 - n/2 = 0.575$, which is the renormalization factor of the lower Hubbard band given by Hubbard I approximation. The lower horizontal line marks $Z_G = \delta = 0.15$, which is the renormalization factor at $T = 0$ given by the Gutzwiller approximation.

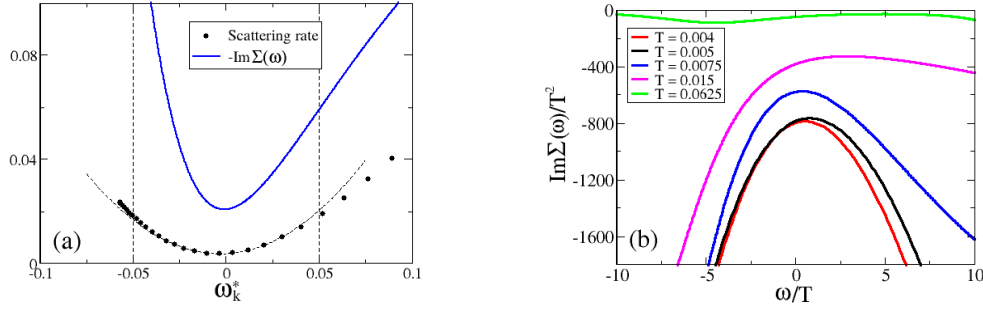


Figure 2.7: (a): QP scattering rate and the imaginary part of self energy. $T = 0.005$. (b): Emergence of Fermi liquid scaling of self energy.

seen from the scaling form of the self energy,

$$\frac{\Im\Sigma(\omega)}{T^2} \propto \left(\frac{\omega}{T}\right)^2 + \pi^2. \quad (2.15)$$

Fig. 2.7 (b) shows $\Im\Sigma(\omega)/\omega^2$ as a function of ω/T for selected temperatures. $\Im\Sigma(\omega)$ collapse to the scaling form of Eq. 2.15 only well below the Fermi liquid temperature, and when $\omega/T \simeq 5$. Therefore, the effective Fermi energy E_F^{eff} is the energy scale below which the QPs are valid representation of fermionic excitations.

Fig. 2.6(b) shows the variation of QP renormalization Z with QP energy. The horizontal lines mark two characteristic values of Z . The upper one is $Z_{Hub} \simeq 1 - n/2 = 0.575$, which is the renormalization factor of the lower Hubbard band in the

$U \rightarrow \infty$ limit, given by the the Hubbard I approximation [52]. The lower one is $Z_G \simeq 1 - n = 0.15$, which is the QP renormalization of the ground state ($T = 0$) given by the Gutzwiller approximation [53]. The hole excitations have larger mass enhancement, $Z \lesssim Z_G$. Then Z varies linearly with QP energy across the E_F^{eff} scale. Above E_F^{eff} for electron excitations, Z approaches to Z_{Hub} and saturates.

2.4 Spin Fluctuations

This section discusses the spin fluctuations in the doped Mott insulator. Both local and lattice spin susceptibilities are calculated.

2.4.1 Local Spin Fluctuations

The local dynamic spin susceptibilities $\chi_S(\omega)$ at selected temperatures presented in this section are obtained using the maximum entropy method.

Local moment regime.

The local moment regime refers to the high temperature regime of $T > T_{BR}$. In this regimes, the single-particle local density of states (LDOS) displays the lower and upper Hubbard bands, but the coherent peak is not well formed (see Fig. 2.1). This corresponds to the situation in the effective impurity Anderson model that the local moment is not screened by the conduction electrons and the Kondo effect has not taken place yet.

Fig. 2.8 shows the imaginary (left) and real (right) part of $\chi_S(\omega)$ in the local moment regime. The evolution with temperature reveals an isosbestic point in $\Im\chi_S(\omega)$, indicating a spectral weight transfer between the high energy part and low energy part. An isosbestic point indicates that there are two components in the spectral function [54] with a conserved total weight. That is, the spectral function can be written as

$$\Im\chi_S(\omega) = \alpha\chi_l(\omega) + (1 - \alpha)\chi_h(\omega), \quad (2.16)$$

where χ_l and χ_h are the low- and high-energy component of the spectral function. Then

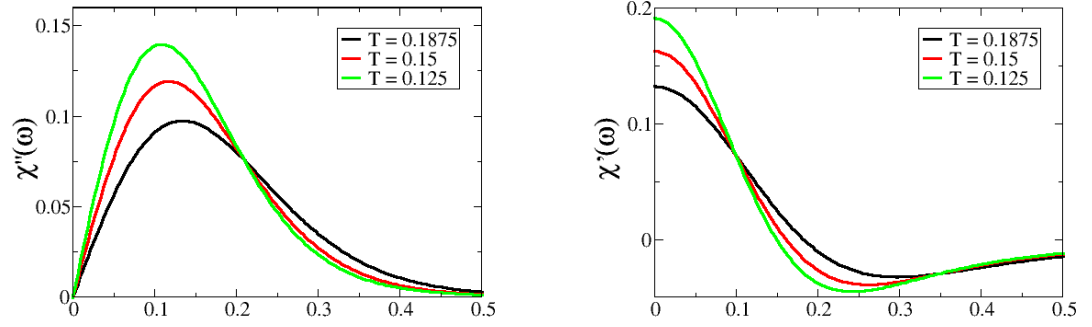


Figure 2.8: $\chi_S(\omega)$ in the local moment regime. Imaginary part (left) and real part (right).

the isosbestic point $\omega = \omega_i$ is determined by $\chi_l(\omega_i) = \chi_h(\omega_h)$, where the low- and high-energy component crosses. In our case, it is $\omega_i \simeq 0.2$, which separates the low-energy and high-energy component in $\Im\chi(S)$.

Hidden Fermi liquid regime.

The hidden Fermi liquid regime represent $T_{FL} < T < T_{BR}$, where the QP scattering rate exhibits a Fermi liquid behavior ($\propto T^2$), while the QP renormalization is strong temperature dependent, giving rise the quasi-linear resistivity. The QP peak in the single-particle LDOS emerges in this regime, indicating the Kondo effect starts to take place.

Fig. 2.9 shows $\chi_S(\omega)$ in this regime. Similar to the local moment regime, the evolution of $\Im\chi_S(\omega)$ reveals a suppression of high energy spectrum and an enhancement of low energy part. But the spectral transfer shows no sign of isosbestic point, this indicates the evolution of spectral weight is not simply due to a redistribution of weight between the low- and high-component.

Fermi liquid regime.

The Fermi liquid regime refers when $T < T_{FL}$ and the QP weight Z is only weakly dependent on temperature and approaching to its $T = 0$ value. The transport behaviors follows Landau's Fermi liquid theory, such as a $\sim T^2$ resistivity.

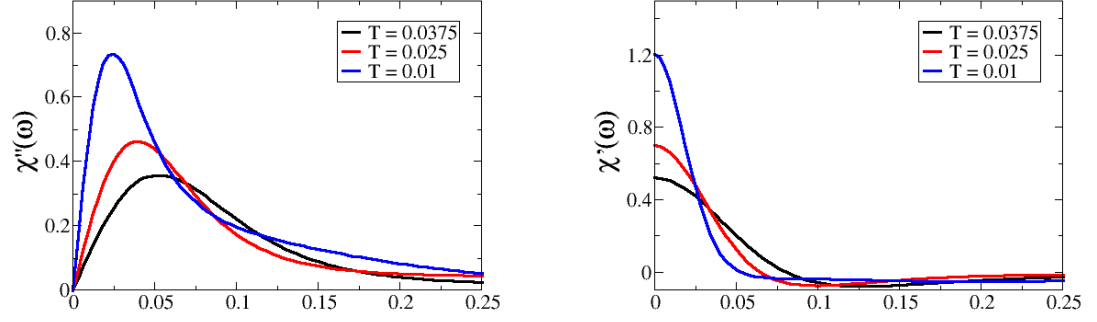


Figure 2.9: $\chi_S(\omega)$ in the hidden Fermi liquid regime. Imaginary part (left) and real part (right).

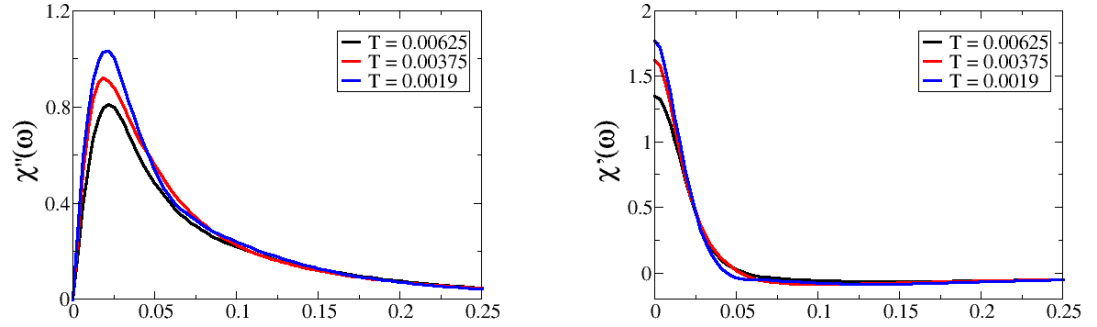


Figure 2.10: $\chi_S(\omega)$ in the Fermi liquid regime. Imaginary part (left) and real part (right).

Fig. 2.10 shows $\chi_S(\omega)$ in the Fermi liquid regime. The main difference from the hidden Fermi liquid regime is that the low energy part of $\Im\chi_S(\omega)$ is enhanced as temperature is lowered while the high energy part of $\omega > 0.1$ is not evolving with temperature.

Cumulative Spectral Weight

Another way of looking at the spectral weight is to compute the cumulative weight. We write

$$S_z^2(\Omega) = \frac{1}{\pi} \int_{-\Omega}^{\Omega} d\omega n_B(\omega) \Im\chi_S(\omega) = \frac{1}{\pi} \int_0^{\Omega} d\omega \left[\omega \coth\left(\frac{\beta\omega}{2}\right) \right] \left[\frac{\Im\chi_S(\omega)}{\omega} \right]. \quad (2.17)$$

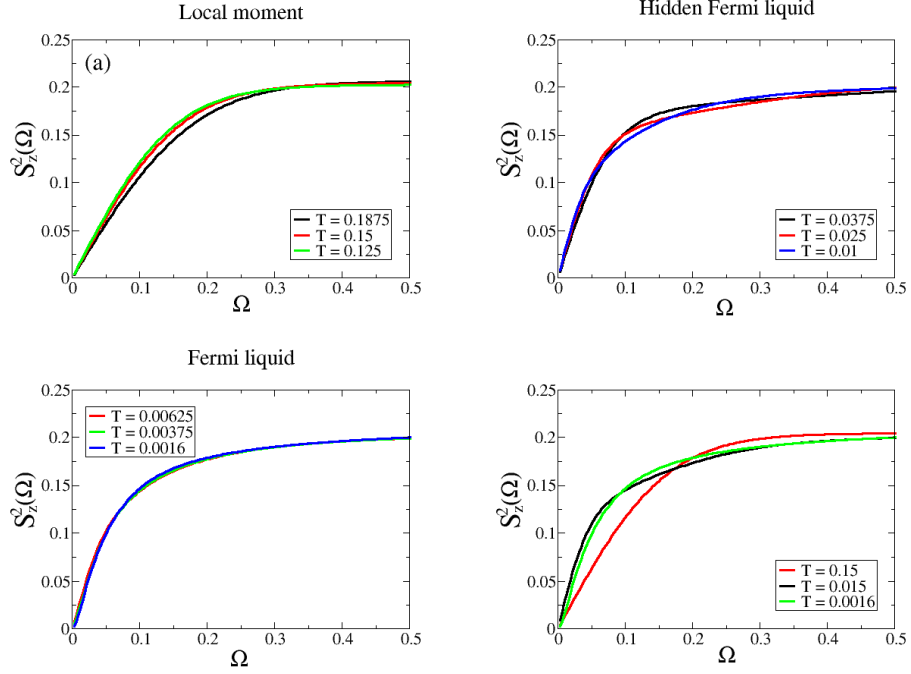


Figure 2.11: Cumulative spectral weight of local dynamic spin susceptibility.

Setting $\Omega = \infty$, we get the sum rule for spin operators,

$$S_z^2(\infty) = \langle \hat{S}_z^2 \rangle \quad (2.18)$$

Fig. 2.11 shows $S_z^2(\Omega)$ for the local moment, hidden Fermi liquid and the Fermi liquid regimes. The last figure compares the representative curves from each regime. First, instead of the $S_z^2(\Omega \rightarrow \infty) = 0.25$, we see $S_z^2(\Omega \rightarrow \infty) \simeq 0.2$. In fact this is not a suprising result. Consider the fermionic representation of spin operators, $\hat{S}_z = (\hat{n}_\uparrow - \hat{n}_\downarrow)/2$,

$$\begin{aligned} \langle \hat{S}_z \hat{S}_z \rangle &= \frac{1}{4} (\langle \hat{n}_\uparrow \hat{n}_\uparrow \rangle + \langle \hat{n}_\downarrow \hat{n}_\downarrow \rangle - \langle \hat{n}_\uparrow \hat{n}_\downarrow \rangle - \langle \hat{n}_\downarrow \hat{n}_\uparrow \rangle) \\ &= \frac{1}{4} (\langle \hat{n}_\uparrow \rangle + \langle \hat{n}_\downarrow \rangle - 2 \langle \hat{n}_\uparrow \hat{n}_\downarrow \rangle) \\ &= \frac{n}{4} - \frac{\langle \hat{n}_\uparrow \hat{n}_\downarrow \rangle}{2}. \end{aligned}$$

In our case, the total density is $n = 0.85$, and the double occupancy is non-zero, $\langle n_\uparrow n_\downarrow \rangle \simeq 0.01$, thus the cumulative spectral weight is $S_z^2(\infty) \simeq 0.21$, expected by Fig. 2.11.

To understand the temperature dependence of the spin fluctuation, the low energy part of $\chi_S(\omega)$ is usually fit to the following model,

$$\tilde{\chi}_S(\omega) = \frac{\chi_S^0 \Gamma}{\Gamma - i\omega}. \quad (2.19)$$

χ_S^0 is the local static susceptibility and Γ is the characteristic energy scale for spin fluctuations. To determine χ_S^0 and Γ , notice that

$$\chi_S^0 = \tilde{\chi}_S(0) = \chi_S(0), \quad (2.20)$$

and

$$\frac{d}{d\omega} \Im \tilde{\chi}_S(\omega=0) = \frac{\chi_S^0}{\Gamma}. \quad (2.21)$$

Thus Γ can be determined by the slope of $\Im \chi_S(\omega)$ at $\omega = 0$. Another usually adopted shortcut to find Γ is to find the maximum position of $\Im \chi_S(\omega)$.

Fig. 2.12 shows χ_S^0 and Γ . In Fig. 2.12(b), points labelled by “slope fit” are obtained by fitting to the slope of $\Im \chi_S(\omega)$ at $\omega = 0$ (see Eq. 2.21). Points labelled by “maximum fit” represents the positions of maximum of $\Im \chi_S(\omega)$.

χ_S^0 follows a Curie-Weiss law,

$$\chi_S^0 \propto \frac{1}{T + T_\theta}, \quad (2.22)$$

with $T_\theta \simeq 0.015 \simeq 2T_{FL}$, which is much smaller than T_{BR} . This Curie-Weiss behavior was also observed in previous QMC calculations on doped Mott insulator [55].

The values of Γ obtained by fitting the low energy slope or the maximum of $\Im \chi_S(\omega)$ agree semi-quantitatively. The temperature dependence of Γ illustrates a “shoulder” near $T \simeq 0.75 \simeq T_{BR}/2$. Above $T_{BR}/2$, Γ is weakly dependent on T in a quasi-linear manner.

The spin-lattice relaxation time T_1 is determined by χ_S^0 and Γ .

$$\frac{1}{T_1 T} \simeq \lim_{\omega \rightarrow 0} \frac{\Im \chi_S(\omega)}{\omega} = \frac{\chi_S^0}{\Gamma}. \quad (2.23)$$

To compute $1/T_1 T$, the values of Γ determined by the low energy slope of $\Im \chi_S(\omega)$ are used. Fig. 2.13 (a) shows the inverse of spin-lattice relaxation time, $1/T_1$. The

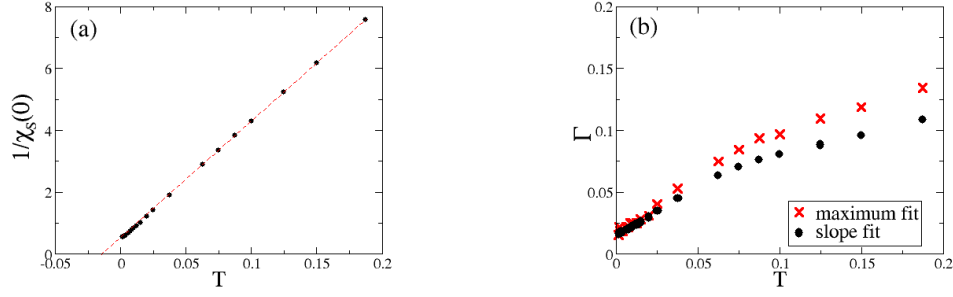


Figure 2.12: (a): Static local susceptibility χ_S^0 . (b): Local spin fluctuation energy scale Γ . Red crosses are found by locating the maximum of $\Im\chi_S(\omega)$. Black dots are obtained by fitting the low energy slope of $\Im\chi_S(\omega)$.

inset shows $1/T_1 T$. The temperature dependence of $1/T_1$ indicates both T_{FL} and T_{BR} . Above $T_{BR}/2$, $1/T_1$ is quasi-linear in T with a negative slope. Below $T_{BR}/2$, it exhibits a maximum at $T \simeq 0.12 \simeq 2T_{FL}$, and decreases steeply towards $T = 0$.

The Korringa-Shiba relation in a Fermi liquid states that

$$\lim_{\omega \rightarrow 0} \frac{\Im\chi_S(\omega)}{\omega(\chi_S^0)^2} \quad (2.24)$$

is a constant determined by the magnetic moment of electron [56]. It is easy to see from Eq. 2.23 that

$$\lim_{\omega \rightarrow 0} \frac{\Im\chi_S(\omega)}{\omega(\chi_S^0)^2} = \frac{1}{\chi_S^0 \Gamma}, \quad (2.25)$$

which is shown in Fig. 2.13(b) to illustrate the deviation from the Korringa-Shiba relation. In general, $\frac{1}{\chi_S^0 \Gamma}$ varies with temperature moderately. In particular, below $T = 0.025$, when the quasiparticles of hidden Fermi liquid have well-formed, $\frac{1}{\chi_S^0 \Gamma}$ exhibits a drop (quasi-)linear in temperature below the shoulder feature at $T = 0.025$.

2.4.2 The Lattice Spin Susceptibility

The lattice spin susceptibility $\chi(\mathbf{Q}, \omega)$ provides more detailed information of the spin excitations. The divergence of the static part $\chi(\mathbf{Q}, \omega = 0)$ at a certain lattice momentum \mathbf{Q}_m and temperature T_m indicates a magnetic phase transition at $T = T_m$ and the magnetic ordering vector is \mathbf{Q}_m . The imaginary part, $\Im\chi(\mathbf{Q}, \omega)$ gives the spectral information of spin excitations, which is usually contrasted with the neutron scattering spectroscopy.

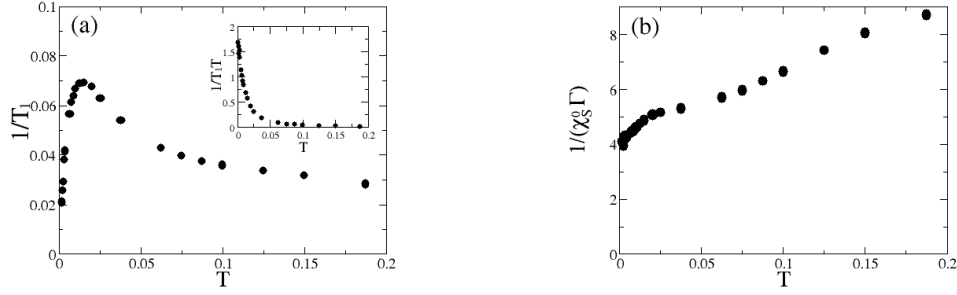


Figure 2.13: (a): Spin-lattice relaxation time. (b) The deviation from Korringa-Shiba relation.

Computing Scheme

A general but not practical method to compute $\chi(\mathbf{Q}, \omega)$ is described as follows.

$\chi(\mathbf{Q}, \omega)$ can be computed by analytical continuation from its Matsubara counterpart, $\chi(\mathbf{Q}, i\Omega)$, which needs the information of the full two-particle correlation function $\chi_{i\mu, i\nu}(\mathbf{Q}, i\Omega)$,

$$\chi(\mathbf{Q}, i\Omega) = \frac{1}{\beta^2} \sum_{i\mu, i\nu} \chi_{i\mu, i\nu}(\mathbf{Q}, i\Omega). \quad (2.26)$$

$\chi_{i\mu, i\nu}(\mathbf{Q}, i\Omega)$ satisfies the Bethe-Salpeter equation,

$$\begin{aligned} \frac{1}{\beta} \chi_{i\mu, i\nu}(\mathbf{Q}, i\Omega) &= \frac{1}{\beta} \chi_{i\mu, i\nu}^0(\mathbf{Q}, i\Omega) \\ &+ \sum_{i\nu', i\nu''} \left(\frac{1}{\beta} \chi_{i\mu, i\nu'}^0(\mathbf{Q}, i\Omega) \right) \left(\frac{1}{\beta} \Gamma_{i\nu', i\nu''}(\mathbf{Q}, i\Omega) \right) \left(\frac{1}{\beta} \chi_{i\nu'', i\nu}(\mathbf{Q}, i\Omega) \right), \end{aligned} \quad (2.27)$$

in which the bubble diagram is

$$\frac{1}{\beta} \chi_{i\mu, i\nu}(\mathbf{Q}, i\Omega) = -\frac{1}{V} \sum_k G_k(i\mu) G_{k+Q}(i\mu + i\Omega) \delta_{\nu, \mu+\Omega}. \quad (2.28)$$

$\Gamma_{i\nu', i\nu''}(\mathbf{Q}, i\Omega)$ is the irreducible vertex function. In the DMFT framework, the one-particle Green's function $G_{\mathbf{k}}(i\omega)$ can be determined by the non-interacting band structure $\epsilon_{\mathbf{k}}$ and the local self energy $\Sigma(i\omega)$. $\Gamma_{i\nu', i\nu''}(\mathbf{Q}, i\Omega)$ is replaced by the local irreducible vertex, $\Gamma_{i\mu, i\mu}^{loc}(i\Omega)$, which can be solved by inverting the Bethe-Salpeter equation of the

impurity problem,

$$\begin{aligned} \frac{1}{\beta} \chi_{i\mu, i\nu}(i\Omega) &= \frac{1}{\beta} \chi_{i\mu, i\nu}^0(i\Omega) \\ &+ \sum_{i\nu', i\nu''} \left(\frac{1}{\beta} \chi_{i\mu, i\nu'}^0(i\Omega) \right) \left(\frac{1}{\beta} \Gamma_{i\nu', i\nu''}(i\Omega) \right) \left(\frac{1}{\beta} \chi_{i\nu'', i\nu}(i\Omega) \right). \end{aligned} \quad (2.29)$$

Therefore after the DMFT self-consistent condition is satisfied, the impurity solver first computes the local two-particle Green's function $\chi_{i\mu, i\nu}^{loc}(i\Omega)$, then by inverting Eq. 2.29 solve for the local irreducible vertex $\Gamma_{i\mu, i\nu}^{loc}(i\Omega)$, which along with the local self-energy is put into Eq. 2.27 to compute $\chi_{i\mu, i\nu}(\mathbf{Q}, i\Omega)$ and then $\chi(\mathbf{Q}, i\Omega)$. Finally the analytical continuation is employed to get the real-frequency quantity $\chi(\mathbf{Q}, \omega)$.

However a numerical implementation of this method is a challenging task, since computing the local two-particle quantities demands considerable computing power. A reliable analytical continuation usually needs the value $\chi(\mathbf{Q}, i\Omega)$ for $i\Omega$ up to the asymptotic regime. For each $i\Omega$, the two-particle Green's function, $\chi_{i\mu, i\nu}^{loc}(i\Omega)$, is a matrix, whose size is determined by the cutoff of $i\mu$ and $i\nu$.

To reduce the computing workload, the following approximation to the irreducible vertex is adopted [57]. A possible method is to approximate the irreducible vertex $\Gamma_{i\nu', i\nu''}(i\Omega)$ by an *effective* interaction, $\Gamma_{i\nu', i\nu''}(i\Omega) = U_{eff}$, that is, to reduce the Bethe-Salpeter equation into an effective RPA approximation, with U_{eff} being the effective bare interaction. That is, the effective two-particle Green's function is

$$\begin{aligned} \frac{1}{\beta} \chi_{i\mu, i\nu}^{eff}(Q, i\Omega) &= \frac{1}{\beta} \chi_{i\mu, i\nu}^0(Q, i\Omega) \\ &+ \sum_{i\nu', i\nu''} \left(\frac{1}{\beta} \chi_{i\mu, i\nu'}^0(Q, i\Omega) \right) \left(\frac{1}{\beta} U_{eff} \right) \left(\frac{1}{\beta} \chi_{i\nu'', i\nu}^{eff}(Q, i\Omega) \right). \end{aligned} \quad (2.30)$$

U_{eff} is calculated by requiring that the RPA approximation can give the correct static susceptibility at $\Omega = 0$,

$$\frac{1}{\beta^2} \sum_{i\mu, i\nu} \chi_{i\mu, i\nu}^{eff}(Q, i\Omega = 0) = \frac{1}{\beta^2} \sum_{i\mu, i\nu} \chi_{i\mu, i\nu}(Q, i\Omega = 0). \quad (2.31)$$

Therefore, only at the first bosonic Matsubara frequency the impurity solver needs to compute the local two-particle Green's function and irreducible vertex. Furthermore, the procedure of analytical continuation is also simplified. The lattice spin susceptibility

in real frequencies is then

$$\chi(Q, \omega) = \frac{\chi^0(Q, \omega)}{1 - U_{eff}\chi^0(Q, \omega)}, \quad (2.32)$$

where $\chi^0(Q, \omega)$ is the bubble term in real frequency,

$$\chi^0(Q, \omega) = \pi \int d\omega' \frac{1}{V} \sum_k A_k(\omega') A_{k+Q}(\omega + \omega') (f(\omega') - f(\omega + \omega')). \quad (2.33)$$

$A_k(\omega) = -\frac{1}{\pi} \text{Im} G_k(\omega)$ is the spectral function and $f(\omega)$ is the Fermi function.

In this chapter, I use this effective RPA method to compute the spectral property of spin excitations in a doped Mott insulator. In Ch. 4, I will use this method to study spin excitations in a heavy fermion system. This method has also been applied to iron pnictides and achieved quantitative agreement with neutron scattering spectra [58].

Spin Excitations in a Doped Mott Insulator

Fig. 2.14 shows on the left the *static* lattice spin susceptibility for various \mathbf{Q} as function of temperature. The \mathbf{Q} -vectors are indicated in the caption of the figure. To help locate the magnetic transition, $1/\chi(\mathbf{Q})$ is presented. The transition temperature is approximately $T_m \simeq 0.008$, and the ordering vector is $\mathbf{Q}_c \simeq (0.88\pi, 0.88\pi)$. Notice $T_m \sim T_{FL} = 0.0075$. On the right of Fig. 2.14 shows the Fermi surface at low temperature ($T = 0.0025$). The black arrow indicates the nesting vector, $\mathbf{Q}_N = (0.95\pi, 0.95\pi)$, which is different from the ordering vector.

Fig. 2.15 show the imaginary part of the lattice dynamic spin susceptibility $\chi''(\mathbf{Q}, \omega)$ along the contour $(0, 0) - (\pi, \pi) - (\pi, 0) - (0, 0)$. At high temperature, the spin excitations show weak dispersion and are heavily damped. In particular, the spin excitation at the ordering vector is gapped at high temperature ($T = 0.25$, $T = 0.125$, and $T = 0.0625$). As temperature is lowered ($T \lesssim 0.025$), the spectral weight starts to “condense” near the ordering vector and form gapless spin excitations with sharp feature, which leads to the magnetic instability.

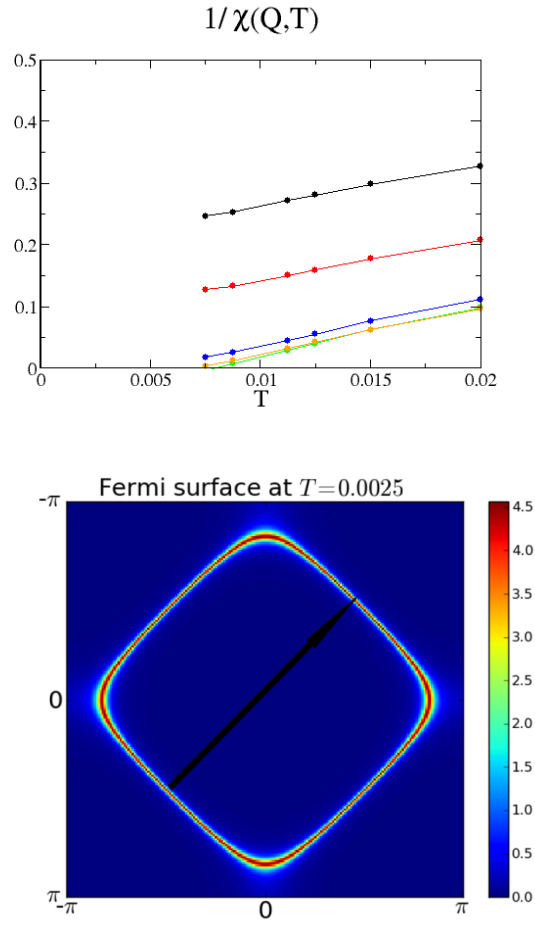


Figure 2.14: Upper: \mathbf{Q} -dependent static magnetic susceptibility for $Q = (0, 0)$ (black), $(\pi/2, \pi/2)$ (red), $(3\pi/4, 3\pi/4)$ (blue), $Q_m \simeq (0.88\pi, 0.88\pi)$ (green) and (π, π) (yellow). Lower: Fermi Surface at $T = 0.0025$. The black arrow indicates the nesting vector, which is $Q_N \simeq (0.95\pi, 0.95\pi)$.

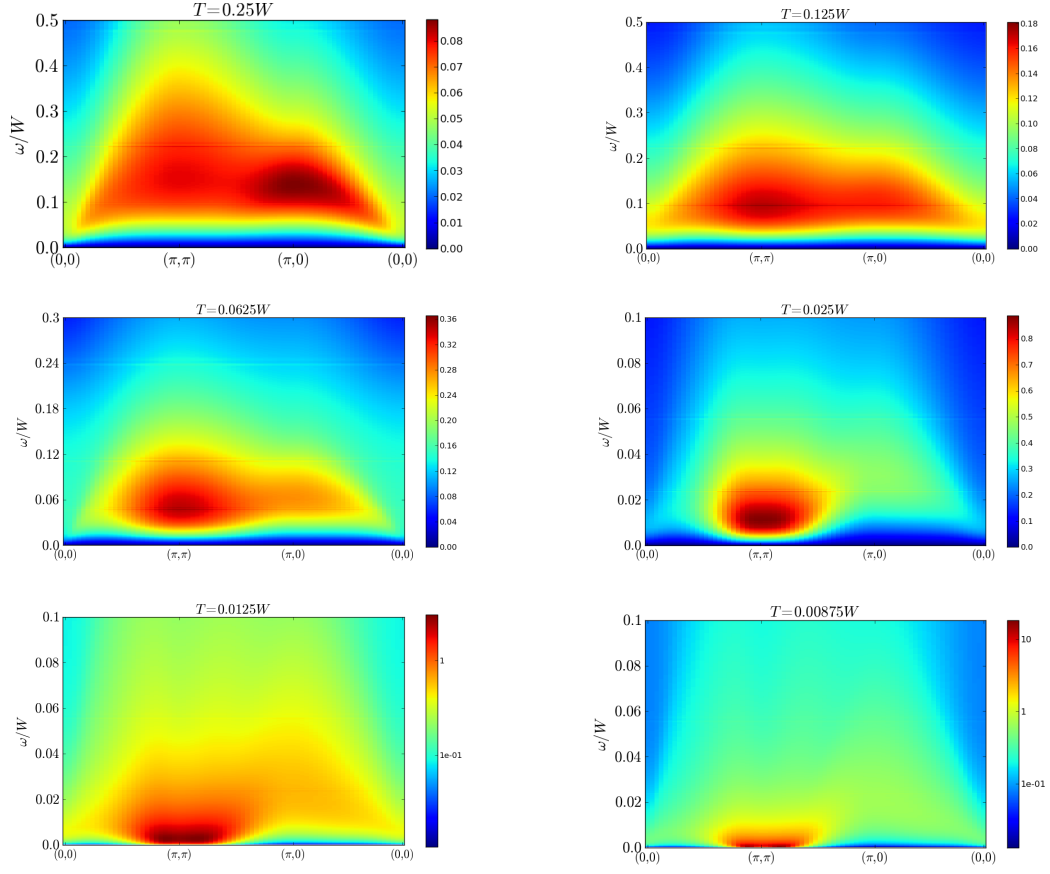


Figure 2.15: \mathbf{Q} -dependent dynamic susceptibility $\chi''(\mathbf{Q}, \omega)$ along the contour $(0,0) - (\pi, \pi) - (\pi, 0) - (0,0)$ for various temperatures.

2.5 Conclusion

We validate the QP picture in describing magneto- and thermo-electric transport properties of a archetypical doped Mott insulator over wide temperature range. We show a characteristic temperature scale T_{sat} demarcating the evolution of spectral function, LDOS and QP scattering rate and mean free path with temperature. Below T_{sat} , we identify a hidden Fermi liquid state. The QP scattering rate of the hidden Fermi liquid follows conventional T^2 behavior, but the QP velocity is renormalized by a temperature-dependent Z , leading to anomalous transport such as linear resistivity. Only below a much lower temperature T_{FL} , Z approaches to a constant value and canonical Fermi-liquid behavior is expected. We point out that the temperature dependence of Z and QP scattering rate can be experimentally investigated using optical conductivity and AC Hall effect.

Further studies should be carried out to ascertain to which extent the DMFT description of transport applies to real materials, but the strong similarities between the experimental features revealed in the phenomenological picture in Ref. [51] and our results are encouraging. Alternating current (ac) transport measurements can be used to extract the temperature dependence of $\tau_{\mathbf{k}_F}^*$. At low frequency, the optical conductivity is parametrized as [59, 60] $\sigma(\omega) = \frac{\omega_{opt}^{*2}}{4\pi} \left(-i\omega + \frac{1}{\tau_{opt}^*}\right)^{-1}$, with $\omega_{opt}^{*2} \simeq 8\pi\Phi^{*xx}(0) = 8\pi Z_{\mathbf{k}_F}\Phi^{xx}(\tilde{\mu})$ and $\tau_{opt}^* \simeq \tau_{\mathbf{k}_F}^*/2$. Similarly in the ac Hall effect [61], $\tan\theta_H(\omega)/B = \frac{\omega_H^{*2}}{4\pi} \left(-i\omega + \frac{1}{\tau_H^*}\right)^{-1}$ follows, with $\omega_H^{*2} \simeq 4\pi \frac{\Phi^{*yx}(0)}{\Phi^{*xx}(0)} = 4\pi \frac{Z_{\mathbf{k}_F}\Phi^{yx}(\tilde{\mu})}{\Phi^{xx}(\tilde{\mu})}$ and $\tau_H^* \simeq \tau_{\mathbf{k}_F}^*/2$. Frequency dependent thermoelectric measurements would give additional information on the asymmetry of the QP dispersion and scattering rate.

The extension from model Hamiltonians to the LDA+DMFT framework is straightforward. It can be used to separate the temperature dependence of transport coefficients arising from the temperature dependence of the QP band and that of the scattering rate, in materials such as the ruthenates [62], the vanadates [63] and the nickelates [64, 44, 65] for which the LDA+DMFT description is known to provide an accurate zeroth order picture of numerous properties [44]. Recent experiments on cuprates [66] have revealed evidence for the temperature dependence of ω_{opt}^{*2} and a T^2 -scattering rate over a broad

range of temperatures. These materials require cluster DMFT studies to describe their momentum space differentiation. Still, it is tempting to interpret the transport properties in terms of QPs to provide an effective description of the transport. Indeed the QP scattering rate computed in the t-J model in Ref. [67], exhibits the saturation behavior described in this work and it would be interesting to reanalyze the results in terms of the QPs of the hidden Fermi liquid. Our findings are related to two earlier theoretical proposals. Anderson introduced the idea of a hidden Fermi liquid [68, 69], requiring $Z_{\mathbf{k}_F}$ to strictly vanish at $T = 0$ in the normal state. Alternatively, our results could be cast into the framework of the extremely correlated Fermi liquid [70] by the temperature dependence of the caparison function.

Chapter 3

Thermoelectric Power in Correlated Metal

Thermoelectric energy harvesting, i.e. the transformation of waste heat into usable electricity, is of great current interest. The main obstacle is the low efficiency of materials for converting heat to electricity [71, 72]. Over the past decade, there has been a renewed interest on thermoelectric materials, mainly driven by experimental results [73].

Computing the thermoelectric power (TEP) in correlated systems is a non-trivial task and several approximation schemes have been used to this intent. The well-known Mott-Heikes formula [74, 75] gives an estimate of the high temperature limit of TEP [76]. Thermoelectric transport at intermediate temperature was investigated in the context of single-band and degenerate Hubbard Hamiltonians by dynamical mean field theory (DMFT) [38, 77, 78]. The Kelvin formula estimates the TEP by the temperature dependence of chemical potential and was revisited recently in Ref. [79].

The high frequency (AC) limit of thermoelectric power is another interesting quantity that provides insight into the thermoelectric transport in correlated materials. The thermoelectric power in the high frequency limit of a degenerate Hubbard model was briefly discussed in Ref. [77]. It was also studied recently by Shastry and collaborators, who developed a formalism for evaluating the AC limit of thermoelectric response using high temperature series expansion and exact diagonalization. The methodology was applied to a single band $t - J$ model on a triangular lattice [80, 81]. The authors point out that the AC limit of TEP (S^*) has similar temperature dependence as S_0 but can be calculated with significantly less effort, while still provides a reliable estimation of S_0 .

This chapter compares various aspects of the AC limit S^* , the estimation of Kelvin formula S_K and Mott-Heikes formula S_{MH} , with the emphasis on their predicting power

as approximations to the transport TEP S_0 in correlated metals. Both analytic and numerical results are presented.

3.1 Thermoelectric power at finite frequency

3.1.1 General formalism

Electrical current can be induced by gradient of electrical potential and temperature.

The linear response equations for static (DC limit) external fields are[19]

$$J_1^x = L_{11}^{xx} E_x + L_{12}^{xx} \left(-\frac{1}{T} \nabla_x T \right), \quad (3.1)$$

$$J_2^x = L_{21}^{xx} E_x + L_{22}^{xx} \left(-\frac{1}{T} \nabla_x T \right). \quad (3.2)$$

We only consider the longitudinal case. J_1^x and J_2^x are x - component of **particle** and **heat** current, respectively. L_{ij}^{xx} are transport coefficients and respect the Onsager relation, $L_{12}^{xx} = L_{21}^{xx}$. Transport properties can be defined in terms of L_{ij}^{xx} . For example, the electric conductivity σ , TEP S , and the thermal conductivity κ are

$$\sigma = e^2 L_{11}^{xx}, \quad (3.3)$$

$$S = -\frac{1}{eT} \frac{L_{12}^{xx}}{L_{11}^{xx}}, \quad (3.4)$$

$$\kappa = \frac{1}{T} \left(L_{22}^{xx} - \frac{(L_{12}^{xx})^2}{L_{11}^{xx}} \right). \quad (3.5)$$

In following context, we use $k_B = e = \hbar = 1$. The practical value of S is recovered by multiplying the factor $k_B/e = 86.3 \mu V/K$, which we use as the unit for TEP.

For conventional thermoelectric transport, L_{xx}^{ij} is defined and measured at the DC limit. The extension to dynamical (frequency dependent) case is absent in standard textbooks but has been studied in detail in Ref. [80]. Here we give the outlines of the formalism. Borrowed from Luttinger's derivation[82], an auxiliary "gravitational" field is coupled to the heat density. An "equivalence" between the fictitious gravitational field and the temperature gradient is proved. That is, the transport coefficient due to the auxiliary field, \hat{L}_{ij} is equal to that due to the temperature gradient, $\hat{L}_{ij} = L_{ij}$. Then the transport coefficients L_{ij}^{xx} can be written in terms of correlation functions between particle current and(or) energy current following standard Kubo's theory, since the quantum mechanical operator of the coupling between the auxiliary field and heat density has an explicit expression, while it is not the case for the temperature gradient

and heat current. In Ref.[80], this formalism is generalized to temporally and spatially periodic external fields, thus the transport coefficients become momentum- and frequency-dependent functions, $L_{ij}^{xx}(\mathbf{q}, \omega)$. More details for the formalism of thermal transport is given in App. D.1.

Some remarks can be made on $L_{ij}^{xx}(\mathbf{q}, \omega)$. On one hand, in the DC limit ($\omega \rightarrow 0$), there are two different ways of taking the thermodynamic limit ($\mathbf{q} \rightarrow 0$) [82, 80] since $\omega \rightarrow 0$ and $\mathbf{q} \rightarrow 0$ do not commute. If we define $v = \frac{\omega}{|\mathbf{q}|}$ as the “phase velocity” of the external perturbation field, the so-called “fast limit” is defined as taking $\mathbf{q} \rightarrow 0$ before $\omega \rightarrow 0$ ($v \rightarrow \infty$). In the fast limit, the transport TEP, or, the conventional DC limit of TEP is obtained. The “slow limit” is defined as $\omega \rightarrow 0$ is taken before $\mathbf{q} \rightarrow 0$, thus $v \rightarrow 0$. Therefore, the perturbation is adiabatic and the charge and energy can redistribute to reach an equilibrium state. The slow limit then gives the Kelvin formula of TEP [79]. On the other hand, in the AC limit ($\omega \rightarrow \infty$), the two limits, $\omega \rightarrow \infty$ and $\mathbf{q} \rightarrow 0$, commute, because the phase velocity v will be infinity in either scenario.

The dynamical transport coefficients with $\mathbf{q} \rightarrow 0$ are given by,

$$L_{ij}^{xx}(\omega) = \frac{1}{\omega V} \int_{-\infty}^{\infty} \exp(i\omega t) \Theta(t) \langle [J_i^x(t), J_j^x(0)] \rangle. \quad (3.6)$$

For a given Hamiltonian H , the current operators are defined by following the conservation laws[19],

$$J_i^x = \frac{\partial O_i^x}{\partial t} = i[H, O_i^x]. \quad (3.7)$$

O_i^x is the x -component of particle and heat polarization operator, that is,

$$O_1^x = \sum_i R_i^x n_i, \quad (3.8)$$

$$O_2^x = \sum_i R_i^x (h_i - \mu n_i), \quad (3.9)$$

where n_i and h_i are local particle and energy density operators. The explicit forms of n_i and h_i are determined by the Hamiltonian of interest. In Sec. 3.1.2, we will write O_i and give J_i for a general multiband model.

At DC limit, the imaginary part of $L_{ij}^{xx}(\omega = 0)$ is zero, thus S_0 is determined by the real parts. For convenience, I define

$$L_{ij}^0 \equiv \text{Re} L_{ij}^{xx}(0), \quad (3.10)$$

then we have

$$S_0 \equiv \mathbf{Re}S(\omega = 0) = -\frac{1}{T} \frac{L_{12}^0}{L_{11}^0}. \quad (3.11)$$

At AC limit, $L_{ij}^{xx}(\omega)$ is dominated by the imaginary part, with a $O(1/\omega)$ leading order,

$$\mathbf{Im}L_{ij}^{xx}(\omega) = \frac{1}{\omega} L_{ij}^* + O(\frac{1}{\omega^2}). \quad (3.12)$$

Using Lehman's representation, it can be shown that L_{ij}^* defined in Eq. 3.12 is, up to a factor of i , the expectation values of commutators between current and polarization operators[77, 80, 81], i.e.,

$$L_{ij}^* = i\langle [J_j^x, O_j^x] \rangle. \quad (3.13)$$

Consequently, TEP at AC limit is

$$S^* \equiv \mathbf{Re}S(\omega \rightarrow \infty) = -\frac{1}{T} \frac{L_{12}^*}{L_{11}^*}. \quad (3.14)$$

L_{ij}^* is related to $\mathbf{Re}L_{ij}(\omega)$ through the Kramers-Kronig relation. Keeping the leading order in $1/\omega$, we have

$$L_{ij}^* = \frac{1}{\pi} \int_{-\infty}^{\infty} d\omega \mathbf{Re}L_{ij}^{xx}(\omega). \quad (3.15)$$

Thus L_{ij}^* is also connected to the sum rules of dynamical quantities. For example, L_{11}^* is proportional to the sum rule of conductivity[83, 43].

$$L_{11}^* = \frac{2}{\pi} \int_0^{\infty} d\omega \mathbf{Re}\sigma(\omega). \quad (3.16)$$

Other sum rules have also been derived in Ref. [80] and [81].

3.1.2 The high-frequency limit L_{ij}^*

Now we explicitly evaluate the commutator in Eq. (3.13) for a general tight-binding Hamiltonian with local interaction, which will determine S^* , the AC limit of TEP. We start with the following Hamiltonian

$$H = - \sum_{ij,\mu\nu} t_{ij}^{\mu\nu} c_{i\mu}^\dagger c_{j\nu} + \sum_{i\mu} \epsilon_\mu c_{i\mu}^\dagger c_{i\mu} + \sum_i \sum_{\alpha\beta\mu\nu} U_{\alpha\beta\mu\nu} c_{i\mu}^\dagger c_{i\beta}^\dagger c_{i\nu} c_{i\mu}. \quad (3.17)$$

i, j are site indices. α, β, μ and ν denote local orbitals. $t_{ij}^{\mu\nu}$ is the hopping integral, and $U_{\alpha\beta\mu\nu}$ is the matrix element for Coulomb interaction between local orbitals. ϵ_μ is energy level of local orbitals. The particle polarization operator is

$$O_1^x = \sum_i R_i^x \sum_\mu c_{i\mu}^\dagger c_{i\mu}, \quad (3.18)$$

and the heat polarization operator is

$$\begin{aligned} O_2^x = & \sum_i R_i^x \left[-\frac{1}{2} \sum_{j,\mu\nu} \left(t_{ij}^{\mu\nu} c_{i\mu}^\dagger c_{j\nu} + t_{ji}^{\nu\mu} c_{j\nu}^\dagger c_{i\mu} \right) \right. \\ & \left. + \sum_{\alpha\beta\mu\nu} U_{\alpha\beta\mu\nu} c_{i\mu}^\dagger c_{i\beta}^\dagger c_{i\nu} c_{i\mu} + \sum_\alpha (\epsilon_\alpha - \mu) c_{i\alpha}^\dagger c_{i\alpha} \right]. \end{aligned} \quad (3.19)$$

The current operators turn out to be

$$J_1^x = i[H, O_1^x] = -i \sum_{ij,\mu\nu} (R_j^x - R_i^x) t_{ij}^{\mu\nu} c_{i\mu}^\dagger c_{j\nu}, \quad (3.20)$$

and

$$\begin{aligned} J_2^x = & i[H, O_2^x] \\ = & \sum_{ijl,\mu\nu\alpha} \frac{i}{2} t_{il}^{\mu\alpha} t_{lj}^{\alpha\nu} (R_j^x - R_i^x) c_{i\mu}^\dagger c_{j\nu} \\ & - \frac{i}{2} \sum_{ij,\alpha\beta} t_{ij}^{\alpha\beta} (R_j^x - R_i^x) (\epsilon_\alpha + \epsilon_\beta - 2\mu) c_{i\alpha}^\dagger c_{j\beta} \\ & - \frac{i}{2} \sum_{ij,\mu\nu} t_{ij}^{\mu\nu} (R_j^x - R_i^x) \times \left(\sum_{\alpha'\mu'\nu'} (U_{\nu\alpha'\mu'\nu'} - U_{\alpha'\nu\mu'\nu'}) c_{i\mu}^\dagger c_{j\alpha'}^\dagger c_{j\nu'} c_{j\mu'} \right. \\ & \left. + \sum_{\alpha'\beta'\nu'} (U_{\alpha'\beta'\mu\nu'} - U_{\alpha'\beta'\nu'\mu}) c_{i\alpha'}^\dagger c_{i\beta'}^\dagger c_{i\nu'} c_{j\nu} \right). \end{aligned} \quad (3.21)$$

Using the equation of motion of fermionic operators $c_{i\mu}$, we can write J_2^x in a more compact form [84],

$$J_2^x = -\frac{1}{2} \sum_{ij,\mu\nu} (R_j^x - R_i^x) t_{ij}^{\mu\nu} \left(\dot{c}_{i\mu}^\dagger c_{j\nu} - c_{i\mu}^\dagger \dot{c}_{j\nu} \right),$$

in which the time derivative of $c_{i\mu}$ follows,

$$\dot{c}_{i\mu}^\dagger = i[H, c_{i\mu}^\dagger].$$

To compute L_{11}^* and L_{12}^* , we need to further evaluate the commutators between current operators and polarization operators. For L_{11}^* , this is simple and straightforward,

$$L_{11}^* = \sum_{ij, \mu\nu} t_{ij}^{\mu\nu} (R_j^x - R_i^x)^2 \langle c_{i\mu}^\dagger c_{j\nu} \rangle. \quad (3.22)$$

L_{12}^* has a complicate form,

$$\begin{aligned} L_{12}^* = & - \sum_{ijl, \mu\nu\alpha} \frac{1}{2} t_{il}^{\mu\alpha} t_{lj}^{\alpha\nu} (R_j^x - R_i^x)^2 \langle c_{i\mu}^\dagger c_{j\nu} \rangle \\ & + \frac{1}{2} \sum_{ij, \mu\nu} t_{ij}^{\mu\nu} (R_j^x - R_i^x)^2 (\epsilon_\mu + \epsilon_\nu - 2\mu) \langle c_{i\mu}^\dagger c_{j\nu} \rangle \\ & + \frac{1}{2} \sum_{ij, \mu\nu} t_{ij}^{\mu\nu} (R_j^x - R_i^x)^2 \times \left(\sum_{\alpha'\mu'\nu'} (U_{\nu\alpha'\mu'\nu'} - U_{\alpha'\nu\mu'\nu'}) \langle c_{i\mu}^\dagger c_{j\alpha'}^\dagger c_{j\nu'} c_{j\mu'} \rangle \right. \\ & \left. + \sum_{\alpha'\beta'\nu'} (U_{\alpha'\beta'\mu\nu'} - U_{\alpha'\beta'\nu'\mu}) \langle c_{i\alpha'}^\dagger c_{i\beta'}^\dagger c_{i\nu'} c_{j\nu} \rangle \right). \end{aligned} \quad (3.23)$$

This formula can be significantly simplified if we check the equation of motion for the single-particle Greens's function,

$$G_{ji}^{\nu\mu}(\tau) = -\langle T_\tau c_{j\nu}(\tau) c_{i\mu}^\dagger \rangle. \quad (3.24)$$

T_τ is the time-ordering operator in imaginary time. Its equation of motion reads,

$$\begin{aligned} \frac{\partial G_{ji}^{\nu\mu}(\tau)}{\partial \tau} = & \sum_{j'\nu'} t_{jj'}^{\nu\nu'} G_{j'i}^{\nu'\mu}(\tau) - (\epsilon_\nu - \mu) G_{ji}^{\nu\mu}(\tau) \\ & - \sum_{\alpha'\mu'\nu'} (U_{\alpha'\nu\mu'\nu'} - U_{\nu\alpha'\mu'\nu'}) \times \langle T_\tau c_{j\alpha'}^\dagger(\tau) c_{j\nu'}(\tau) c_{j\mu'}(\tau) c_{i\mu}^\dagger \rangle. \end{aligned}$$

Taking the $\tau \rightarrow 0^-$ limit leads to

$$\begin{aligned} & \sum_{\alpha'\mu'\nu'} (U_{\nu\alpha'\mu'\nu'} - U_{\alpha'\nu\mu'\nu'}) \langle c_{i\mu}^\dagger c_{j\alpha'}^\dagger c_{j\nu'} c_{j\mu'} \rangle \\ & = - \lim_{\tau \rightarrow 0^-} \frac{\partial G_{ji}^{\nu\mu}(\tau)}{\partial \tau} + \sum_{j'\nu'} t_{jj'}^{\nu\nu'} \langle c_{i\mu}^\dagger c_{j'\nu'} \rangle - (\epsilon_\nu - \mu) \langle c_{i\mu}^\dagger c_{j\nu} \rangle. \end{aligned} \quad (3.25)$$

Substituting the last term in Eq. (3.23) by the right hand side of Eq. (3.25), we get

$$L_{12}^* = -\frac{1}{2} \sum_{ijl, \mu\nu\alpha} t_{il}^{\mu\alpha} t_{lj}^{\alpha\nu} \left[(R_j^x - R_i^x)^2 - (R_l^x - R_i^x)^2 - (R_j^x - R_l^x)^2 \right] \langle c_{i\mu}^\dagger c_{j\nu} \rangle - \sum_{ij, \mu\nu} t_{ij}^{\mu\nu} (R_j^x - R_i^x)^2 \lim_{\tau \rightarrow 0^-} \frac{\partial}{\partial \tau} G_{ji}^{\nu\mu}(\tau). \quad (3.26)$$

Using

$$\langle c_{i\mu}^\dagger c_{j\nu} \rangle = \lim_{\tau \rightarrow 0^-} G_{ji}^{\nu\mu}(\tau),$$

and Fourier transform in both real space and imaginary time, we get

$$L_{11}^* = \frac{1}{\beta} \sum_{\omega_n} e^{-i\omega_n 0^-} \sum_{k, \mu\nu} \left(\frac{\partial^2 \epsilon_k^{\mu\nu}}{\partial k_x^2} \right) G_k^{\nu\mu}(i\omega_n), \quad (3.27)$$

and,

$$L_{12}^* = \frac{1}{\beta} \sum_{\omega_n} e^{-i\omega_n 0^-} \sum_{k, \mu\nu} \left[\sum_{\alpha} \left(\frac{\partial \epsilon_k^{\mu\alpha}}{\partial k_x} \right) \left(\frac{\partial \epsilon_k^{\alpha\nu}}{\partial k_x} \right) + i\omega_n \left(\frac{\partial^2 \epsilon_k^{\mu\nu}}{\partial k_x^2} \right) \right] G_k^{\nu\mu}(i\omega_n). \quad (3.28)$$

$\epsilon_k^{\mu\nu}$ is Fourier transformation of hopping amplitudes,

$$\epsilon_k^{\mu\nu} = - \sum_R e^{ikR} t^{\mu\nu}(R), \quad (3.29)$$

where we have utilized the translational invariance,

$$t_{ij}^{\mu\nu} = t^{\mu\nu}(R_j - R_i). \quad (3.30)$$

It is straightforward to convert the Matsubara summation to the integration in real frequencies.

$$L_{11}^* = \int_{-\infty}^{\infty} d\omega \sum_{k, \mu\nu} \left(\frac{\partial^2 \epsilon_k^{\mu\nu}}{\partial k_x^2} \right) f(\omega) A_k^{\nu\mu}(\omega), \quad (3.31)$$

and

$$L_{12}^* = \int_{-\infty}^{\infty} d\omega \sum_{k, \mu\nu} \left[\sum_{\alpha} \left(\frac{\partial \epsilon_k^{\mu\alpha}}{\partial k_x} \right) \left(\frac{\partial \epsilon_k^{\alpha\nu}}{\partial k_x} \right) + \omega \left(\frac{\partial^2 \epsilon_k^{\mu\nu}}{\partial k_x^2} \right) \right] f(\omega) A_k^{\nu\mu}(\omega). \quad (3.32)$$

$f(\omega) = 1/(1 + \exp(\beta\omega))$ is the Fermi function. $A_k^{\nu\mu}(\omega) = -\frac{1}{\pi} G_k^{\nu\mu}(\omega)$ is the spectral function.

Eq. (3.27), Eq. (3.28), Eq. (3.31) and Eq. (3.32) are main results in this section. They are derived from a general formalism of dynamical thermoelectric transport outlined in Sec. 3.1.1 and a multiband Hamiltonian, Eq. (3.17). The equation of motion is exact and no approximation is assumed in the derivation. These equations indicate that L_{11}^* and L_{12}^* , and thus S^* are determined by single-particle properties.

3.2 Kelvin formula

The Kelvin formula involves the slow limit, or the thermodynamic limit, that is, $\omega \rightarrow 0$ is taken before $\mathbf{q} \rightarrow 0$. The derivation of Kelvin formula (cf. Ref. [79]) starts from the general expression of transport coefficient $L_{ij}(\mathbf{q}, \omega)$ for finite \mathbf{q} and ω and compute the leading order for small \mathbf{q} . It turns out in the slow limit,

$$\lim_{\mathbf{q} \rightarrow 0} \lim_{\omega \rightarrow 0} L_{12}(\mathbf{q}, \omega) = \frac{\partial \langle H \rangle}{\partial \mu} - \mu \frac{\partial \langle N \rangle}{\partial \mu} = T \left(\frac{\partial s}{\partial \mu} \right)_{T,V}, \quad (3.33)$$

where s is the entropy (lower case is used for entropy to differentiate from TEP), and

$$\lim_{\mathbf{q} \rightarrow 0} \lim_{\omega \rightarrow 0} L_{11}(\mathbf{q}, \omega) = \left(\frac{\partial \langle N \rangle}{\partial \mu} \right)_{T,V}. \quad (3.34)$$

Then the Kelvin formula turns out to be

$$S_K = - \frac{(\partial s / \partial \mu)_{T,V}}{(\partial N / \partial \mu)_{T,V}} = - \left(\frac{\partial s}{\partial \mu} \right)_{T,V} = \left(\frac{\partial \mu}{\partial T} \right)_{N,V}. \quad (3.35)$$

The last equality in Eq. 3.35 makes use of the Maxwell's relations.

3.3 Analytic and Numerical Results in a One-band Hubbard Model

In this section, we discuss S_0 , S^* , and S_K of one-band Hubbard model and present numerical results from dynamical mean field theory (DMFT).

The Hamiltonian of one-band Hubbard model is

$$H = - \sum_{ij,\sigma} t_{ij} c_{i\sigma}^\dagger c_{j\sigma} + U \sum_i n_{i\uparrow} n_{i\downarrow}. \quad (3.36)$$

In DMFT, it is mapped to a single-impurity Anderson model[26] supplemented by the self-consistent condition which reads,

$$\frac{1}{i\omega_n + \mu - \Delta(i\omega_n) - \Sigma(i\omega_n)} = \sum_k G_k(i\omega_n). \quad (3.37)$$

On the left hand side is the local Green's function of the effective impurity model. $\Delta(i\omega_n)$ is the hybridization function of the impurity. On the right hand side, $G_k(i\omega_n)$ is the Green's function of lattice electrons,

$$G_k(i\omega_n) = \frac{1}{i\omega_n + \mu - \epsilon_k - \Sigma(i\omega_n)},$$

with ϵ_k the non-interacting dispersion relation of the lattice model, and $\Sigma(i\omega_n)$ the self energy for both local and lattice Green's function in the self-consistent condition. In DMFT, both coherent and incoherent excitations in a correlated metal can be treated on the same footing [27].

In DMFT, the evaluation of transport coefficients, e.g., Eq. (3.6), can be significantly simplified in one-band model. Since the k -dependence falls solely on the non-interacting dispersion ϵ_k , the vertex corrections vanishes[35]. Consequently, $\mathbf{Re}L_{ij}(\omega)$ can be written in terms of single-particle spectral function,

$$\begin{aligned} \mathbf{Re}L_{ij}(\omega) = & \pi T \sum_{k,\sigma} \left(\frac{\partial \epsilon_k}{\partial k_x} \right)^2 \int_{-\infty}^{\infty} d\omega' \left(\omega' + \frac{\omega}{2} \right)^{i+j-2} \\ & \times \left(\frac{f(\omega') - f(\omega' + \omega)}{\omega} \right) A_k(\omega') A_k(\omega' + \omega). \end{aligned} \quad (3.38)$$

A subtle issue arises involving the sum rule of the $\mathbf{Re}L_{ij}(\omega)$. That is, if we calculate the integrated weight of $\mathbf{Re}L_{ij}(\omega)$ in Eq. (3.38) by Eq. 3.15, will it give the same expression of L_{ij}^* as in Eq. 3.31 and 3.32? Remember that Eq. 3.31 and 3.32 are exact results and so as that the integrated transport coefficient L_{ij}^* only depends on single-particle Green's functions, while the dependence solely on the single-particle spectral function in Eq. 3.38 is a consequence of infinite-dimension in one-band model. Fortunately, the answer is yes and I will show a brief proof for the one-band case but the extension to multiband case is straightforward. This means that ignoring vertex correction could modify the distribution of weight in $\mathbf{Re}L_{ij}(\omega)$, but will not change the integrated weight.

Now we calculate L_{ij}^* for the one-band case. Using Eq. (3.15),

$$L_{12}^* = \sum_{k,\sigma} \left(\frac{\partial \epsilon_k}{\partial k_x} \right)^2 \int d\omega d\omega' \left(\omega' + \frac{\omega}{2} \right) \left(\frac{f(\omega') - f(\omega' + \omega)}{\omega} \right) A_k(\omega') A_k(\omega' + \omega). \quad (3.39)$$

Changing variables,

$$\begin{aligned} \omega_1 &= \omega + \omega', \\ \omega_2 &= \omega, \end{aligned}$$

leads to

$$L_{12}^* = \sum_{k,\sigma} \left(\frac{\partial \epsilon_k}{\partial k_x} \right)^2 \int d\omega_1 d\omega_2 f(\omega_2) A_k(\omega_1) A_k(\omega_2) \\ + 2 \sum_{k,\sigma} \left(\frac{\partial \epsilon_k}{\partial k_x} \right)^2 \int d\omega_1 d\omega_2 \frac{\omega_2}{\omega_1 - \omega_2} f(\omega_2) A_k(\omega_1) A_k(\omega_2). \quad (3.40)$$

The sum rule $\int d\omega_1 A_k(\omega_1) = 1$ simplifies the first term to

$$\sum_{k,\sigma} \left(\frac{\partial \epsilon_k}{\partial k_x} \right)^2 \int d\omega_2 f(\omega_2) A_k(\omega_2).$$

In the second term, Kramer-Kronig relation can be used to eliminate the integral over ω_1 , i.e.,

$$\int d\omega_1 \frac{A_k(\omega_1)}{\omega_1 - \omega_2} = -\mathbf{Re}G_k(\omega_2).$$

Then we use the fact that

$$2\mathbf{Re}G_k(\omega)\mathbf{Im}G_k(\omega) = \mathbf{Im}G_k^2(\omega)$$

and

$$\frac{\partial}{\partial k_x} G_k(\omega) = G_k^2(\omega) \frac{\partial \epsilon_k}{\partial k_x},$$

to simplify the second term on the right hand side of Eq. (3.40) into

$$\sum_{k,\sigma} \left(\frac{\partial \epsilon_k}{\partial k_x} \right) \int d\omega_2 \omega_2 f(\omega_2) \left(\frac{1}{\pi} \right) \frac{\partial}{\partial k_x} \mathbf{Im}G_k(\omega_2).$$

Applying integration by part over k , we are left with

$$\sum_{k,\sigma} \left(\frac{\partial^2 \epsilon_k}{\partial k_x^2} \right) \int d\omega_2 \omega_2 f(\omega_2) A_k(\omega_2). \quad (3.41)$$

Combined with the first term, we have

$$L_{12}^* = \sum_{k,\sigma} \int d\omega \left(\left(\frac{\partial \epsilon_k}{\partial k_x} \right)^2 + \omega \left(\frac{\partial^2 \epsilon_k}{\partial k_x^2} \right) \right) f(\omega) A_k(\omega). \quad (3.42)$$

The calculation for L_{11}^* is similar and straightforward, which results in

$$L_{11}^* = \sum_{k,\sigma} \int d\omega \left(\frac{\partial^2 \epsilon_k}{\partial k_x^2} \right) f(\omega) A_k(\omega). \quad (3.43)$$

Apparently, the general multi-band expression Eq. 3.31 and Eq. 3.32 collapse to Eq. 3.43 and Eq. 3.42 in the one-band case.

The DC limit of $\mathbf{Re}L_{ij}(\omega)$, L_{ij}^0 can be obtained by taking the limit $\omega \rightarrow 0$, which gives,

$$L_{ij}^0 = \pi T \sum_{k,\sigma} \left(\frac{\partial \epsilon_k}{\partial k_x} \right)^2 \int_{-\infty}^{\infty} d\omega \omega^{i+j-2} \left(-\frac{\partial f(\omega)}{\partial \omega} \right) A_k(\omega)^2. \quad (3.44)$$

Summarily, in the framework of DMFT, S_0 is computed from Eq. (3.44). The AC limit, S^* can be computed from Eq. (3.27) and Eq. (3.28), or Eq. (3.31) and Eq. (3.31). In principle, Matsubara frequency and integration over real frequency should give identical results. But in practice, especially in numerical computations of correlated systems, correlation functions in Matsubara frequencies are more easily accessible. For example, among various impurity solvers in DMFT, quantum Monte Carlo method(QMC), i.e., Hirsch-Fye method[33] and recently developed continuous time QMC[30, 32] are implemented in imaginary time. To get correlation functions in real frequencies, numerical implementation of analytic continuation has to be employed, such as maximum entropy method, which is an involved procedure. In this case, formulae in Matsubara frequencies will significantly simplify the calculation.

Due to the bad convergence of the series, Eq. (3.27) and Eq. (3.28) are not appropriate for direct implementation into numerical computations. Following standard recipe (separating and analytically evaluating the badly convergent part), we transform them in a form more friendly to numerics. For the one-band Hubbard model,

$$L_{11}^* = \sum_{k,\sigma} \left(\frac{\partial^2 \epsilon_{k\sigma}}{\partial k_x^2} \right) \left(\frac{1}{\beta} \sum_{\omega_n} \mathbf{Re} G_k(i\omega_n) - \frac{1}{2} \right), \quad (3.45)$$

and

$$L_{12}^* = \sum_{k,\sigma} \left(\frac{\partial \epsilon_k}{\partial k_x} \right)^2 \frac{1}{\beta} \sum_{\omega_n} \mathbf{Re} G_k(i\omega_n) \times [1 + 2\omega_n \mathbf{Im} G_k(i\omega_n)]. \quad (3.46)$$

The Fermi function $f(\omega)$ shows up in Eq. 3.42 and Eq. 3.43, instead of the derivative $\partial f(\omega)/\partial \omega$ which usually appears in DC transport functions. This indicates the integral involves all energies below Fermi surface, and that at low temperature, L_{11}^* and L_{12}^* converges to finite value. So S^* will diverge as $1/T$? which is certainly not the universal behavior of TEP at low temperature. For metals, $S_0 \propto T$. To make the high frequency limit a better approximation of the DC thermoelectric power at low temperature and

for metallic systems, Ref. [42] defines S^{**} by subtracting the finite value of L_{11}^* at zero temperature (the reactive part),

$$S^{**}(T) = -\frac{1}{T} \frac{L_{12}^*(T) - L_{12}^*(T=0)}{L_{11}^*(T)}. \quad (3.47)$$

As will be shown later, at low temperature, $S^{**}(T) \propto T$ has the correct temperature dependence for a Fermi liquid.

3.3.1 Low temperature limit.

At low temperatures, the derivative of Fermi function, $(-\partial f(\omega)/\partial \omega)$ in the integrand of Eq. (3.44) becomes Dirac- δ function-like, thus only the low energy part of the spectral weight near Fermi surface contributes to the integral. The low energy part of the self energy of a Fermi liquid $\Sigma(\omega)$ can be approximated by a Taylor expansion in terms of ω and T .

$$\mathbf{Re}\Sigma(\omega) \simeq \left(1 - \frac{1}{Z}\right) \omega, \quad (3.48)$$

$$\mathbf{Im}\Sigma(\omega) \simeq \frac{\gamma_0}{Z^2}(\omega^2 + \pi^2 T^2) + \frac{1}{Z^3}(a_1 \omega^2 + \omega T^2). \quad (3.49)$$

Previous studies [38, 85] showed that at low temperature, $L_{11}^0 \propto Z^2/T$ and $L_{12}^0 \propto ZT$, thus $S_0 = -L_{12}^0/(TL_{11}^0) \propto T/Z$.

Since we are interested in the relation between S_0 and S^* , it would be convenient to separate from L_{12}^* and L_{11}^* the contribution from the conventional band velocity, $(\partial \epsilon_k / \partial k_x)^2$ and derivative of Fermi function. This can be achieved by performing integration by part on the summation over k in Eq. (3.31) and Eq. 3.32, then we have

$$L_{ij}^* = L_{ij,I}^* + L_{ij,II}^*,$$

with

$$L_{ij,I}^* = \sum_{k,\sigma} \left(\frac{\partial \epsilon_k}{\partial k_x} \right)^2 \int d\omega \left(-\frac{\partial f(\omega)}{\partial \omega} \right) \times \omega^{i+j-2} \left(-\frac{1}{\pi} \right) \mathbf{Im} [G_k(\omega) Z(\omega)], \quad (3.50)$$

$$L_{ij,II}^* = \sum_{k,\sigma} \left(\frac{\partial \epsilon_k}{\partial k_x} \right)^2 \int d\omega f(\omega) \left(-\frac{1}{\pi} \right) \times \mathbf{Im} \left[G(\epsilon, \omega) \frac{\partial}{\partial \omega} (\omega^{i+j-2} (1 - Z(\omega))) \right]. \quad (3.51)$$

We have introduced

$$Z(\omega) = \frac{1}{1 - \partial \Sigma(\omega) / \partial \omega},$$

which is dependent on the derivative of self energy with respect to energy ω . The integrand in $L_{ij,I}^*$ (Eq.(3.50)) has the derivative of Fermi function. Also notice that at low temperature, $Z(\omega = 0) = Z$, which is the renormalization factor of correlated Fermi liquid. Then $L_{ij,I}^*$ resembles L_{12}^0 except for the power of $\text{Im}G_k(\omega)$. Low temperature expansion show that $L_{11,I}^* \propto Z$, and $L_{12,I}^* \propto T^2$. Therefore, if $L_{11,II}^*$ and $L_{12,II}^*$ were absent, $S^* = -(TL_{12,I}^*)/L_{11,I}^* \propto T/Z$, which is similar to the low temperature behavior of S_0 .

However, $L_{11,II}^*$ and $L_{12,II}^*$ do not vanish in general at low temperature. First, at low-T limit, the integral over ω in Eq. (3.51)

$$\int_{-\infty}^{\infty} d\omega f(\omega) \quad \text{is replaced by} \quad \int_{-\infty}^0 d\omega.$$

Then both the real and imaginary part of $G_k(\omega)$ and $Z(\omega)$ below Fermi surface have to contribute to the leading order of $L_{ij,II}^*$. The exception is when $\Sigma(\omega)$ is independent, or weakly dependent on ω , leading $Z(\omega) \simeq 1$, and then the integrand in $L_{ij,II}^*$ would vanish. This is true for an uncorrelated or weakly-correlated Fermi liquid. But for a correlated Fermi liquid phase near the Mott transition of Hubbard model, $\Sigma(\omega)$ contains the information of coherent quasiparticles at Fermi surface as well as that of incoherent excitations in high-energy Hubbard bands, thus $\Sigma(\omega)$ will depend on ω in very different ways at these separated energy scales. At low energy scale, $Z(\omega \simeq 0) \simeq Z$, and Z is significantly less than 1 near Mott transition. Therefore, at low temperature, $L_{ij,II}^*$ should have a finite value in general. So the total value of L_{12}^* will be dominated by $L_{12,II}^*$ instead of the $\sim T^2$ contribution from $L_{12,I}^*$. The finiteness of L_{11}^* can be also justified by the general sum rule Eq. (3.31), which indicates that L_{11}^* is proportional to the kinetic energy. Consequently, S^* will diverge $1/T$ -like at low-T limit for a correlated Fermi liquid. However, as pointed out by Ref. [42], by subtracting the “reactive part” in L_{12}^* , that is, the limiting term $L_{12}^*(T \rightarrow 0)$, the authors defined the modified high frequency limit of TEP S^{**} as in Eq. 3.47.

There are other circumstance in which $Z(\omega) = 1$ and $L_{ij,II}^*$ vanishes. One example

is that in a static mean field theory, such as Hartree-Fock approximation, $\Sigma(\omega)$ is independent on ω , thus in static mean field theory, it is possible that S^* can show a similar behavior to that of S_0 at low temperature.

In Bloch-Boltzmann theory, the low temperature TEP of a weakly correlated metal can be written as

$$S_0 = T \frac{\pi^2 k_B^2}{3q_e} \frac{d}{d\mu} \ln[\rho(\mu) \langle (v_p^x)^2 \tau(p, \mu) \rangle_\mu]. \quad (3.52)$$

$\rho(\mu)$ is the density of states at Fermi surface, v_p^x represents the band velocity, and $\tau(p, \mu)$ is a phenomenological relaxation time depending on momentum and energy. $\langle \dots \rangle_\mu$ means the average is over the Fermi surface. In Eq.(3.52), the term of $\ln \rho(\mu)$ is similar to the definition of entropy, suggesting the thermodynamical contribution and $\ln \langle (v_p^x)^2 \tau(p, \mu) \rangle_\mu$ represents the transport contribution to TEP.

It can be shown that at low temperature, S_0 of a correlated Fermi liquid is also linear in T , and has a form similar to Eq. 3.52. At low temperature, the self energy of a Fermi liquid is written in Eq. 3.48 and Eq. 3.49, if the momentum-dependence of self energy is ignored, as in DMFT. Z is the renormalization factor. Then [85, 38]

$$S_0(T) = -\frac{1}{Z} \frac{k_B^2}{|e|} \left(\frac{d \ln \Phi(\tilde{\mu})}{d\tilde{\mu}} \frac{E_2^1}{E_0^1} - \frac{a_1 E_4^2 + a_2 E_2^2}{\gamma_0 E_0^1} \right) T. \quad (3.53)$$

$\tilde{\mu} = \mu - \Sigma(0)$ is the renormalized chemical potential. E_m^n are coefficients. $\Phi(\tilde{\mu})$ is the ,

$$\Phi(\tilde{\mu}) \equiv \sum_k \left(\frac{\partial \epsilon_k}{\partial k_x} \right)^2 \delta(\tilde{\mu} - \epsilon_k) \langle (v_p^x)^2 \rangle_{\tilde{\mu}} D(\tilde{\mu}). \quad (3.54)$$

Hence the first term in the bracket of Eq. 3.53 is similar to Eq. 3.52 up to the renormalization factor and some constant. The second term of Eq. 3.53 comes from the higher order correction of self energy which breaks the particle-hole symmetry[85].

To compute S_K , we need μ as a function of temperature. From textbook, we know for an electron gas, $\mu(T) = \mu(0) + O(T^2)$, so we expect for a Fermi liquid, the T^2 correction is still valid. Then Kelvin formula will give S_K also linear in T .

Let n be the average electron density, then

$$n = \int_{-\infty}^{\infty} d\omega d\epsilon f(\omega) D(\epsilon) \rho(\epsilon, \omega),$$

where $f(\omega) = \frac{1}{1+\exp(\beta T)}$ is the Fermi function and

$$D(\epsilon) = \frac{1}{L} \sum_k \delta(\epsilon - \epsilon_k)$$

is the density of states of the bare band.

$$\rho(\epsilon, \omega) = -\frac{1}{\pi} \text{Im} G(\epsilon, \omega) = \frac{1}{\pi} \text{Im} \left(\frac{1}{\omega + \mu - \epsilon - \Sigma(\omega)} \right)$$

is the spectral function. In DMFT, $\Sigma(\omega)$ is momentum-independent. For convenience, lets define functions $N(\omega)$ and $Q(\omega)$ as

$$N(\omega) = \int_{-\infty}^{\infty} d\epsilon D(\epsilon) \rho(\epsilon, \omega),$$

and

$$Q(\omega) = \int_{-\infty}^{\omega} d\omega' N(\omega').$$

Then,

$$n = \int_{-\infty}^{\infty} d\omega f(\omega) N(\omega) = \int_{-\infty}^{\infty} d\omega f(\omega) \frac{dQ(\omega)}{d\omega}.$$

Integration by parts gives

$$n = f(\omega) Q(\omega) \Big|_{-\infty}^{\infty} + \int_{-\infty}^{\infty} d\omega \left(-\frac{df(\omega)}{d\omega} \right) Q(\omega).$$

The first term is zero because $f(\infty) = 0$ and $Q(-\infty) = 0$. The second term allows a Sommerfeld expansion,

$$\begin{aligned} n &= \int_{-\infty}^{\infty} d\omega \left(-\frac{df(\omega)}{d\omega} \right) \left(Q(0) + \frac{1}{2} Q''(0) \omega^2 \right). \\ n &= Q(0) + \frac{1}{2} Q''(0) \int_{-\infty}^{\infty} d\omega \left(-\frac{df(\omega)}{d\omega} \right) \omega^2. \end{aligned} \quad (3.55)$$

Let us first consider the second term in Eq.(3.55). The integral

$$\int_{-\infty}^{\infty} d\omega \left(-\frac{df(\omega)}{d\omega} \right) \omega^2 = \frac{\pi^2}{3} T^2,$$

so we only need to compute the leading order of $Q''(0)$. By the definition of $Q(\omega)$, $Q''(0)$ can be written as

$$\begin{aligned} Q''(0) &= \left. \frac{dN(\omega)}{d\omega} \right|_{\omega=0} \\ &= \left. \frac{d}{d\omega} \right|_{\omega=0} \int_{-\infty}^{\infty} d\epsilon D(\epsilon) \rho(\epsilon, \omega) \\ &= \left. \frac{d}{d\omega} \right|_{\omega=0} \int_{-\infty}^{\infty} d\epsilon D(\epsilon) \left(-\frac{1}{\pi} \right) \frac{\Sigma''(\omega)}{(\omega + \mu - \epsilon - \Sigma'(\omega))^2 + (\Sigma''(\omega))^2}. \end{aligned}$$

When $\omega \sim 0$, $\rho(\epsilon, \omega)$ is peaked at $\epsilon \sim \omega + \mu - \Sigma'(\omega)$, therefore,

$$\begin{aligned} Q''(0) &= \left. \frac{d}{d\omega} \right|_{\omega=0} \left(D(\omega + \mu - \Sigma'(\omega)) \left(-\frac{1}{\pi} \right) \int_{-\infty}^{\infty} d\epsilon \frac{\Sigma''(\omega)}{(\omega + \mu - \epsilon - \Sigma'(\omega))^2 + (\Sigma''(\omega))^2} \right) \\ &= \left. \frac{d}{d\omega} \right|_{\omega=0} D(\omega + \mu - \Sigma'(\omega)) \\ &= D'(\tilde{\mu}) \left(1 - \frac{d\Sigma'(\omega)}{d\omega} \right) \Big|_{\omega=0}. \end{aligned}$$

$\tilde{\mu} = \mu - \Sigma'(0)$ is the renormalized chemical potential. Using quasiparticle approximation, we have $\left(1 - \frac{d\Sigma'(\omega)}{d\omega} \right) \Big|_{\omega=0} = \frac{1}{Z}$, Z is the renormalization factor. Therefore, $Q''(0) = \frac{1}{Z} D'(\tilde{\mu})$.

Now we compute $n - Q(0)$ in Eq.(3.55).

$$Q(0) = \int_{-\infty}^0 d\omega \int_{-\infty}^{\infty} d\epsilon D(\epsilon) \rho(\epsilon, \omega, T, \mu(T)). \quad (3.56)$$

Here temperature T and the dependence of μ on T are written in $\rho(\epsilon, \omega, T, \mu(T))$ explicitly. Since we are interested the leader order correction of $\mu(T)$ to its zero temperature value $\mu(T=0)$ for the same electron density n , we can write n at $T=0$ as

$$n = \int_{-\infty}^0 d\omega \int_{-\infty}^{\infty} d\epsilon D(\epsilon) \rho(\epsilon, \omega, T=0, \mu(T=0)). \quad (3.57)$$

Notice its difference from Eq.(3.56) is that the spectral function is at $T=0$. In the Fermi liquid regime and at low temperature, the difference between $Q(0)$ and n is determined by the difference between $\rho(\epsilon, \omega, T, \mu(T))$ and $\rho(\epsilon, \omega, T=0, \mu(T=0))$ around the Fermi surface, that is, $\omega \sim 0$, at most in a range $|\omega| < T$. So the part of integral over ϵ that is relevant to this difference is also confined to $\epsilon \sim \omega$, and

$$\begin{aligned} n - Q(0) &= \int_{-\infty}^0 d\omega \int_{-\infty}^{\infty} d\epsilon D(\epsilon) (\rho(\epsilon, \omega, T=0, \mu(T=0)) - \rho(\epsilon, \omega, T, \mu(T))) \\ &= \int_{-\infty}^0 d\omega (D(\omega + \mu(0) - \Sigma'(\omega)) - D(\omega + \mu(T) - \Sigma'(\omega))). \end{aligned}$$

For a Fermi liquid,

$$\omega + \mu(T) - \Sigma'(\omega) = \frac{1}{Z} \omega + \mu(T) - \Sigma'(0).$$

Changing the integral variables we get,

$$\begin{aligned}
n - Q(0) &= \int_{-\infty}^{\mu(0) - \Sigma'(0)} d\tilde{\omega} Z D(\tilde{\omega}) - \int_{-\infty}^{\mu(T) - \Sigma'(0)} d\tilde{\omega} Z D(\tilde{\omega}) \\
&= D(\mu(0) - \Sigma'(0)) Z(\mu(0) - \mu(T)) \\
&= D(\tilde{\mu}) Z(\mu(0) - \mu(T)).
\end{aligned} \tag{3.58}$$

Consequently, from Eq.(3.55) we have

$$D(\tilde{\mu}(0)) Z(\mu(0) - \mu(T)) = \frac{\pi^2}{6} \frac{1}{Z} D'(\tilde{\mu}(T)) T^2.$$

Thus the leading order correction is of T^2 ,

$$\mu(T) = \mu(0) - \frac{\pi^2}{6} \frac{1}{Z^2} \frac{D'(\tilde{\mu}(0))}{D(\tilde{\mu}(0))} T^2. \tag{3.59}$$

$$= \mu(0) - \frac{\pi^2}{6} \frac{1}{Z^2} \frac{d \ln D(\tilde{\mu})}{d\tilde{\mu}} T^2. \tag{3.60}$$

Therefore, the Kelvin formula,

$$S_K = \frac{1}{|e|} \left(\frac{\partial \mu}{\partial T} \right)$$

will give

$$S_K = -\frac{\pi^2 k_B^2}{3|e|} \frac{1}{Z^2} \left(\frac{d \ln D(\tilde{\mu})}{d\tilde{\mu}} \right) T. \tag{3.61}$$

Now it is helpful to compare Eq.(3.61) with Eq.(3.53). First the prefactor in Eq.(3.61) is $1/Z^2$, while the prefactor in Eq.(3.53) is $1/Z$. So S_K will overestimates S_0 of a correlated metal by a factor of $1/Z$. Second, we see S_K captures the thermodynamical contribution term $d \ln(D(\tilde{\mu})/d\tilde{\mu})$, but it misses the transport contribution $d \ln(\langle v_p^x \rangle^2)/d\tilde{\mu}$. This is consistent with “slow limit” picture of the definition of Kelvin formula.

3.3.2 High temperature limit.

In the literature, the high temperature limit of TEP [74], or known as Mott-Heikes formulor, has been widely used as a benchmark of thermoelectric capability [76] of correlated materials. Here we discuss the high temperature limit implied from the formalism we have derived.

At high temperature, the system is dominated by incoherent excitations, thus the band velocity is not any more a meaningful quantity to describe the motion of electrons.

In this sense, the TEP should be mainly contributed by the thermodynamical part, that is, the entropy s . In fact, the leading term of S_0 in high temperature expansion is [74],

$$S_0 = \frac{\mu}{T} + O\left(\frac{1}{T}\right). \quad (3.62)$$

Since

$$\frac{\mu}{T} = -\frac{\partial s}{\partial N},$$

S_0 is determined by the entropy at high temperature.

Usually two kinds of high temperature limit are of interest. One is the **strongly** correlated case, $U \gg T \gg D$, and the other is the **weakly** correlated one, $T \gg U, D$. U is the on-site Coulomb interaction and D is the bandwidth. In the former case, U is the dominant energy scale, so all possible states have to satisfy the condition of single occupation. In the latter case, the temperature dominates, so the thermal fluctuations are strong enough to break the single-occupation and the system will have different set of possible configurations and thus entropy from that of a correlated system. Explicitly, for hole-doped case, the Mott-Heikes formula is

$$S_{MH} = -\frac{k_B}{e} \ln\left(\frac{2(1-n)}{n}\right), \quad \text{for strongly correlated case;} \quad (3.63)$$

$$S_{MH} = -\frac{k_B}{e} \ln\left(\frac{2-n}{n}\right), \quad \text{for weakly correlated case.} \quad (3.64)$$

Apparently, for a given density n , the Mott-Heikes formula gives only a number, not a function of temperature. Besides, for real materials, the condition $T \gg D, U$ is quite impractical, because this mean $T \sim 10^5 K$. For correlated material, usually U/D is around 2-4, more or less comparable to 1. So the condition $U \gg T \gg D$ is not so practical either. It looks like S_{MH} is of little guidance for understanding thermoelectric effect in realistic materials. But recent experimental study on $La_{1-x}Sr_xVO_3$ [2] shows that S_{MH} is applicable to correlated materials at $T > 200K$ when the transport is dominated by incoherent excitations.

A direct consequence from Mott-Heikes formula is that the high temperature limit of S_K is equivalent to S_{MH} . This is easy to see since $S_{MH} \propto \mu/T$ is a number for given density, which means μ is proportional to T at high temperature, and hence $\mu/T = \partial\mu/\partial T$, and $S_{MH} = S_K$.

To compute the high frequency limit S^* at high temperature, first we approximate the single particle spectral function by a rigid band picture, namely,

$$\tilde{A}_k(\omega) = A_k(\omega - \mu). \quad (3.65)$$

$\tilde{A}_k(\omega)$ is a function of ω but independent of temperature and chemical potential. Applying these simplification to Eq. 3.31 and Eq. 3.32, and keeping the leading order in T , we have

$$\begin{aligned} L_{11}^* &= \frac{1}{1 + e^{-\beta\mu}} \int d\omega \sum_{k,\sigma} \left(\frac{\partial^2 \epsilon_k}{\partial k_x^2} \right) \tilde{A}_k(\omega), \\ L_{12}^* &= \frac{-\mu}{1 + e^{-\beta\mu}} \int d\omega \sum_{k,\sigma} \left(\frac{\partial^2 \epsilon_k}{\partial k_x^2} \right) \tilde{A}_k(\omega). \end{aligned}$$

Therefore, at high temperature limit,

$$S^* = -\frac{L_{12}^*}{TL_{11}^*} = \frac{\mu}{T}. \quad (3.66)$$

This is the same result to the high temperature limit of S_0 in Eq. 3.62. Thus the leading order of S^* is identical to the leading order of S_0 and S_K at high temperature.

Since the rigid band picture should be a good approximation as long as the incoherent excitations dominate in the system, no matter how strong the Coulomb interaction could be, we expect Eq. 3.66 has included both the case of $T \gg U, D$ and $U \gg T \gg D$.

3.3.3 Numerical results

In this section I present numerical results on one-band Hubbard model with nearest neighbor hopping on a square lattice. Two cases are studied. One is a strong coupling case, $U = 1.75D$ with the electron density is $n = 0.85$. The other is an intermediate coupling case, $U = 0.75D$ with $n = 0.8$. At half-filling ($n = 1.0$), the critical value of Coulomb interaction for the Mott transition at $T = 0$ is $U_{c2} \simeq 1.5D$. Hence the strong coupling case corresponds to a doped Mott insulator.

Fig. 3.1(a) compares S_0 , S_K , S^* , S^{**} , S_K and also S_{MH} . The upper dashed line denotes S_{MH} of the strongly correlated limit, $U \gg T \gg D$, and the lower dashed line denotes the weakly correlated limit, $T \gg U, D$. S_0 displays multiple sign changes.

The first sign change happens in the crossover regime from coherent Fermi liquid to incoherent regime. This sign change is due to the competition between the coherent and incoherent excitations. The second sign change happens in the incoherent regime. It is due to the balance between the incoherent excitations of the upper and lower Hubbard band [77, 86]. It is evident that from $T = 0.1D$ to $0.5D$, S_K is quantitatively following the trend of S_0 . More specifically, S_0 and S_K change sign around $T \simeq 0.1D$ and they reach the maximum at $T \simeq 0.25D$. Besides, the maximum value of S_0 and S_K is close to S_{MH} for the strongly correlated case for $U \gg T \gg D$. This indicates that the sign change near $T \simeq 0.1D$ and the temperature-dependent behavior of S_0 below $T \simeq 0.5D$ is mainly driven by entropy. S^* diverges at low temperature, and converges to the weak-correlated limit ($T \gg U, D$) of S_{MH} at $T \simeq 0.6D$. S_K also converges to the weak-correlated S_{MH} beyond $T \simeq 0.8D$. S_0 is also expected to converge to this value when $T \gg U, D$. But S_0 is converging slower than S_K and S^* . As expected, S^{**} eliminates the divergence and recovers the linear-in- T behavior at low temperature. S^{**} also shows a sign change at $T \simeq 0.1D$, which is close to that of S_K and S_0 . Above $T = 0.1D$, S^{**} turns to positive and shows a very weak trend of decreasing. Qualitatively, the deduction of divergent part does make S^{**} a better approximation of S_0 than S^* .

Fig. 3.1(b) shows the chemical potential as a function of temperature. The red dots represent values used in DMFT simulations to keep a fixed density $n = 0.85$. The black line is a smooth interpolation of the red dots, so that numerical derivative can be adopted to compute S_K given in Fig. 3.1(a). The blue line is the chemical potential for the atomic limit μ_{atom} , that is, μ_{atom} satisfies

$$n = \frac{2e^{\beta\mu_{atom}} + 2e^{\beta(2\mu_{atom}-U)}}{1 + 2e^{\beta\mu_{atom}} + e^{\beta(2\mu_{atom}-U)}}.$$

Above $T = 0.2D$, μ_{atom} and μ for Hubbard model have similar non-monotonic dependence on T . Toward high temperature, they become parallel.

Fig. 3.2 shows compares S_0 , S_K , S^* , S^{**} , S_K and S_{MH} for intermediate coupling case, $U = 0.75U$ and $n = 0.8$. Similar to the strong coupling case, S_0 shows sign change, at $T \simeq 0.15D$ and $T \simeq 0.3D$. So the second sign change happens at lower temperature than that in Fig. 3.1(a). Roughly, S_K follows S_0 between $T \simeq 0.1D$ and $T \simeq 0.4D$,

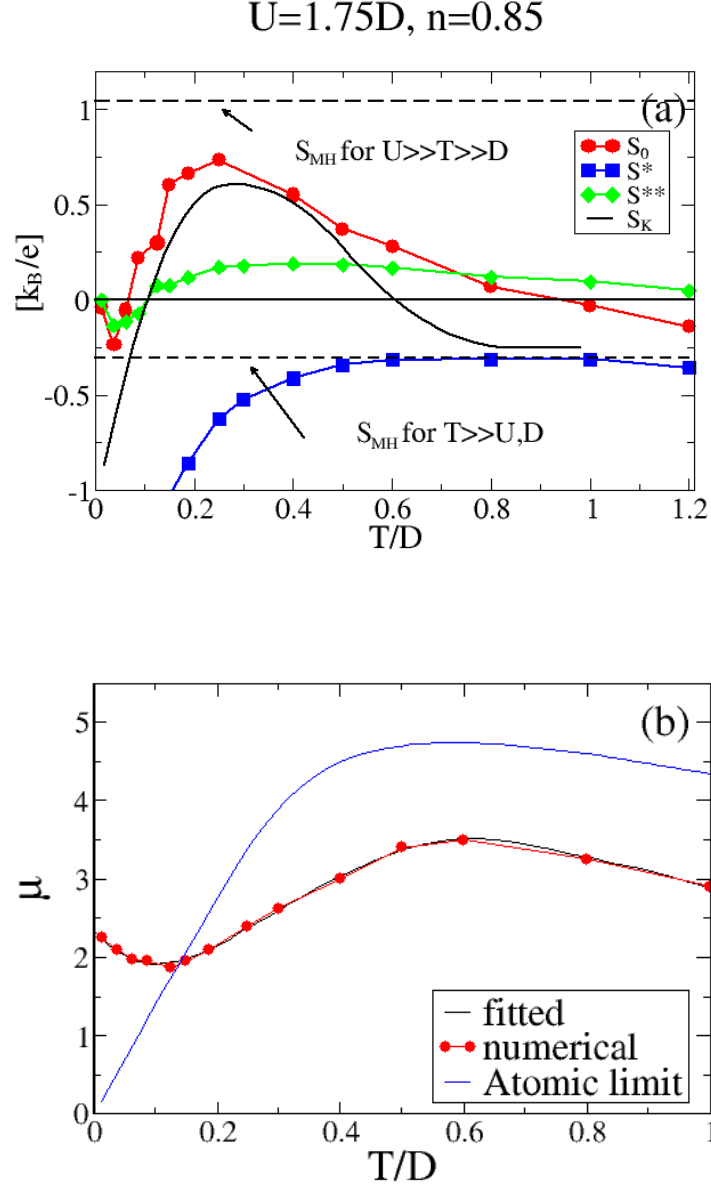


Figure 3.1: $U = 1.75D$ and $n = 0.85$. (a): S_0 , S_K , S^* and S^{**} as function of temperature. The dashed lines represent the high temperature limit S_{MH} using Mott-Heikes formula. (b): Chemical potential μ . Red dots are from DMFT simulation with n fixed to 0.85. Black line is interpolation to the red dots. Blue line is computed from atomic limit.

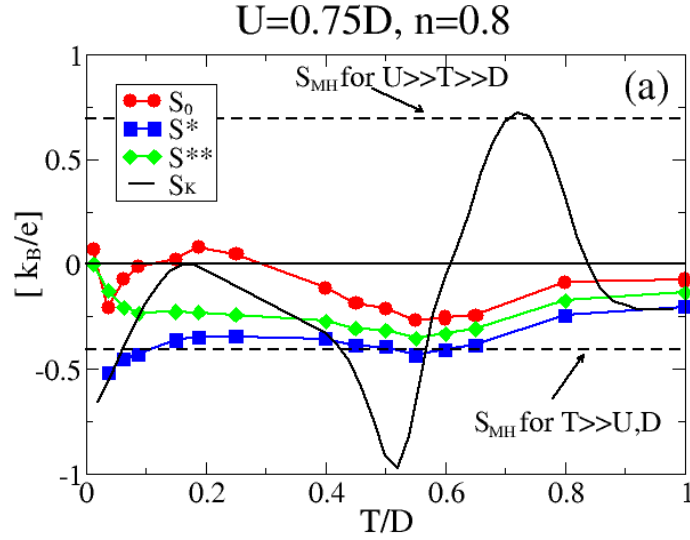


Figure 3.2: $U = 0.75D$ and $n = 0.8$. S_0 , S_K , S^* and S^{**} as function of temperature. The dashed lines represents the high temperature limit S_{MH} using Mott-Heikes formula.

in a qualitative way. Between $T \simeq 0.4D$ and $T \simeq 0.9D$, S_K obvious deviates from S_0 . Above $T \simeq 0.4D$, S^* and S^{**} show similar non-monotonic behavior on T with that of S_0 . The divergence of S^* at low temperature is weaker than that in Fig. 3.1(a). S^{**} does not improve much between $T \simeq 0.1D$ and $T \simeq 0.4D$, but it is closer to S_0 between $T \simeq 0.4D$ and $T \simeq 0.9D$ than S^* . Besides, we see S_0 never gets close to the strongly correlated S_{MH} .

Unlike S_0 and S_K , there is an implicit dominant scale in S^* , that is, the frequency $\omega \rightarrow \infty$. When deriving Eq. 3.31 and Eq. 3.32, we start from a Hubbard-type Hamiltonian [40], so the Coulomb interaction is kept finite when the high-frequency limit is taken. Physically, the high-frequency perturbation could excite states with double occupations, which is supposed to be suppressed when U is large. Therefore, for strongly correlated system, computing S^* using Eq. 3.31 and Eq. 3.31 can have non-physical states included. Therefore, we see for intermediate temperatures, $0.1D < T < 0.4D$, S_K qualitatively agrees with S_0 but S^* deviates significantly. Besides, comparing Fig. 3.1(a) and Fig. 3.2, we see S^* can approximate S_0 better when the correlation is weaker.

3.4 Conclusion

In this chapter, we calculate TEP S_0 and several approximations. These approximations include S_K from the Kelvin formula, S^* from the high-frequency limit, and S^{**} of a modified high-frequency limit which subtracts the divergent term toward zero temperature. The low temperature behavior of S_K is derived based on a quasiparticle self energy. We show that S_K is linear in temperature as S_0 , but S_K overestimates S_0 by a factor of $1/Z$, where Z is the renormalization factor of the Fermi liquid. Besides, S_K misses the contribution from the transport part. Based on an entropy argument and rigid band picture at high temperature, two kinds of high-temperature limit are discussed, the weak coupling case, $T \gg U, D$, and the strong coupling case, $U \gg T \gg D$, where U is the on-site Coulomb interaction and D is the bandwidth. Although it appears that the high-temperature limit of S_K and S^* is the same as that of S_0 , we point out that concerning the ratio U/D and the practical temperature for real materials, this equivalence between S_K , S^* and S_0 may not be always true. Finally, we give numerical results on single-band Hubbard model using dynamical mean field theory(DMFT) to investigate S_0 and the approximations in the intermediate temperature range. We see that for strong coupling case, $U \gg D$, S_K is a better estimation of S_0 than S^* and S^{**} over the intermediate to high temperature range. If $U \sim D$, S^{**} is the best estimation of S_0 , and the superiority of S^* over S_K is also evident.

Chapter 4

Local Magnetism in Periodic Anderson Model

Periodic Anderson model is a prototypical model for heavy fermion systems, in which itinerant conduction electrons (c -electrons) hybridize with a lattice of localized f -electrons. Strong on-site Coulomb interaction within the f -orbitals leads to the formation of a lattice of local moments. The hybridization between c - and f -electrons leads to two kinds of coupling. One is the Kondo coupling between the localized spins and itinerant electrons, which tends to screen the local moments and eventually form a coherent heavy Fermi liquid. Roughly speaking, Kondo coupling can be characterized by a Kondo temperature T_K , below which the temperature dependence of paramagnetic susceptibility starts to deviates the Curie's law ($\chi \propto 1/T$) of isolated spins. Another energy scale, T_{FL} is also used to characterize the formation of heavy Fermi liquid, below which the resistivity shows quadratic temperature dependence. Usually T_{FL} is much smaller than T_K . Another coupling is the RKKY interaction between local moments, which is mediated by itinerant electrons. RKKY interaction tends to form a long range (usually antiferromagnetic) order of the local moments and can be characterized by the Néel temperature T_N . The competition between Kondo coupling and RKKY interaction remains a fundamental issue in understanding the phase diagram and the nature of quantum phase transition in heavy fermion materials [87, 88, 89, 90, 91].

This chapter studies the heavy fermion system from the perspective of dynamical mean field theory (DMFT). In particular, we study the spin fluctuations and the instability toward an antiferromagnetic ordering of the paramagnetic state of a heavy fermion system by computing the \mathbf{Q} -dependent static and dynamic spin susceptibility in DMFT. DMFT has been widely used to study correlated electron systems [25, 27, 92] and has long been used to study magnetic transition in periodic Anderson model [93] and

a phase diagram assembling to that of Doniach [87] phase diagram was obtained [94, 95]. But in previous studies, usually a commensurate antiferromagnetic ordering of $(\pi/2, \pi/2, \pi/2)$ was assumed such that a closed set of self-consistent equations can be written down for two sub-lattices of up- and down-spins. This setup can however hardly be extended to incommensurate ordering, which is very common in heavy fermion systems. Besides, to calculate the dynamic spin fluctuations in the paramagnetic state, local two-particle quantities (the local spin correlation and vertex functions) are needed but can not be obtained directly from DMFT self-consistent equations, which only deals with single-particle Green's function. The method of computing the \mathbf{Q} -dependent magnetic susceptibility via local irreducible vertex function was introduced [35, 27], yet it has not been widely implemented to study the magnetic fluctuations in correlated systems except a few recent works [96, 58]. Here we extend this method to periodic Anderson lattice. Using hybridization as a tuning parameter, we give a detailed description of the evolution of spin susceptibility along with the vanishing of Fermi liquid scale T_{FL} and emergence of antiferromagnetic instability.

We consider the periodic Anderson model on a three-dimensional cubic lattice with one conduction band, and one localized f -orbital on each site. The Hamiltonian is

$$\begin{aligned}
H = & \sum_{k,\sigma} \epsilon_k c_{k\sigma}^\dagger c_{k\sigma} + V \sum_{i,\sigma} \left(c_{i\sigma}^\dagger f_{i\sigma} + h.c. \right) - \mu \sum_{i,\sigma} \left(c_{i\sigma}^\dagger c_{i\sigma} + f_{i\sigma}^\dagger f_{i\sigma} \right) \\
& + \epsilon_f \sum_{i,\sigma} f_{i\sigma}^\dagger f_{i\sigma} + U \sum_i f_{i\uparrow}^\dagger f_{i\uparrow} f_{i\downarrow}^\dagger f_{i\downarrow}.
\end{aligned} \tag{4.1}$$

The dispersion relation of the bare conduction band is $\epsilon_k = -2t(\cos k_x + \cos k_y + \cos k_z)$. V is the hybridization amplitude between c - and f - electrons. ϵ_f is the atomic level of localized f -orbitals. U is the onsite Coulomb interaction between spin-up and spin-down states of f -orbital.

The parameters of the model in our calculation are chosen as follows. The hopping constant of c -electrons is the energy unit, $t = 1.0$. $U = 12.0$. The total density is approximately $n_c + n_f \simeq 2.3$. V is the tuning parameter in the phase diagram.

4.1 Phase diagram

The V - T phase diagram of periodic Anderson model is the main result in this chapter. Fig. 4.1 (a) shows the evolution of Fermi surface. The phase of “small” Fermi surface indicates the conduction electrons are decoupled from the localized moments. Hence the total volume of Fermi surface only counts the total states of conduction electrons. However, at low temperature, as the Kondo screening takes place, the conduction electrons and local moments of f -orbitals combine to form composite quasiparticles, or the heavy Fermi liquid. The volume of the heavy Fermi surface is “large” since it counts the total states of both the conduction and localized electrons. The transformation from localized to itinerant character of the f -orbitals can also be cast into a scenario of Mott insulator-to-metal transition. A solid line of Mott transition at finite temperature is drawn for $V < 1.5$. Above $V = 1.5$, the Mott transition turns into a crossover region, which also exhibits a sudden uprise from the solid below $V = 1.5$.

Fig. 4.1 (b) zooms in the low temperature and focuses on the consequences from two-particle properties. When $V > 1.5$, the resistivity reveals a T^2 behavior at low temperature, characterized by the Fermi liquid scale T_{FL} and indicating the coherence of heavy quasiparticles. T_{FL} diminishes as V approaches to 1.5. Below $V = 1.5$, antiferromagnetic instability emerges. The magnetic susceptibility $\chi(\mathbf{Q})$ in the region of small Fermi surface is computed, and the magnetic transition temperature T_N is found by extrapolating the inverse of $\chi(\mathbf{Q})$ to zero. Therefore the vanishing of T_{FL} and emergence of magnetic ordering happens in the vicinity of termination of the finite-temperature Mott transition. Thus the behavior of spin fluctuation in this region is of interest and will be discussed in Sec. 4.3.2.

4.2 The heavy Fermi liquid

Fig. 4.2 shows the dependence of resistivity ρ on squared temperature. At low temperatures, ρ is proportional to T^2 , as indicated by the dashed lines. Although it is difficult to get a precise value of T_{FL} by fitting the $\rho \propto T^2$ behavior since the numerical errors becomes more interruptive as temperature is lowered, the trend is evident that $\rho(T)$

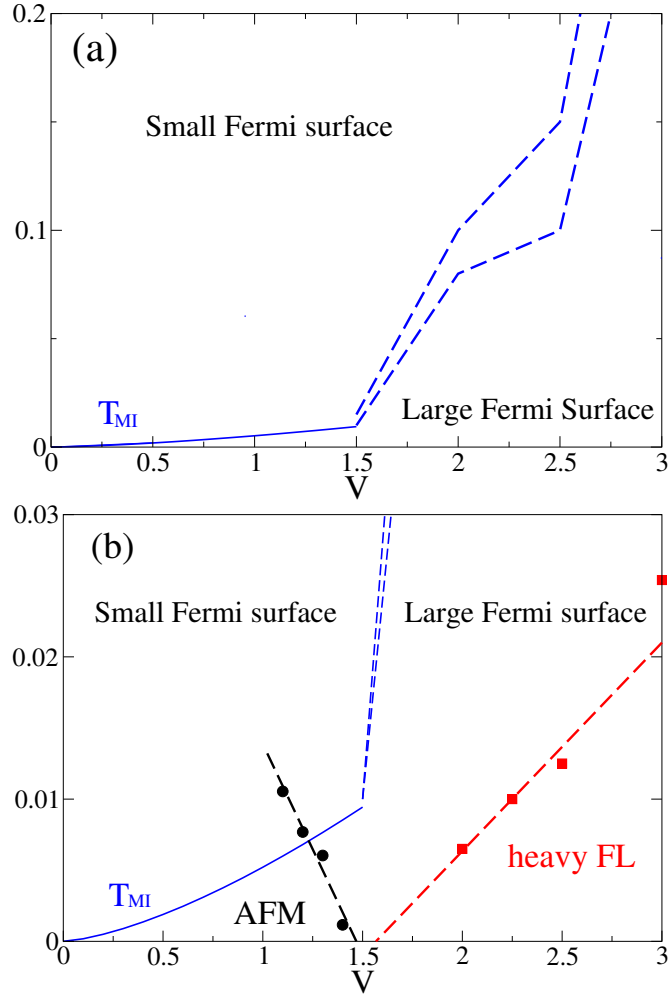


Figure 4.1: V - T phase diagram of periodic Anderson model. (a) “Small Fermi surface” denotes the phase with decoupled conduction electrons and local moments. “Large Fermi surface” denotes the phase of heavy Fermi liquid, where the composite quasiparticles have a large Fermi surface. They are separated for small V by a line of orbital selective Mott transition (T_{MI}), which extends to a crossover for larger values of V , as indicated by blue dashed lines. See Sec. 4.3.3. (b) The red dashed line marks the trend of T_{FL} extracted from T^2 behavior of resistivity (See Sec. 4.2). The black dashed line makes the antiferromagnetic ordering temperature (See. 4.3.1).

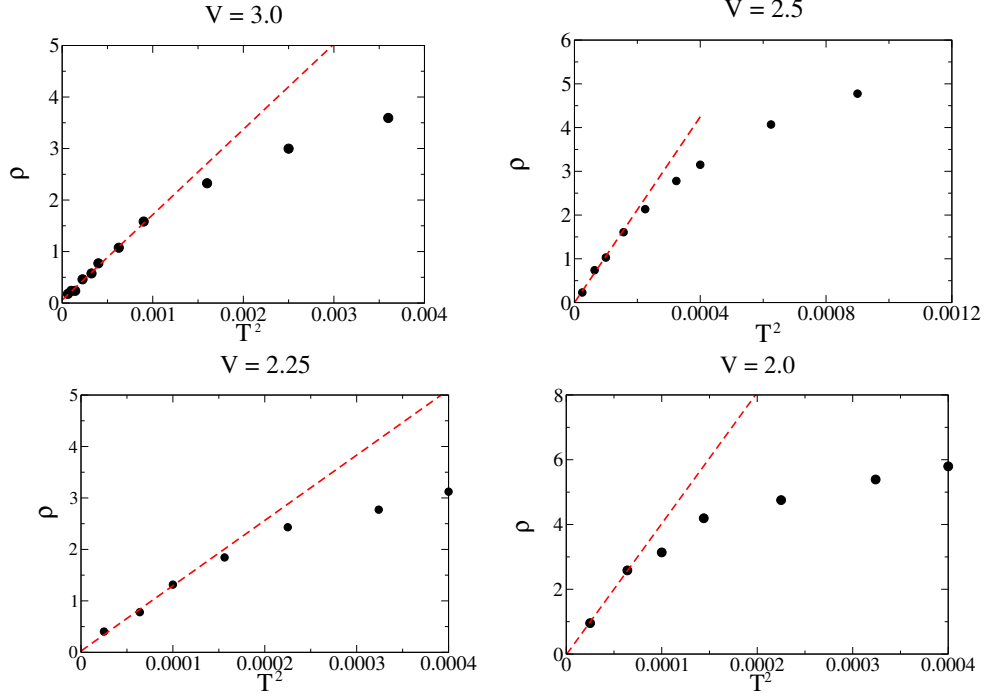


Figure 4.2: Resistivity ρ as a function of T^2 for $V = 3.0, 2.5, 2.25, 2.0$. The dashed line is obtained by fitting a few points at lowest temperatures along with the origin ($T^2 = 0, \rho = 0$) to a linear function.

starts to deviate from the Fermi liquid behavior at lower temperatures as V becomes smaller and is shown in Fig. 4.1(b).

It is instructive to look at the quasiparticle weight (renormalization factor) and scattering rate of the c -electrons, which are shown in Fig. 4.3 for $V = 3.0$ and $V = 2.25$. The scattering rate follows similar temperature dependence as the resistivity, in particular the T^2 -behavior at low temperature indicates the same T_{FL} . On the other hand, the quasiparticle weight shows only slight temperature dependence. This means unlikely the hidden Fermi liquid as discussed in Ch. 2, the deviation from Landau's Fermi liquid behavior above T_{TL} here in the heavy Fermi liquid system is **not** due to the temperature dependence of quasiparticle renormalization.

The formation of the Fermi liquid coherence at low temperatures is also observable in magnetic susceptibility. Fig. 4.4 shows bulk susceptibility for periodic Anderson lattice with $V = 3.0$ and $V = 2.5$. At high temperature, the bulk susceptibility follows Curie's law. At low temperature, it saturates, which is the behavior of Pauli's paramagnetism

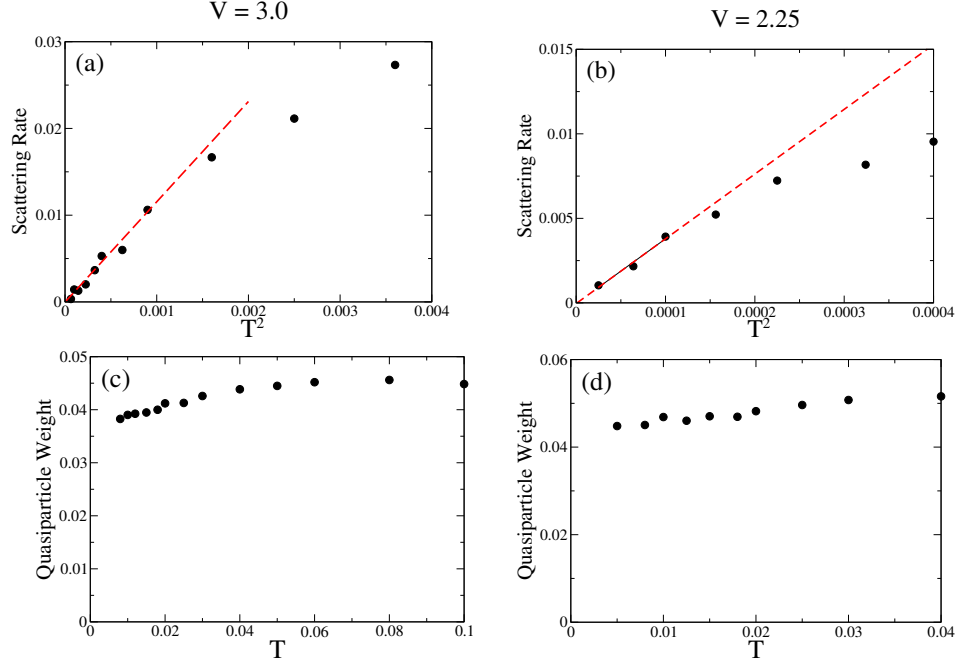


Figure 4.3: The quasiparticle scattering rate and quasiparticle weight of c -electrons , for $V = 3.0$ ((a) and (c)) and $V = 2.25$ ((b) and (d)). The scattering rate is dependent on T^2 to emphasize its similar behavior to resistivity.

and a feature of a Fermi liquid. Besides, from the theoretical result, we see that for $V = 3.0$, χ starts to saturates at $T \simeq 0.03$, while for $V = 2.5$, the saturations happens below $T \simeq 0.02$. This is consistent with the evolution of T_{FL} with hybridization as shown in Fig. 4.1 (b).

4.3 Lattice susceptibility and antiferromagnetic ordering

4.3.1 Static susceptibility

This section presents the results of \mathbf{Q} -dependent magnetic susceptibility $\chi(\mathbf{Q})$ which also reveals the emergence of magnetic instability at an incommensurate ordering vector.

Fig. 4.5 shows the static susceptibility $\chi(\mathbf{Q})$ for $V = 2.5$ and $V = 2.0$. On the left side shows $\chi(\mathbf{Q})$ as a function of \mathbf{Q} along the diagonal direction $(0, 0, 0)$ to (π, π, π) in the Brillouin zone for selected temperatures . On the right side shows the temperature dependence of $\chi(\mathbf{Q})$ for selected lattice momenta, $\mathbf{Q} = (0, 0, 0)$ (bulk susceptibility) and $\mathbf{Q} = \mathbf{Q}_N = (0.72\pi, 0.72\pi, 0.72\pi)$, along with the local susceptibility χ_{loc} . \mathbf{Q}_N , as will

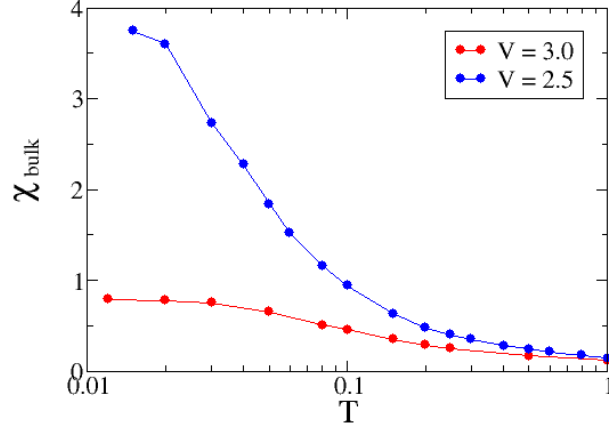


Figure 4.4: Bulk susceptibility of a heavy Fermi liquid system.

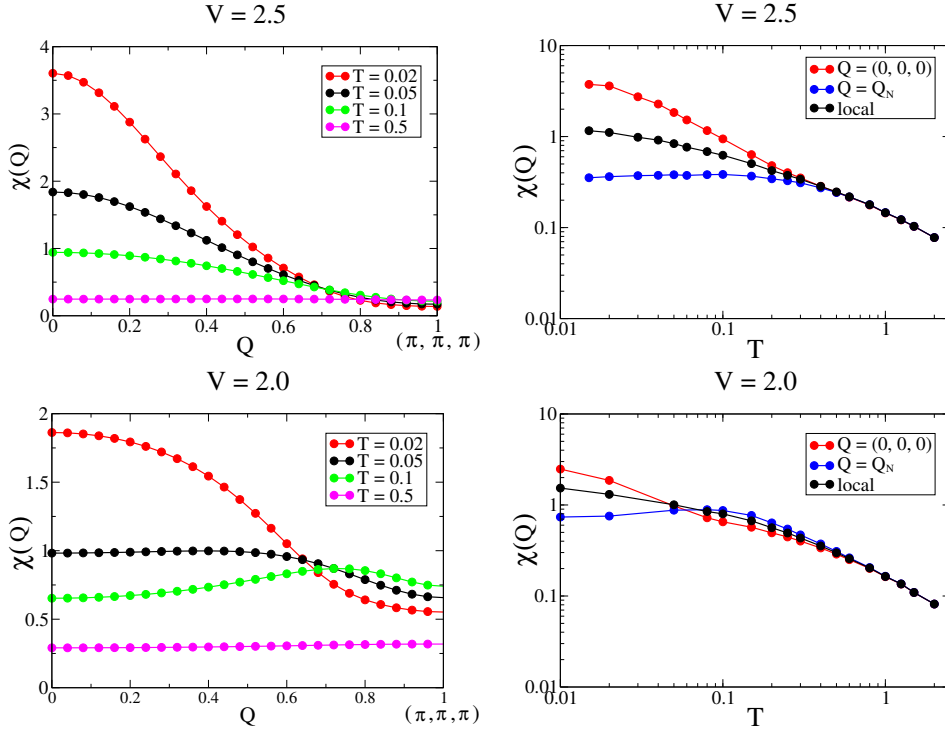


Figure 4.5: Static magnetic susceptibility $\chi(\mathbf{Q})$ for (from above to below) $V = 2.5$ and $V = 2.0$. On the left side is $\chi(\mathbf{Q})$ as a function of \mathbf{Q} along $(0, 0, 0)$ to (π, π, π) for different temperatures. On the right hand side is $\chi(\mathbf{Q}, T)$ as a function of temperature T for $\mathbf{Q} = 0$ (bulk susceptibility), $\mathbf{Q} = \mathbf{Q}_N = (0.72\pi, 0.72\pi, 0.72\pi)$ and also local susceptibility χ_{loc} , on logarithmic scales.

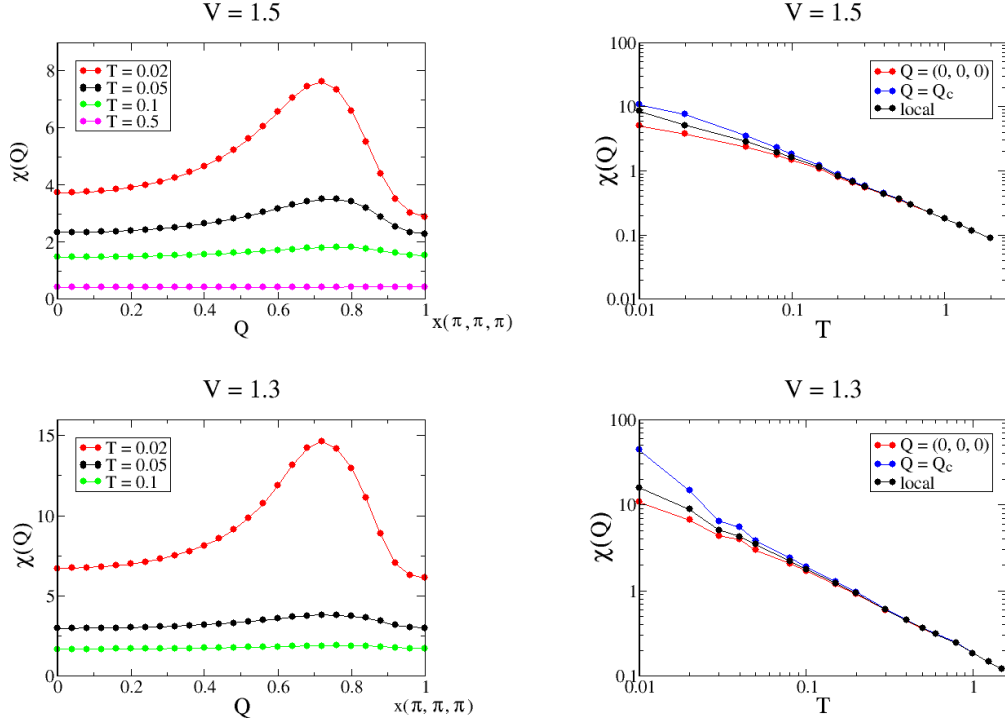


Figure 4.6: Static magnetic susceptibility $\chi(\mathbf{Q})$ for (from above to below) $V = 1.75$ and $V = 1.5$. On the left side is $\chi(\mathbf{Q})$ as a function of \mathbf{Q} along $(0, 0, 0)$ to (π, π, π) for different temperatures. On the right hand side is $\chi(\mathbf{Q}, T)$ as a function of temperature T for $\mathbf{Q} = 0$ (bulk susceptibility), $\mathbf{Q} = \mathbf{Q}_N = (0.72\pi, 0.72\pi, 0.72\pi)$ and also local susceptibility χ_{loc} , on logarithmic scales.

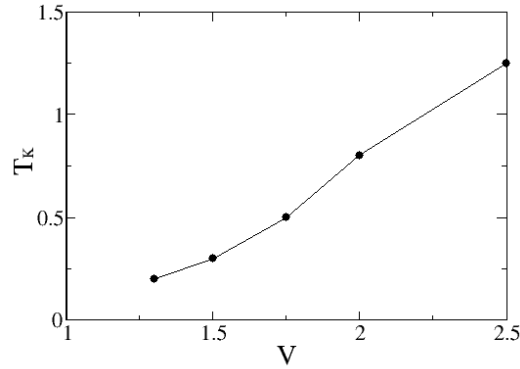


Figure 4.7: The Kondo temperature T_K as a function of hybridization.

be shown later, is the antiferromagnetic ordering vector. Fig. 4.6 shows same quantities for smaller hybridization $V = 1.5$ and $V = 1.3$. The common feature in Fig. 4.5 and Fig. 4.6 is that $\chi(\mathbf{Q})$ is \mathbf{Q} -independent at high temperatures. This fact is reflected by the merging of $\chi(\mathbf{Q}_N)$, $\chi(\mathbf{Q}_N)$ and χ_{loc} to a tail at high temperature for all values of V presented. Besides, the high temperature tail follows the Curie's law, $\chi \propto 1/T$ at high temperature. The Curie's behavior is expected since localized moments are decoupled from the c -electrons at high temperature. As temperature decreases, Kondo screening becomes effective and $\chi(\mathbf{Q})$ starts to develop \mathbf{Q} -dependence and deviates from the $\propto 1/T$ behavior. The temperature where the deviation starts to show up indicates the Kondo temperature, which is shown in Fig. 4.7.

The evolution of $\chi(\mathbf{Q})$ with decreasing temperature shows distinct behaviors for different hybridization. In Fig. 4.5, as temperature is lowered and $\chi(\mathbf{Q})$ starts to develop \mathbf{Q} -dependence, the bulk susceptibility $\chi(\mathbf{Q} = (0, 0, 0))$ quickly increases while $\chi(\mathbf{Q})$ for \mathbf{Q} near (π, π, π) is suppressed. For $V = 2.0$, the system is able to develop a little stronger antiferromagnetic at intermediate temperatures when $\chi(\mathbf{Q})$ starts to show \mathbf{Q} -dependence. But this tendency to antiferromagnetism quickly vanishes and the bulk susceptibility still wins at low temperature. Because the spin fluctuations of local moments are mediated by the RKKY interaction, we can perceive this behavior of $\chi(\mathbf{Q})$ as that the RKKY interaction finally loses the competition against the Kondo screening in above two cases.

But in Fig. 4.6, where the hybridization is smaller, the temperature dependence of $\chi(\mathbf{Q})$ is quite different. Toward lower temperature, $\chi(\mathbf{Q})$ for all \mathbf{Q} s are enhanced and the obvious maximum emerges at $\mathbf{Q} = \mathbf{Q}_N \equiv (0.72\pi, 0.72\pi, 0.72\pi)$, as shown in the left column of Fig. 4.6. As a function of temperature, $\chi(\mathbf{Q}_N)$ shows a diverging behavior down to the lowest temperature ($T = 0.01$) that can be reached in our calculation, indicating an antiferromagnetic instability.

To find the magnetic transition temperatures, we plot the inverse of \mathbf{Q} -dependent susceptibility with respect to temperature in Fig. 4.8 for selected \mathbf{Q} . For $V = 1.4$ and $V = 1.3$, $1/\chi(\mathbf{Q})$ is linear in T . Extrapolated to $1/\chi(\mathbf{Q}) = 0$, the intercept on the temperature axis gives the antiferromagnetic transition temperature for the corresponding \mathbf{Q} . The \mathbf{Q} with the largest transition temperature is the T_N of the system, with $\mathbf{Q} = \mathbf{Q}_N$ the ordering vector. The inverse of bulk ($\mathbf{Q} = (0, 0, 0)$) and staggered ($\mathbf{Q} = (\pi, \pi, \pi)$) susceptibility are also linear with T , with a smaller transition temperature, and the linearity is parallel with that of $1/\chi(\mathbf{Q}_N)$. This suggests that in the vicinity above T_N , the temperature dependence of $\chi(\mathbf{Q})$ is independent of \mathbf{Q} , and $\chi(\mathbf{Q})$ can be written as

$$\chi(\mathbf{Q}) = \frac{C}{(T - T_N(\mathbf{Q}))}. \quad (4.2)$$

C is a constant independent of \mathbf{Q} . The critical exponent is also \mathbf{Q} -independent and has the mean-field value of 1. $T_N(\mathbf{Q})$ is the \mathbf{Q} -dependent transition temperature, and it has maximum and positive value when $\mathbf{Q} = \mathbf{Q}_N$.

4.3.2 Dynamic susceptibility

This section investigate the dynamic properties of spin fluctuations in the vicinity of antiferromagnetic instability.

Fig. 4.9 shows the imaginary part of dynamic susceptibility $\Im\chi(\mathbf{Q} = \mathbf{Q}_N, E)$ near the ordering vector \mathbf{Q}_N for $V = 2.0$ (above) and $V = 1.5$ (below) at selected temperatures. $\Im\chi(\mathbf{Q}, E)$ is computed using a RPA-like approximation, which is shown to a good approximation for itinerant systems [58] and has also been explained in Sec. 2.4.2. The transfer of spectral weight For $V = 2.0$, the spectral weight at low energy is shifted to higher energy as temperature is lowered. Hence as the heavy Fermi liquid forms, the

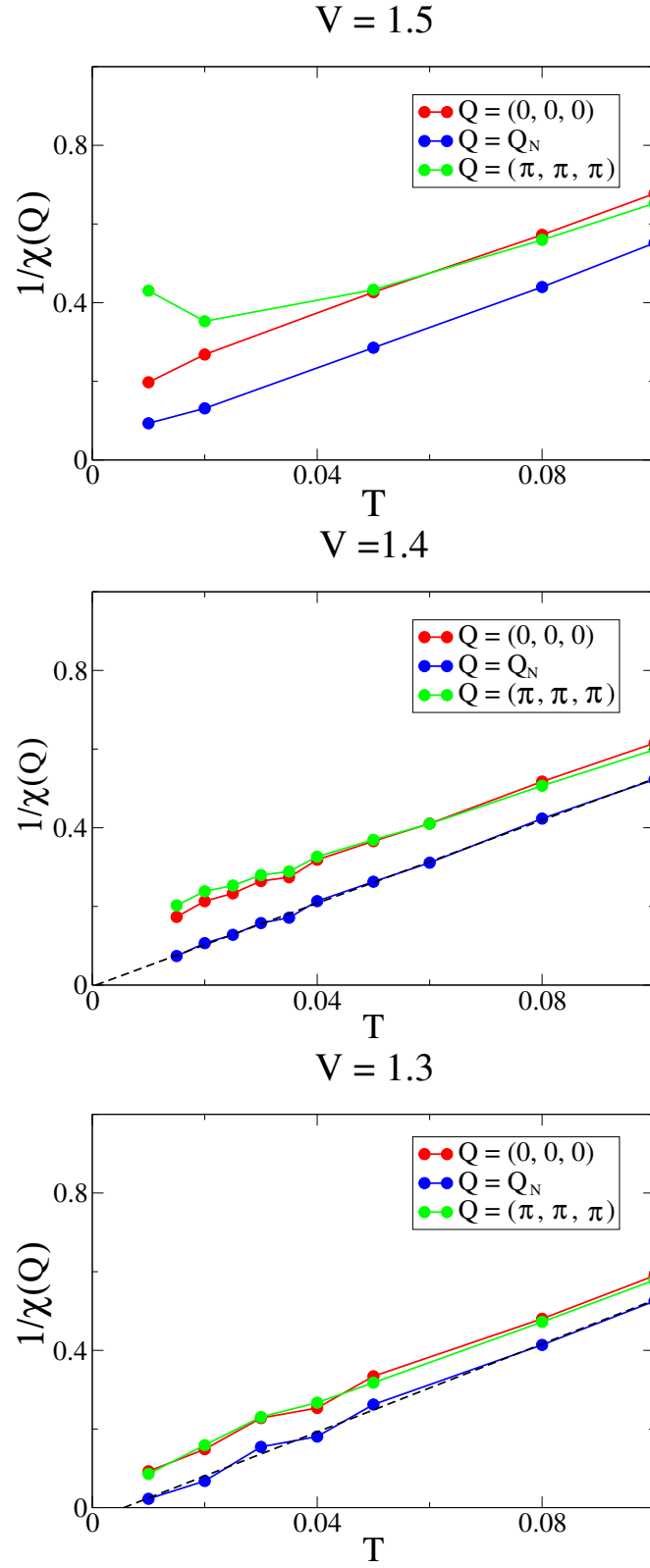


Figure 4.8: $1/\chi(Q)$ for $V = 1.5$, $V = 1.4$ and $V = 1.3$ at low temperatures.

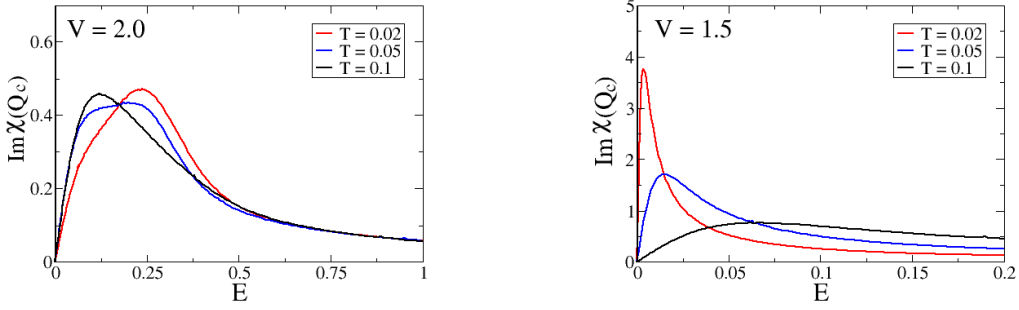


Figure 4.9: Imaginary part of dynamic magnetic susceptibility $\Im\chi(\mathbf{Q}, E)$ with $\mathbf{Q} = \mathbf{Q}_N = (0.72\pi, 0.72\pi, 0.72\pi)$ at selected temperatures. $V = 2.0$ leads to a paramagnetic Fermi liquid ground state, while $V = 1.5$ is in the close vicinity of antiferromagnetic instability at $T_N \simeq 0$.

low energy antiferromagnetic fluctuations are suppressed. However, the evolution of $\Im\chi(\mathbf{Q}_N, E)$ for $V = 1.5$ is quite different. The spectral weight shifts to the low energy and forms sharp peak as temperature is lowered, indicating the formation of spin-wave excitations.

Fig. 4.10 shows a full picture of $\Im\chi(\mathbf{Q}, E)$ for $V = 2.0$ (left) and $V = 1.5$ (right) and \mathbf{Q} along the contour of $(0, 0, 0) - (\pi, \pi, \pi) - (\pi, 0, 0) - (0, 0, 0)$. The brightness indicates the spectral weight. The differentiation in momentum space shows distinct features of evolution with temperature.

For $V = 2.0$, as temperature is lowered, spectral weight near $\mathbf{Q} = (0, 0, 0)$ shifts down to lower energy, which is associated with the enhancement of bulk susceptibility in the crossover regime above T_{FL} . It also displays a dispersion at low energy that assembles the excitations spectrum of paramagnons in a ferromagnet. This indicates that ferromagnetic fluctuations are the dominant low-lying excitations in the crossover regime. In this model calculation, the ferromagnetic fluctuations do not leads to ferromagnetic transition, since the bulk susceptibility saturates below T_{FL} , that is, the set-in of coherent Fermi phase. However, the paramagnetic fluctuations may be tuned to be critical by external magnetic field and induce field-driven quantum critical point as observed in YbRh_2Si_2 [97]. The effect of a magnetic field is left for future work. Near $\mathbf{Q} = (\pi, \pi, \pi)$, the spectrum becomes gapped at $\omega \sim 0.2$.

For $V = 1.5$, the spin fluctuations evolve with temperature in a very different manner. At $T = 0.2$, the distribution of spectral weight of $\Im\chi(\mathbf{Q}, \omega)$ shows weak \mathbf{Q} -dependence thus no dispersion is discernible. As temperature is lowered, the spectral weight becomes concentrated within narrower range of energy, and near the antiferromagnetic ordering momentum $\mathbf{Q}_N \simeq 0.72(\pi, \pi, \pi)$, the spectral weight is significantly larger than other regions in the Brillouin zone. Although the spectral weight exhibits strong momentum-differentiation, the spectrum still does not show an evident dispersion expected for an antiferromagnetic spin waves. In fact, a nearly **flat** band of spectral weight moves to low energy. This means when the antiferromagnetic ordering at $\mathbf{Q} = \mathbf{Q}_N$ emerges, spin-fluctuations for all \mathbf{Q} s are **equally** critical near the antiferromagnetic transition. Along the flat band, spectral weight becomes more denser near $\mathbf{Q} = \mathbf{Q}_N$ as temperature is lowered, and consequently the antiferromagnetic ordering has the leading instability at $\mathbf{Q} = \mathbf{Q}_N$.

This uniformity of spin fluctuations is compared to the outcome of inelastic neutron scattering in $\text{CeCu}_{5.9}\text{Au}_{0.1}$. The quantum criticality of $\text{CeCu}_{5.9}\text{Au}_{0.1}$ can not be addressed by SDW theory of itinerant quantum magnets, and thus provides a main motivation of the theory of local quantum criticality, or the Kondo-breakdown scenario [98]. Fig. 4.11 shows the cut of $\Im\chi(\mathbf{Q}, E)$ at $E = 0.001$ along the diagonal direction $\mathbf{Q} = (0, 0, 0)$ to (π, π, π) for $V = 1.5$. The experimental data is from Ref. [3] and shows the similarity in the evolution of the energy cut curve. The common feature is that as temperature decreases, the spectral weight along the energy cut is enhanced simultaneously over a significant portion of the Brillouin zone.

4.3.3 The Fermi surface

The spin susceptibility of the periodic Anderson model points to a localized picture of antiferromagnetic instability, which suggests that the magnetism emerges when the Kondo screening is suppressed. To further understand the effect of Kondo screening near the antiferromagnetic instability, we also study the single-particle properties of the system near $V = 1.5$. Fig. 4.12 shows the cut of single-particle spectral function $A_{\mathbf{k}}(\omega = 0^+)$ for conduction (left) and f -electrons on the $k_z = 0$ plane for $V = 2.0$

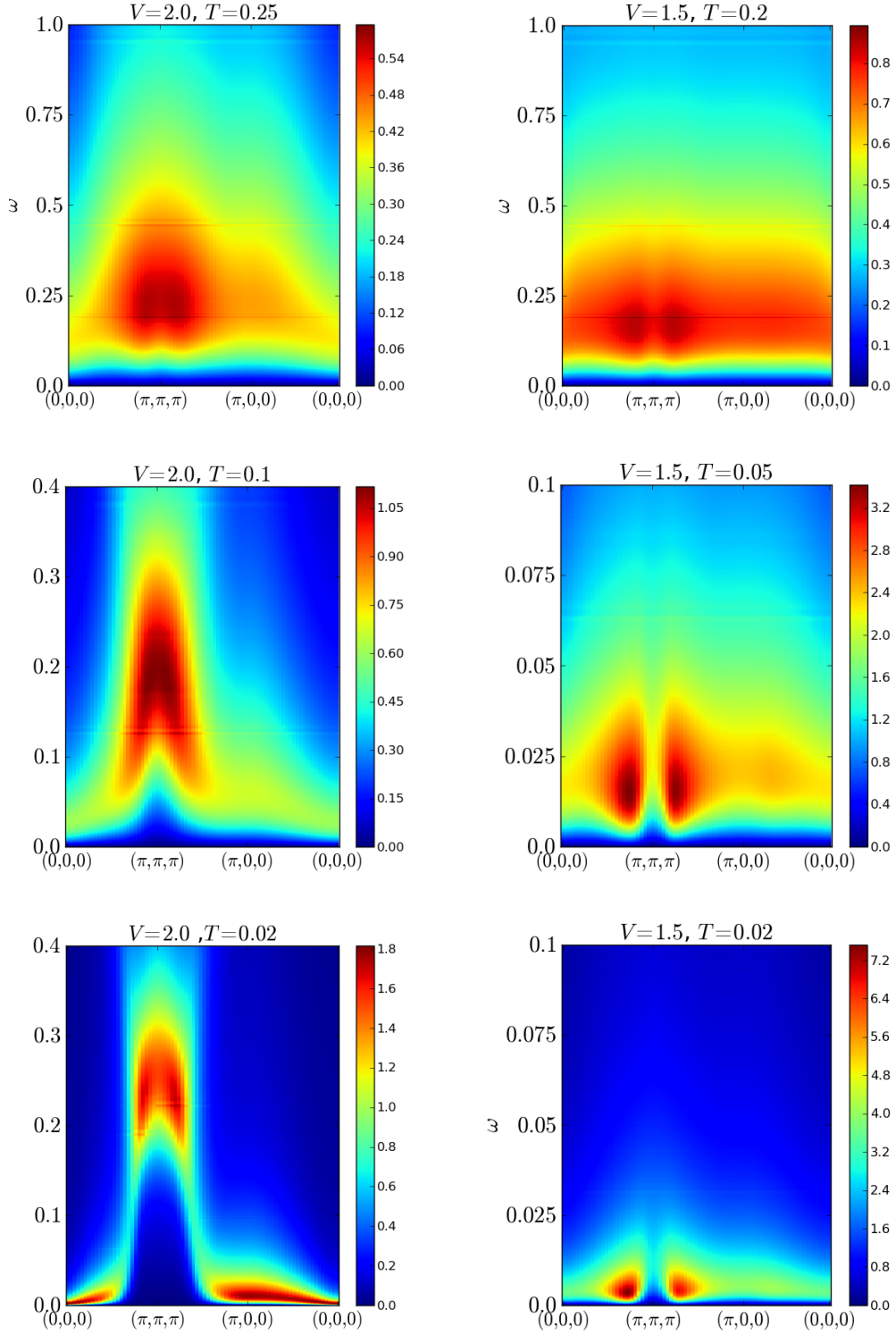


Figure 4.10: Imaginary part of dynamic susceptibility along the selected contour in Brillouin zone $((0,0,0) - (\pi,\pi,\pi) - (\pi,0,0) - (0,0,0))$ for $V = 2.0$ (left) and $V = 1.5$ (right) at selected temperatures.

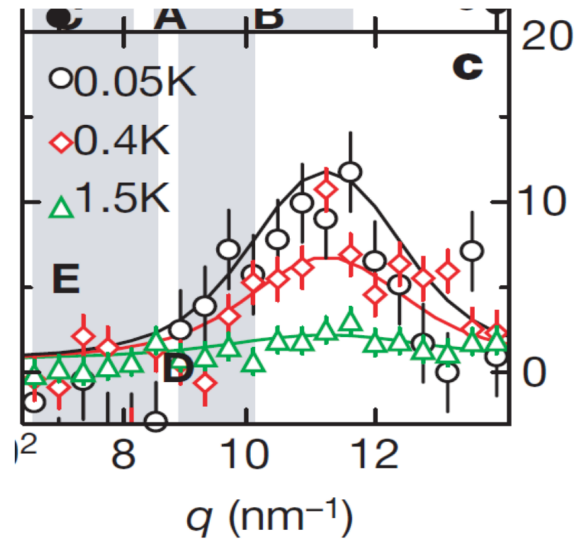
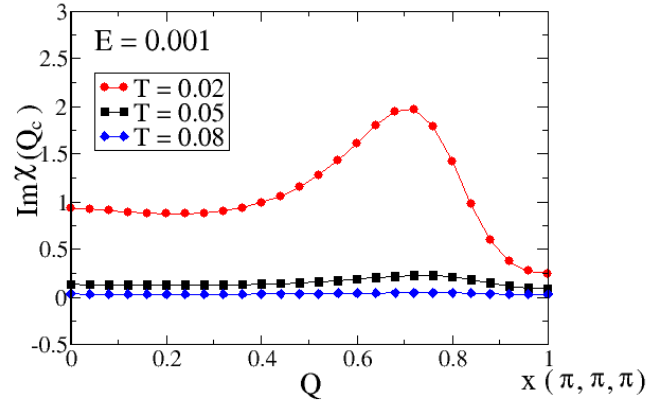


Figure 4.11: Energy cut of dynamic magnetic susceptibility. Figure in the above shows the energy cut at $E = 0.001$ of $\Im\chi(\mathbf{Q}, E)$ of periodic Anderson lattice with $V = 1.5$, for selected temperatures. \mathbf{Q} along the diagonal direction from $(0, 0, 0)$ to (π, π, π) . Figure in the below shows experimental data from inelastic neutron scattering on $\text{CeCu}_{5.9}\text{Au}_{0.1}$. Reprinted by permission from Macmillan Publishers Ltd: Nature ([3]), copyright (2000).

(above), $V = 1.5$ (middle) and $V = 1.3$ (below) at $T = 0.01$. For $V = 2.0$, the Fermi surface of c - and f -electrons is sharp and identical, which means the local moments are screened and form the heavy Fermi liquid quasiparticles with the c -electrons. As hybridization is decreased, the c -electron Fermi surface expands and the spectral weight of f -electrons decreases rapidly. For comparing, Fig. 4.13 shows the cut, on the same plane for $V = 2.0$, but at a much higher temperature $T = 1.0$, which is above the Kondo scale T_K in Fig. 4.7. The c -electrons form a smaller closed Fermi surface than the one at $T = 0.01$, and the spectral weight of f -electrons spreads uniformly in the majority of the Brillouin zone. These facts make clear that above T_K , f -electrons remain localized and decoupled from conduction electrons.

The similarity between the high temperature Fermi surface in Fig. 4.13 and the low temperature Fermi surface for $V = 1.3$ in Fig. 4.12 indicates that near the emergence of the antiferromagnetic instability at $V = 1.5$, the local moments remains decoupled from, or at most very weakly coupled to the c -electrons.

It remains an interesting issue that whether there could be a critical value of hybridization that the local moments are completely decouple from c -electrons at the ground state, that is, $T = 0$. For this purpose I calculate the effective local hybridization between c - and f -electrons defined by $V_{eff} = -\sum_k \Re G_{cf}(k, i\omega_1 = i\pi T)$. To approach very low temperatures, exact diagonalization (ED) is used as the impurity solver. In Fig. 4.14, we show V_{eff} as a function of V for low temperatures. Points at $T = 0.02$ are obtained from CTQMC, and points at $T = 0.005$ and $T = 0.0025$ are computed from ED impurity solver. Fig. 4.14 shows that as temperature is lowered, V_{eff} remains positive and smooth as a function of hybridization, though at low temperature, V_{eff} displays a sharper decrease near $V = 1.5$. Therefore, it is **unlikely** that there is a quantum critical point V_c at $T = 0$ which separates a heavy Fermi liquid ground state and a gas of decoupled c -electrons and local moments. In other words, a Kondo breakdown at $T = 0$ does not happen.

The absence of a quantum critical hybridization suggests that the localized picture of antiferromagnetic instability as seen in Sec. 4.3 does not have to accompany the orbital-selective Mott transition or a Kondo breakdown in heavy fermion systems [99].

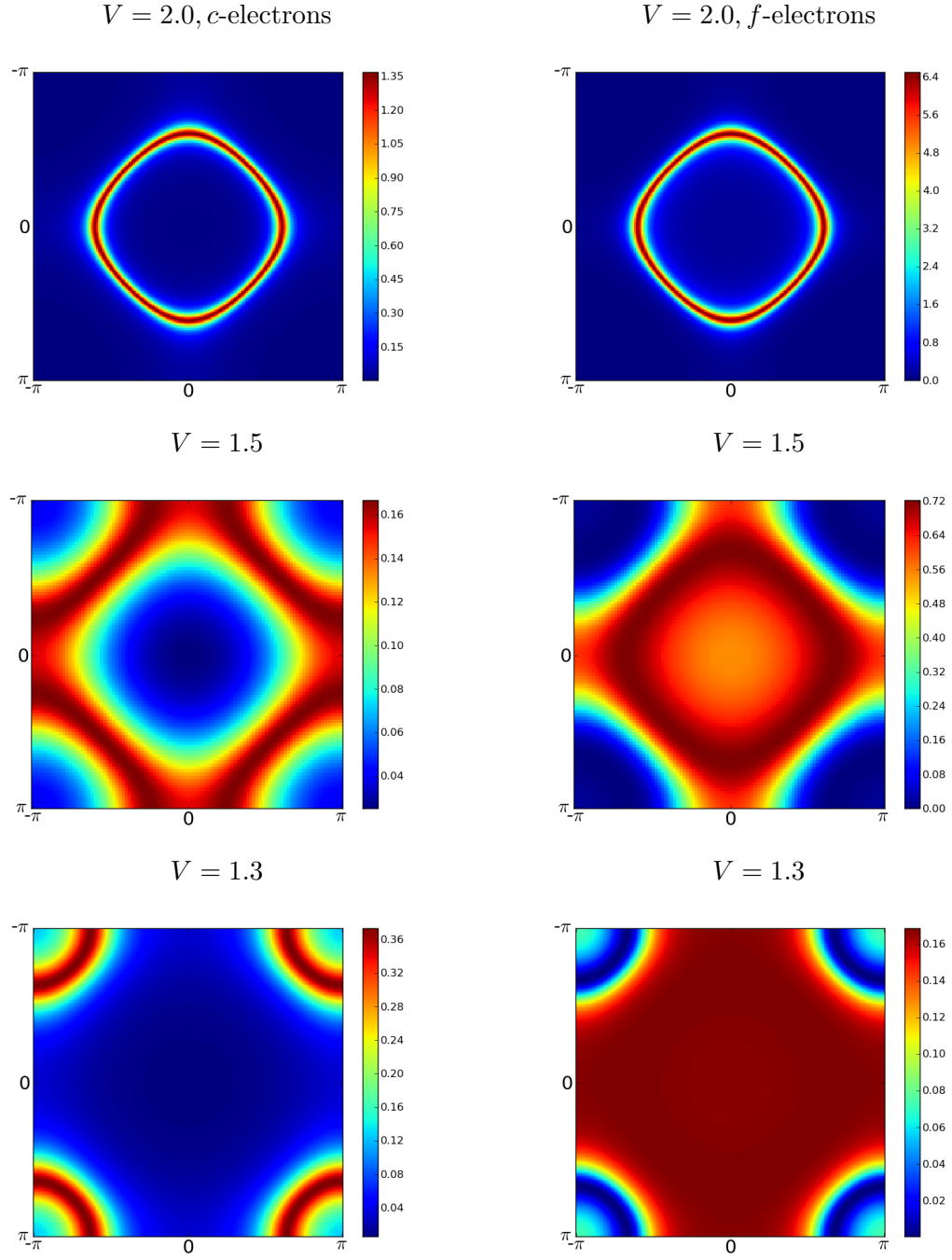


Figure 4.12: Cut of Fermi surface at $k_z = 0$ for $V = 2.0$ (above), $V = 1.5$ (middle) and $V = 1.3$ (below). On the left is the Fermi surface cut of c -electrons. On the right is the Fermi surface cut of f -electrons. $T = 0.01$.

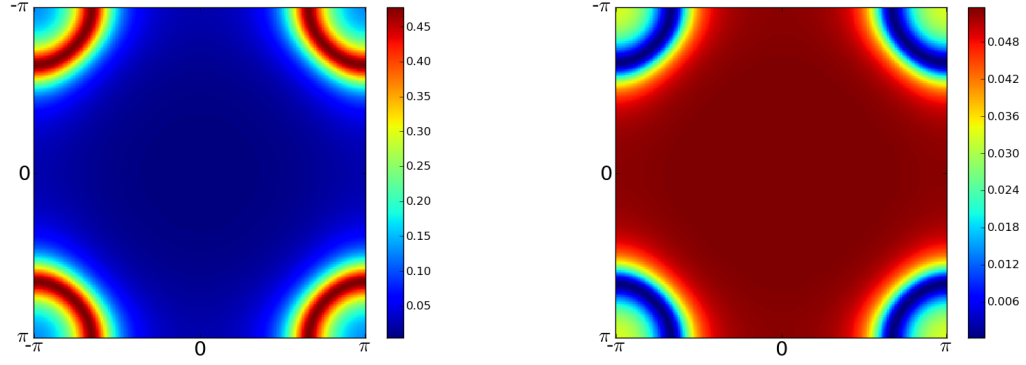


Figure 4.13: Cut of Fermi surface at $k_z = 0$ for $V = 2.0$ for $T = 1.0$. On the left is the Fermi surface cut of c -electrons. On the right is the Fermi surface cut of f -electrons.

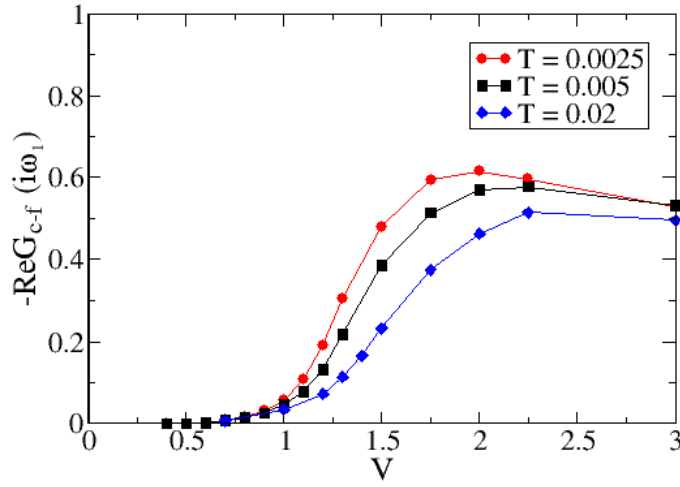


Figure 4.14: Effective hybridization, defined as $-\sum_k G_{cf}(k, i\omega = \pi T)$, as a function of V at $T = 0.02$, $T = 0.005$ and $T = 0.0025$. Points of $T = 0.02$ are obtained by CTQMC, and points at $T = 0.005$ and $T = 0.0025$ are obtained using ED impurity solver.

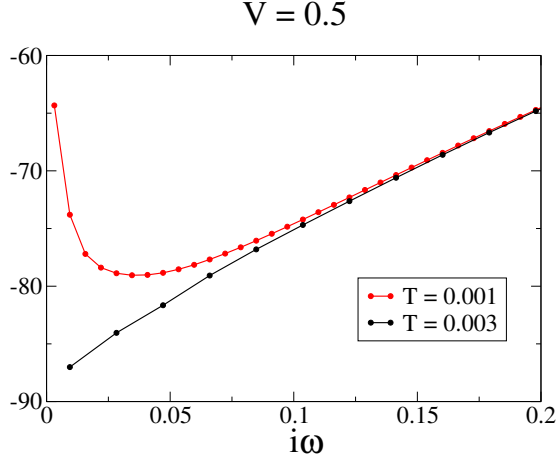


Figure 4.15: $\Im\Sigma_f(i\omega)$ for $V = 0.5$.

In the scenario of orbital-selective Mott transition, the phase of Kondo breakdown is perceived as that f -electrons remains a Mott insulating state due to the Coulomb repulsion while c -electrons are metallic, while in the heavy Fermi liquid phase both type of electrons are metallic.

In fact, to achieve a orbital-selective Mott transition, a small but non-zero dispersion of localized f -orbitals is needed in Ref. [99], which uses a slave-boson approach. As pointed out in Ref. [100], in single-site DMFT, an arbitray small hybridization would be able to kill the orbital-selective Mott transition at zero temperature, and non-local correlation has to be included by cluster DMFT to realize the quantum critical point of orbital selective Mott transition [101]. The effective hybridization V_{eff} shown in Fig. 4.14 is indeed consistent with this conclusion.

Although there is no orbital-selective Mott transition at zero temperature, it is still possible at finite temperature. Fig. 4.15 shows the self energy of f -electrons $\Im\Sigma(i\omega_n)$ at low temperatures when $V = 0.5$. This data are obtained by ED impurity solver. At $T = 0.003$, $\Im\Sigma(i\omega_n)$ shows the diverging feature of an insulator, while at $T = 0.001$, f -electrons become metallic, which indicates that for $V = 0.5$, the orbital-selective Mott transition temperature is $T_{MI} \simeq 0.002$. For larger values of V , the Mott transition turns into a crossover regime, as shown by the blue dashed lines in Fig. 4.1 (a).

4.4 Conclusion

This chapter focuses on the antiferromagnetic ordering and spin fluctuations in the periodic Anderson model. The hybridization-temperature (V - T) phase diagram is investigated. When V is large, the ground state is a heavy Fermi liquid. The Fermi liquid temperature scale T_{FL} is identified by the quadratic temperature dependence of resistivity and the set-in of Pauli paramagnetism. As V becomes smaller, the Fermi liquid scale vanishes (at $V \simeq 1.5$ in the our case), and antiferromagnetic instability emerges. The antiferromagnetic transition is studied in the DMFT framework of two-particle response functions. Local and lattice spin susceptibilities are calculated. It turns out the magnetic ordering is incommensurate, and the spin fluctuations in the vicinity of the magnetic transition exhibits a “localized” (\mathbf{Q} -independent) critical behavior. Furthermore, the possibility selective Mott-transition at $T = 0$ is ruled out, indicating that the localize nature of the magnetic fluctuations is not related to a quantum critical point of Kondo breakdown scenario.

Chapter 5

Thermoelectricity in FeSb₂

FeSb₂ is a narrow gap correlated semiconductor with conduction and valence band characterized by *d*-electrons. Colossal thermopower (S) of tens of mV/K at approximately $T = 10K$ is observed in FeSb₂ [102], which has attracted considerable interest in a long-lasting search for efficient thermoelectric conversion material at low temperatures.

The effect of strong electronic correlation in FeSb₂ has been confirmed by accumulating experimental facts, for example the spectral weight transfer over a wide energy window ($\sim 1eV$) in optical spectroscopy [103, 104]. The sign of the colossal thermopower in FeSb₂ at low temperature is negative, in agreement with the domination of electron band in transport, which is also confirmed by the Hall measurement at $T < 30K$. One leading mystery in FeSb₂ is the incompatibility between the narrow gap and the colossal thermopower. The resistivity measurement [102, 105] exhibits an activation behavior between $50K$ and $100K$ with an activation energy of $26meV$, while from $20K$ to $10K$, the resistivity shows a shoulder with an activation energy of $3meV$. The optical conductivity reveals a gap of $37meV$ at low temperatures [104]. At low temperature, the thermopower follows the activation behavior of

$$S \propto \frac{k_B}{e} \frac{\Delta}{T} \simeq 86\mu V/K \times \frac{\Delta}{T}, \quad (5.1)$$

where Δ is the activation energy. None of the gap values mentioned above, from resistivity or optical measurement, is large enough to account for the colossal thermopower, $S \simeq 45mK/V$ at $T = 10K$.

Recently, a comprehensive investigation of the transport properties of FeSb₂ has been reported in Ref. [4]. The authors find the colossal thermopower at low temperature is accompanied by exotic behaviors of two other quantities, the magnetoresistance

($MT(T)$) and Nernst coefficient ($\nu(T)$). This chapter provides a phenomenological analysis of S , MT , and ν based on a Boltzmann transport theory of single conduction band. Although this simple theory can not fully account for the colossal thermopower, it does reveal that the exotic behaviors of $MT(T)$ and $\nu(T)$ are rooted in the strong energy dependence of electron relaxation time. In particular, the energy dependence leads to the mismatch between the electric Hall conductivity, μ_H , and its thermal counterpart, the “thermal” Hall conductivity, μ_t , giving rise to the giant Nernst coefficient.

5.1 Linear Response Theory in a Weak Magnetic Field

This section provides a brief review of linear response theory of the longitudinal and transverse electric and thermal transport in a weak magnetic field.

Charge current can be induced by external electric field \mathbf{E} or thermal gradient ∇T ,

$$\mathbf{J} = \bar{\sigma} \cdot \mathbf{E} - \bar{\alpha} \cdot \nabla T. \quad (5.2)$$

We consider the case that \mathbf{E} , ∇T , and \mathbf{J} are in the $x-y$ plane. Hence the conductivity functions $\bar{\sigma}$ and $\bar{\alpha}$ are 2×2 tensors.

First we define resistivity and thermopower without the magnetic field. The effect of a weak magnetic field will be discussed later. Resistivity, ρ , is determined by the diagonal component of $\bar{\sigma}$,

$$\rho = \frac{1}{\sigma^{xx}}. \quad (5.3)$$

Thermopower, or the Seebeck coefficient, S , is defined as

$$S \equiv \frac{E_x}{\nabla_x T}. \quad (5.4)$$

In an experimental setup, S is measured when the charge current is zero, that is, the current driven by the electric field is neutralized by that driven by the thermal gradient. Consequently,

$$J_x = \sigma_{xx} E_x - \alpha_{xx} \nabla_x T = 0, \quad (5.5)$$

and

$$S = \frac{\alpha^{xx}}{\sigma^{xx}}. \quad (5.6)$$

The Hall mobility μ_H , magnetoresistance MR , and Nernst coefficient ν are defined in the presence of magnetic field \mathbf{B} . We assume the magnetic field is perpendicular to the $x - y$ plane, so $\mathbf{B} = B\hat{z}$. The Lorentz force induces transverse motion of carriers when electric field and/or thermal gradient is applied along the x direction. Therefore μ_H , MR , and μ involve the off-diagonal component of conductivity tensors. Eventually, the charge accumulating on the sides of the sample will produce a transverse field E_y , which counteracts the Lorentz force and annihilates the transverse current. That is,

$$J^y = \sigma^{yx} E_x + \sigma^{yy} E_y = 0, \quad (5.7)$$

and the Hall mobility is defined as

$$\mu_H = \frac{E_y}{BE_x} = -\frac{\sigma^{yx}}{B\sigma^{xx}}. \quad (5.8)$$

Another quantity commonly used for Hall effect the Hall coefficient,

$$R_H \equiv -\frac{\sigma^{yx}}{(\sigma^{xx})^2 B} = \rho \mu_H. \quad (5.9)$$

The magnetic field also has an effect on the longitudinal transport. In fact, $J^y = 0$ leads to $E_y = -\frac{\sigma^{yx}}{\sigma^{yy}} E_x$. Substituting E_y into $J^x = \sigma^{xx} E_x + \sigma^{xy} E_y$, we have

$$J^x = \left(\sigma^{xx} - \frac{\sigma^{yx}\sigma^{xy}}{\sigma^{xx}} \right) E_x. \quad (5.10)$$

When B is small, the leading term in σ^{yx} and σ^{xy} are proportional to B (see App. D for a detailed derivation). Furthermore, the longitudinal component σ^{xx} has a subleading term $\delta\sigma^{xx} \propto B^2$. Using σ_0^{xx} and ρ_0 to denote the longitudinal conductivity and resistivity when B is absent, we get

$$J^x = \left(\sigma_0^{xx} + \frac{\delta\sigma^{xx}}{B^2} + \sigma_0^{xx} B^2 \mu_H^2 \right) E_x. \quad (5.11)$$

Then

$$\begin{aligned} \rho &= \frac{1}{\sigma_0^{xx} \left[1 + \left(\frac{\delta\sigma^{xx}}{B^2 \sigma_0^{xx}} + \sigma_0^{xx} \mu_H^2 \right) B^2 \right]} \\ &= \rho_0 - \left(\frac{\delta\sigma^{xx}}{B^2 (\sigma_0^{xx})^2} + \frac{\mu_H^2}{\sigma_0^{xx}} \right) B^2. \end{aligned} \quad (5.12)$$

Define

$$\delta\rho \equiv - \left(\frac{\delta\sigma^{xx}}{B^2 (\sigma_0^{xx})^2} + \frac{\mu_H^2}{\sigma_0^{xx}} \right) B^2, \quad (5.13)$$

and the magnetoresistance is

$$MR \equiv \frac{\delta\rho}{\rho_0} = - \left(\frac{\delta\sigma^{xx}}{B^2 \sigma_0^{xx}} + \mu_H^2 \right) B^2. \quad (5.14)$$

We have assumed the isotropy in x - y plane such that $\sigma^{xx} = \sigma^{yy}$ and $\sigma^{yx} = -\sigma^{xy}$.

The Nernst coefficient ν is the transverse analog of the Seebeck coefficient. ν is defined as

$$\begin{aligned} \nu &\equiv \frac{E_y}{B \nabla_x T} \\ &= \frac{1}{B} \frac{\alpha^{yx} \sigma^{xx} - \alpha^{xx} \sigma^{yx}}{\sigma^{xx} \sigma^{yy} - \sigma^{yx} \sigma^{xy}} \\ &\simeq \frac{\alpha^{xx}}{\sigma^{xx}} \left(-\frac{1}{B} \frac{\sigma^{yx}}{\sigma^{xx}} - \left(-\frac{1}{B} \frac{\alpha^{yx}}{\alpha^{xx}} \right) \right) \\ &= S(\mu_H - \mu_t). \end{aligned} \quad (5.15)$$

Notice the thermal analog, μ_t , of the Hall mobility is defined,

$$\mu_t = -\frac{1}{B} \frac{\alpha^{yx}}{\alpha^{xx}}. \quad (5.16)$$

It is a useful quantity when analyzing the exotic Nernst behavior in FeSb₂.

5.2 Experimental Facts on FeSb₂

In this section I summarize the main findings in Ref. [4]. Transport measurements on FeAs₂ are also presented in parallel with those of FeSb₂ to highlight the unique behavior in magnetoresistance and Nernst effect of FeSb₂.

The main panel of Fig. 5.1 shows the resistivity $\rho(T)$ of FeSb₂ and FeAs₂. The temperature dependence in FeSb₂ can be divided into three regions. (i) Between 40K and 100K, $\rho(T)$ follows the thermal activation law and yields an activation gap $E_g \simeq 28meV$. (ii) Between 10K and 20K, a shoulder connects the activation behavior above 40K and below 15K. (iii) The activation behavior below 15K reveals a small gap 6meV. The thermal activation behavior in FeAs₂ above 200K, on the other hand, confirms an energy gap of $E_g \simeq 0.2eV$. In fact, electronic structure calculations based

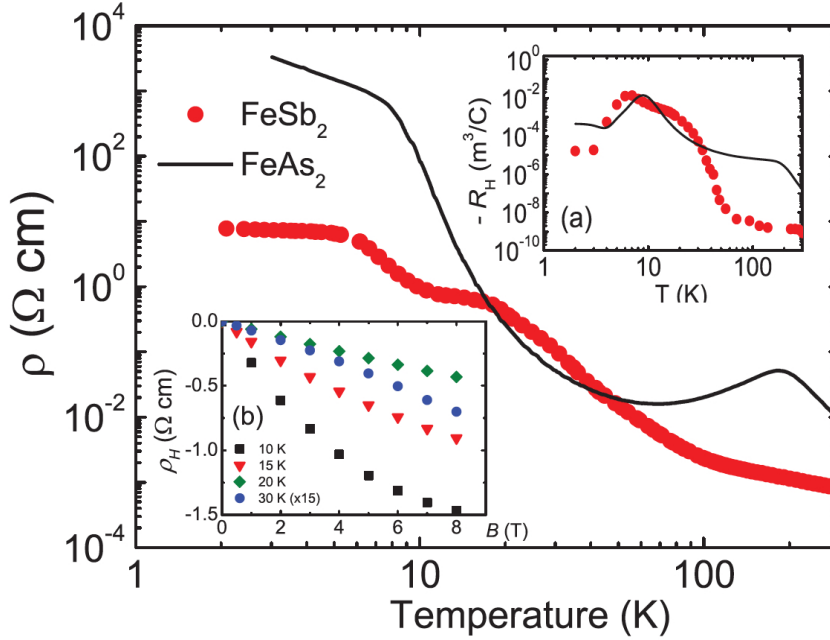


Figure 5.1: Resistivity $\rho(T)$ (main panel) and Hall coefficient $R_H(T)$ measured at $B = 1T$ [inset (a)] for FeSb_2 and FeAs_2 . Inset (b): isothermal Hall resistivity $\rho_H(B)$ for FeSb_2 . Reprinted from Ref. [4]. Copyright (2013) by the American Physical Society.

on generalized gradient approximation (GGA) produced the band structure of FeAs_2 with a direct gap of $0.2eV$. However, correlation effects had to be taken into account by, e.g., GW method, in electronic structure calculations, to capture the correct magnitude of the gap ($\simeq 28meV$) in FeSb_2 . This also indicates the important role of electron correlation in FeSb_2 .

The main panels of Fig. 5.2 present the thermopower $S(T)$ and Nernst coefficient $\nu(T)$. For FeAs_2 , $S(T)$ above $T = 15K$ roughly follows the activation behavior, Eq. 5.1, which gives $S(T = 15K) \sim 10mV/K$, given that the thermal activation is controlled by the gap $E_g \simeq 0.2eV$ from resistivity measurement. However, the thermopower of FeSb_2 , reaches a maximum of $18mV/K$ at $T = 10K$, and can not be accounted for by the activation gap $E_g \simeq 28meV$.

The difference in Nernst coefficient is even more drastic. $\nu(T)$ of FeSb_2 dwarfs that of FeAs_2 by two orders in magnitude, as shown in the inset of Fig. 5.2 (b). Using Eq. 5.9, we can determine the Hall mobility μ_H from the Hall coefficient R_H (shown in inset (a) of Fig. 5.1) and $\rho(T)$. Then from Eq. 5.15 we can determine the thermal

Hall mobility μ_t , μ_H and μ_t of FeSb₂ and FeAs₂ are compared in Fig. 5.3. I will show in Sec. 5.3 that a non-dispersive scattering rate will lead to a cancellation between μ_t and μ_H , and give rise to vanishing Nernst effect. Therefore, Fig. 5.3 suggests that the source of the giant Nernst coefficient in FeSb₂ could be a non-dispersive scattering rate.

Fig. 5.4 compares the temperature dependence of magnetoresistance $MR(T)$ with that of $\mu_H^2(T)$. The inset shows the case of FeAs₂. $MR(T)$ and $\mu_H^2(T)$ coincide between 20K and 100K by a proper re-scaling. On the other hand, FeSb₂ exhibits quite different temperature dependence for $MR(T)$ and $\mu_H^2(T)$. The main panel of Fig. 5.4 shows $MR(T)$ at several selected magnetic fields. None of these curves can coincide with the curve of $\mu_H^2(T)$. This indicates the behavior of $MR(T)$ is more challenging to understand than that of giant Nernst effect. As will be shown in the following section, although a high-dispersive scattering rate can produce a finite $\nu(T)$, it is not sufficient to differentiate the temperature dependence of $MR(T)$ from that of a re-scaled $\mu_H^2(T)$.

5.3 The Boltzmann Transport Theory

This section adopts the approximate expressions for conductivity tensors in terms of quasiparticle attributes (effective mass, band velocity and curvature, and scattering rate) as derived in Ch. 2, to investigate the behavior of thermo- and magneto-electric transport of a correlated semiconductor in the non-degenerate limit. As a relevant case for FeSb₂, a single electron band is considered, since within the temperature range of interest (5K to 30K), the electrical transport in FeSb₂ is dominated by the electron band, as verified by the Hall coefficient measurement (see Fig. 5.1, inset (a)).

The conductivity tensors are given by the following expressions [106, 39],

$$\sigma_0^{xx} \simeq \frac{2e^2}{V} \sum_{\mathbf{k}} \left(-\frac{\partial f(\epsilon)}{\partial \epsilon} \right)_{\epsilon=\epsilon_{\mathbf{k}}^*} (v_{\mathbf{k}}^{*x})^2 (\tau_{\mathbf{k}}^*), \quad (5.17)$$

$$\alpha_0^{xx} \simeq -\frac{2ek_B}{V} \sum_{\mathbf{k}} \left(-\frac{\partial f(\epsilon)}{\partial \epsilon} \right)_{\epsilon=\epsilon_{\mathbf{k}}^*} (v_{\mathbf{k}}^{*x})^2 \left(\frac{\epsilon_{\mathbf{k}}^* + \Delta}{k_B T} \right) (\tau_{\mathbf{k}}^*), \quad (5.18)$$

$$\frac{\sigma^{yx}}{B} \simeq \frac{2e^3}{V} \sum_{\mathbf{k}} \left(-\frac{\partial f(\epsilon)}{\partial \epsilon} \right)_{\epsilon=\epsilon_{\mathbf{k}}^*} v_{\mathbf{k}}^{*y} (v_{\mathbf{k}}^{*xy} v_{\mathbf{k}}^{*x} - v_{\mathbf{k}}^{*xx} v_{\mathbf{k}}^{*y}) (\tau_{\mathbf{k}}^*)^2, \quad (5.19)$$

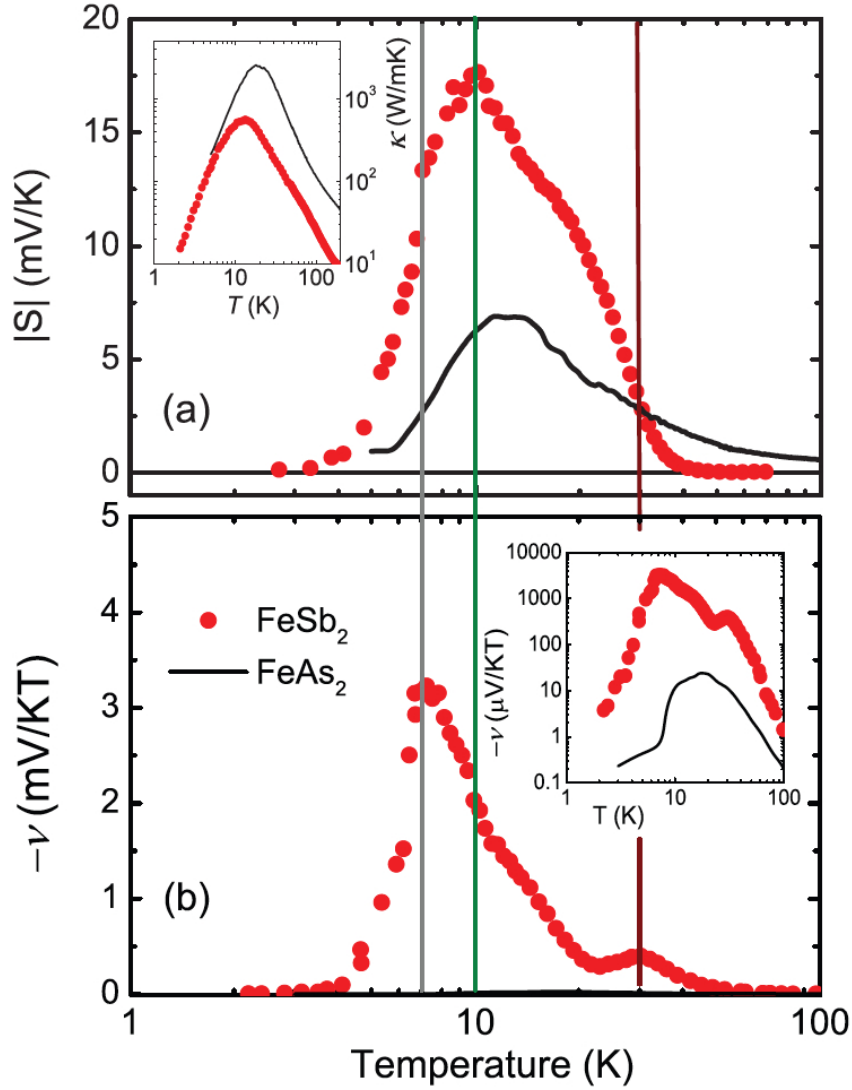


Figure 5.2: (a) Thermopower $S(T)$ and (b) Nernst coefficient $\nu(T)$ for FeSb_2 and FeAs_2 . The inset of (a) shows the thermal conductivity. The inset of (b) shows $\nu(T)$ in a double-log scale. Notice that the magnitude of $\nu(T)$ of FeSb_2 is larger than that of FeAs_2 by two orders. Reprinted from Ref. [4]. Copyright (2013) by the American Physical Society.

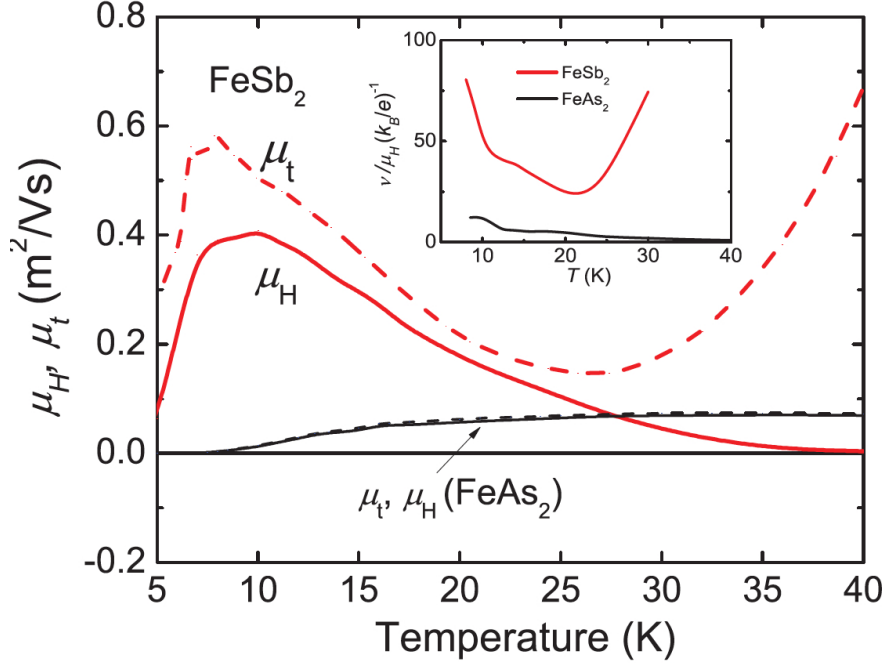


Figure 5.3: Electrical and thermal Hall mobility, μ_H and μ_t , of FeSb₂ and FeAs₂. The inset shows the dimensionless ratio $(\nu/\mu_H)/(k_B/e)$ for the two systems. Reprinted from Ref. [4]. Copyright (2013) by the American Physical Society.

$$\frac{\alpha^{yx}}{B} \simeq -\frac{2e^2 k_B}{V} \sum_{\mathbf{k}} \left(-\frac{\partial f(\epsilon)}{\partial \epsilon} \right)_{\epsilon=\epsilon_{\mathbf{k}}^*} v_{\mathbf{k}}^{*y} (v_{\mathbf{k}}^{*xy} v_{\mathbf{k}}^{*x} - v_{\mathbf{k}}^{*xx} v_{\mathbf{k}}^{*y}) \left(\frac{\epsilon_{\mathbf{k}}^* + \Delta}{k_B T} \right) (\tau_{\mathbf{k}}^*)^2, \quad (5.20)$$

$$\begin{aligned} \frac{\delta \sigma^{xx}}{B^2} &= \frac{2e^4}{V} \sum_{\mathbf{k}} \left(-\frac{\partial f(\epsilon)}{\partial \epsilon} \right)_{\epsilon=\epsilon_{\mathbf{k}}^*} \{ \epsilon_{\mathbf{k}}^{*xxx} \epsilon_{\mathbf{k}}^{*x} (\epsilon_{\mathbf{k}}^{*y})^2 - 2 \epsilon_{\mathbf{k}}^{*xxy} (\epsilon_{\mathbf{k}}^{*x})^2 \epsilon_{\mathbf{k}}^{*y} \\ &\quad + \epsilon_{\mathbf{k}}^{*xyy} (\epsilon_{\mathbf{k}}^{*x})^3 - (\epsilon_{\mathbf{k}}^{*x})^2 [\epsilon_{\mathbf{k}}^{*xx} \epsilon_{\mathbf{k}}^{*yy} - (\epsilon_{\mathbf{k}}^{*xy})^2] \} (\tau_{\mathbf{k}}^*)^3. \end{aligned} \quad (5.21)$$

$f(\epsilon)$ is the Fermi distribution function,

$$f(\epsilon) = \frac{1}{1 + \exp \left(\frac{\epsilon + \Delta}{k_B T} \right)}. \quad (5.22)$$

I assume a single conduction band with a parabolic dispersion,

$$\epsilon_{\mathbf{k}}^* = \frac{\hbar^2 k^2}{2m^*}. \quad (5.23)$$

m^* is the effective mass. The band velocity and higher order derivative are written as

$$v_{\mathbf{k}}^{\alpha\beta\dots} = \frac{\partial \epsilon_{\mathbf{k}}}{(\hbar \partial k_{\alpha})(\hbar \partial k_{\beta})\dots}. \quad (5.24)$$

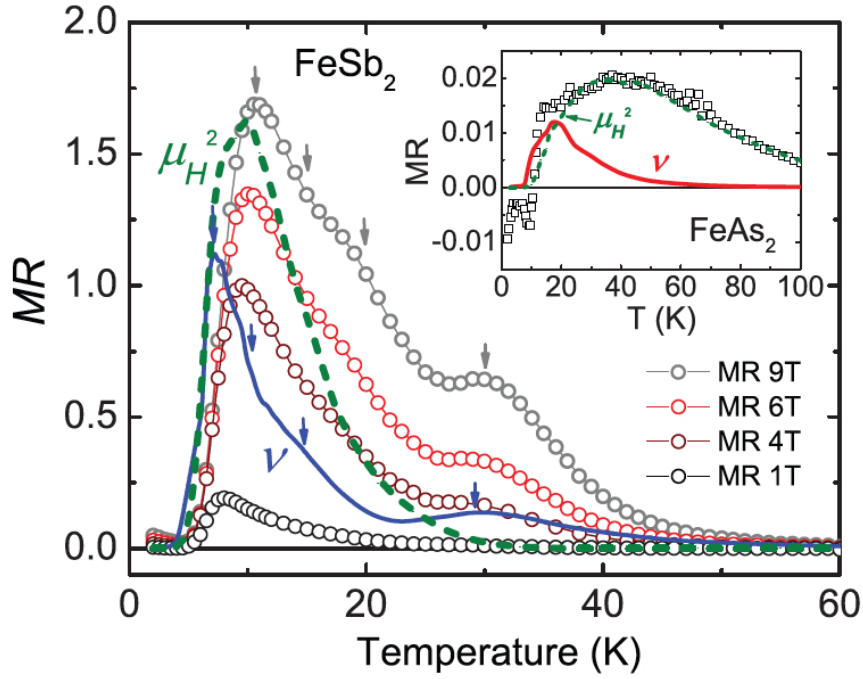


Figure 5.4: The magnetoresistance $MR(T)$ for FeSb₂ (main panel) and FeAs₂ (inset) at selected magnetic fields. Re-scaled squared Hall mobility, $\mu_H^2(T)$ is shown by the green dashed lines. For FeAs₂, the similar temperature dependence of $MR(T)$ and $\mu_H^2(T)$ is evident over a broad range of temperature ($10K < T < 100K$), while for FeSb₂, $MR(T)$ and $\mu_H^2(T)$ show very different temperature dependence. Reprinted from Ref. [4]. Copyright (2013) by the American Physical Society.

$\mu = -\Delta$ is the chemical potential. Δ is the activation energy. The non-degenerate limit is defined by when

$$\Delta \gg k_B T. \quad (5.25)$$

The relaxation time, $\tau_{\mathbf{k}}$, of a carrier with energy $\epsilon_{\mathbf{k}}$ is determined by the scattering rate $\Gamma_{\mathbf{k}}$,

$$\tau_{\mathbf{k}} = \frac{\hbar}{2\Gamma_{\mathbf{k}}(\epsilon_{\mathbf{k}})}. \quad (5.26)$$

In the following I consider a phenomenological scenario for quasiparticle scattering. In this scenario, the quasiparticle scattering rate (relaxation) has a dispersive component which is dependent on the quasiparticle energy.

$$\Gamma_{\mathbf{k}} \simeq \Gamma_0(T) + \Gamma_1 \left(\frac{\epsilon_{\mathbf{k}}}{k_B T} \right)^{-r}. \quad (5.27)$$

$\Gamma_0(T)$ is the non-dispersive component in the relaxation. Γ_1 is the coefficient for the dispersive component. The power-law form is usually adopted when discussing the scattering mechanism in semiconductors [107]. When $r = -1$, the scattering rate is linear in the quasiparticle energy. In correlated metals, this linear dispersion of scattering rate can have significant contribution to thermopower and Nernst coefficient.

I will stress on several aspects from the Boltzmann theory in the non-degenerate limit. The first aspect is the activation behavior of resistivity and thermopower. The second is the magnitude of Nernst coefficient, in particular the dimensionless quantity $\nu/(S\mu_H)$. The third aspect is the temperature dependence of $MR(T)$, in particular, the scaling between $MR(T)$ and $(\mu_H(T))^2$

Dispersive Scattering Rate

For a non-dispersive scattering rate ($\Gamma_1 = 0$ in Eq. 5.27), $\rho(T)$ and $S(T)$ have the activation behavior when $\Delta \gg k_B T$,

$$\rho(T) \simeq \left(\frac{2\pi}{k_B T} \right)^{3/2} \frac{\hbar^3}{e^2 (m^*)^{1/2} \tau_0} \exp \left(\frac{\Delta}{k_B T} \right), \quad (5.28)$$

$$S(T) \simeq -\frac{k_B}{e} \left(\frac{\Delta}{k_B T} + \frac{5}{2} \right). \quad (5.29)$$

The Hall mobility μ_H and its thermal counterpart μ_t are simply

$$\mu_H = \mu_t = \frac{e\tau_0}{m^*}. \quad (5.30)$$

In fact the result in Eq. 5.30 does not require the non-degenerate limit. Therefore, μ_H and μ_t cancel exactly in the Nernst effect, $\nu = S(\mu_t - \mu_H)$, leading to a vanishing ν . Also, the two terms on the right hand side of Eq. 5.14 cancel, leading to vanishing magnetoresistance.

For the case that the dispersive component dominates the quasiparticle relaxation, let us assume $\Gamma_0 = 0$. It is straightforward to derive that the conductivity tensors have the following expressions,

$$\sigma^{xx} \simeq \frac{2\sqrt{2}}{3\pi^2} \left(\frac{e^2}{\hbar^2} \right) (m^* k_B T)^{1/2} \left(\frac{k_B T}{\Gamma_1^*} \right) J_1^0 \left(\frac{\Delta}{k_B T}, r \right), \quad (5.31)$$

$$\alpha^{xx} \simeq \left(\frac{k_B}{e} \right) \frac{2\sqrt{2}}{3\pi^2} \left(\frac{e^2}{\hbar^2} \right) (m^* k_B T)^{1/2} \left(\frac{k_B T}{\Gamma_1^*} \right) J_1^1 \left(\frac{\Delta}{k_B T}, r \right), \quad (5.32)$$

$$\frac{\sigma^{yx}}{B} \simeq -\frac{\sqrt{2}}{3\pi^2} \left(\frac{e^3}{\hbar} \right) \frac{1}{(m_0 k_B T)^{1/2}} \left(\frac{k_B T}{\Gamma_1^*} \right)^2 J_2^0 \left(\frac{\Delta}{k_B T}, r \right), \quad (5.33)$$

$$\frac{\alpha^{yx}}{B} \simeq -\left(\frac{k_B}{e} \right) \frac{\sqrt{2}}{3\pi^2} \left(\frac{e^3}{\hbar} \right) \frac{1}{(m^* k_B T)^{1/2}} \left(\frac{k_B T}{\Gamma_1^*} \right)^2 J_2^1 \left(\frac{\Delta}{k_B T}, r \right), \quad (5.34)$$

$$\frac{\delta\sigma^{xx}}{B^2} = -\frac{\sqrt{2}}{6\pi^2} \frac{e^4}{(m^* k_B T)^{3/2}} \left(\frac{k_B T}{\Gamma_1^*} \right)^3 J_3^0 \left(\frac{\Delta}{k_B T} \right). \quad (5.35)$$

The function $J_n^m(\Delta/(k_B T), r)$ is defined as

$$J_n^m \left(\frac{\Delta}{k_B T}, r \right) = \int_{\frac{\Delta}{k_B T}}^{\infty} dx \frac{x^{3/2+nr} \left(x + \frac{\Delta}{k_B T} \right)^m}{4 \cosh^2 \left(\frac{x}{2} + \frac{\Delta}{2k_B T} \right)}. \quad (5.36)$$

In deriving Eq. 5.31 — 5.35, I have also transformed the summation over \mathbf{k} into integral over energy,

$$\sum_{\mathbf{k}} \rightarrow \frac{V}{4\pi^2} \left(\frac{2m^*}{\hbar^2} \right)^{3/2} \int_0^{\infty} \sqrt{\epsilon^*} d\epsilon^*, \quad (5.37)$$

based on the parabolic shape of the quasiparticle band.

In the non-degenerate limit, $\Delta \gg k_B T$,

$$\frac{1}{4 \cosh^2 \left(\frac{x}{2} + \frac{\Delta}{2k_B T} \right)} \simeq \exp \left(-\frac{\Delta}{k_B T} \right) \exp(-x), \quad (5.38)$$

which simplifies the integral in the definition of $J_n^m(\Delta/(k_B T), r)$ and leads to

$$\rho \simeq \frac{3\pi^2}{2\sqrt{2}} \left(\frac{\hbar}{e}\right)^2 (m^* k_B T)^{-1/2} \exp\left(\frac{\Delta}{k_B T}\right) \Gamma\left(\frac{5}{2} + r\right), \quad (5.39)$$

$$S \simeq -\left(\frac{k_B}{e}\right) \left(\frac{\Delta}{k_B T} + \frac{5}{2} + r\right), \quad (5.40)$$

$$\mu_H \simeq \frac{1}{2} \left(\frac{\hbar e}{m^*}\right) \left(\frac{1}{\Gamma_1^*}\right) \frac{\Gamma\left(\frac{5}{2} + 2r\right)}{\Gamma\left(\frac{5}{2} + r\right)}, \quad (5.41)$$

$$\mu_t \simeq \frac{1}{2} \left(\frac{\hbar e}{m^*}\right) \left(\frac{1}{\Gamma_1^*}\right) \frac{\Gamma\left(\frac{5}{2} + 2r\right)}{\Gamma\left(\frac{5}{2} + r\right)} \left(1 + \frac{k_B T}{\Delta} r\right) = \mu_H \left(1 + \frac{k_B T}{\Delta} r\right). \quad (5.42)$$

Here the Γ -function is used,

$$\Gamma(z) = \int_0^\infty dx x^{z-1} \exp(-x). \quad (5.43)$$

Hence $\nu(T)$ in the non-degenerate limit is

$$\nu = S(\mu_H - \mu_t) \simeq S\mu_H \left(-\frac{k_B T}{\Delta} r\right). \quad (5.44)$$

We can compare Eq. 5.39, Eq. 5.40, and Eq. 5.44 with the results of a non-dispersive scattering rate, Eq. 5.28, Eq. 5.29, and Eq. 5.30. In both cases, $\rho(T)$ and $S(T)$ are dominated by the thermal activation, $\rho(T) \propto \exp(\Delta/(k_B T))$ and the leading term of $S(T) \propto \Delta/(k_B T)$.

While μ_H and μ_t cancel for non-dispersive scattering rate and leads to a vanishing $\nu(T)$, a dispersive scattering rate gives rise to the mismatch between μ_H and μ_t and leads to a finite $\nu(T)$. Since

$$\frac{\mu_t(T)}{\mu_H(T)} - 1 \simeq \frac{k_B T}{\Delta} r. \quad (5.45)$$

We can estimate the value of r . At $T = 10K$, $\mu_t/\mu_T - 1 \simeq 0.25$ (see Fig. 5.3). If we employ the activation gap from resistivity measurement, $\Delta \sim 28meV$ (although it is not consistent with the magnitude of thermopower), it yields $r \sim 7$. This value would suggest a highly dispersive scattering rate in Eq. 5.27. This value is much larger than that of acoustic-phonon ($r = -1/2$) or ionized impurity ($r = 3/2$) scattering [107]. What scattering mechanism could result in such highly dispersive quasiparticle relaxation is unknown so far.

The magnetoresistance turns out to be

$$\frac{MR}{B^2} = \mu_H^2 \left(\frac{\Gamma(\frac{5}{2} + 3r) \Gamma(\frac{5}{2} + r)}{\Gamma(\frac{5}{2} + 2r) \Gamma(\frac{5}{2} + 2r)} - 1 \right). \quad (5.46)$$

The Γ -function has poles for some values of r . But this is an artifact of the simplified formulation. It can be eliminated by including a small non-dispersive component Γ_0 in the scattering rate. Eq. 5.46 indicates $MR(T)$ follows the same temperature dependence of $\mu_H^2(T)$, although the rescaling factor may dependent on the specific form of relaxation dispersion.

5.4 Conclusion

In this chapter we attempt to understand the effect of dispersive quasiparticle relaxation in the anomalous thermo- and magneto-electric transport of the correlated semiconductor FeSb₂. The colossal Nernst coefficient suggests a notable mismatch between the Hall mobility μ_H and its thermal counterpart μ_t , which can be a consequence of a highly dispersive quasiparticle relaxation time. However the dispersive relaxation is incapable of reconciling the giant thermoelectric power and the small activation gap $\Delta \simeq 28meV$ from resistivity measurement.

Appendix A

Retarded two-particle correlation function in the Keldysh formalism

In the real-time formalism, we start with the retarded two-particle correlation function,

$$\begin{aligned}\Pi_{\alpha\beta}(t) &= (-i)\Theta(t)\langle[\hat{j}_\alpha^{e\dagger}(\mathbf{q}, t), \hat{j}_\beta(\mathbf{q}, 0)]\rangle \\ &= (-i)\Theta(t)\sum_{\mathbf{k}, \mathbf{k}'} e^2 v_\alpha(\mathbf{k}) v_\beta(\mathbf{k}') \langle [c_{\mathbf{k}-\mathbf{q}/2}^\dagger(t) c_{\mathbf{k}+\mathbf{q}/2}(t), c_{\mathbf{k}'+\mathbf{q}/2}^\dagger(0) c_{\mathbf{k}'-\mathbf{q}/2}(0)] \rangle.\end{aligned}\tag{A.1}$$

Since $\Pi_{\alpha\beta}(t)$ is a **retarded** correlation function of current operators at finite temperature, a few pre-processing steps are needed before writing it into a form ready for perturbative expansion of contour-ordered correlation functions in the **Keldysh formalism** [108, 109, 110].

Without losing generality, I consider the retarded correlation function $\Pi_{1234}^R(t)$ with simplified indices,

$$\Pi_{1234}^R(t) = (-i)\Theta(t)\langle[c_1^\dagger(t)c_2(t), c_3^\dagger(0)c_4(0)]\rangle.\tag{A.2}$$

The indices 1, 2, 3, and 4 in Eq. A.2 replace the momentum indices of the fermionic operators in Eq. A.1.

To write Eq. A.2 into a form of contour-ordered correlation function, let me consider the following contour-ordered correlation function,

$$\begin{aligned}\Pi_1(t) &= (-i)\langle\mathcal{T}_c\left(c_1^\dagger(t_F^+)c_2(t_F)c_3^\dagger(0_F^+)c_4(0_F)\right)\rangle \\ &\quad - (-i)^2\langle\mathcal{T}_c\left(c_1^\dagger(t_F^+)c_2(t_F)c_3^\dagger(0_B^+)c_4(0_B)\right)\rangle.\end{aligned}\tag{A.3}$$

T_c is the **contour-ordering operator** defined on the closed-contour. The subscript ‘ F ’ and ‘ B ’ denotes the **forward** and **backward** branch of the contour, respectively.

$t^+ \equiv t + 0^+$ with 0^+ the infinitesimal. When $t > 0$,

$$\begin{aligned}\Pi_1(t) &= (-i)\langle c_1^\dagger(t^+) c_2(t) c_3^\dagger(0^+) c_4(0) \rangle + (-i)\langle c_4(0) c_3^\dagger(0^+) c_1^\dagger(t^+) c_2(t) \rangle \\ &= (-i)\langle [c_1^\dagger(t) c_2(t), c_3^\dagger(0) c_4(0)] \rangle + (-i)\langle c_1^\dagger(t) c_2(t) \rangle.\end{aligned}\quad (\text{A.4})$$

When $t < 0$,

$$\begin{aligned}\Pi_1(t) &= (-i)\langle c_3^\dagger(0) c_4(0) c_1^\dagger(t) c_2(t) \rangle + (-i)\langle c_4(0) c_3^\dagger(0) c_1^\dagger(t) c_2(t) \rangle \\ &= (-i)\langle c_1^\dagger(t) c_2(t) \rangle.\end{aligned}$$

$\langle c_1^\dagger(t) c_2(t) \rangle$ would give rise to the expectation value of current $\langle j_\alpha^\dagger \rangle$ when we recover the full expression for $\Pi_{\alpha\beta}^R(t)$, which is zero in the equilibrium state. In a similar way, we can check

$$\begin{aligned}\Pi_2(t) &= (-i)\langle \mathcal{T}_c \left(c_1^\dagger(t_B^+) c_2(t_B) c_3^\dagger(0_B^+) c_4(0_B) \right) \rangle \\ &\quad - (-i)\langle \mathcal{T}_c \left(c_1^\dagger(t_B^+) c_2(t_B) c_3^\dagger(0_F^+) c_4(0_F) \right) \rangle.\end{aligned}\quad (\text{A.5})$$

When $t \geq 0$,

$$\Pi_2(t) = (-i)\langle [c_3^\dagger(0) c_4(0), c_1^\dagger(t) c_2(t)] \rangle (-i) - (-i)\langle c_1^\dagger(t) c_2(t) \rangle. \quad (\text{A.6})$$

When $t < 0$,

$$\Pi_2(t) = (-i) - (-i)\langle c_1^\dagger(t) c_2(t) \rangle.$$

Therefore, up to a time-independent number which eventually vanishes when the full momentum summation in $\Pi_{\alpha\beta}^R(t)$ is considered, the retarded two-particle correlation function $\Pi_{1234}^R(t)$ can be written as a sum of four contour-ordered correlation functions with the time variables assigned to proper branches of the closed-contour,

$$\begin{aligned}\Pi_{1234}^R(t) &= \left(\frac{-i}{2}\right) \left\{ \langle \mathcal{T}_c c_1^\dagger(t_F^+) c_2(t_F) c_3^\dagger(0_F^+) c_4(0_F) \rangle - \langle \mathcal{T}_c c_1^\dagger(t_F^+) c_2(t_F) c_3^\dagger(0_B^+) c_4(0_B) \rangle \right. \\ &\quad \left. + \langle \mathcal{T}_c c_1^\dagger(t_B^+) c_2(t_B) c_3^\dagger(0_F^+) c_4(0_F) \rangle - \langle \mathcal{T}_c c_1^\dagger(t_B^+) c_2(t_B) c_3^\dagger(0_B^+) c_4(0_B) \rangle \right\}\end{aligned}\quad (\text{A.7})$$

The contour-ordered two-particle correlation functions are ready for a perturbative expansion.

In general, the **contour-ordered** two-particle correlation functions in the Keldysh formalism is a 4×4 **matrix** since each fermionic operator could be assigned to either branch of the closed-contour. Eq. A.7 indicates that only 4 matrix elements are relevant for the **retarded** two-particle correlation function. The ladder structure and the Bethe-Salpeter equation for the contour-ordered two-particle correlation functions as shown in Fig. 1.5 and Fig. 1.6 now presume a matrix product over the contour degree of freedom,

$$\begin{aligned}\mathbf{\Pi} &= \mathbf{G}\mathbf{G} + \mathbf{G}\mathbf{G}\mathbf{\Gamma}^i\mathbf{G}\mathbf{G} + \mathbf{G}\mathbf{G}\mathbf{\Gamma}^i\mathbf{G}\mathbf{G}\mathbf{\Gamma}^i\mathbf{G}\mathbf{G} + \dots \\ &= \mathbf{G}\mathbf{G} + \mathbf{G}\mathbf{G}\mathbf{\Gamma}^f\mathbf{G}\mathbf{G},\end{aligned}\tag{A.8}$$

$$\mathbf{\Gamma}^f = \mathbf{\Gamma}^i + \mathbf{\Gamma}^f\mathbf{G}\mathbf{G}\mathbf{\Gamma}^i.\tag{A.9}$$

$\mathbf{\Pi}$, $\mathbf{\Gamma}^f$ and $\mathbf{\Gamma}^i$ in Eq. A.8 and Eq. A.9 are 4×4 matrix of two-particle correlation functions, full vertex, and irreducible vertex functions. The inner integration over time (frequency) and space (momentum) degrees of freedom are omitted. \mathbf{G} is 2×2 matrix of single-particle correlation function,

$$\mathbf{G}(t) = \begin{pmatrix} G(t) & G^<(t) \\ G^>(t) & \tilde{G}(t) \end{pmatrix}.\tag{A.10}$$

$\mathbf{G}\mathbf{G}$ represents an **outer product** of

$$\mathbf{G}_{23}\mathbf{G}_{14} = \begin{pmatrix} G_{23}(t) & G_{23}^<(t) \\ G_{23}^>(t) & \tilde{G}_{23}(t) \end{pmatrix} \otimes \begin{pmatrix} G_{14}(t) & G_{14}^>(t) \\ G_{14}^<(t) & \tilde{G}_{14}(t) \end{pmatrix}\tag{A.11}$$

The single-particle Green's functions in real-time are defined as

$$G_{ij}(t) = (-i)\langle T_t c_i(t) c_j^\dagger(0) \rangle,\tag{A.12}$$

$$G_{ij}^>(t) = (-i)\langle c_i(t) c_j^\dagger(0) \rangle,\tag{A.13}$$

$$G_{ij}^<(t) = i\langle c_j^\dagger(0) c_i(t) \rangle,\tag{A.14}$$

$$\tilde{G}_{ij}(t) = (-i)\langle \tilde{T}_t c_i(t) c_j^\dagger(0) \rangle.\tag{A.15}$$

T_t is the ordering operator on the real-time axis. \tilde{T}_t is the anti-time ordering operator.

It is convenient to apply the **Keldysh rotation** from the closed-contour indices

(‘ F ’ and ‘ B ’) to the **Keldysh indices**, or the “ R/A ” basis,

$$\mathbf{U} \begin{pmatrix} G(t) & G^<(t) \\ G^>(t) & \tilde{G}(t) \end{pmatrix} \mathbf{U}^\dagger = \begin{pmatrix} 0 & G^A(t) \\ G^R(t) & G^K(t) \end{pmatrix} \equiv \mathbf{G}^{\mathbf{K}}(t). \quad (\text{A.16})$$

The matrix of **Keldysh rotation** is

$$U = \frac{1}{\sqrt{2}} \begin{pmatrix} 1 & -1 \\ 1 & 1 \end{pmatrix}. \quad (\text{A.17})$$

The retarded, advanced, and Keldysh Green’s function are defined as

$$G_{ij}^R(t) = -i\Theta(t)\langle [c_i(t), c_j^\dagger(0)]_+ \rangle, \quad (\text{A.18})$$

$$G_{ij}^A(t) = i\Theta(-t)\langle [c_i(t), c_j^\dagger(0)]_+ \rangle, \quad (\text{A.19})$$

$$G_{ij}^K(t) = -i\langle [c_i(t), c_j^\dagger(0)] \rangle, \quad (\text{A.20})$$

The same Keldysh rotation in Eq. A.16 can be made to two-particles quantities,

$$\mathbf{\Pi}^{\mathbf{K}} = (U \otimes U^*) \mathbf{\Pi} (U \otimes U^*)^\dagger, \quad (\text{A.21})$$

$$\mathbf{\Gamma}^{\mathbf{K}(i,f)} = (U \otimes U^*) \mathbf{\Gamma}^{(i,f)} (U \otimes U^*)^\dagger. \quad (\text{A.22})$$

In the equilibrium state, the real-time single-particle Green’s functions satisfy the fluctuation-dissipation theorem,

$$G^K(\omega) = (G^R(\omega) - G^A(\omega)) \tanh \frac{\omega}{2k_B T}. \quad (\text{A.23})$$

Therefore, in equilibrium, 4 types of quadratic product of real-time Green’s functions should appear in the ladder expansion and Bethe-Salpeter equation, which are

$$g_{1234}^{(1)}(\epsilon, \omega) = G_{23}^R(\omega + \epsilon) G_{41}^R(\epsilon), \quad (\text{A.24})$$

$$g_{1234}^{(2)}(\epsilon, \omega) = G_{23}^R(\omega + \epsilon) G_{41}^A(\epsilon), \quad (\text{A.25})$$

$$g_{1234}^{(3)}(\epsilon, \omega) = G_{23}^A(\omega + \epsilon) G_{41}^A(\epsilon), \quad (\text{A.26})$$

$$g_{1234}^{(4)}(\epsilon, \omega) = G_{23}^A(\omega + \epsilon) G_{41}^R(\epsilon). \quad (\text{A.27})$$

(The convention of indices follow Eq. A.2.)

As indicated by Eq. A.7, the retarded correlation in real-time $\Pi_{1234}(t)$ can be written as a combination of 4 matrix elements of the contour-ordered correlation function $\mathbf{\Pi}_{1234}$. Thus we can substitute the ladder expansion of each element from the matrix version of ladder expansion for the **contour-ordered** correlation function in Eq. A.8 into Eq. A.7.

However, it will not be an obvious consequence in this Keldysh formalism that the **retarded** two-particle correlation function would also have a series of ladder expansion, and the corresponding vertex functions would satisfy the Bethe-Salpeter equation, although it is true in the imaginary-time formalism. In the following I will attempt to write down the Bethe-Salpeter equation in the Keldysh formalism since it would certainly provide great convenience for computing the vertex correction of two-particle correlation functions.

Let me start with the leading (zeroth-order) term with no vertex correction. The Wick's theorem on the closed-contour leads Eq. A.7 to

$$\begin{aligned}
 \Pi_{1234}^{R,0}(t) &= \begin{array}{c} 2 \longrightarrow 3 \\ 1 \longleftarrow 4 \end{array} \\
 &= \left(\frac{-i}{2} \right) \left[G_{41}(-t)G_{23}(t) - G_{41}^>(-t)G_{23}^<(t) + G_{41}^<(-t)G_{23}^>(t) - \tilde{G}_{41}(-t)\tilde{G}_{23}^<(t) \right].
 \end{aligned} \tag{A.28}$$

The upper index '0' in $\Pi_{1234}^{R,0}(t)$ indicates that it is the zeroth order in interaction vertex.

The Keldysh rotation simplifies the expression,

$$\Pi_{1234}^{R,0}(t) = -\frac{i}{2} (G_{23}^K(t)G_{41}^A(-t) + G_{23}^R(t)G_{41}^K(-t)). \tag{A.29}$$

In real frequency, it turns out to be

$$\begin{aligned}
 \Pi_{1234}^{R,0}(\omega) &= \int_{-\infty}^{\infty} dt \exp(i\omega t) \Pi^R(t) \\
 &= -\frac{i}{2} \int d\omega' (G_{23}^K(\omega + \omega')G_{41}^A(\omega') + G_{23}^R(\omega + \omega')G_{41}^K(\omega')). \tag{A.30}
 \end{aligned}$$

In the equilibrium state, the fluctuation-dissipation theorem (Eq. A.23) applies. $\Pi_{1234}^{R,0}(\omega)$

turns into

$$\begin{aligned} \Pi^{R,0}(\omega) = & -\frac{i}{2} \int_{-\infty}^{\infty} d\epsilon \left[\left(\tanh \frac{\epsilon}{2k_B T} \right) g_{1234}^{(1)}(\epsilon, \omega) + \left(\tanh \frac{\omega + \epsilon}{2k_B T} - \tanh \frac{\epsilon}{2k_B T} \right) \right. \\ & \left. g_{1234}^{(2)}(\epsilon, \omega) + \left(\tanh \frac{\omega + \epsilon}{2k_B T} \right) g_{1234}^{(3)}(\epsilon, \omega) \right], \end{aligned} \quad (\text{A.31})$$

Notice that the term $g_{1234}^{(4)}(\epsilon, \omega) = G_{23}^A(\omega + \epsilon)G_{41}^R(\epsilon)$ does **not** appear in the zeroth-order term.

Introducing the full ladder expansion in Eq. A.8 and Eq. A.9 into $\Pi^R(t)$, and separating terms involving only $g^{(1)}$, $g^{(2)}$, and $g^{(3)}$ from those also involving $g^{(4)}$, $\Pi^R(\omega) = \int dt e^{i\omega t} \Pi(t)$ has the following expression,

$$\begin{aligned} \Pi^R(\omega) = & \int d\epsilon_1 \mathbf{Tanh}(\epsilon_1, \omega) \left[\mathbf{g}(\epsilon_1, \omega) + \mathbf{g}(\epsilon_1, \omega) \int d\epsilon_2 \mathcal{T}^f(\epsilon_1, \epsilon_2; \omega) \mathbf{g}(\epsilon_2, \omega) \right] \\ & + (g^{(4)}\text{-terms}), \end{aligned} \quad (\text{A.32})$$

with

$$\mathbf{Tanh}(\epsilon, \omega) = \begin{pmatrix} \tanh \frac{\epsilon}{2k_B T} & 0 & 0 \\ 0 & \tanh \frac{\epsilon + \omega}{2k_B T} - \tanh \frac{\epsilon}{2k_B T} & 0 \\ 0 & 0 & -\tanh \frac{\epsilon + \omega}{2k_B T} \end{pmatrix}, \quad (\text{A.33})$$

and

$$\mathbf{g}(\epsilon, \omega) = \begin{pmatrix} g^{(1)}(\epsilon, \omega) & 0 & 0 \\ 0 & g^{(2)}(\epsilon, \omega) & 0 \\ 0 & 0 & g^{(3)}(\epsilon, \omega) \end{pmatrix}. \quad (\text{A.34})$$

$\mathcal{T}^f(\epsilon_1, \epsilon_2; \omega)$ is a 3×3 matrix of **full** vertex functions which satisfy the Bethe-Salpeter equation,

$$\begin{aligned} \mathcal{T}^f(\epsilon_1, \epsilon_2; \omega) = & \mathcal{T}^i(\epsilon_1, \epsilon_2; \omega) \\ & + \int d\epsilon' \mathcal{T}^i(\epsilon_1, \epsilon'; \omega) \mathbf{g}(\epsilon', \omega) \mathcal{T}^f(\epsilon', \epsilon_2; \omega). \end{aligned} \quad (\text{A.35})$$

The matrix elements of irreducible vertex functions $\mathcal{T}^{(i)}(\epsilon_1, \epsilon_2; \omega)$ for the **retarded** correlation functions are related to the elements of the **contour-ordered** correlation functions $\mathbf{\Gamma}^{\mathbf{K}^{(i)}}(\epsilon_1, \epsilon_2; \omega)$ in the Keldysh indices. The same expressions also apply to full vertex function $\mathcal{T}^f(\epsilon_1, \epsilon_2; \omega)$ and $\mathbf{\Gamma}^{\mathbf{K}^{(f)}}(\epsilon_1, \epsilon_2; \omega)$, which is as listed below.

In this appendix, I list the expressions of vertex function matrix \mathcal{T} for the retarded two-particle correlation functions in terms of the vertex function matrix $\mathbf{\Gamma}^{\mathbf{K}}$ of the contour-ordered two-particle correlation functions in **Keldysh** indices. \mathcal{T} is a 3×3 matrix and $\mathbf{\Gamma}^{\mathbf{K}}$ is 4×4 matrix.

$$\mathcal{T}_{11}(\epsilon, \epsilon'; \omega) = \mathbf{\Gamma}_{23}^{\mathbf{K}}(\epsilon, \epsilon'; \omega) + \mathbf{\Gamma}_{24}^{\mathbf{K}}(\epsilon, \epsilon'; \omega) \tanh \frac{\epsilon' + \omega}{2k_B T}, \quad (\text{A.36})$$

$$\mathcal{T}_{12}(\epsilon, \epsilon'; \omega) = \left(\tanh \frac{\epsilon'}{2k_B T} - \tanh \frac{\epsilon' + \omega}{2k_B T} \right) \mathbf{\Gamma}_{24}^{\mathbf{K}}(\epsilon, \epsilon'; \omega), \quad (\text{A.37})$$

$$\mathcal{T}_{13}(\epsilon, \epsilon'; \omega) = \mathbf{\Gamma}_{22}^{\mathbf{K}}(\epsilon, \epsilon'; \omega) - \mathbf{\Gamma}_{24}^{\mathbf{K}}(\epsilon, \epsilon'; \omega) \tanh \frac{\epsilon'}{2k_B T}, \quad (\text{A.38})$$

$$\begin{aligned} \mathcal{T}_{21}(\epsilon, \epsilon'; \omega) = & \left(\tanh \frac{\epsilon}{2k_B T} - \tanh \frac{\epsilon + \omega}{2k_B T} \right)^{-1} \\ & \times \left[\mathbf{\Gamma}_{13}^{\mathbf{K}}(\epsilon, \epsilon'; \omega) + \mathbf{\Gamma}_{14}^{\mathbf{K}}(\epsilon, \epsilon'; \omega) \tanh \frac{\epsilon' + \omega}{2k_B T} \right. \\ & + \tanh \frac{\epsilon + \omega}{2k_B T} \left(\mathbf{\Gamma}_{23}^{\mathbf{K}}(\epsilon, \epsilon'; \omega) + \tanh \frac{\epsilon' + \omega}{2k_B T} \mathbf{\Gamma}_{24}^{\mathbf{K}}(\epsilon, \epsilon'; \omega) \right) \\ & \left. + \tanh \frac{\epsilon + \omega}{2k_B T} \left(\mathbf{\Gamma}_{33}^{\mathbf{K}}(\epsilon, \epsilon'; \omega) + \tanh \frac{\epsilon' + \omega}{2k_B T} \mathbf{\Gamma}_{34}^{\mathbf{K}}(\epsilon, \epsilon'; \omega) \right) \right], \quad (\text{A.39}) \end{aligned}$$

$$\begin{aligned} \mathcal{T}_{22}(\epsilon, \epsilon'; \omega) = & \left(\tanh \frac{\epsilon}{2k_B T} - \tanh \frac{\epsilon + \omega}{2k_B T} \right)^{-1} \left(\tanh \frac{\epsilon'}{2k_B T} - \tanh \frac{\epsilon' + \omega}{2k_B T} \right) \\ & \times \left[\mathbf{\Gamma}_{14}^{\mathbf{K}}(\epsilon, \epsilon'; \omega) + \mathbf{\Gamma}_{34}^{\mathbf{K}}(\epsilon, \epsilon'; \omega) \tanh \frac{\epsilon}{2k_B T} - \mathbf{\Gamma}_{24}^{\mathbf{K}}(\epsilon, \epsilon'; \omega) \tanh \frac{\epsilon + \omega}{2k_B T} \right], \quad (\text{A.40}) \end{aligned}$$

$$\begin{aligned} \mathcal{T}_{23}(\epsilon, \epsilon'; \omega) = & \left(\tanh \frac{\epsilon}{2k_B T} - \tanh \frac{\epsilon + \omega}{2k_B T} \right)^{-1} \\ & \times \left[\mathbf{\Gamma}_{12}^{\mathbf{K}}(\epsilon, \epsilon'; \omega) + \mathbf{\Gamma}_{14}^{\mathbf{K}}(\epsilon, \epsilon'; \omega) \tanh \frac{\epsilon'}{2k_B T} \right. \\ & + \tanh \frac{\epsilon + \omega}{2k_B T} \left(-\mathbf{\Gamma}_{22}^{\mathbf{K}}(\epsilon, \epsilon'; \omega) + \tanh \frac{\epsilon'}{2k_B T} \mathbf{\Gamma}_{24}^{\mathbf{K}}(\epsilon, \epsilon'; \omega) \right) \\ & \left. + \tanh \frac{\epsilon}{2k_B T} \left(\mathbf{\Gamma}_{32}^{\mathbf{K}}(\epsilon, \epsilon'; \omega) - \tanh \frac{\epsilon'}{2k_B T} \mathbf{\Gamma}_{34}^{\mathbf{K}}(\epsilon, \epsilon'; \omega) \right) \right], \quad (\text{A.41}) \end{aligned}$$

$$\mathcal{T}_{31}(\epsilon, \epsilon'; \omega) = \mathbf{\Gamma}_{33}^{\mathbf{K}}(\epsilon, \epsilon'; \omega) + \mathbf{\Gamma}_{34}^{\mathbf{K}}(\epsilon, \epsilon'; \omega) \tanh \frac{\epsilon' + \omega}{2k_B T}, \quad (\text{A.42})$$

$$\mathcal{T}_{32}(\epsilon, \epsilon'; \omega) = - \left(\tanh \frac{\epsilon'}{2k_B T} - \tanh \frac{\epsilon' + \omega}{2k_B T} \right) \mathbf{\Gamma}_{34}^{\mathbf{K}}(\epsilon, \epsilon'; \omega), \quad (\text{A.43})$$

$$\mathcal{T}_{33}(\epsilon, \epsilon'; \omega) = \mathbf{\Gamma}_{32}^{\mathbf{K}}(\epsilon, \epsilon'; \omega) - \mathbf{\Gamma}_{34}^{\mathbf{K}}(\epsilon, \epsilon'; \omega) \tanh \frac{\epsilon'}{2k_B T}. \quad (\text{A.44})$$

In fact, starting from the ladder expansion in the imaginary-time formalism, Eliashberg [111] performed analytic continuation from imaginary to real axis, and derived the Eq. A.32 with vanishing g^4 -terms and Eq. A.35.

Appendix B

Analytical Continuation

B.1 Padé Approximant

The Padé approximant is a rational approximation of a function $f(z)$. Given integer m and n , a Padé approximant has the form of [112, 113]

$$R(z) = \frac{r_0 + r_1 z + r_2 z^2 + \cdots + r_m z^m}{1 + t_1 z + t_2 z^2 + \cdots + t_n z^n}. \quad (\text{B.1})$$

The coefficients r_i and t_i are determined by the requirement that $R(z)$ has the same Taylor series of $f(z)$ at $z = 0$ up to the order of $m + n$,

$$\begin{aligned} f(0) &= R(0), \\ f'(0) &= R'(0), \\ &\cdots, \\ f^{(n+m)}(0) &= R^{(n+m)}(0). \end{aligned}$$

Padé approximant often gives excellent approximation of $f(z)$ even where the truncated Taylor series does not converge, which makes Padé approximant a convenient tool for analytic continuation of correlation functions on imaginary axis.

Given the values of correlation function $G(i\omega_n)$ on selected Matsubara frequencies, the coefficients for the Padé approximant of $G(i\omega_n)$ can be found by a fast algorithm which makes use of continuous fraction to represent the approximant [22],

$$R_N(z) = \frac{a_1}{1 + \frac{a_2(z-i\omega_1)}{1 + \frac{a_3(z-i\omega_2)}{1 + \cdots \frac{a_N(z-i\omega_{N-1})}{1}}}}. \quad (\text{B.2})$$

N points on the imaginary axis are needed to find the coefficients a_1, a_2, \cdots, a_N . There is no unique way of selecting the number N and the set of N points on the

imaginary axis. It is quite reasonable to choose those low frequency points. In some implementation, a subset of high frequency points are also included [114]. Besides, a check of convergence is necessary to assure the reliability of the approximant.

The Padé approximant is determined by

$$R_N(i\omega_n) = G(i\omega_n), \quad n = 1, 2, \dots, N. \quad (\text{B.3})$$

The coefficients a_1, a_2, \dots, a_N in Eq. B.2 are given by the recursive relation,

$$a_i = g_i(i\omega_i), \quad (\text{B.4})$$

$$g_1(i\omega_i) = G(i\omega_i), \quad i = 1, 2, \dots, N, \quad (\text{B.5})$$

$$g_p(z) = \frac{g_{p-1}(i\omega_{p-1}) - g_{p-1}(z)}{(z - i\omega_{p-1})g_{p-1}(z)}, \quad p \geq 2. \quad (\text{B.6})$$

The Padé approximant, Eq. B.1 can be recovered also by recursive relation,

$$R_N(z) = \frac{A_N(z)}{B_N(z)}, \quad (\text{B.7})$$

where

$$A_{n+1}(z) = A_n(z) + (z - i\omega_n)a_{n+1}A_n(z), \quad (\text{B.8})$$

$$B_{n+1}(z) = B_n(z) + (z - i\omega_n)a_{n+1}B_n(z), \quad (\text{B.9})$$

with

$$A_0 = 0, \quad (\text{B.10})$$

$$A_1 = a_1, \quad (\text{B.11})$$

$$B_0 = B_1 = 1. \quad (\text{B.12})$$

B.2 Maximum Entropy Method

A pedagogical discussion of maximum entropy method can be found in Ref. [23]. Here only main steps are summarized.

The maximum entropy method (MaxEnt) seeks to find the most probable solution of the spectral function $A(\omega) = -\frac{1}{\pi}\Im G^R(\omega)$ satisfying

$$G(\tau) = \int_{-\infty}^{\infty} d\omega \frac{A(\omega) \exp(-\tau\omega)}{1 \pm \exp(-\beta\omega)} = \int_{-\infty}^{\infty} d\omega K(\tau, \omega) A(\omega), \quad (\text{B.13})$$

given $G(\tau)$ the time-ordered Green's function in imaginary time, which is usually sampled by quantum Monte Carlo (QMC) methods on a selected set of $\{\tau_i\}$.

The goal of MaxEnt is to maximize the conditional probability of $A(\omega)$ given $G(\tau)$, written as $P(A|G)$. By Bayes theorem,

$$P(A, G) = P(A)P(A|G) = P(G)P(G|A), \quad (\text{B.14})$$

where $P(A, G)$ is the joint probability of A and G . Therefore

$$P(A|G) = \frac{P(G|A)P(A)}{P(G)}. \quad (\text{B.15})$$

$P(G|A)$ is also known as the “likelihood” function, and $P(A)$ is known as the prior probability. We consider only one specific set of data of $G(\tau_i)$ given by a converged QMC run, thus $P(G)$ is a constant.

The prior probability is determined by the entropy S of $A(\omega)$, $P(A) = \exp(\alpha S)$, with

$$S = \int d\omega \left[A(\omega) - m(\omega) - A(\omega) \ln \frac{A(\omega)}{m(\omega)} \right]. \quad (\text{B.16})$$

$m(\omega)$ is the “default” model, usually chosen as a smooth and featureless function. α is a parameter controlling the competition between S and $P(G|A)$. Several ways of setting α is discussed in Ref. [23].

The likelihood function is given by $P(G|A) = \exp(-\chi^2/2)$, where

$$\chi^2 = \sum_i \left(\frac{G(\tau_i) - \sum_l K(\tau_i, \omega_l) A(\omega_l)}{\sigma_i} \right)^2. \quad (\text{B.17})$$

$\{\omega_l\}$ is the set of mesh points on the real axis. Thus the problem of analytic continuation turns into an optimization problem of maximizing $P(A|G) = \exp(\alpha S - \chi^2/2)$ with respect to $A(\omega)$.

B.3 Dynamic Local Spin Susceptibility

This section presents analytic continuation of dynamic local spin susceptibility in a doped Mott insulator. The dynamic susceptibility is from one-band Hubbard model with nearest-neighbor hopping and electron density $n = 0.85$. Coulomb repulsion

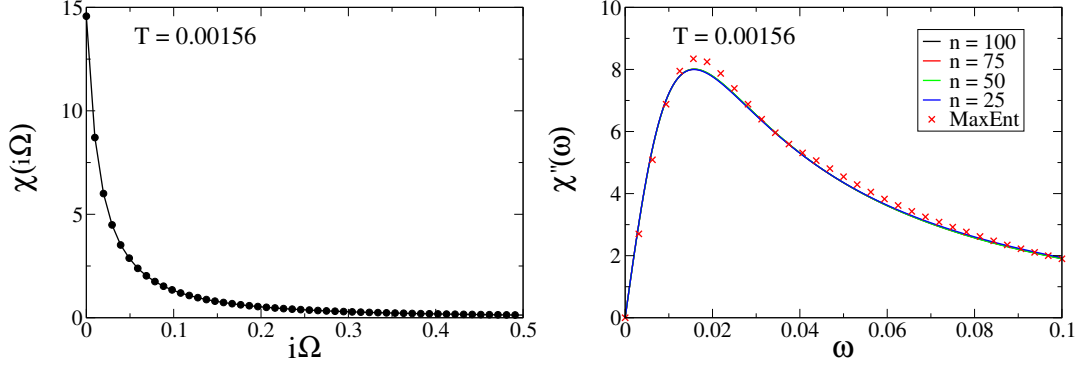


Figure B.1: Dynamic local susceptibility at $T \simeq 0.00156$. Left: $\chi_S(i\Omega)$ on imaginary axis. Right: $\Im\chi_S(\omega)$ on real axis, obtained by Padé approximants using values of $\chi_S(i\Omega)$ of different number on Matsubara frequencies, and obtained by the MaxEnt method (red cross).

$U = 1.75W$, where W is the full width of the bare band and is used at energy and temperature unit. The physics of this model is thoroughly discussed in Ch. 2. Here it is used as an illustrating example of Padé approximants and MaxEnt as methods of analytic continuation. The model is solved by dynamical mean field theory with continuous time quantum Monte Carlo (CTQMC) as the impurity solver. The local spin susceptibility, $\chi_S(i\Omega_n)$, sampled by CTQMC is given in Matsubara frequencies. $\chi_S(i\Omega_n)$ has only real part since it is correlation function of spin (bosonic) operators.

Fig. B.1 shows the local spin susceptibility at $T \simeq 0.00156$. On the left $\chi(i\Omega)$ at the Matsubara frequencies is shown. On the right compares Padé approximants and MaxEnt. Padé approximants obtained by values of $\chi(i\Omega)$ on the lowest $n = 25, 50, 75$, and 100 Matsubara points are shown. Evidently, the lines of Padé approximants are on top of each other thus the Padé approximants are robust against the number of input Matsubara points. Furthermore, MaxEnt agrees well with Padé approximants in all aspects, such as the low energy slope and the position and height of the spectral maximum. The information of the slope at $\omega = 0$ and at the spectral maximum are important to find the relaxation time of spin fluctuation.

Fig. B.2 shows $\chi(i\Omega)$ and $\Im\chi(\omega)$ at $T = 0.0075$. The convergence of Padé approximants is still evident. There is visible discrepancy between Padé approximants and MaxEnt in the position of the maximum. But the slope near $\omega = 0$ shows good agreement.

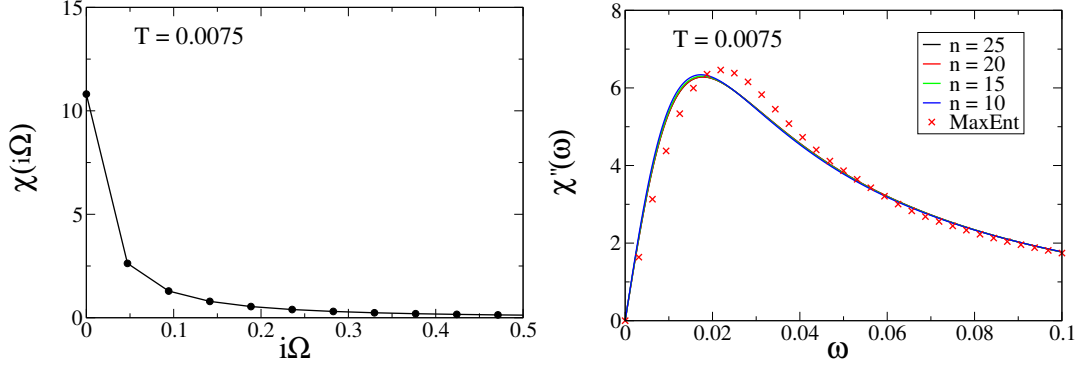


Figure B.2: Dynamic local susceptibility at $T = 0.0075$. Left: $\chi_S(i\Omega)$ on imaginary axis. Right: $\Im\chi_S(\omega)$ on real axis, obtained by Padé approximants and the MaxEnt method.

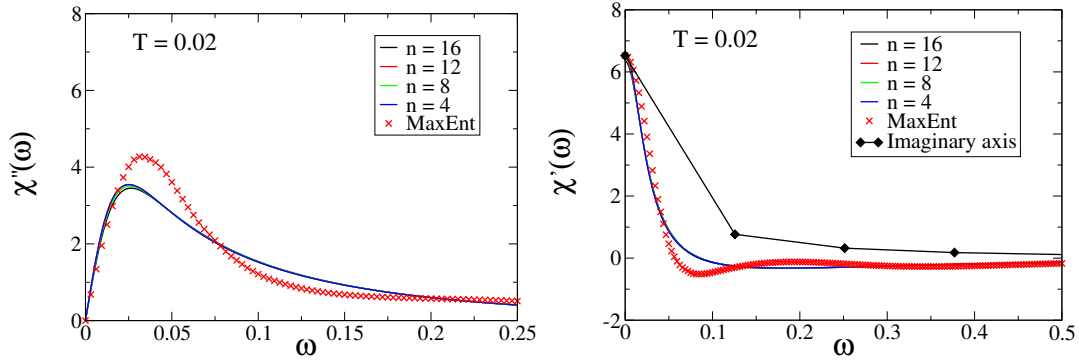


Figure B.3: Dynamic susceptibility at $T = 0.02$. Left: $\Im\chi_S(\omega)$. Right: $\Re\chi_S(\omega)$ and $\chi_S(i\Omega)$.

Fig. B.3 shows the case for $T = 0.02$. On the left shows $\Im\chi(\omega)$ and on the right shows $\Re\chi(\omega)$ and $\chi(i\Omega)$. Clearly, the discrepancy in the distribution of spectral weight of $\Im\chi(\omega)$ between Padé and MaxEnt becomes more evident at higher temperature. Consequently the position and height of the maximum are moderately different. But the slope at $\omega = 0$ given by Padé and MaxEnt are nearly the same. Besides, the asymptotic tail of $\Re\chi(\omega)$, which is determined by the integrated weight of $\Im\chi(\omega)$ ¹, also shows little inconformity.

¹ $\Re\chi(\omega)$ in the asymptotic limit, by the Kronig-Kramers theorem, is

$$\lim_{\omega \rightarrow \infty} \Re\chi(\omega) = \lim_{\omega \rightarrow \infty} \frac{1}{\pi} \int d\omega' \frac{\Im\chi(\omega')}{\omega' - \omega} \simeq -\frac{1}{\pi} \frac{1}{\omega} \int d\omega' \Im\chi(\omega') + O\left(\frac{1}{\omega^2}\right).$$

Appendix C

General Sommerfeld Expansion

This appendix supplements the discussion in Sec. 2.2.

We consider the low temperature behavior of the integral

$$I_n = \int \frac{d\epsilon}{T} \left(\frac{\epsilon}{T} \right)^n \frac{1}{4 \cosh^2(\frac{\epsilon}{2T})} \frac{F(\epsilon)}{G(\epsilon)}. \quad (\text{C.1})$$

I_n evaluates the conductivities when $F(\epsilon)$ and $G(\epsilon)$ are chosen properly. For $F(\epsilon) = \Phi^{*xx}(\epsilon)$ and $G(\epsilon) = \Gamma^*(\epsilon) = (\tau^*(\epsilon))^{-1}$, I_0 gives the longitudinal conductivity σ_{xx}^0 and I_1 gives the thermal counterpart σ_{xx}^1 . For $F(\epsilon) = \Phi^{*yx}(\epsilon)$ and $G(\epsilon) = (\Gamma^*(\epsilon))^2$, I_0 gives transverse conductivity σ_{yx}^0 and I_1 gives σ_{yx}^1 .

At low temperature, $\Phi^{*xx}(\epsilon)$ and $\Phi^{*yx}(\epsilon)$ are regular functions that vary smoothly for $|\epsilon| \lesssim T$. Thus for the purpose of evaluating the intergral, they can be expanded as,

$$\Phi^{*xx}(\epsilon) \simeq \Phi^{*xx}(0) + \Phi^{*xx'}(0)\epsilon, \quad (\text{C.2})$$

$$\Phi^{*yx}(\epsilon) \simeq \Phi^{*yx}(0) + \Phi^{*yx'}(0)\epsilon, \quad (\text{C.3})$$

where $\Phi^{*xx'}(0) = d\Phi^{*xx}(0)/d\epsilon$ and $\Phi^{*yx'}(0) = d\Phi^{*yx}(0)/d\epsilon$.

The quasiparticle scattering rate $\Gamma^*(\epsilon)$ in a Fermi liquid is dominated by the particle-hole symmetric part at low temperature, and has the quadratic form

$$\Gamma^*(\epsilon) \simeq g_0 + g_2 \epsilon^2. \quad (\text{C.4})$$

In a clean system, $g_0 \propto T^2$ and consequently, $\Gamma^*(\epsilon)^{-1}$ becomes a Lorentzian function with vanishing width when $T \rightarrow 0$. Hence $\Gamma^*(\epsilon)^{-1}$ is asymptotically singular for $|\epsilon| \lesssim T$ and the standard Sommerfeld treatment is no longer appropriate [38]. Furthermore, the particle-hole asymmetric part in $\Gamma^*(\epsilon)$ is in particular important for thermoelectric transport. The asymmetric part can be approximated by the linear and cubic order in

ϵ as corrections to the quadratic scattering rate [85]. Thus we write

$$\Gamma^*(\epsilon) \simeq g_0 + g_2\epsilon^2 + g_1\epsilon + g_3\epsilon^3. \quad (\text{C.5})$$

This also leads to the corrections to the Lorentzian form of $\Gamma^*(\epsilon)^{-1}$, which are expressed as

$$\frac{1}{\Gamma^*(\epsilon)} \simeq \frac{1}{g_0 + g_2\epsilon^2} - \frac{g_1\epsilon}{(g_0 + g_2\epsilon^2)^2} - \frac{g_3\epsilon^3}{(g_0 + g_2\epsilon^2)^2}, \quad (\text{C.6})$$

$$\frac{1}{\Gamma^*(\epsilon)^2} \simeq \frac{1}{(g_0 + g_2\epsilon^2)^2} - \frac{2g_1\epsilon}{(g_0 + g_2\epsilon^2)^3} - \frac{2g_3\epsilon^3}{(g_0 + g_2\epsilon^2)^3}. \quad (\text{C.7})$$

By changing the variable $\epsilon = xT$, we define the following integral,

$$E_m^n = \int dx \frac{1}{4 \cosh^2(x/2)} \frac{x^n}{(g_0/T^2 + g_2x^2)^m}, \quad (\text{C.8})$$

and the longitudinal conductivity is estimated by

$$\begin{aligned} \sigma_{xx}^0 \simeq & \frac{1}{T^2} \left(\Phi^{*xx}(0)E_1^0 - g_1\Phi^{*xx'}(0)E_2^2 \right. \\ & \left. - g_3T^2\Phi^{*xx'}(0)E_2^4 \right). \end{aligned} \quad (\text{C.9})$$

The first term is determined by the leading quadratic term in Eq. C.6. The second and third terms are determined by the linear and cubic corrections, i.e., proportional to g_1 and g_3 respectively. Similarly, for other conductivities, we have

$$\begin{aligned} \sigma_{xx}^1 \simeq & \frac{1}{T} \left(\Phi^{*xx'}(0)E_1^2 - \frac{g_1}{T^2}\Phi^{*xx}(0)E_2^2 \right. \\ & \left. - g_3\Phi^{*xx}(0)E_2^4 \right), \end{aligned} \quad (\text{C.10})$$

$$\begin{aligned} \sigma_{yx}^0 \simeq & \frac{1}{T^4} \left(\Phi^{*yx}(0)E_2^0 - 2g_1\Phi^{*yx'}(0)E_3^2 \right. \\ & \left. - 2g_3T^2\Phi^{*yx'}(0)E_3^4 \right), \end{aligned} \quad (\text{C.11})$$

$$\begin{aligned} \sigma_{yx}^1 \simeq & \frac{1}{T^3} \left(\Phi^{*yx'}(0)E_2^2 - \frac{2g_1}{T^2}\Phi^{*yx}(0)E_3^2 \right. \\ & \left. - 2g_3\Phi^{*yx}(0)E_3^4 \right). \end{aligned} \quad (\text{C.12})$$

In each expansion, the second and third term will be simply called the g_1 and g_3 term.

Eq. C.9 — Eq. C.12 define the “general” Sommerfeld expansion in Sec. 2.2.

In general, g_0 , g_1 , g_2 and g_3 vary with temperature, thus E_m^n also depends on T in a non-trivial way. But for a Fermi liquid without impurity scattering, when $T \rightarrow 0$, $(g_0 + g_2\epsilon^2) \propto (\pi^2 T^2 + \epsilon^2)$, hence E_m^n is a constant independent of T . Besides, $g_1 \propto T^2$ as $T \rightarrow 0$ [85]. Then we can obtain the low-temperature leading terms of conductivities. σ_{xx}^0 and σ_{yx}^0 are dominated respectively by the T^{-2} and T^{-4} divergence in the first term. The prefactors are determined by the QP band structure ($\Phi^{*xx}(0)$ and $\Phi^{*yx}(0)$). For the thermoelectric transport, all three terms lead to the same power law (T^{-1} for σ_{xx}^1 and T^{-3} for σ_{yx}^1), and the prefactors are determined by the asymmetry of QP band structure ($\Phi^{*xx'}(0)$ and $\Phi^{*yx'}(0)$) and the scattering rate (g_1 and g_3).

The Sommerfeld expansion is equivalent to neglecting the $g_2\epsilon^2$ term in the expansion of scattering rate in Eq. C.6 and Eq. C.7. Above T_{FL} , g_2 is small, and the Sommerfeld expansion can give quantitative estimation that correctly captures the variation of conductivities with temperature. The Mott relations for thermoelectric transport, i.e.,

$$I_0 \simeq \frac{F(0)}{G(0)} \quad \text{and} \quad I_1 \simeq \frac{\pi^2}{3} T \frac{d}{d\epsilon} \left(\frac{F(0)}{G(0)} \right), \quad (\text{C.13})$$

are based on the Sommerfeld expansion [49, 50], thus they still provide convenient rules for estimating the Seebeck and Nernst coefficient when $T_{FL} < T < T_{sat}/2$. Below T_{FL} , the $g_2\epsilon^2$ term will lead to different prefactors (Eq. C.8), but the Fermi liquid power law at low temperature is not changed.

We compute conductivities for $T \lesssim T_{sat}/2$ using Eq. C.1 (“QP approx.”) and using the general Sommerfeld expansion of Eq. C.9 — Eq. C.12. The results are compared in Fig. C.1. The agreement between the two sets of data is evident. Therefore Eq. C.9 — Eq. C.12 provide a convenient way to decompose the transport properties. In our calculation, σ_{xx}^0 is dominated by the first term of the expansion. Hence the resistivity is determined by $\Phi^{*xx}(0)$ and the quasiparticle scattering rate at the Fermi level ($\Gamma^*(0)$ is equivalent to $\Gamma_{\mathbf{k}_F}$ defined in the main text.). Similar observation can be drawn for σ_{yx}^0 . In σ_{xx}^1 , the g_3 term is negligible but the first and the g_1 term have opposite signs and both change sign below $T_{sat}/2$. This is due to the different temperature dependence of the asymmetry of the quasiparticle band structure and the scattering rate and they together determine σ_{xx}^1 and thermopower. σ_{yx}^1 is dominated by the first term because

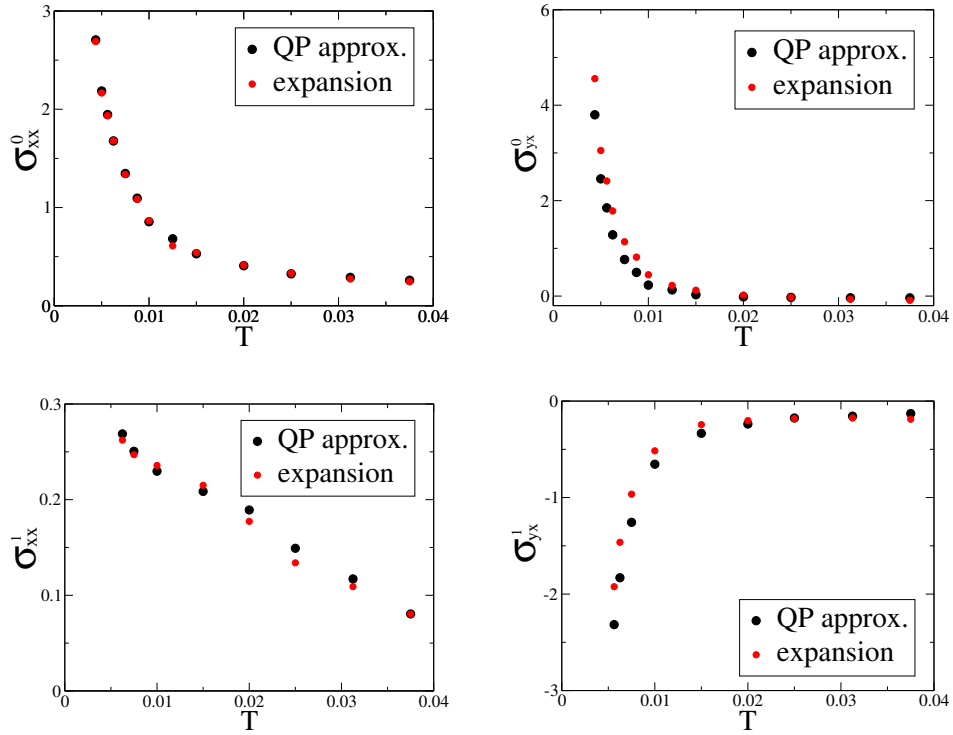


Figure C.1: Conductivities computed using Eq. C.1 (“QP approx.”) and using the general Sommerfeld expansion of Eq. C.9 — C.12 (“expansion”).

$\Phi^{*yx'}(0)$ is close to its singularity at half-filling.

Appendix D

Linear Response Theory of Thermo- and Magneto-electric Transport

D.1 Thermal Transport

For charge transport, the perturbation due to the electric field can be formally written as the coupling between charge (particle) density and scalar potential,

$$H' = e \int d^3r n(\mathbf{r}) \phi(\mathbf{r}), \quad (\text{D.1})$$

the electrical conductivity in terms of current-current correlation functions. However, it is difficult to write a quantum-mechanical operator which can describe the coupling between thermal current and external thermal gradient.

To derive the thermal response functions, Luttinger [82] suggested a formalism based on a fictitious “gravitational” field $\psi(\mathbf{r})$ coupled to the heat “mass” density operator $m(\mathbf{r})$ of the grand canonical ensemble, $K(\mathbf{r}) = H(\mathbf{r}) - \mu(\mathbf{r})n(\mathbf{r}) = m(\mathbf{r})c^2$. Recently, Shastry argued that this formalism can be extended a time dependent field $\psi(\mathbf{r}, t)$ to derive the dynamical thermal response functions [80]. In this appendix, I briefly introduce this argument.

Phenomenologically, the linear response equations in the presence of electrical field, temperature gradient, and the fictitious field are

$$J_x = L_{11}E_x + L_{12}(-\nabla_x T/T) + \hat{L}_{12}(-\nabla_x \psi(\mathbf{r}, t)), \quad (\text{D.2})$$

$$J_x^Q = L_{21}E_x + L_{22}(-\nabla_x T/T) + \hat{L}_{12}(-\nabla_x \psi(\mathbf{r}, t)). \quad (\text{D.3})$$

It is convenient to consider only the x -component and a single Fourier component, q_x and ω .

$$J_x(q_x, \omega) = L_{11}(q_x, \omega)(iq_x)\phi_q + (iq_x) \left[L_{12}(iq_x, \omega) \frac{\delta T_q}{T} + \hat{L}_{12}(q_x, \omega) \psi_q \right]. \quad (\text{D.4})$$

The main conclusion in Luttinger and Shastry's argument is that

$$L_{ij}(q_x, \omega) = \hat{L}_{ij}(q_x, \omega). \quad (\text{D.5})$$

Then to calculate the transport coefficient $L_{12}(q_x, \omega)$ and $L_{22}(q_x, \omega)$, we only need to calculate the fictitious counterpart $\hat{L}_{12}(q_x, \omega)$ and $\hat{L}_{22}(q_x, \omega)$, for which the quantum-mechanical coupling operator is

$$H'_{thermal} = \int d^3r K(\mathbf{r}) \psi(\mathbf{r}), \quad (\text{D.6})$$

analogous to the coupling between charge and electric field in Eq. D.1.

Notice that H'_{charge} in Eq. D.1 is equivalent to the coupling between current density and vector potential. To see this point, we use the equation of continuity, $\partial n / \partial t = \nabla \cdot \mathbf{j}$. The ω -component in the frequency domain gives

$$n_\omega = \frac{-1}{i\omega} \nabla \cdot \mathbf{j}. \quad (\text{D.7})$$

Hence

$$\begin{aligned} H'_{charge} &= e \int d^3r n(\mathbf{r}) \phi(\mathbf{r}) = \frac{-e}{i\omega} \int d^3r (\nabla \cdot \mathbf{j}) \phi(\mathbf{r}) \\ &= \frac{1}{i\omega} \int d^3r \mathbf{j}_e \cdot \nabla \phi = \frac{-1}{i\omega} \int d^3r \mathbf{j}_e \cdot \mathbf{E}, \end{aligned} \quad (\text{D.8})$$

where $\mathbf{j}_e = e\mathbf{j}$ is the charge current operator. Similarly, for thermal transport, we can consider the fictitious coupling

$$H'_{thermal} = \int d^3r K(\mathbf{r}) \psi(\mathbf{r}) = \frac{-1}{i\omega} \int d^3r \mathbf{j}_Q \cdot (-\nabla \psi(\mathbf{r})), \quad (\text{D.9})$$

where \mathbf{j}_Q is the heat current operator, satisfying the equation of continuity,

$$\frac{\partial K(\mathbf{r})}{\partial t} = \nabla \cdot \mathbf{j}_Q. \quad (\text{D.10})$$

The transport coefficient due to the electric field and the fictitious field are given by

$$\begin{aligned} \hat{L}_{12}(\mathbf{q}, \omega) &= \hat{L}_{21}(\mathbf{q}, \omega) \\ &= \frac{1}{\omega V} \int_{-\infty}^{\infty} \exp(i\omega t) \Theta(t) \langle [j_e^\dagger(\mathbf{q}, t), j_Q(\mathbf{q}, 0)] \rangle, \end{aligned} \quad (\text{D.11})$$

$$\hat{L}_{22}(\mathbf{q}, \omega) = \frac{1}{\omega V} \int_{-\infty}^{\infty} \exp(i\omega t) \Theta(t) \langle [j_Q^\dagger(\mathbf{q}, t), j_Q(\mathbf{q}, 0)] \rangle, \quad (\text{D.12})$$

which also gives the physical transport coefficients $L_{ij}(q_x, \omega)$ by Eq. D.5.

As pointed out by Luttinger [82], the relation of $L_{ij}(\mathbf{q}, \omega) = \hat{L}_{ij}(\mathbf{q}, \omega)$ is true only in the case of **slow** or **thermodynamic** limit, that is, first taking $\omega \rightarrow 0$ then $q_x \rightarrow 0$.

Nevertheless, following a somewhat different argument based on irreversible process, we can write down the perturbation operator due to a thermal current, and show that Eq. D.11 and Eq. D.12 are valid for the transport limit, or the fast limit, which take $\mathbf{q} \rightarrow 0$ first and then $\omega \rightarrow 0$. Details of this argument is presented in Mahan's textbook [19].

Consider a perturbation $H' = e^{i\eta t} F$. $\eta = 0^+$ thus $e^{i\eta t}$ adiabatically switches on the perturbation. F is time independent and is the consequence of an external generalized force \mathbf{X} driving a steady current \mathbf{J} . The transport coefficient is defined by $\mathbf{J}_i = \sum_j \mathbf{Z}_{ij} \cdot \mathbf{X}_j$. i and j are indices for generalize force instead of direction. Apparently there is no unique way to define \mathbf{X} and \mathbf{Z} . For example, we can use either $-\nabla T$ or $\nabla(1/T)$ as the driving force of heat current, and the factor of $1/T^2$ can be absorbed by \mathbf{X} . The transport process is an irreversible process where there is a net generation of entropy. If we require the rate of change of entropy be expressed as

$$\frac{\partial s}{\partial t} = \sum_i \mathbf{J}_i \cdot \mathbf{X}_i, \quad (\text{D.13})$$

then the Onsager relation will be satisfied, $\mathbf{Z}_{ij} = \mathbf{Z}_{ji}$ and the ambiguity in definition of generalized form will be eliminated.

Following similar steps of Eq. 1.4 to Eq. 1.10 in Ch. 1, we can compute the correction to the density matrix due to the perturbation F and the current is

$$\mathbf{J}_i = - \int_0^\infty dt \exp(-\eta t) \int_0^\beta d\beta' Tr \left[\rho_0 \frac{\partial F(-t - i\beta')}{\partial t} \mathbf{j}_i \right]. \quad (\text{D.14})$$

ρ_0 is the density matrix in equilibrium, $F(t) = \exp(iHt) F \exp(-iHt)$ is the Heisenberg picture of F .

$\partial F / \partial t$ can be understood as the rate of change of the energy, as dissipated by the transport process, thus

$$\frac{\partial F}{\partial t} = \frac{dQ}{dt} = T \frac{\partial s}{\partial t} = T \sum_i \mathbf{j}_i \cdot \mathbf{X}_i. \quad (\text{D.15})$$

Combining Eq. D.14 and Eq. D.15, we have the transport coefficient

$$\mathbf{Z}_{ik} = -\frac{1}{\beta} - \int_0^\infty dt \exp(-\eta t) \int_0^\beta d\beta' \text{Tr} [\rho_0 \mathbf{j}_k(-t - i\beta') \mathbf{j}_i]. \quad (\text{D.16})$$

Using Lehmann representation, it is straightforward to show that Eq. D.16, up to a factor a T , is identical to Eq. D.11 and Eq. D.12 in the transport limit.

D.2 Hall Conductivity in a Weak Magnetic Field

This section discusses the conductivity tensor in the presence of a weak magnetic field.

In general, the conductivity tensor is expressed as correlation functions of current operators. In Matsubara frequencies, it is written as

$$\sigma_{\mathbf{q}}^{\alpha\beta}(i\Omega_n) = -\frac{1}{\Omega_n} \int_0^\beta d\tau e^{i\Omega_n \tau} \langle T J_{\mathbf{q}}^\alpha(\tau) J_{\mathbf{0}}^\beta(0) \rangle_B. \quad (\text{D.17})$$

$J_{\mathbf{q}}^\alpha$ is the α -component of current operator in the presence of magnetic field B . $\langle \dots \rangle_B$ is grand canonical ensemble average in the magnetic field. $\sigma_{\mathbf{q}}^{\alpha\beta}(\omega)$ can be expanded in orders of B when the magnetic field is weak. To do this expansion, first we need to expand the current operator and the Hamiltonian.

A general tight-binding model is written as,

$$H = \sum_{\langle ij \rangle} t_{ij} c_{i\sigma}^\dagger c_{j\sigma} + H_I \quad (\text{D.18})$$

H_I is the interaction term. The magnetic field is introduced by the vector potential $\mathbf{A}(\mathbf{r})$ and replacing t_{ij} in the kinetic (hopping) term with

$$t_{ij} \rightarrow t_{ij} \exp \left(\frac{ie}{\hbar} \int_i^j \mathbf{A}(\mathbf{r}) \cdot d\mathbf{r} \right). \quad (\text{D.19})$$

This is the Peierls substitution. The form of the interaction term is not affected by the vector potential. The current operator is given by the functional derivative of H ,

$$J^\alpha = \frac{\delta H}{\delta A^\alpha}. \quad (\text{D.20})$$

Therefore, expanding H in orders of \mathbf{A} also gives rise to expansion of the current operator in \mathbf{A} .

The hopping term is expanded as

$$H_t \simeq \sum_{\langle ij \rangle} t_{ij} \sum_n \frac{1}{n!} \left(\frac{ie}{\hbar} \right)^n (\mathbf{A}(\mathbf{R}_{ij}) \cdot \mathbf{r}_{ij})^n, \quad (\text{D.21})$$

where $\mathbf{R}_{ij} = (\mathbf{r}_i + \mathbf{r}_j)/2$ and $\mathbf{r}_{ij} = \mathbf{r}_j - \mathbf{r}_i$. The Fourier transforms for c_i and $\mathbf{A}(\mathbf{R}_{ij})$ are given by

$$c_i = \frac{1}{\sqrt{N}} \sum_{\mathbf{p}} \exp(i\mathbf{p} \cdot \mathbf{r}_i) c_{\mathbf{p}}, \quad (\text{D.22})$$

$$\mathbf{A}(\mathbf{R}_{ij}) = \sum_{\mathbf{q}} \exp(i\mathbf{q} \cdot \mathbf{R}_{ij}) \mathbf{A}_{\mathbf{q}}. \quad (\text{D.23})$$

This leads to

$$\frac{1}{n!} \left(\frac{ie}{\hbar} \right)^n \sum_{\langle ij \rangle} (\mathbf{A}(\mathbf{R}_{ij}) \cdot \mathbf{r}_{ij})^n = \frac{1}{n!} \left(\frac{e}{\hbar} \right)^n \sum_{\mathbf{p}, \mathbf{q}, \mathbf{q}_\alpha} c_{\mathbf{p}}^\dagger c_{\mathbf{q}} \epsilon_{\mathbf{p}/2 + \mathbf{q}/2}^{\delta_1 \dots \delta_n} (A_{\mathbf{q}_1}^{\delta_1} \dots A_{\mathbf{q}_n}^{\delta_n}). \quad (\text{D.24})$$

$\epsilon_{\mathbf{p}} = \sum_{\langle ij \rangle} t_{ij} \exp(i\mathbf{p} \cdot \mathbf{r}_{ij})$ is the bare dispersion relation. Upper indices in $\epsilon_{\mathbf{p}}^{\delta \dots}$ denote the corresponding derivatives, *i.e.*, $\epsilon_{\mathbf{p}}^\delta = \partial \epsilon_{\mathbf{p}} / \partial p_\delta$. The momenta in the summation satisfy the conservation law, $\mathbf{p} + \mathbf{q} + \sum_\alpha \mathbf{q}_\alpha = 0$.

To compute the first-order correction of the current operator, the Hamiltonian has to be expanded to the second order, which is

$$\begin{aligned} H_t \simeq & \sum_{\mathbf{p}} \epsilon_{\mathbf{p}} c_{\mathbf{p}}^\dagger c_{\mathbf{p}} + \frac{e}{\hbar} \sum_{\mathbf{p}, \mathbf{q}} c_{\mathbf{p}}^\dagger c_{\mathbf{q}} \epsilon_{\mathbf{p}/2 + \mathbf{q}/2}^\delta A_{\mathbf{p}-\mathbf{q}}^\delta \\ & + \frac{1}{2} \left(\frac{e}{\hbar} \right)^2 \sum_{\mathbf{p}, \mathbf{q}, \mathbf{q}_1} c_{\mathbf{p}}^\dagger c_{\mathbf{q}} \epsilon_{\mathbf{p}/2 + \mathbf{q}/2}^{\alpha\beta} A_{\mathbf{q}_1}^\alpha A_{\mathbf{p}-\mathbf{q}-\mathbf{q}_1}^\beta \end{aligned} \quad (\text{D.25})$$

Then the \mathbf{q} -component of current operator given by

$$J_{\mathbf{q}}^\alpha \simeq \frac{e}{\hbar} \sum_{\mathbf{p}} c_{\mathbf{p}-\mathbf{q}}^\dagger c_{\mathbf{p}} \epsilon_{\mathbf{p}-\mathbf{q}/2}^\alpha + \frac{e^2}{\hbar^2} \sum_{\mathbf{p}, \mathbf{q}_1} c_{\mathbf{p}-\mathbf{q}+\mathbf{q}_1}^\dagger c_{\mathbf{p}} \epsilon_{\mathbf{p}-\mathbf{q}/2 + \mathbf{q}_1/2}^{\alpha\beta} A_{\mathbf{q}_1}^\beta \quad (\text{D.26})$$

We define

$$\begin{aligned} \Pi_{\mathbf{q}}^{\alpha\beta}(i\Omega_n) & \equiv \int_0^\beta \exp(i\Omega_n \tau) \langle T J_{\mathbf{q}}^\alpha(\tau) J_{\mathbf{0}}^\beta(0) \rangle_H \\ & = \int_0^\beta d\tau \exp(i\Omega_n \tau) \frac{\int D[\bar{c}c] e^{-S_B} J_{\mathbf{q}}^\alpha(\tau) J_{\mathbf{0}}^\beta(0)}{\int D[\bar{c}c] e^{-S_B}}, \end{aligned} \quad (\text{D.27})$$

then $\sigma_{\mathbf{q}}^{\alpha\beta}(i\Omega_n) = -\frac{1}{\Omega_n} \Pi_{\mathbf{q}}^{\alpha\beta}(i\Omega_n)$. The action in the magnetic field B $S_B = S_0 + S_1$. S_0 is the action without the magnetic field and S_1 is the first order correction in B ,

$$S_1 = \int_0^\beta d\tau \frac{e}{\hbar} \sum_{\mathbf{p}, \mathbf{q}} c_{\mathbf{p}+\mathbf{q}}^\dagger(\tau) c_{\mathbf{p}}(\tau) \epsilon_{\mathbf{p}+\mathbf{q}/2}^\alpha A_{\mathbf{q}}^\alpha. \quad (\text{D.28})$$

We summarize the leading (zeroth) and first-order correction to current operator $J_{\mathbf{q}}^{\alpha}(\tau)$ and $J_{\mathbf{0}}^{\beta}$,

$$J_{\mathbf{q}}^{0\alpha}(\tau) = \frac{e}{\hbar} \sum_{\mathbf{p}} c_{\mathbf{p}-\mathbf{q}}^{\dagger}(\tau) c_{\mathbf{p}}(\tau) \epsilon_{\mathbf{p}-\mathbf{q}/2}^{\alpha}, \quad (\text{D.29})$$

$$J_{\mathbf{q}}^{1\alpha}(\tau) = \frac{e^2}{\hbar^2} \sum_{\mathbf{p}, \mathbf{q}_1} c_{\mathbf{p}-\mathbf{q}-\mathbf{q}_1}^{\dagger}(\tau) c_{\mathbf{p}}(\tau) \epsilon_{\mathbf{p}-\mathbf{q}/2-\mathbf{q}_1/2}^{\alpha\gamma} A_{-\mathbf{q}_1}^{\gamma}, \quad (\text{D.30})$$

$$J_{\mathbf{0}}^{0\beta} = \frac{e}{\hbar} \sum_{\mathbf{p}} c_{\mathbf{p}}^{\dagger} c_{\mathbf{p}} \epsilon_{\mathbf{p}}^{\beta}, \quad (\text{D.31})$$

$$J_{\mathbf{0}}^{1\beta} = \frac{e^2}{\hbar^2} \sum_{\mathbf{p}, \mathbf{q}} c_{\mathbf{p}-\mathbf{q}}^{\dagger} c_{\mathbf{p}} \epsilon_{\mathbf{p}-\mathbf{q}/2}^{\beta\gamma} A_{-\mathbf{q}}^{\gamma}. \quad (\text{D.32})$$

Consequently, $\Pi_{\mathbf{q}}^{\alpha\beta}(i\Omega_n)$ has three terms of the first order of A . For convenience, they are written as

$$\Pi_1 = \int_0^{\beta} \exp(i\Omega_n \tau) \langle T J_{\mathbf{q}}^{1\alpha}(\tau) J_{\mathbf{0}}^{0\beta} \rangle, \quad (\text{D.33})$$

$$\Pi_2 = \int_0^{\beta} \exp(i\Omega_n \tau) \langle T J_{\mathbf{q}}^{0\alpha}(\tau) J_{\mathbf{0}}^{1\beta} \rangle, \quad (\text{D.34})$$

$$\Pi_3 = - \int_0^{\beta} \exp(i\Omega_n \tau) \langle S_1 J_{\mathbf{q}}^{0\alpha}(\tau) J_{\mathbf{0}}^{0\beta} \rangle. \quad (\text{D.35})$$

Note that the thermodynamical average in Eq. D.33 — Eq. D.35 is with respect to the Hamiltonian **without** the magnetic field.

We will be interested in the bubble diagram in the following since within the framework of DMFT, the vertex corrections vanish for transport coefficients in one-band models.

The bubble diagram of Π_1 turns out to be

$$\begin{aligned} \Pi_1 &= \frac{e^3}{\hbar^3} \sum_{\mathbf{p}_1, \mathbf{p}_2, \mathbf{q}_1} \epsilon_{\mathbf{p}_1-\mathbf{q}/2-\mathbf{q}_1/2}^{\alpha\gamma} \epsilon_{\mathbf{p}_2}^{\beta} A_{-\mathbf{q}_1}^{\gamma} \int d\tau \exp(i\Omega_n \tau) \langle c_{\mathbf{p}_1-\mathbf{q}-\mathbf{q}_1}^{\dagger}(\tau) c_{\mathbf{p}_1}(\tau) c_{\mathbf{p}_2}^{\dagger} c_{\mathbf{p}_2} \rangle \\ &= \frac{e^3}{\hbar^3} \sum_{\mathbf{p}} \epsilon_{\mathbf{p}}^{\alpha\gamma} \epsilon_{\mathbf{p}}^{\beta} A_{\mathbf{q}}^{\gamma} \int d\tau \exp(i\Omega_n \tau) \langle c_{\mathbf{p}}^{\dagger}(\tau) c_{\mathbf{p}}(\tau) c_{\mathbf{p}}^{\dagger} c_{\mathbf{p}} \rangle \\ &= -\frac{e^3}{\hbar^3} \sum_{\mathbf{p}} \epsilon_{\mathbf{p}}^{\alpha\gamma} \epsilon_{\mathbf{p}}^{\beta} A_{\mathbf{q}}^{\gamma} \frac{1}{\beta} \sum_{i\omega_m} G_{\mathbf{p}}(i\Omega_n + i\omega_m) G_{\mathbf{p}}(i\omega_m) \\ &= 0. \end{aligned} \quad (\text{D.36})$$

The last step uses the fact that by changing $\mathbf{p} \rightarrow -\mathbf{p}$, $\epsilon_{\mathbf{p}}^{\alpha\gamma} \epsilon_{\mathbf{p}}^{\beta}$ changes sign while the

Matsubara summation does not and thus Π_1 is zero. Following similar steps,

$$\begin{aligned}
\Pi_2 &= \frac{e^3}{\hbar^3} \sum_{\mathbf{p}_1, \mathbf{p}_2} \sum_{\mathbf{q}_1} \epsilon_{\mathbf{p}_1 - \mathbf{q}/2}^\alpha \epsilon_{\mathbf{p}_2 - \mathbf{q}_1/2}^{\beta\gamma} A_{-\mathbf{q}_1}^\gamma \int d\tau \exp(i\Omega_n \tau) \langle T c_{\mathbf{p}_1 - \mathbf{q}}^\dagger(\tau) c_{\mathbf{p}_1}(\tau) c_{\mathbf{p}_2 - \mathbf{q}_1}^\dagger c_{\mathbf{p}_2} \rangle \\
&= \frac{e^3}{\hbar^3} \sum_{\mathbf{p}} \epsilon_{\mathbf{p} + \mathbf{q}/2}^\alpha \epsilon_{\mathbf{p} + \mathbf{q}/2}^{\beta\gamma} A_{\mathbf{q}}^\gamma \int d\tau \exp(i\Omega_n \tau) \langle T c_{\mathbf{p}}^\dagger(\tau) c_{\mathbf{p} + \mathbf{q}}(\tau) c_{\mathbf{p} + \mathbf{q}}^\dagger c_{\mathbf{p}} \rangle \\
&= -\frac{e^3}{\hbar^3} \sum_{\mathbf{p}} \epsilon_{\mathbf{p} + \mathbf{q}/2}^\alpha \epsilon_{\mathbf{p} + \mathbf{q}/2}^{\beta\gamma} A_{\mathbf{q}}^\gamma \frac{1}{\beta} \sum_{i\omega_m} G_{\mathbf{p} + \mathbf{q}}(i\Omega_n + i\omega_m) G_{\mathbf{p}}(i\omega_m). \tag{D.37}
\end{aligned}$$

Expanding $\epsilon_{\mathbf{p} + \mathbf{q}/2}$ and $G_{\mathbf{p} + \mathbf{q}}(i\Omega_n)$ to linear order in \mathbf{q} , there are one zeroth order term and three first order terms in Π_2 , written as follows,

$$\begin{aligned}
\Pi_2 &= -\frac{e^3}{\hbar^3} \sum_{\mathbf{p}} \epsilon_{\mathbf{p}}^\alpha \epsilon_{\mathbf{p}}^{\beta\gamma} A_{\mathbf{q}}^\gamma \frac{1}{\beta} \sum_{i\omega_m} G_{\mathbf{p}}(i\Omega_n + i\omega_m) G_{\mathbf{p}}(i\omega_m) \\
&\quad -\frac{e^3}{\hbar^3} \sum_{\mathbf{p}} \epsilon_{\mathbf{p}}^\alpha \epsilon_{\mathbf{p}}^{\beta\gamma} A_{\mathbf{q}}^\gamma \frac{1}{\beta} \sum_{i\omega_m} G_{\mathbf{p}}^2(i\Omega_n + i\omega_m) (q^\delta \epsilon_{\mathbf{p}}^\delta) G_{\mathbf{p}}(i\Omega_n) \\
&\quad -\frac{e^3}{\hbar^3} \sum_{\mathbf{p}} \epsilon_{\mathbf{p}}^{\alpha\delta} \frac{q^\delta}{2} \epsilon_{\mathbf{p}}^{\beta\gamma} A_{\mathbf{q}}^\gamma \frac{1}{\beta} \sum_{i\omega_m} G_{\mathbf{p}}(i\Omega_n + i\omega_m) G_{\mathbf{p}}(i\omega_m) \\
&\quad -\frac{e^3}{\hbar^3} \sum_{\mathbf{p}} \epsilon_{\mathbf{p}}^\alpha \epsilon_{\mathbf{p}}^{\beta\gamma\delta} \frac{q^\delta}{2} A_{\mathbf{q}}^\gamma \frac{1}{\beta} \sum_{i\omega_m} G_{\mathbf{p}}(i\Omega_n + i\omega_m) G_{\mathbf{p}}(i\omega_m) \tag{D.38}
\end{aligned}$$

The leading term is 0, following the same argument that has led to $\Pi_1 = 0$. The fourth term, using integration by parts, can be written as

$$\begin{aligned}
&-\frac{e^3}{\hbar^3} \sum_{\mathbf{p}} \epsilon_{\mathbf{p}}^\alpha \epsilon_{\mathbf{p}}^{\beta\gamma\delta} \frac{q^\delta}{2} A_{\mathbf{q}}^\gamma \frac{1}{\beta} \sum_{i\omega_m} G_{\mathbf{p}}(i\Omega_n + i\omega_m) G_{\mathbf{p}}(i\omega_m) \\
&= \frac{e^3}{\hbar^3} \sum_{\mathbf{p}} \epsilon_{\mathbf{p}}^{\alpha\delta} \epsilon_{\mathbf{p}}^{\beta\gamma} \frac{q^\delta}{2} A_{\mathbf{q}}^\gamma \frac{1}{\beta} \sum_{i\omega_m} G_{\mathbf{p}}(i\Omega_n + i\omega_m) G_{\mathbf{p}}(i\omega_m) \\
&\quad + \frac{e^3}{\hbar^3} \sum_{\mathbf{p}} \epsilon_{\mathbf{p}}^\alpha \epsilon_{\mathbf{p}}^{\beta\gamma} \frac{q^\delta}{2} A_{\mathbf{q}}^\gamma \frac{1}{\beta} \sum_{i\omega_m} \frac{\partial}{\partial p^\delta} (G_{\mathbf{p}}(i\Omega_n + i\omega_m) G_{\mathbf{p}}(i\omega_m)), \\
&= \frac{e^3}{\hbar^3} \sum_{\mathbf{p}} \epsilon_{\mathbf{p}}^{\alpha\delta} \epsilon_{\mathbf{p}}^{\beta\gamma} \frac{q^\delta}{2} A_{\mathbf{q}}^\gamma \frac{1}{\beta} \sum_{i\omega_m} G_{\mathbf{p}}(i\Omega_n + i\omega_m) G_{\mathbf{p}}(i\omega_m) \\
&\quad + \frac{e^3}{\hbar^3} \sum_{\mathbf{p}} \epsilon_{\mathbf{p}}^\alpha \epsilon_{\mathbf{p}}^{\beta\gamma} \epsilon_{\mathbf{p}}^\delta \frac{q^\delta}{2} A_{\mathbf{p}}^\gamma \frac{1}{\beta} \sum_{i\omega_m} G_{\mathbf{p}}(i\Omega_n + i\omega_m) G_{\mathbf{p}}^2(i\omega_m) \\
&\quad + \frac{e^3}{\hbar^3} \sum_{\mathbf{p}} \epsilon_{\mathbf{p}}^\alpha \epsilon_{\mathbf{p}}^{\beta\gamma} \epsilon_{\mathbf{p}}^\delta \frac{q^\delta}{2} A_{\mathbf{p}}^\gamma \frac{1}{\beta} \sum_{i\omega_m} G_{\mathbf{p}}(i\omega_m - i\Omega_n) G_{\mathbf{p}}^2(i\omega_m). \tag{D.39}
\end{aligned}$$

Combining Eq. D.39 with the second and third term in Eq. D.38, we have

$$\Pi_2 = \frac{e^3}{\hbar^3} \sum_{\mathbf{p}} \epsilon_{\mathbf{p}}^\alpha \epsilon_{\mathbf{p}}^{\beta\gamma} \epsilon_{\mathbf{p}}^\delta \frac{q^\delta}{2} A_{\mathbf{p}}^\gamma \frac{1}{\beta} \sum_{i\omega_m} G_{\mathbf{p}}^2(i\omega_m) (G_{\mathbf{p}}(i\omega_m + i\Omega_n) - G_{\mathbf{p}}(i\omega_m - i\Omega_n)). \tag{D.40}$$

Now we compute Π_3 .

$$\begin{aligned}
\Pi_3 &= - \int d\tau \exp(i\Omega_n \tau) \langle T S_1 J_{\mathbf{q}}^{0\alpha}(\tau) J_0^{0\beta} \rangle \\
&= - \frac{e^3}{\hbar^3} \sum_{\mathbf{p}_1, \mathbf{p}_2, \mathbf{p}_3} \sum_{\mathbf{q}_1} \epsilon_{\mathbf{p}_1 + \mathbf{q}_1/2}^\gamma A_{\mathbf{q}_1}^\gamma \epsilon_{\mathbf{p}_2 - \mathbf{q}/2}^\alpha \epsilon_{\mathbf{p}_3}^\beta \int \exp(i\Omega_n \tau) d\tau \\
&\quad \times \int d\tau' \langle c_{\mathbf{p}_1 + \mathbf{q}_1}^\dagger(\tau') c_{\mathbf{p}_1}(\tau') c_{\mathbf{p}_2 - \mathbf{q}}^\dagger(\tau) c_{\mathbf{p}_2}(\tau) c_{\mathbf{p}_3}^\dagger c_{\mathbf{p}_3} \rangle \\
&= - \frac{e^3}{\hbar^3} \sum_{\mathbf{p}} \epsilon_{\mathbf{p} + \mathbf{q}/2}^\gamma A_{\mathbf{q}}^\gamma \epsilon_{\mathbf{p} + \mathbf{q}/2}^\alpha \epsilon_{\mathbf{p} + \mathbf{q}}^\beta \int \exp(i\Omega_n \tau) d\tau d\tau' G_{\mathbf{p}}(\tau' - \tau) G_{\mathbf{p} + \mathbf{q}}(\tau) G_{\mathbf{p} + \mathbf{q}}(-\tau') \\
&\quad - \frac{e^3}{\hbar^3} \sum_{\mathbf{p}} \epsilon_{\mathbf{p} + \mathbf{q}/2}^\gamma A_{\mathbf{q}}^\gamma \epsilon_{\mathbf{p} + \mathbf{q}/2}^\alpha \epsilon_{\mathbf{p}}^\beta \int \exp(i\Omega_n \tau) d\tau d\tau' G_{\mathbf{p} + \mathbf{q}}(\tau - \tau') G_{\mathbf{p}}(\tau') G_{\mathbf{p}}(-\tau) \\
&= - \frac{e^3}{\hbar^3} \sum_{\mathbf{p}} \epsilon_{\mathbf{p}}^\alpha \epsilon_{\mathbf{p} + \mathbf{q}/2}^\beta \epsilon_{\mathbf{p}}^\gamma A_{\mathbf{q}}^\gamma \frac{1}{\beta} \sum_{i\omega_m} G_{\mathbf{p} - \mathbf{q}/2}(i\omega_m) G_{\mathbf{p} + \mathbf{q}/2}(i\omega_m) G_{\mathbf{p} + \mathbf{q}/2}(i\omega_m + i\Omega_n) \\
&\quad - \frac{e^3}{\hbar^3} \sum_{\mathbf{p}} \epsilon_{\mathbf{p}}^\alpha \epsilon_{\mathbf{p} - \mathbf{q}/2}^\beta \epsilon_{\mathbf{p}}^\gamma A_{\mathbf{q}}^\gamma \frac{1}{\beta} \sum_{i\omega_m} G_{\mathbf{p} + \mathbf{q}/2}(i\omega_m) G_{\mathbf{p} - \mathbf{q}/2}(i\omega_m) G_{\mathbf{p} - \mathbf{q}/2}(i\omega_m - i\Omega_n).
\end{aligned} \tag{D.41}$$

The zeroth order in \mathbf{q} is zero. There will be four terms in the first order of \mathbf{q} . Two are from derivative of $\epsilon_{\mathbf{p} \pm \mathbf{q}/2}^\beta$ and the other two are from derivative of $G_{\mathbf{p} \pm \mathbf{q}/2}(i\omega_m \pm i\Omega_n)$. Thus,

$$\begin{aligned}
\Pi_3 &= - \frac{e^3}{\hbar^3} \sum_{\mathbf{p}} \epsilon_{\mathbf{p}}^\alpha \epsilon_{\mathbf{p}}^{\beta\delta} \epsilon_{\mathbf{p}}^\gamma \frac{q^\delta}{2} A_{\mathbf{q}}^\gamma \frac{1}{\beta} \sum_{i\omega_m} G_{\mathbf{p}}^2(i\omega_m) G_{\mathbf{p}}(i\omega_m + i\Omega_n) \\
&\quad + \frac{e^3}{\hbar^3} \sum_{\mathbf{p}} \epsilon_{\mathbf{p}}^\alpha \epsilon_{\mathbf{p}}^{\beta\delta} \epsilon_{\mathbf{p}}^\gamma \frac{q^\delta}{2} A_{\mathbf{q}}^\gamma \frac{1}{\beta} \sum_{i\omega_m} G_{\mathbf{p}}^2(i\omega_m) G_{\mathbf{p}}(i\omega_m - i\Omega_n) \\
&\quad - \frac{e^3}{\hbar^3} \sum_{\mathbf{p}} \epsilon_{\mathbf{p}}^\alpha \epsilon_{\mathbf{p}}^\beta \epsilon_{\mathbf{p}}^\gamma A_{\mathbf{q}}^\gamma \frac{1}{\beta} \sum_{i\omega_m} G_{\mathbf{p}}^2(i\omega_m) G_{\mathbf{p}}^2(i\omega_m + i\Omega_n) (\epsilon_{\mathbf{p}}^\delta \frac{\mathbf{q}^\delta}{2}) \\
&\quad + \frac{e^3}{\hbar^3} \sum_{\mathbf{p}} \epsilon_{\mathbf{p}}^\alpha \epsilon_{\mathbf{p}}^\beta \epsilon_{\mathbf{p}}^\gamma A_{\mathbf{q}}^\gamma \frac{1}{\beta} \sum_{i\omega_m} G_{\mathbf{p}}^2(i\omega_m) G_{\mathbf{p}}^2(i\omega_m - i\Omega_n) (\epsilon_{\mathbf{p}}^\delta \frac{\mathbf{q}^\delta}{2})
\end{aligned} \tag{D.42}$$

The last two terms sum up to zero, because $\frac{1}{\beta} \sum_{i\omega_m} G_{\mathbf{p}}^2(i\omega_m) G_{\mathbf{p}}^2(i\omega_m + i\Omega_n)$ is an even function of $i\Omega_n$. The first two terms lead to

$$\Pi_3 = - \frac{e^3}{\hbar^3} \sum_{\mathbf{p}} \epsilon_{\mathbf{p}}^\alpha \epsilon_{\mathbf{p}}^{\beta\delta} \epsilon_{\mathbf{p}}^\gamma \frac{q^\delta}{2} A_{\mathbf{q}}^\gamma \frac{1}{\beta} \sum_{i\omega_m} G_{\mathbf{p}}^2(i\omega_m) (G_{\mathbf{p}}(i\omega_m + i\Omega_n) - G_{\mathbf{p}}(i\omega_m - i\Omega_n)). \tag{D.43}$$

Combining Eq. D.40 and Eq. D.43, we have

$$\Pi_{\mathbf{q}}^{\alpha\beta}(i\Omega_n) = \frac{1}{2} \frac{e^3}{\hbar^3} \sum_{\mathbf{p}} \epsilon_{\mathbf{p}}^{\alpha} (\epsilon_{\mathbf{p}}^{\beta\gamma} \epsilon_{\mathbf{p}}^{\delta} - \epsilon_{\mathbf{p}}^{\beta\delta} \epsilon_{\mathbf{p}}^{\gamma}) q^{\delta} A_{\mathbf{q}}^{\gamma} \Pi_{\mathbf{p}}(i\Omega_n). \quad (\text{D.44})$$

$$\Pi_{\mathbf{p}}(i\Omega_n) = \frac{1}{\beta} \sum_{i\omega_m} G_{\mathbf{p}}^2(i\omega_m) G_{\mathbf{p}}(i\omega_m + i\Omega_n). \quad (\text{D.45})$$

Exchanging indices $\gamma \leftrightarrow \delta$ in the second term leads to

$$\Pi_{\mathbf{q}}^{\alpha\beta}(i\Omega_n) = \frac{1}{2} \frac{e^3}{\hbar^3} \sum_{\mathbf{p}} \epsilon_{\mathbf{p}}^{\alpha} \epsilon_{\mathbf{p}}^{\beta\gamma} \epsilon_{\mathbf{p}}^{\delta} (q^{\delta} A_{\mathbf{q}}^{\gamma} - q^{\gamma} A_{\mathbf{q}}^{\delta}) \Pi_{\mathbf{p}}(i\Omega_n). \quad (\text{D.46})$$

Remind that $\mathbf{B}(\mathbf{r}) = \nabla \times \mathbf{A}(\mathbf{r})$. Hence $\mathbf{B}_{\mathbf{q}} = i\mathbf{q} \times \mathbf{A}_{\mathbf{q}}$. In the long wavelength limit, we have for transverse conductivity ($\alpha = y, \beta = x$),

$$\sigma_{\mathbf{0}}^{1yx}(i\Omega_n) = B_z \frac{1}{2} \frac{e^3}{\hbar^3} \sum_{\mathbf{p}} \epsilon_{\mathbf{p}}^y (\epsilon_{\mathbf{p}}^{xy} \epsilon_{\mathbf{p}}^x - \epsilon_{\mathbf{p}}^{xx} \epsilon_{\mathbf{p}}^y) \left[\frac{1}{-i\Omega_n} \Pi_{\mathbf{p}}(i\Omega_n) \right]. \quad (\text{D.47})$$

The first order correction to longitudinal conductivity ($\alpha = x, \beta = x$) is

$$\sigma_{\mathbf{0}}^{1xx}(i\Omega_n) = B_z \frac{1}{2} \frac{e^3}{\hbar^3} \sum_{\mathbf{p}} \epsilon_{\mathbf{p}}^x (\epsilon_{\mathbf{p}}^{xy} \epsilon_{\mathbf{p}}^x - \epsilon_{\mathbf{p}}^{xx} \epsilon_{\mathbf{p}}^y) \left[\frac{1}{-i\Omega_n} \Pi_{\mathbf{p}}(i\Omega_n) \right]. \quad (\text{D.48})$$

It is easy to see that $\sigma_{\mathbf{0}}^{1xx}(i\Omega_n) = 0$ because of the symmetry of $\epsilon_{\mathbf{p}}$ in $\mathbf{p} \leftrightarrow -\mathbf{p}$. Therefore the leading non-vanishing correction to longitudinal conductivity is at least in the second order of \mathbf{B} .

The analytic continuation to real frequencies is straightforward for bubble terms, which involves only single-particle Green's functions. The procedure is standard: first directly perform the Matsubara summation in the expression of $\Pi_{\mathbf{p}}(i\Omega_n)$, and then replace $i\Omega_n \rightarrow \Omega + i0^+$. We will use the spectral representation of Green's function,

$$G_{\mathbf{p}}(z) = \int d\omega \frac{A_{\mathbf{p}}(\omega)}{z - \omega}. \quad (\text{D.49})$$

z is a complex number. $A_{\mathbf{p}}(\omega) = -\frac{1}{\pi} \Im G_{\mathbf{p}}(\omega)$ is the spectral function. Also we will use Kramer-Kronig relation frequently, which is written as,

$$\chi_1(\omega) = \frac{1}{\pi} \int_{-\infty}^{\infty} d\omega' \frac{\chi_2(\omega')}{\omega' - \omega}, \quad (\text{D.50})$$

$$\chi_2(\omega) = -\frac{1}{\pi} \int_{-\infty}^{\infty} d\omega' \frac{\chi_1(\omega')}{\omega' - \omega}. \quad (\text{D.51})$$

$\chi_1(\omega)$ and $\chi_2(\omega)$ are respectively the real and imaginary part of a complex function analytic in the upper half plane.

With the spectral representation, the Matsubara summation over $i\omega_m$ in $\Pi_{\mathbf{p}}(i\Omega_n)$ can be easily performed. Straightfowardly we have

$$\begin{aligned}
& \frac{1}{\beta} \sum_{i\omega_m} \frac{1}{i\omega_m + i\Omega_n - \omega_1} \frac{1}{i\omega_m - \omega_2} \frac{1}{i\omega_m - \omega_3} \\
&= \frac{1}{\omega_2 - \omega_3} \frac{1}{\beta} \sum_{i\omega_m} \frac{1}{i\omega_m + i\Omega_n - \omega_1} \left(\frac{1}{i\Omega_n - \omega_2} - \frac{1}{i\Omega_n - \omega_3} \right) \\
&= \frac{1}{\omega_2 - \omega_3} \left[\frac{f(\omega_2) - f(\omega_1)}{i\Omega_n + \omega_2 - \omega_1} - \frac{f(\omega_3) - f(\omega_1)}{i\Omega_n + \omega_3 - \omega_1} \right]. \tag{D.52}
\end{aligned}$$

This leads to

$$\Pi_{\mathbf{p}}(i\Omega_n) = \Pi_1 - \Pi_2, \tag{D.53}$$

$$\begin{aligned}
\Pi_1 &= \int d\omega_1 d\omega_2 d\omega_3 A_{\mathbf{p}}(\omega_1) A_{\mathbf{p}}(\omega_2) A_{\mathbf{p}}(\omega_3) \\
&\quad \times \left[\frac{f(\omega_1)}{\omega_2 - \omega_3} \left(\frac{1}{\omega_1 - i\Omega_n - \omega_2} - \frac{1}{\omega_1 - i\Omega_n - \omega_3} \right) \right. \\
&\quad \left. + \frac{1}{\omega_2 - \omega_3} \left(\frac{f(\omega_2)}{\omega_2 + i\Omega_n - \omega_1} - \frac{f(\omega_3)}{\omega_3 + i\Omega_n - \omega_1} \right) \right], \tag{D.54}
\end{aligned}$$

$$\begin{aligned}
\Pi_2 &= \int d\omega_1 d\omega_2 d\omega_3 A_{\mathbf{p}}(\omega_1) A_{\mathbf{p}}(\omega_2) A_{\mathbf{p}}(\omega_3) \\
&\quad \times \left[\frac{f(\omega_1)}{\omega_2 - \omega_3} \left(\frac{1}{\omega_1 + i\Omega_n - \omega_2} - \frac{1}{\omega_1 + i\Omega_n - \omega_3} \right) \right. \\
&\quad \left. + \frac{1}{\omega_2 - \omega_3} \left(\frac{f(\omega_2)}{\omega_2 - i\Omega_n - \omega_1} - \frac{f(\omega_3)}{\omega_3 - i\Omega_n - \omega_1} \right) \right] \tag{D.55}
\end{aligned}$$

Now we can replace $i\Omega_n \rightarrow \Omega + i0^+$ to complete the analytic continuation. We only need to compute the **real** part of $\Pi_{\mathbf{p}}(\Omega)$. For simplicity, we write $(d\omega) \equiv d\omega_1 d\omega_2 d\omega_3$.

The first term in Π_1 :

$$\begin{aligned}
& \int (d\omega) A_{\mathbf{p}}(\omega_1) A_{\mathbf{p}}(\omega_2) A_{\mathbf{p}}(\omega_3) \frac{f(\omega_1)}{\omega_1 - i\Omega_n - \omega_2} \frac{1}{\omega_2 - \omega_3} \\
\rightarrow & \int (d\omega) A_{\mathbf{p}}(\omega_1) A_{\mathbf{p}}(\omega_2) A_{\mathbf{p}}(\omega_3) \frac{f(\omega_1)}{\omega_1 - \omega_2 - \Omega} \frac{1}{\omega_2 - \omega_3} \\
= & \int d\omega_1 d\omega_2 \frac{f(\omega_1)}{\omega_1 - \omega_2 - \Omega} A_{\mathbf{p}}(\omega_1) A_{\mathbf{p}}(\omega_2) \int d\omega_3 \frac{A_{\mathbf{p}}(\omega_3)}{\omega_2 - \omega_3} \\
= & \int d\omega_1 d\omega_2 \frac{f(\omega_1)}{\omega_1 - \omega_2 - \Omega} A_{\mathbf{p}}(\omega_1) A_{\mathbf{p}}(\omega_2) \Re G_{\mathbf{p}}(\omega_2) \\
= & \int d\omega_1 f(\omega_1) A_{\mathbf{p}}(\omega_1) \left(-\frac{1}{2\pi} \right) \int d\omega_2 \frac{\Im G_{\mathbf{p}}^2(\omega_2)}{\omega_1 - \omega_2 - \Omega} \\
= & \frac{1}{2} \int d\omega_1 f(\omega_1) A_{\mathbf{p}}(\omega_1) \Re G_{\mathbf{p}}^2(\omega_1 - \Omega). \tag{D.56}
\end{aligned}$$

Simply by exchanging ω_2 and ω_3 in Eq. D.57, the second term in Π_2 is

$$\begin{aligned}
& \int (d\omega) A_{\mathbf{p}}(\omega_1) A_{\mathbf{p}}(\omega_2) A_{\mathbf{p}}(\omega_3) \frac{f(\omega_1)}{\omega_1 - i\Omega_n - \omega_2} \frac{1}{\omega_2 - \omega_3} \\
\rightarrow & \frac{1}{2} \int d\omega_1 f(\omega_1) A_{\mathbf{p}}(\omega_1) \Re G_{\mathbf{p}}^2(\omega_1 - \Omega). \tag{D.57}
\end{aligned}$$

The third term in Π_1 is

$$\begin{aligned}
& \int (d\omega) A_{\mathbf{p}}(\omega_1) A_{\mathbf{p}}(\omega_2) A_{\mathbf{p}}(\omega_3) \frac{f(\omega_2)}{\omega_2 + i\Omega_n - \omega_1} \frac{1}{\omega_2 - \omega_3} \\
\rightarrow & \int (d\omega) A_{\mathbf{p}}(\omega_1) A_{\mathbf{p}}(\omega_2) \frac{f(\omega_2)}{\omega_2 + \Omega - \omega_1} \int d\omega_3 \frac{A_{\mathbf{p}}(\omega_3)}{\omega_2 - \omega_3} \\
= & \int d\omega_2 f(\omega_2) A_{\mathbf{p}}(\omega_2) \Re G_{\mathbf{p}}(\omega_2) \int d\omega_1 \frac{A_{\mathbf{p}}(\omega_1)}{\omega_2 + \Omega - \omega_1} \\
= & \int d\omega_2 f(\omega_2) A_{\mathbf{p}}(\omega_2) \Re G_{\mathbf{p}}(\omega_2) \Re G_{\mathbf{p}}(\omega_2 + \Omega). \tag{D.58}
\end{aligned}$$

Exchanging $\omega_2 \leftrightarrow \omega_3$ in the equation above, leads to the fourth term in Π_1

$$\begin{aligned}
& \int (d\omega) A_{\mathbf{p}}(\omega_1) A_{\mathbf{p}}(\omega_2) A_{\mathbf{p}}(\omega_3) \frac{f(\omega_3)}{\omega_3 + i\Omega_n - \omega_1} \frac{1}{\omega_3 - \omega_2} \\
\rightarrow & \int d\omega_3 f(\omega_3) A_{\mathbf{p}}(\omega_3) \Re G_{\mathbf{p}}(\omega_3) \Re G_{\mathbf{p}}(\omega_3 + \Omega). \tag{D.59}
\end{aligned}$$

Summarily,

$$\Pi_1 = \int d\omega f(\omega + \Omega) A_{\mathbf{p}}(\omega + \Omega) \Re G_{\mathbf{p}}^2(\omega) + 2 \int d\omega f(\omega) A_{\mathbf{p}}(\omega) \Re G_{\mathbf{p}}(\omega) \Re G_{\mathbf{p}}(\omega + \Omega). \tag{D.60}$$

Π_2 is computed in a similar way, which turns out to be

$$\Pi_2 = \int d\omega f(\omega - \Omega) A_{\mathbf{p}}(\omega - \Omega) \Re G_{\mathbf{p}}^2(\omega) + 2 \int d\omega f(\omega) A_{\mathbf{p}}(\omega) \Re G_{\mathbf{p}}(\omega) \Re G_{\mathbf{p}}(\omega - \Omega). \tag{D.61}$$

Consequently,

$$\begin{aligned}
\frac{1}{-i\Omega_n}\Pi(i\Omega_n) &\rightarrow \frac{1}{-\Omega}\Pi(\Omega) \\
&= 2 \int d\omega \frac{f(\omega + \Omega)A_{\mathbf{p}}(\omega + \Omega) - f(\omega - \Omega)A_{\mathbf{p}}(\omega - \Omega)}{2\Omega} \Re G_{\mathbf{p}}^2(\omega) \\
&\quad + 4 \int d\omega f(\omega)A_{\mathbf{p}}(\omega) \Re G_{\mathbf{p}}(\omega) \frac{\Re G_{\mathbf{p}}(\omega + \Omega) - \Re G_{\mathbf{p}}(\omega - \Omega)}{2\Omega}. \quad (\text{D.62})
\end{aligned}$$

Taking the static limit, $\Omega \rightarrow 0$,

$$\begin{aligned}
\lim_{\Omega \rightarrow 0} \frac{1}{-\Omega}\Pi(\Omega) &= 2 \int d\omega \frac{\partial}{\partial \omega} (f(\omega)A_{\mathbf{p}}(\omega)) \Re G_{\mathbf{p}}^2(\omega) + 4 \int d\omega f(\omega)A_{\mathbf{p}}(\omega) \Re G_{\mathbf{p}}(\omega) \frac{\partial}{\partial \omega} (\Re G_{\mathbf{p}}(\omega)) \\
&= 2 \int d\omega \frac{\partial}{\partial \omega} (f(\omega)A_{\mathbf{p}}(\omega)) \Re G_{\mathbf{p}}^2(\omega) + 2 \int d\omega f(\omega)A_{\mathbf{p}}(\omega) \frac{\partial}{\partial \omega} (\Re G_{\mathbf{p}}(\omega))^2 \\
&= -2 \int d\omega \frac{\partial (f(\omega)A_{\mathbf{p}}(\omega))}{\partial \omega} (\Im G_{\mathbf{p}}(\omega))^2 \\
&= -2\pi^2 \int d\omega \frac{\partial (f(\omega)A_{\mathbf{p}}(\omega))}{\partial \omega} A_{\mathbf{p}}^2(\omega) \\
&= \frac{2\pi^2}{3} \int d\omega \left(-\frac{\partial f(\omega)}{\partial \omega} \right) A_{\mathbf{p}}^3(\omega). \quad (\text{D.63})
\end{aligned}$$

Thus the transverse conductivity in the long wavelength and static limit is

$$\sigma_{yx} = \frac{2\pi^2}{3} B_z \sum_{\mathbf{p}} \epsilon_{\mathbf{p}}^y (\epsilon_{\mathbf{p}}^{xy} \epsilon_{\mathbf{p}}^x - \epsilon_{\mathbf{p}}^{xx} \epsilon_{\mathbf{p}}^y) \int d\omega \left(-\frac{\partial f(\omega)}{\partial \omega} \right) A_{\mathbf{p}}^3(\omega) \quad (\text{D.64})$$

References

- [1] O. Gunnarsson, M. Calandra, and J. E. Han, “*Colloquium* : Saturation of electrical resistivity,” *Rev. Mod. Phys.*, vol. 75, pp. 1085–1099, Oct 2003.
- [2] M. Uchida, K. Oishi, M. Matsuo, W. Koshibae, Y. Onose, M. Mori, J. Fujioka, S. Miyasaka, S. Maekawa, and Y. Tokura, “Thermoelectric response in the incoherent transport region near Mott transition: The case study of $\text{La}_{1-x}\text{Sr}_x\text{VO}_3$,” *Phys. Rev. B*, vol. 83, p. 165127, Apr 2011.
- [3] A. Schroder, G. Aeppli, R. Coldea, M. Adams, Q. Stockert, H. Lohneysen, E. Bucher, R. Ramazashvili, and P. Coleman, “Onset of antiferromagnetism in heavy-fermion metals,” *Nature*, vol. 407, pp. 351–355, Sep 2000.
- [4] P. Sun, W. Xu, J. M. Tomczak, G. Kotliar, M. S ndergaard, B. B. Iversen, and F. Steglich, “Highly dispersive electron relaxation and colossal thermoelectricity in the correlated semiconductor FeSb_2 ,” *Phys. Rev. B*, vol. 88, p. 245203, Dec 2013.
- [5] N. W. Ashcroft and N. D. Mermin, *Solid State Physics*. Orlando, FL: Harcourt College Publishers, 1976.
- [6] P. Hohenberg and W. Kohn, “Inhomogeneous electron gas,” *Phys. Rev.*, vol. 136, pp. B864–B871, Nov 1964.
- [7] W. Kohn and L. J. Sham, “Self-consistent equations including exchange and correlation effects,” *Phys. Rev.*, vol. 140, pp. A1133–A1138, Nov 1965.
- [8] L. Hedin, “New method for calculating the one-particle green’s function with application to the electron-gas problem,” *Phys. Rev.*, vol. 139, pp. A796–A823, Aug 1965.
- [9] J. P. Perdew, “Density-functional approximation for the correlation energy of the inhomogeneous electron gas,” *Phys. Rev. B*, vol. 33, pp. 8822–8824, Jun 1986.
- [10] J. P. Perdew, K. Burke, and M. Ernzerhof, “Generalized gradient approximation made simple,” *Phys. Rev. Lett.*, vol. 77, pp. 3865–3868, Oct 1996.
- [11] L. Landau, “The theory of a fermi liquid,” *Sov. Phys. JETP*, vol. 3, no. 6, p. 920, 1957.
- [12] P. Nozieres, *Theory of interacting Fermi systems*. Addison-Wesley, 1964.
- [13] R. Shankar, “Renormalization-group approach to interacting fermions,” *Rev. Mod. Phys.*, vol. 66, pp. 129–192, Jan 1994.
- [14] A. A. Abrikosov, L. P. Go rkov, and I. E. Dzyaloshinski, *Methods of quantum field theory in statistical physics*. Courier Dover Publications, 1975.

- [15] G. Palsson, *Computational Studies of Thermoelectricity in Strongly Correlated Electron Systems*. PhD thesis, Rutgers University, New Brunswick, NJ, 5 2001.
- [16] V. J. Emery and S. A. Kivelson, “Superconductivity in bad metals,” *Phys. Rev. Lett.*, vol. 74, pp. 3253–3256, Apr 1995.
- [17] G. R. Stewart, “Non-fermi-liquid behavior in d - and f -electron metals,” *Rev. Mod. Phys.*, vol. 73, pp. 797–855, Oct 2001.
- [18] R. Kubo, “Statistical-mechanical theory of irreversible processes. I. general theory and simple applications to magnetic and conduction problems,” *Journal of the Physical Society of Japan*, vol. 12, no. 6, pp. 570–586, 1957.
- [19] G. D. Mahan, *Many-particle physics*. Springer, 2000.
- [20] A. L. Fetter and J. D. Walecka, *Quantum theory of many-particle systems*. Courier Dover Publications, 2003.
- [21] A. Altland and B. D. Simons, *Condensed matter field theory*. Cambridge University Press, 2010.
- [22] H. Vidberg and J. Serene, “Solving the eliashberg equations by means ofn-point padé approximants,” *Journal of Low Temperature Physics*, vol. 29, no. 3, pp. 179–192, 1977.
- [23] M. Jarrell and J. Gubernatis, “Bayesian inference and the analytic continuation of imaginary-time quantum monte carlo data,” *Physics Reports*, vol. 269, no. 3, pp. 133 – 195, 1996.
- [24] W. Metzner and D. Vollhardt, “Correlated lattice fermions in $d = \infty$ dimensions,” *Phys. Rev. Lett.*, vol. 62, pp. 324–327, Jan 1989.
- [25] G. Kotliar and D. Vollhardt, “Strongly correlated materials: Insights from dynamical mean field theory,” *Physics Today*, vol. 57, p. 57, Mar 2004.
- [26] A. Georges and G. Kotliar, “Hubbard model in infinite dimensions,” *Phys. Rev. B*, vol. 45, pp. 6479–6483, Mar 1992.
- [27] A. Georges, G. Kotliar, W. Krauth, and M. J. Rozenberg, “Dynamical mean-field theory of strongly correlated fermion systems and the limit of infinite dimensions,” *Rev. Mod. Phys.*, vol. 68, pp. 13–125, Jan 1996.
- [28] V. Zlatić and B. Horvatić, “The local approximation for correlated systems on high dimensional lattices,” *Solid State Communications*, vol. 75, no. 3, pp. 263–267, 1990.
- [29] M. J. Rozenberg, G. Kotliar, and H. Kajueter, “Transfer of spectral weight in spectroscopies of correlated electron systems,” *Phys. Rev. B*, vol. 54, pp. 8452–8468, Sep 1996.
- [30] P. Werner, A. Comanac, L. de’ Medici, M. Troyer, and A. J. Millis, “Continuous-time solver for quantum impurity models,” *Phys. Rev. Lett.*, vol. 97, p. 076405, Aug 2006.

- [31] E. Gull, A. J. Millis, A. I. Lichtenstein, A. N. Rubtsov, M. Troyer, and P. Werner, “Continuous-time Monte Carlo methods for quantum impurity models,” *Rev. Mod. Phys.*, vol. 83, pp. 349–404, May 2011.
- [32] K. Haule, “Quantum Monte Carlo impurity solver for cluster dynamical mean-field theory and electronic structure calculations with adjustable cluster base,” *Phys. Rev. B*, vol. 75, p. 155113, Apr 2007.
- [33] J. E. Hirsch and R. M. Fye, “Monte Carlo method for magnetic impurities in metals,” *Phys. Rev. Lett.*, vol. 56, pp. 2521–2524, Jun 1986.
- [34] R. E. Prange and L. P. Kadanoff, “Transport theory for electron-phonon interactions in metals,” *Phys. Rev.*, vol. 134, pp. A566–A580, May 1964.
- [35] T. Pruschke, D. L. Cox, and M. Jarrell, “Hubbard model at infinite dimensions: Thermodynamic and transport properties,” *Phys. Rev. B*, vol. 47, pp. 3553–3565, Feb 1993.
- [36] T. Pruschke, M. Jarrell, and J. Freericks, “Anomalous normal-state properties of high- T_c superconductors: intrinsic properties of strongly correlated electron systems?,” *Advances in Physics*, vol. 44, no. 2, pp. 187–210, 1995.
- [37] H. Kajueter, G. Kotliar, and G. Moeller, “Doped Mott insulator: Results from mean-field theory,” *Phys. Rev. B*, vol. 53, pp. 16214–16226, Jun 1996.
- [38] G. Pálsson and G. Kotliar, “Thermoelectric response near the density driven Mott transition,” *Phys. Rev. Lett.*, vol. 80, pp. 4775–4778, May 1998.
- [39] E. Lange and G. Kotliar, “Magnetotransport in the doped Mott insulator,” *Phys. Rev. B*, vol. 59, pp. 1800–1807, Jan 1999.
- [40] W. Xu, C. Weber, and G. Kotliar, “High-frequency thermoelectric response in correlated electronic systems,” *Phys. Rev. B*, vol. 84, p. 035114, Jul 2011.
- [41] X. Deng, J. Mravlje, R. Žitko, M. Ferrero, G. Kotliar, and A. Georges, “How bad metals turn good: Spectroscopic signatures of resilient quasiparticles,” *Phys. Rev. Lett.*, vol. 110, p. 086401, Feb 2013.
- [42] L.-F. Arsenault, B. S. Shastry, P. Sémon, and A.-M. S. Tremblay, “Entropy, frustration, and large thermopower of doped Mott insulators on the fcc lattice,” *Phys. Rev. B*, vol. 87, p. 035126, Jan 2013.
- [43] M. J. Rozenberg, G. Kotliar, H. Kajueter, G. A. Thomas, D. H. Rapkine, J. M. Honig, and P. Metcalf, “Optical conductivity in Mott-Hubbard systems,” *Phys. Rev. Lett.*, vol. 75, pp. 105–108, Jul 1995.
- [44] J. Merino and R. H. McKenzie, “Transport properties of strongly correlated metals: A dynamical mean-field approach,” *Phys. Rev. B*, vol. 61, pp. 7996–8008, Mar 2000.
- [45] P. Limelette, P. Wzietek, S. Florens, A. Georges, T. A. Costi, C. Pasquier, D. Jérôme, C. Mézière, and P. Batail, “Mott transition and transport crossovers in the organic compound κ -(BEDT-TTF) $_2$ Cu[N(CN) $_2$]Cl,” *Phys. Rev. Lett.*, vol. 91, p. 016401, Jul 2003.

- [46] J. Merino, M. Dumm, N. Drichko, M. Dressel, and R. H. McKenzie, “Quasiparticles at the verge of localization near the Mott metal-insulator transition in a two-dimensional material,” *Phys. Rev. Lett.*, vol. 100, p. 086404, Feb 2008.
- [47] D. S. Fisher, G. Kotliar, and G. Moeller, “Midgap states in doped Mott insulators in infinite dimensions,” *Phys. Rev. B*, vol. 52, pp. 17112–17118, Dec 1995.
- [48] P. Grete, S. Schmitt, C. Raas, F. B. Anders, and G. S. Uhrig, “Kinks in the electronic dispersion of the Hubbard model away from half filling,” *Phys. Rev. B*, vol. 84, p. 205104, Nov 2011.
- [49] M. Jonson and G. D. Mahan, “Mott’s formula for the thermopower and the Wiedemann-Franz law,” *Phys. Rev. B*, vol. 21, pp. 4223–4229, May 1980.
- [50] K. Behnia, “The Nernst effect and the boundaries of the Fermi liquid picture,” *Journal of Physics: Condensed Matter*, vol. 21, no. 11, p. 113101, 2009.
- [51] N. Hussey, K. Takenaka, and H. Takagi, “Universality of the Mott–Ioffe–Regel limit in metals,” *Philosophical Magazine*, vol. 84, no. 27, pp. 2847–2864, 2004.
- [52] J. Hubbard, “Electron correlations in narrow energy bands,” *Proceedings of the Royal Society of London. Series A. Mathematical and Physical Sciences*, vol. 276, no. 1365, pp. 238–257, 1963.
- [53] W. F. Brinkman and T. M. Rice, “Application of Gutzwiller’s variational method to the metal-insulator transition,” *Phys. Rev. B*, vol. 2, pp. 4302–4304, Nov 1970.
- [54] M. Eckstein, M. Kollar, and D. Vollhardt, “Isosbestic points in the spectral function of correlated electrons,” *Journal of Low Temperature Physics*, vol. 147, no. 3–4, pp. 279–293, 2007.
- [55] M. Jarrell and T. Pruschke, “Anomalous properties of the Hubbard model in infinite dimensions,” *Phys. Rev. B*, vol. 49, pp. 1458–1461, Jan 1994.
- [56] A. C. Hewson, *The Kondo problem to heavy fermions*. Cambridge university press, 1997.
- [57] H. Park, *The Study of Two-Particle Response Functions in Strongly Correlated Electron Systems Within the Dynamical Mean Field Theory*. PhD thesis, Rutgers University, New Brunswick, New Jersey, October 2011.
- [58] H. Park, K. Haule, and G. Kotliar, “Magnetic excitation spectra in BaFe₂As₂: A two-particle approach within a combination of the density functional theory and the dynamical mean-field theory method,” *Phys. Rev. Lett.*, vol. 107, p. 137007, Sep 2011.
- [59] D. Van der Marel, H. Molegraaf, J. Zaanen, Z. Nussinov, F. Carbone, A. Damascelli, H. Eisaki, M. Greven, P. Kes, M. Li, *et al.*, “Quantum critical behaviour in a high-T_c superconductor,” *Nature*, vol. 425, pp. 271–274, Sep 2003.
- [60] D. N. Basov, R. D. Averitt, D. van der Marel, M. Dressel, and K. Haule, “Electrodynamics of correlated electron materials,” *Rev. Mod. Phys.*, vol. 83, pp. 471–541, Jun 2011.

- [61] H. Drew, S. Wu, and H. S. Lihn, “The ac Hall effect in high-superconductors,” *Journal of Physics: Condensed Matter*, vol. 8, no. 48, p. 10037, 1996.
- [62] J. Mravlje, M. Aichhorn, T. Miyake, K. Haule, G. Kotliar, and A. Georges, “Coherence-incoherence crossover and the mass-renormalization puzzles in Sr_2RuO_4 ,” *Phys. Rev. Lett.*, vol. 106, p. 096401, Mar 2011.
- [63] R. Arita, K. Held, A. V. Lukoyanov, and V. I. Anisimov, “Doped Mott insulator as the origin of heavy-fermion behavior in LiV_2O_4 ,” *Phys. Rev. Lett.*, vol. 98, p. 166402, Apr 2007.
- [64] M. K. Stewart, C.-H. Yee, J. Liu, M. Kareev, R. K. Smith, B. C. Chapler, M. Varela, P. J. Ryan, K. Haule, J. Chakhalian, and D. N. Basov, “Optical study of strained ultrathin films of strongly correlated LaNiO_3 ,” *Phys. Rev. B*, vol. 83, p. 075125, Feb 2011.
- [65] X. Deng, M. Ferrero, J. Mravlje, M. Aichhorn, and A. Georges, “Hallmark of strong electronic correlations in LaNiO_3 : Photoemission kink and broadening of fully occupied bands,” *Phys. Rev. B*, vol. 85, p. 125137, Mar 2012.
- [66] S. I. Mirzaei, D. Stricker, J. N. Hancock, C. Berthod, A. Georges, E. van Heumen, M. K. Chan, X. Zhao, Y. Li, M. Greven, N. Barišić, and D. van der Marel, “Evidence for a Fermi liquid in the pseudogap phase of high- T_c cuprates,” *ArXiv e-prints*, July 2012.
- [67] K. Haule and G. Kotliar, “Strongly correlated superconductivity: A plaquette dynamical mean-field theory study,” *Phys. Rev. B*, vol. 76, p. 104509, Sep 2007.
- [68] P. W. Anderson, “Hidden fermi liquid: The secret of high- T_c cuprates,” *Phys. Rev. B*, vol. 78, p. 174505, Nov 2008.
- [69] P. A. Casey and P. W. Anderson, “Hidden fermi liquid: Self-consistent theory for the normal state of high- T_c superconductors,” *Phys. Rev. Lett.*, vol. 106, p. 097002, Feb 2011.
- [70] B. S. Shastry, “Extremely correlated Fermi liquids,” *Phys. Rev. Lett.*, vol. 107, p. 056403, Jul 2011.
- [71] G. Mahan, “Good thermoelectrics,” in *Solid State Physics* (H. EHRENREICH and F. SPAEPEN, eds.), vol. 51, pp. 81 – 157, Academic Press, 1997.
- [72] G. Mahan, B. Sales, and J. Sharp, “Thermoelectric materials: New approaches to an old problem,” *Physics Today*, vol. 50, no. 3, pp. 42–47, 1997.
- [73] G. J. Snyder and E. S. Toberer, “Complex thermoelectric materials,” *Nature Mater.*, vol. 7, pp. 105–114, 2008.
- [74] P. M. Chaikin and G. Beni, “Thermopower in the correlated hopping regime,” *Phys. Rev. B*, vol. 13, pp. 647–651, Jan 1976.
- [75] G. Beni, “Thermoelectric power of the narrow-band Hubbard chain at arbitrary electron density: Atomic limit,” *Phys. Rev. B*, vol. 10, pp. 2186–2189, Sep 1974.

- [76] W. Koshibae, K. Tsutsui, and S. Maekawa, “Thermopower in cobalt oxides,” *Phys. Rev. B*, vol. 62, pp. 6869–6872, Sep 2000.
- [77] V. S. Oudovenko and G. Kotliar, “Thermoelectric properties of the degenerate Hubbard model,” *Phys. Rev. B*, vol. 65, p. 075102, Jan 2002.
- [78] S. Chakraborty, D. Galanakis, and P. Phillips, “Emergence of particle-hole symmetry near optimal doping in high-temperature copper oxide superconductors,” *Phys. Rev. B*, vol. 82, p. 214503, Dec 2010.
- [79] M. R. Peterson and B. S. Shastry, “Kelvin formula for thermopower,” *Phys. Rev. B*, vol. 82, p. 195105, Nov 2010.
- [80] B. S. Shastry, “Electrothermal transport coefficients at finite frequencies,” *Reports on Progress in Physics*, vol. 72, no. 1, p. 016501, 2009.
- [81] B. S. Shastry, “Sum rule for thermal conductivity and dynamical thermal transport coefficients in condensed matter,” *Phys. Rev. B*, vol. 73, p. 085117, Feb 2006.
- [82] J. M. Luttinger, “Theory of thermal transport coefficients,” *Phys. Rev.*, vol. 135, pp. A1505–A1514, Sep 1964.
- [83] D. Pines and P. Nozières, *The Theory of Quantum Liquids*. New York: W. A. Benjamin, Inc., 1966.
- [84] I. Paul and G. Kotliar, “Thermal transport for many-body tight-binding models,” *Phys. Rev. B*, vol. 67, p. 115131, Mar 2003.
- [85] K. Haule and G. Kotliar, “Thermoelectrics near the Mott localization-delocalization transition,” *Properties and Applications of Thermoelectric Materials*, pp. 119–131, 2009.
- [86] M. Matsuo, S. Okamoto, W. Koshibae, M. Mori, and S. Maekawa, “Nonmonotonic temperature dependence of thermopower in strongly correlated electron systems,” *Phys. Rev. B*, vol. 84, p. 153107, Oct 2011.
- [87] S. Doniach, “The Kondo lattice and weak antiferromagnetism,” *Physica B+C*, vol. 91, no. 0, pp. 231 – 234, 1977.
- [88] P. Coleman, C. Ppin, Q. Si, and R. Ramazashvili, “How do Fermi liquids get heavy and die?,” *Journal of Physics: Condensed Matter*, vol. 13, no. 35, p. R723, 2001.
- [89] H. v. Löhneysen, A. Rosch, M. Vojta, and P. Wölfle, “Fermi-liquid instabilities at magnetic quantum phase transitions,” *Rev. Mod. Phys.*, vol. 79, pp. 1015–1075, Aug 2007.
- [90] P. Gegenwart, Q. Si, and F. Steglich, “Quantum criticality in heavy-fermion metals,” *Nature Physics*, vol. 4, pp. 186–197, Mar 2008.
- [91] Q. Si and F. Steglich, “Heavy fermions and quantum phase transitions,” *Science*, vol. 329, pp. 1161–1166, Sep 2010.

- [92] G. Kotliar, S. Y. Savrasov, K. Haule, V. S. Oudovenko, O. Parcollet, and C. A. Marianetti, “Electronic structure calculations with dynamical mean-field theory,” *Rev. Mod. Phys.*, vol. 78, pp. 865–951, Aug 2006.
- [93] M. J. Rozenberg, “Zero-temperature magnetism in the periodic anderson model in the limit of large dimensions,” *Phys. Rev. B*, vol. 52, pp. 7369–7377, Sep 1995.
- [94] P. Sun and G. Kotliar, “Understanding the heavy fermion phenomenology from a microscopic model,” *Phys. Rev. Lett.*, vol. 95, p. 016402, Jun 2005.
- [95] D. Tanasković, K. Haule, G. Kotliar, and V. Dobrosavljević, “Phase diagram, energy scales, and nonlocal correlations in the Anderson lattice model,” *Phys. Rev. B*, vol. 84, p. 115105, Sep 2011.
- [96] L. Boehnke, H. Hafermann, M. Ferrero, F. Lechermann, and O. Parcollet, “Orthogonal polynomial representation of imaginary-time Green’s functions,” *Phys. Rev. B*, vol. 84, p. 075145, Aug 2011.
- [97] P. Gegenwart, J. Custers, Y. Tokiwa, C. Geibel, and F. Steglich, “Ferromagnetic quantum critical fluctuations in $\text{YbRh}_2(\text{Si}_{0.95}\text{Ge}_{0.05})_2$,” *Phys. Rev. Lett.*, vol. 94, p. 076402, Feb 2005.
- [98] Q. Si, S. Rabello, K. Ingersent, and J. L. Smith, “Locally critical quantum phase transitions in strongly correlated metals,” *Nature*, vol. 413, pp. 804–808, Oct 2001.
- [99] C. Pépin, “Kondo breakdown as a selective Mott transition in the Anderson lattice,” *Phys. Rev. Lett.*, vol. 98, p. 206401, May 2007.
- [100] L. de’ Medici, A. Georges, G. Kotliar, and S. Biermann, “Mott transition and Kondo screening in f -electron metals,” *Phys. Rev. Lett.*, vol. 95, p. 066402, Aug 2005.
- [101] L. De Leo, M. Civelli, and G. Kotliar, “ $T = 0$ heavy-fermion quantum critical point as an orbital-selective Mott transition,” *Phys. Rev. Lett.*, vol. 101, p. 256404, Dec 2008.
- [102] A. Bentien, S. Johnsen, G. K. H. Madsen, B. B. Iversen, and F. Steglich, “Colossal Seebeck coefficient in strongly correlated semiconductor FeSb_2 ,” *EPL (Europhysics Letters)*, vol. 80, no. 1, p. 17008, 2007.
- [103] A. Perucchi, L. Degiorgi, R. Hu, C. Petrovic, and V. F. Mitrovi, “Optical investigation of the metal-insulator transition in FeSb_2 ,” *The European Physical Journal B - Condensed Matter and Complex Systems*, vol. 54, no. 2, pp. 175–183, 2006.
- [104] A. Herzog, M. Marutzky, J. Sichelschmidt, F. Steglich, S. Kimura, S. Johnsen, and B. B. Iversen, “Strong electron correlations in FeSb_2 : An optical investigation and comparison with RuSb_2 ,” *Phys. Rev. B*, vol. 82, p. 245205, Dec 2010.
- [105] C. Petrovic, J. W. Kim, S. L. Bud’ko, A. I. Goldman, P. C. Canfield, W. Choe, and G. J. Miller, “Anisotropy and large magnetoresistance in the narrow-gap semiconductor FeSb_2 ,” *Phys. Rev. B*, vol. 67, p. 155205, Apr 2003.

- [106] W. Xu, K. Haule, and G. Kotliar, “Hidden Fermi liquid, scattering rate saturation, and Nernst effect: A dynamical mean-field theory perspective,” *Phys. Rev. Lett.*, vol. 111, p. 036401, Jul 2013.
- [107] K. Seeger, *Semiconductor Physics*. Berlin: Springer-Verlag, 1991.
- [108] J. Schwinger, “Brownian motion of a quantum oscillator,” *Journal of Mathematical Physics*, vol. 2, no. 3, pp. 407–432, 1961.
- [109] L. Keldysh, “Diagram technique for nonequilibrium processes,” *Sov. Phys. JETP*, vol. 20, no. 4, pp. 1018–1026, 1965.
- [110] J. Rammer, *Quantum field theory of non-equilibrium states*. Cambridge University Press, 2007.
- [111] G. Eliashberg, “Transport equation for a degenerate system of Fermi particles,” *SOVIET PHYSICS JETP*, vol. 14, no. 4, 1962.
- [112] Wikipedia, “Padé approximant — wikipedia, the free encyclopedia,” 2014. [Online; accessed 31-August-2014].
- [113] G. Baker and P. Graves-Morris, “Padé approximants (encyclopedia of mathematics and its applications vol 59),” 1996.
- [114] K.-H. Lee and K. J. Chang, “Analytic continuation of the dynamic response function using an N -point Padé approximant,” *Phys. Rev. B*, vol. 54, pp. R8285–R8288, Sep 1996.